



SAKARYA ÜNİVERSİTESİ

# FEN BİLİMLERİ ENSTİTÜSÜ DERGİSİ

Sakarya University Journal of Science (SAUJS)



SAKARYA  
ÜNİVERSİTESİ

e-issn: 2147-835X

Volume: 28

Issue: 2

April 2024

VOLUME: 28 ISSUE: 2  
E-ISSN 2147-835X

APRIL 2024  
<https://dergipark.org.tr/tr/pub/sofenbilder>

# SAKARYA UNIVERSITY JOURNAL OF SCIENCE



**SAKARYA**  
ÜNİVERSİTESİ

---

---

# The Owner on Behalf of Sakarya University

---

---

Prof. Dr. Hamza Al  
Sakarya University, Sakarya-Türkiye

---

---

## Publishing Manager

---

---

Hüseyin Özkan Toplan  
Department of Engineering  
Sakarya University, Sakarya-Türkiye  
toplano@sakarya.edu.tr

---

---

## Editor in Chief

---

---

Ömer Tamer  
Department of Physics  
Sakarya University, Sakarya-Türkiye  
omertamer@sakarya.edu.tr

---

---

## Associate Editors

---

---

İhsan Hakan Selvi  
Department of Information Systems Engineering  
Sakarya University, Sakarya-Türkiye  
ihselvi@sakarya.edu.tr

---

---

## Editorial Board

---

---

Asude Ateş  
Department of Environmental Sciences and  
Engineering  
Sakarya University  
Sakarya - Türkiye  
aates@sakarya.edu.tr

Bahadır Respect  
Department of Nuclear Physics  
Ankara University  
Ankara - Türkiye  
bsaygi@ankara.edu.tr

Berrin Denizhan  
Department of Supply Chain and Logistics  
Management  
Sakarya University  
Sakarya - Türkiye  
denizhan@sakarya.edu.tr

Hüseyin Aksoy  
Department of Biology  
Sakarya University  
Sakarya - Türkiye  
haksoy@sakarya.edu.tr

Mehmet Uysal  
Department Coating Technology  
Composite Materials Nanomaterials  
Sakarya University  
Sakarya - Türkiye  
mehmetu@sakarya.edu.tr

Muhammed Fatih Adak  
Department of Computer Science and Engineering  
Sakarya University  
Sakarya - Türkiye  
fatihadak@sakarya.edu.tr

Muhammet Hilmi Nişancı  
Department of Electromagnetic, Microwave and  
Antenna Technologies  
Sakarya University  
Sakarya - Türkiye  
nisanci@sakarya.edu.tr

Mustafa Gülfen  
Department Analytical Chemistry  
Sakarya University  
Sakarya - Türkiye  
mgulfen@sakarya.edu.tr

Osman Sönmez  
Department of Fluid Mechanics  
Coastal Sciences and Engineering  
Sakarya University  
Sakarya - Türkiye  
osonmez@sakarya.edu.tr

Serap Coşansu  
Department of Food Hygiene and Production, Food  
Microbiology  
Sakarya University  
Sakarya - Türkiye  
scosansu@sakarya.edu.tr

Tahsin Turgay  
Department of Architecture, Design and  
Planning, Civil Engineering  
Sakarya University  
Sakarya - Türkiye  
turgay@sakarya.edu.tr

Ufuk Durmaz  
Department of Fluid Mechanics, Heat Transfer  
Thermodynamics, Renewable Energy Sources  
Sakarya University  
Sakarya - Türkiye  
udurmaz@sakarya.edu.tr

---

---

## Section Editor (Civil Engineering)

---

---

Elif Ağcakoca  
Department of Civil Engineering  
Sakarya University  
Sakarya - Türkiye  
elifd@sakarya.edu.tr

Faruk Fırat Çalım  
Department of Civil Engineering  
Adana Alparslan Türkeş  
Science and Technology University  
Adana - Türkiye  
ffcalim@atu.edu.tr

Issa Al-Harthy  
Department of Civil and Architectural Engineering  
Sultan Qaboos University  
Oman  
aissa@squ.edu.om

Jamal Khatib  
Department of Civil Engineering  
University of Wolverhampton  
United Kingdom  
jmkhatib@wlv.ac.uk

Khalifa Al-Jabri  
Department of Civil and Architectural Engineering  
Sultan Qaboos University  
Oman  
aljabri@squ.edu.om

Hakan Alp  
Department of Marine Science and  
Technology, Geophysical Engineering  
İstanbul University-Cerrahpaşa  
İstanbul - Türkiye  
hakanalp@iuc.edu.tr



Tuba Tatar  
Department Civil Engineering, Reinforced Concrete  
Structures, Earthquake, Engineering Design  
Sakarya University  
Sakarya - Türkiye  
ttatar@sakarya.edu.tr

Gokhan Dok  
Department Reinforced Concrete Structures  
Earthquake, Structural Dynamics, Structural  
Mechanics  
Sakarya University of Applied Sciences  
Sakarya - Türkiye  
gokhandok@subu.edu.tr

---

---

## Section Editor (Chemistry)

---

---

Can Serkan Keskin  
Department Analytical Chemistry  
Sakarya University  
Sakarya - Türkiye  
ckeskin@sakarya.edu.tr

Gražyna Simha Martynková  
Department of Chemistry Education Vsb-Technical  
University of Ostrava  
Czech Republic  
grazyna.simha@vsb.cz

Murat Tuna  
Department of Chemistry  
Sakarya University  
Sakarya - Türkiye  
tuna@sakarya.edu.tr

Aligholi Niaie  
Department Chemical Engineering  
University of Tabriz  
Iran  
aniaei@tabrizu.ac.ir

Nahit Gencer  
Department of Biochemistry  
Balıkesir University  
Sakarya - Türkiye  
ngencer@balikesir.edu.tr

---

---

## Section Editor (Biology)

---

---

Cansu Akbulut  
Department of Biology, Cell Biology, Histology and  
Embryology, Toxicology  
Sakarya University  
Sakarya - Türkiye  
cansua@sakarya.edu.tr

Luis Materon  
Department of Biology  
University of Texas Rio Grande Valley  
USA  
luis.materon@utrgv.edu

Nazan Deniz Yön Ertuğ  
Department of Biology, Hydrobiology  
Cell Biology, Aquaculture  
Sakarya University  
Sakarya - Türkiye  
nkoc@sakarya.edu.tr

Nihan Akıncı Kenanoğlu  
Department of Biology  
Çanakkale Onsekiz Mart University  
Çanakkale - Türkiye  
nakinci@comu.edu.tr

Oğuz Kurt  
Department of Hydrobiology  
Manisa Celal Bayar University  
Manisa - Türkiye  
oguz.kurt@cbu.edu.tr

Sezgi Somuncu  
Department of Biology  
Sakarya University  
Sakarya - Türkiye  
sezgisomuncu@sakarya.edu.tr

Sezen Toksoy Köseoğlu  
Department of Biology  
Sakarya University  
Sakarya - Türkiye  
sezentoksoy@sakarya.edu.tr

---

---

## Section Editor (Mathematics)

---

---

Murat Güzeltepe  
Department of Algebraic Number Theory  
Sakarya University  
Sakarya - Türkiye  
mguzeltepe@sakarya.edu.tr

Murat Sarduvan  
Department Fundamentals of Mathematics and  
Mathematical Logic  
Sakarya University  
Sakarya - Türkiye  
msarduvan@sakarya.edu.tr

Ali Demir  
Department of Mathematics, Analysis and  
Theory of Functions  
Kocaeli University  
Kocaeli - Türkiye  
ademir@kocaeli.edu.tr

Luan Hoang  
Department of Mathematical Analysis, Applied  
Mathematics Texas Tech University  
USA  
luan.hoang@ttu.edu

Selma Özçağ  
Department of Statistics  
Hacettepe University  
Ankara - Türkiye  
sozcag@hacettepe.edu.tr

Necati Olgun  
Department of Statistics  
Gaziantep University  
Gaziantep - Türkiye  
olgun@gantep.edu.tr

---

---

## Section Editor (Computer Science and Engineering)

---

---

Fahrettin Horasan  
Department of Computer Science and  
Engineering Information Security and Cryptology  
Kırıkkale University  
Kırıkkale - Türkiye  
fhorasan@kku.edu.tr

Kevser Ovaz Akpınar  
Department Cyber Security, Artificial Intelligence  
Programming  
Rochester Dubai Institute of Technology  
Dubai  
kxocad1@rit.edu

Muhammed Maruf Öztürk  
Department Computer Software  
Süleyman Demirel University  
Isparta - Türkiye  
muhammedozturk@sdu.edu.tr

Mustafa Akpınar  
Department Computer Science and  
Engineering Information Systems  
High Tech Collages  
United Arab Emirates  
mustafakpınar@gmail.com

---

---

## Section Editor (Physics)

---

---

Ceren Tayran  
Department Physics, Condensed Matter Physics  
Gazi University  
Ankara - Türkiye  
c.tayran@gazi.edu.tr

Grzegorz Jaworski  
Department of Nuclear Physics  
University of Warsaw  
Poland  
grzegorz.jaworski@pwr.edu.pl

---

---

## Section Editor (Industrial Engineering)

---

---

Feyza Gürbüz  
Department Industrial Engineering  
Erciyes University  
Kayseri - Türkiye  
feYZa@erciyes.edu.tr

Caner Erden  
Department Data Mining, Artificial Intelligence  
Algorithms and Theory of Computation  
Sakarya University of Applied Sciences  
Sakarya - Türkiye  
cerden@subu.edu.tr

Hatice Esen  
Department of Ergonomics and  
Human Factors Management  
Kocaeli University  
Kocaeli - Türkiye  
hatice.ERIS@kocaeli.edu.tr

Mehmet Emin Aydın  
Department Machine Learning  
Artificial Intelligence  
University of The West of England Bristol  
England  
mehmet.aydin@uwe.ac.uk,

Barış Yüce  
Department Industrial Engineering  
University of Exeter  
United Kingdom  
b.yuce@exeter.ac.uk

Benjamin Durakovic  
Department of Industrial and Mechanical Engineering  
International University of Sarajevo  
Bosnia and Herzegovina  
bdurakovic@ius.edu.ba

---

---

## Section Editor (Mechanical Engineering)

---

---

Elif Eker Kahveci  
Department of Engineering, Mechanical Engineering  
Sakarya University  
Sakarya - Türkiye  
eeker@sakarya.edu.tr

Erman Aslan  
Mechanical Engineering, Fluid Mechanics  
Computational Fluid Dynamics, Heat Transfer  
Kocaeli University  
Kocaeli - Türkiye  
erman.aslan@kocaeli.edu.tr

Mohammad Sukri Bin Mustapa  
Department of Mechanical and Manufacturing  
Engineering  
University Tun Hussein Onn Malaysia  
Malaysia  
sukri@uthm.edu.my

Raja Mazuir Bin Raja Ahsan Shah  
Department of Mechanical Engineering  
Coventry University  
United Kingdom  
ac9217@coventry.ac.uk

Seong Jin Park  
Department of Mechanical Engineering  
Pohang University of Science and Technology  
Korea  
sjpark87@postech.ac.kr

Abderrahmane Benbrik  
Department of Mechanical Engineering  
M'hamed Bougara University  
Egypt  
abderrahmane.benbrik@univ-boumerdes.dz

Ali Cemal Benim  
Department of Mechanical and Process Engineering  
Düsseldorf University of Applied Sciences  
Germany  
alicemal@prof-benim.com

Herman Nied  
Department of Solid Mechanics  
Lehigh University  
USA  
hfn2@lehigh.edu

Shi-Chune Yao  
Department Energy Technologies, Heat Transfer  
Carnegie Mellon University  
USA  
sy0d@andrew.cmu.edu

Tauseef Aized  
Energy Management and Conservation in  
Construction and Industrial Sectors  
Uet Lahore  
Pakistan  
tauseef.aized@uet.edu.pk

---

---

## Section Editor (Environmental Sciences and Engineering)

---

---

Ece Ümmü Deveci  
Department of Environmental Sciences and  
Engineering  
Niğde Omer Halisdemir University  
Niğde - TÜRKİYE  
eudeveci@ohu.edu.tr

Senay Çetin Doğruparmak  
Department of Environmental Engineering  
Kocaeli University  
Kocaeli - Türkiye  
senayc@kocaeli.edu.tr

---

---

## Section Editor (Food Science)

---

---

Aslı Uçar  
Department of Nutrition and Dietetics  
Ankara University  
Ankara - Türkiye  
aucar@ankara.edu.tr

Edgar Perez Esteve  
Department of Food Sciences  
Polytechnic University of Valencia  
Spain  
edpees@upv.es

Syed Abbas  
Department of Cereal Technology, Food Microbiology  
Curtin University  
Australia  
s.abbas@curtin.edu.au

---

---

## Section Editor (Electrical and Electronics Engineering)

---

---

Abdullah Oğuz Kızılçay  
Department of Electromagnetics  
Microwave and Antenna Technologies  
Zonguldak Bülent Ecevit University  
Zonguldak - Türkiye  
oguzkizilcay@yyu.edu.tr

İbrahim Bahadır Başığit  
Department of Electromagnetics  
Microwave and Antenna Technologies  
Isparta University of Applied Sciences  
Isparta - Türkiye  
bahadirbasyigit@isparta.edu.tr

Francesco De Paulis  
Department of Electromagnetics  
Microwave and Antenna Technologies  
L'Aquila University  
Italy  
francesco.depaulis@univaq.it

Mesut Baran  
Department of Electrical and  
Computer Engineering  
North Carolina State University  
USA  
baran@ncsu.edu

Ozan Erdinç  
Department of Electrical and  
Electronics Engineering  
Yıldız Technical University  
İstanbul - Türkiye  
oerdinc@yildiz.edu.tr

Rıfki Terzioğlu  
Department of Superconductors  
Electrical Energy and Power Systems  
Bolu Abant İzzet Baysal University  
Bolu - Türkiye  
rifkiterzioğlu@ibu.edu.tr

---

---

## Section Editor (Architecture)

---

---

İsmail Hakkı Demir  
Department of Architectural Design, Project and Production Management, Urban Design  
Sakarya University  
Sarkaya - Türkiye  
idemir@sakarya.edu.tr

---

---

## Section Editor (Materials Science)

---

---

Miraç Alaf  
Department Metallurgical and Materials  
Engineering, Coating Technology  
Bilecik Şeyh Edebali University  
Bilecik - Türkiye  
mirac.alaf@bilecik.edu.tr

Kamaruzzaman Sopian  
Department of Materials Science and Technology  
Mechanical Engineering  
Universiti Kebangsaan  
Malaysia  
ksopian@ukm.edu.my

---

---

## English Language Editor

---

---

Seçkin Arı  
Department of Computer Engineering  
Sakarya University, Sakarya-Türkiye  
ari@sakarya.edu.tr

---

---

## Editorial Assistant

---

---

Evrım Yüksel  
Department of Environmental Engineering  
Institute of Sciences, Sakarya University  
Sakarya-Türkiye  
eyuksel@sakarya.edu.tr

---

---

## Statistical Editor

---

---

Önder Gökmen Yıldız  
Department of Mathematics  
Bilecik Şeyh Edebali University, Bilecik-Türkiye  
ogokmen.yildiz@bilecik.edu.tr

---

---

## Managing Editor

---

---

Hüseyin Yasin Uzunok  
Department of Physics  
Sakarya University, Sakarya-Türkiye  
hyuzunok@sakarya.edu.tr

---

---

## Technical Editor

---

---

Hatice Vural  
Department of Electrical and Electronics Engineering  
Amasya University, Amasya-Türkiye  
hatice.vural@amasya.edu.tr

---

---

## Layout Editor

---

---

Mehmet Emin Çolak  
Scientific Journals Coordinatorship  
Sakarya University  
Sakarya-Türkiye  
mehmetcolak@sakarya.edu.tr

Yakup Beriş  
Scientific Journals Coordinatorship  
Sakarya University  
Sakarya-Türkiye  
yakupberis@sakarya.edu.tr

---

# Indexing

---






# Contents

## Research Article

- 1 The Oxidase Mimicking Activity of MnOx NPs/Co3O4 NPs Hybrid Nanozyme for Glucose Oxidation  
*Bekir Çakıroğlu* . . . . . 237-248
- 2 Effect of Signal Features and Model Variables on Energy-Traced Arrival Time Picking of Acoustic Signals Used for Structural Damage Detection  
*Sena Tayfur* . . . . . 249-258
- 3 Bitcoin Price Prediction with Fuzzy Logic  
*Gulcihan Ozdemir* . . . . . 259-269
- 4 Machine Learning Based Classification for Spam Detection  
*Serkan Keskin, Onur Sevli* . . . . . 270-282
- 5 Morphological and Structural Characterization of Low-Cost Graphene Produced by Electrochemical Exfoliation Method  
*Tamer Güzel, Yasemin İşlek, Oğuzhan Yıldız* . . . . . 283-293
- 6 Potential Anti-SARS-CoV-2 Effects of Gossypol and AT-101: Molecular Docking Study Against Angiotensin Converting Enzyme 2  
*Süleyman İlhan, Harika Atmaca İlhan* . . . . . 294-303
- 7 The Effect of Peptizing Agent Concentration on Processing and Properties of Alumina Based Catalyst Support  
*Servet Turan, Irmak Su Ökten, Cem Acıksarı, Serdar Çelebi, Umut Savacı, Erhan Ayas* . . . . . 304-313
- 8 DFT Calculations, Molecular Docking, and Pharmacological Properties Investigation for 5-Benzoxazolecarboxylic Acid as a Target Anti-Cancer Agent  
*Ceyhan Küçük* . . . . . 314-325
- 9 Semiconducting Characteristic of Antiferromagnetic Al4X3Mn (X = P, As and Sb) Compounds with Ab Initio Simulation Methods  
*Buğra Yıldız, Aytaç Erkişi* . . . . . 326-332
- 10 Repair Analysis of Overlay Woven Fabric CFRP Laminates  
*Osman Caglar Baysalli, Alihan Cambaz, Yasin Furkan Görgülü, Arman Uluoğlu, Umur Ulas Harman* . . . . . 333-343
- 11 Optical Signal Investigation of Monolayer MoS2 Grown Via Glass-Assisted CVD On Patterned Surfaces  
*Aydan Yeltik* . . . . . 344-352
- 12 Ensuring Photocatalyst Properties on Cellulosic Fabric by Using Citric Acid Modified with TiO2 Degussa P25 Nanoparticles  
*Sabiha Sezgin Bozok* . . . . . 353-363
- 13 The Class of Demi-Strongly Order Bounded Operators  
*Gül Sinem Keleş, Birol Altın* . . . . . 364-370
- 14 The Effect of Different Proportions of Waste Rubber Substitution on Alkali-Silica Reaction and Mechanical Properties in Mortars  
*Ufuk Kandil, H. Alperen Bulut* . . . . . 371-380

15	Morphological, Molecular Identification and Virulence of Entomopathogenic Fungi Isolated From <i>Dendroctonus micans</i> (Kugelann,1794) (Coleoptera: Curculionidae) <i>Seda Biryol, Ali Soyding, Sevda İşık</i> . . . . .	381-391
16	Myrmecofauna (Hymenoptera, Formicidae) of Gökçeada Island, Türkiye <i>Esra Sert, Celal Karaman</i> . . . . .	392-409
17	Schwarz Problem for Model Partial Differential Equations with One Complex Variable <i>Bahriye Karaca</i> . . . . .	410-417
18	Computer Vision-Based Lane Detection and Detection of Vehicle, Traffic Sign, Pedestrian Using YOLOv5 <i>Gülyeter Öztürk, Osman Eldoğan, Raşit Köker</i> . . . . .	418-430
19	A Note on the Laplacian Energy of the Power Graph of a Finite Cyclic Group <i>Nurşah Mutlu Varhoğlu, Şerife Büyükköse</i> . . . . .	431-437
20	Comparison of Deep Learning Models and Optimization Algorithms in the Detection of Scoliosis and Spondylolisthesis from X-Ray Images <i>Harun Güneş, Cengiz Hark, Abdullah Erhan Akkaya</i> . . . . .	438-451

## The Oxidase Mimicking Activity of MnO<sub>x</sub> NPs/Co<sub>3</sub>O<sub>4</sub> NPs Hybrid Nanozyme for Glucose Oxidation

Bekir Çakıroğlu Sakarya University, Biomedical, Magnetic and Semiconductor Materials Research Center (BIMAS-RC), Sakarya, Türkiye, [bekircakiroglu@sakarya.edu.tr](mailto:bekircakiroglu@sakarya.edu.tr)

### ARTICLE INFO

### ABSTRACT

Keywords:  
Nanozyme  
Co<sub>3</sub>O<sub>4</sub> NPs  
MnO<sub>x</sub> NPs  
Colorimetric Assay  
Sustainability

#### Article History:

Received: 05.10.2022

Accepted: 08.01.2024

Online Available: 22.04.2024

Herein, the hybrid nanozyme MnO<sub>x</sub> NPs/Co<sub>3</sub>O<sub>4</sub> NPs on indium tin oxide coated glass substrate (ITO) was manufactured by imparting the porous morphology with its distinct merits: its surface valence states, oxygen vacancies, large surface area, and abundant active sites. The oxidase-like activity was investigated via the catalytic oxidation of chromogenic substrate in the presence of glucose visualized by the eyes. MnO<sub>x</sub> NPs containing Mn<sup>2+</sup> and Mn<sup>3+</sup> have a superior ability to oxidize glucose by reducing dissolved oxygen and producing H<sub>2</sub>O<sub>2</sub>. Co<sub>3</sub>O<sub>4</sub> NPs, in turn, reduce H<sub>2</sub>O<sub>2</sub> with concomitant 3,3',5,5'-tetramethylbenzidine (TMB) oxidization. Thus, the nanozyme mimics the dual roles of glucose oxidase and peroxidase. The oxidase-like activity of hybrid nanozyme for glucose was found to be higher than those of single components. The nanozyme responded to glucose with a linear range from 60 μM to 1200 μM. The acceptable performance is probably due to the facilitated access of glucose to the proximity of the sensor surface. Good reproducibility was accomplished by virtue of the meticulous construction of NPs. Without functionalization and enzyme utilization, the fabricated nanozyme holds promise as a substitute for peroxidase and oxidase for detecting glucose.

## 1. Introduction

Natural enzymes have been widely used due to their effective and specific catalytic activity on substrates under mild conditions [1–4]. However, enzymes face inherent drawbacks, such as high-cost purification and low storage and operational stability [5–6]. Additionally, they are susceptible to pH, temperature, ionic strength, surfactants, and organic solvents, and digestion by proteases hampers their widespread use [7]. Since the exciting breakthrough of Fe<sub>3</sub>O<sub>4</sub> MNPs exhibiting peroxidase-like activity in 2007 [8], considerable efforts have been devoted to exploring efficient artificial enzymes with intrinsic enzyme-like activities, aka "nanozymes", to address these difficulties [9].

Nanozymes have been at the forefront as a viable alternative to facilitate analyte sensing owing to

their striking merits [10]. These include adjustable catalytic activity, high stability against harsh environments, facile surface modification, and low-cost and straightforward production [11–12]. However, nanozymes could not selectively catalyze one specific substrate like enzymes [13]. Improving the asymmetric selectivity of nanozymes is one of the potential challenges [14].

Hitherto, the enzymatic activity and selectivity of nanozymes have been tailored by surface modification [15], particle size adjustment [16], heterogeneous atomic doping [17], and morphology [18]. The large surface area exposes more active sites, and preferential exposure of catalytically active atoms increases the activity [19]. Surface defects such as ledges, adatoms, vacancies and kinks are coordinatively

unsaturated reactive sites and strongly adsorb substrates [20].

Encouragingly, the catalytic performance of nanozymes has been synergically improved by functionally assembling several nanozymes showing the same enzyme-mimicking activity [21].

Up to now, most of the reported nanozymes have mirrored peroxidase-like activity; thus, the oxidase-like nanozymes are becoming more attractive [12, 22–23]. Noble metal nanoparticles such as Au NPs and their alloys have exhibited GOx-like activity owing to their remarkable oxygen reduction catalytic activities [12]. However, high-cost production hinders widespread applications. Multivalent manganese(II,III) oxide ( $\text{MnO}_x$ ) was reported to possess intrinsic oxidase-like activity due to its multiple oxidation states, along with satisfying features such as low-cost production, remarkable catalytic activity, non-toxicity, and environmental friendliness [24–26]. Likewise, cobalt(II, III) oxide ( $\text{Co}_3\text{O}_4$ ) nanomaterials have rich redox properties depending on their morphology and multiple catalytic activities, closely correlated to medium pH. Also,  $\text{Co}_3\text{O}_4$  nanozymes catalyze  $\text{H}_2\text{O}_2$  by showing peroxidase-like activity [17–18].

Conventional glucose detection has been performed by combining the corresponding oxidase enzyme and peroxidase nanozyme [27]. However, the different reaction conditions render the operation intricate. Thus, one-step colorimetric glucose-sensing will impel the development of nanozyme-based sensors [28–30].

In this article, a nano-structured hybrid nanozyme was reported for glucose oxidation. Its oxidase mimics activity was investigated in the presence of a chromogenic substrate.

## 2. Materials and Methods

### 2.1. Reagents and chemicals

ITO glass slides, ethanol (anhydrous,  $\geq 99.8\%$ ), manganese(II) chloride tetrahydrate ( $\text{MnCl}_2 \cdot 4\text{H}_2\text{O}$ ), Cobalt(II) chloride hexahydrate and D-

(+)-glucose monohydrate were obtained from Merck. TMB, sodium hydroxide (NaOH), isopropyl alcohol, potassium iodide (KI), ethylenediaminetetraacetic acid (EDTA), iron(II) sulfate heptahydrate, sucrose, lactose, and maltose were purchased from Sigma-Aldrich. Acetate buffer solution (ABS) was prepared using glacial acetic acid (Merck) and sodium acetate (Sigma-Aldrich). Hydrochloric acid-potassium chloride buffer (0.1 M, pH 2.0) was prepared using potassium chloride (Sigma-Aldrich) and hydrochloric acid (Merck). All chemicals were used as received, and deionized water (DW) was obtained from a Labconco Water Pro BT purification system.

### 2.2. Preparation of $\text{Co}_3\text{O}_4$ NPs

The ITO electrodes (50 mm length  $\times$  10 mm width  $\times$  1.1 mm thickness; surface resistivity 8–12  $\Omega/\text{sq}$ ) were consecutively pre-cleaned by sonication in acetone, 1 M NaOH, ethanol/DW mixture (1:1, v/v), and DW for 15 min, before being dried in a vacuum oven.

$\text{Co}_3\text{O}_4$  NPs were manufactured as follows. 0.1 M  $\text{CoCl}_2$  in isopropanol was applied on the glass surfaces, and the substrates were kept in the oven at 75 °C for 24 h and calcined at 450 °C for 12 h in a muffle furnace to crystallize the samples. The resulting product is designated as  $\text{Co}_3\text{O}_4$  NPs/ITO.

### 2.3. Preparation of $\text{MnO}_x$ NPs on $\text{Co}_3\text{O}_4$ NPs

The successful ionic layer adsorption and reaction (SILAR) was used to attain  $\text{MnO}_x$  deposition. The free-standing substrates were dipped into the cationic precursor of 0.3 M  $\text{MnCl}_2$  (pH: 1) for 20 s to deposit  $\text{Mn}^{2+}$  on the substrate. The substrate was then rinsed with DW and then soaked in an anionic precursor of 0.01 M NaOH (pH: 13) for 20 s, where  $\text{OH}^-$  ions react with  $\text{Mn}^{2+}$  to obtain a manganese oxide layer followed by rinsing with DW to eliminate loosely bound species. This cycle was repeated 5, 10, and 15 times for structural optimization, and the product ( $\text{MnO}_x$  NPs/ $\text{Co}_3\text{O}_4$  NPs/ITO) was dried at 60 °C in an oven.

## 2.4. Oxidase-like activity measurements

For the detection of glucose, 2.5 mL of 0.4 mM TMB aliquots was prepared in 200 mM ABS pH 3.8 with free-standing nanozyme substrate, and 50  $\mu$ L of varying glucose concentrations (0-1600  $\mu$ M) were added into the above mixture and incubated for 8 min at 35 °C in cuvettes. Then, the free-standing substrate (MnO<sub>x</sub> NPs/Co<sub>3</sub>O<sub>4</sub> NPs/ITO) was removed from the reaction medium, and the absorbance measurements were carried out at 652 nm. Each experiment was repeated at least four times.

## 2.5. Characterization

The morphological features of nanozyme components were characterized by field emission scanning electron microscopy (FESEM) recorded on a FEI Quanta FEG 450. The crystalline planes were elucidated by X-ray diffraction (XRD, RIGAKU D/Max 2200), using monochromatized Cu radiation resource ( $\lambda = 1.5045$  Å). UV visible (UV-Vis) absorbance and diffuse reflectance spectroscopy (DRS, BaSO<sub>4</sub> as reference) spectra were recorded using a Shimadzu UV-2600 spectrophotometer at 200-800 nm.

## 3. Results and Discussions

### 3.1. Characterization of free-standing nanozyme substrate

An outstanding nanozyme for glucose detection was fabricated, as illustrated in Figure 1. The solution-based nanozymes have an unwanted effect on the absorption spectrum, whereas the free-standing nanozymes can negate this interference by removing it from the post-reaction medium. The nanozyme preserved the multi-enzyme-mimicking activity in months of usage without additional storage conditions. The top-view TEM image of Co<sub>3</sub>O<sub>4</sub> NPs displayed flakes of nanoparticle aggregates. The size of the Co<sub>3</sub>O<sub>4</sub> NPs estimated from the image is 23 nm (Figure 2A). After MnO<sub>x</sub> NPs' deposition, the morphological alteration is evident that MnO<sub>x</sub> NPs are deposited on Co<sub>3</sub>O<sub>4</sub> NPs (Figure 2B). The size of the deposited MnO<sub>x</sub> NPs was calculated to be around 25 nm nearly the same size as Co<sub>3</sub>O<sub>4</sub> NPs. The NP-coated substrates

exhibited opalescence under the light (Figure 2B inset).

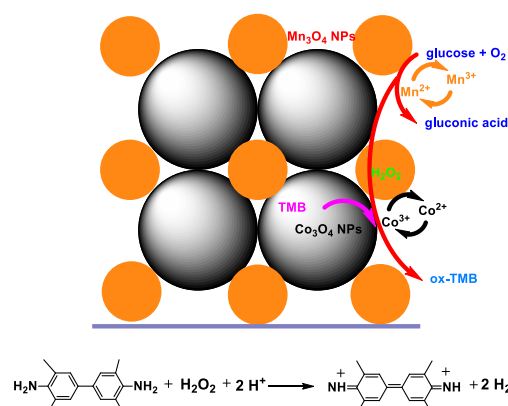


**Figure 1.** The one-pot nonenzymatic colorimetric glucose detection using the free-standing nanozyme hybrid

Figure 2C shows the XRD pattern of the hybrid nanozyme. The peaks located at  $2\theta = 19.0^\circ$ ,  $31.3^\circ$ ,  $36.8^\circ$ ,  $38.5^\circ$ ,  $44.8^\circ$ ,  $55.6^\circ$ ,  $59.3^\circ$ , and  $65.2^\circ$ , respectively, correspond to the (111), (220), (311), (222), (400), (422), (511), and (440) planes of face-centered cubic (fcc) spinel Co<sub>3</sub>O<sub>4</sub> (JCPDS No. 74-2120) [31]. The prominent diffraction peaks of MnO NPs appearing at  $35.12^\circ$ ,  $41.26^\circ$ ,  $59.16^\circ$ , and  $71.42^\circ$  indexed to (111), (200), (220), and (311) crystalline planes of MnO spheres (JCPDS no. 07-0230) implying that MnO was formed on Co<sub>3</sub>O<sub>4</sub> NPs. The peak at  $32.75^\circ$  corresponds to the main peak of Mn<sub>2</sub>O<sub>3</sub> NPs (222) (JCPDS no. 71-0636), which can efficiently oxidase TMB [32]. Additional diffraction peaks could be associated with the indium tin oxide layer on the glass.



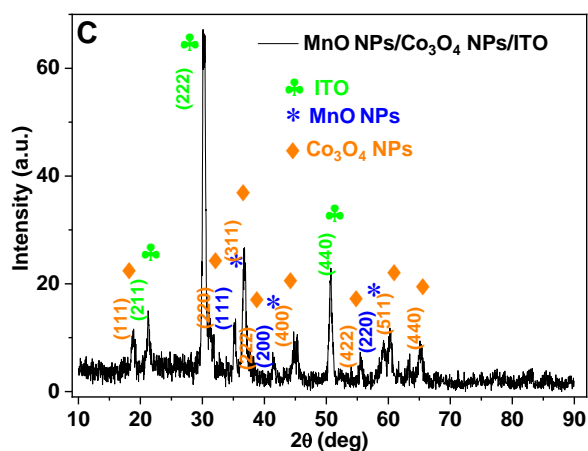
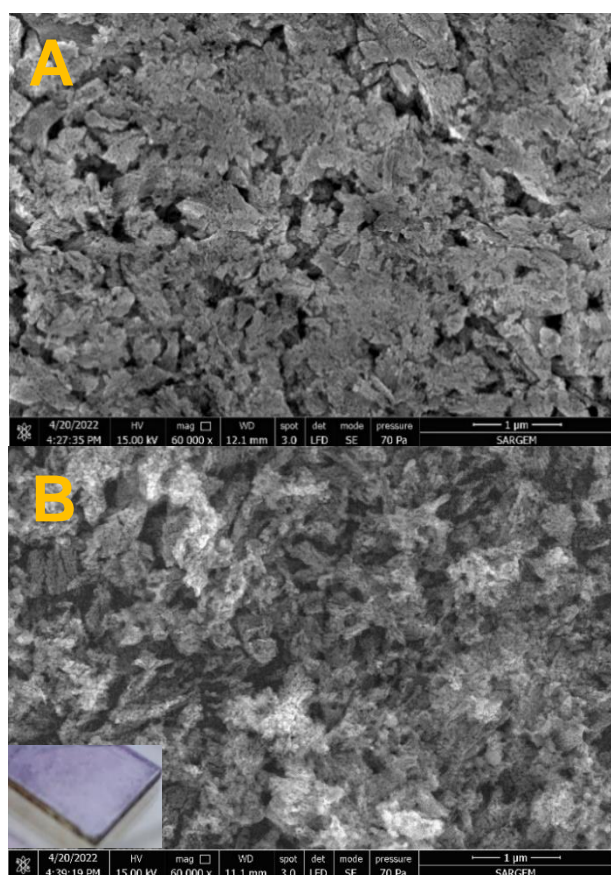


**Figure 2** A. The top-view SEM images of  $\text{Co}_3\text{O}_4$  NPs/ITO and B.  $\text{MnO}_x$  NPs/ $\text{Co}_3\text{O}_4$  NPs/ITO (inset: the photograph of  $\text{MnO}_x$  NPs/ $\text{Co}_3\text{O}_4$  NPs/ITO); C. XRD pattern of  $\text{MnO}_x$  NPs/ $\text{Co}_3\text{O}_4$  NPs/ITO

Figure 3A exhibits the reflection spectra of NP-coated substrates. NPs display intense and typical reflection bands due to their photonic properties. After the  $\text{MnO}_x$  deposition, the reflection band was blue-shifted owing to the narrowing pore size of NPs. UV-Vis spectrum revealed the absorbance band of the nanozyme in the visible region (Figure 3B).

### 3.2. Mechanism of peroxidase- and oxidase-like activities of the hybrid nanozyme

The time-dependent absorbance intensity of TMB reaches the maximum after 8 min of incubation, suggesting that the redox process between TMB and nanozyme is a surface-mediated reaction. The medium pH effect was screened in 200 mM ABS at various pH values ranging from 2 to 5.8. Owing to the similar structure of TMB with a diamine, basic pH brings about poor solubility of TMB. The hybrid nanozyme activity demonstrated a volcano-shaped dependence on pH with the optimal point of pH 3.8 and is stable over a broad temperature range from 15 °C to 40 °C with an optimal value of 35 °C.

A significant absorbance was observed at the maximum wavelength (652 nm) for  $\text{Co}_3\text{O}_4$  NPs/ITO in the presence of 5 mM glucose in 200 mM in ABS pH 3.8 at optimal temperature, confirming the oxidase and peroxidase-like activity of NPs (Figure 3C). Also, the hybrid nanozyme exhibited boosted absorbance at 652 nm relative to  $\text{Co}_3\text{O}_4$  NPs/ITO, implying that both  $\text{Co}_3\text{O}_4$  NPs and  $\text{MnO}_x$  NPs were inevitable to enhance the intrinsic oxidase-like activity. According to the absorbance spectra, the optimal SILAR cycle for  $\text{MnO}_x$  NP deposition was ten cycles (Figure 3C).

The absorbance spectra were measured in the presence of various scavengers and activators to understand the mechanism of hybrid nanozyme (Figure 3D). The glucose oxidase-like activity was enormously inhibited upon adding catalase and  $\text{Fe(II) EDTA}$ , ascertaining the generation of  $\text{H}_2\text{O}_2$  [33].

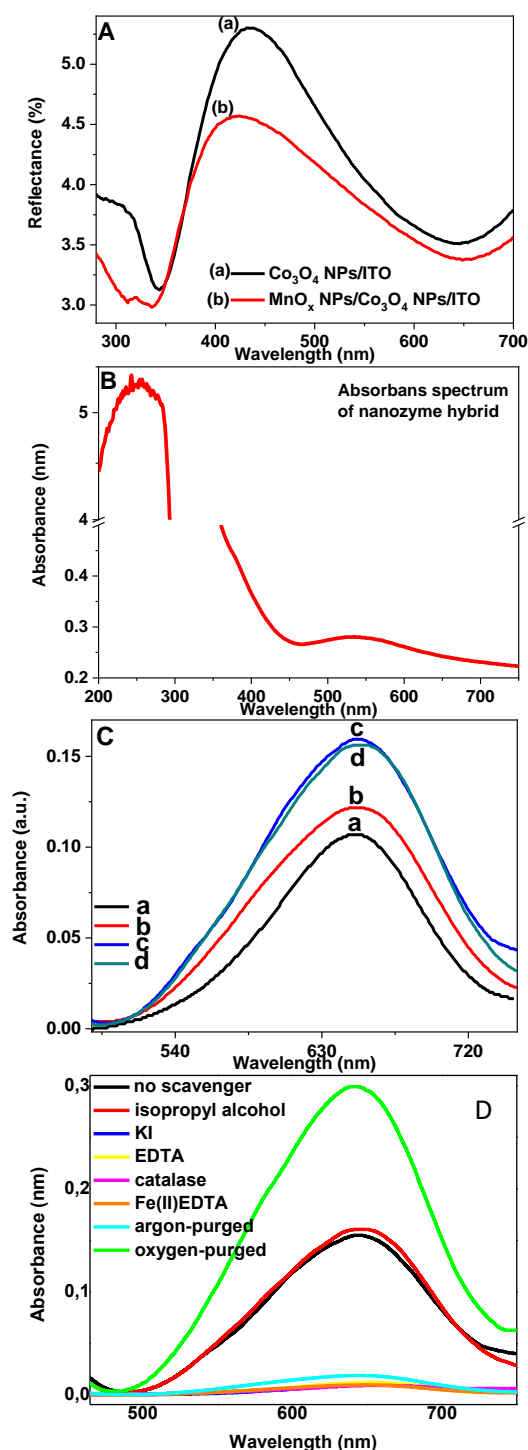


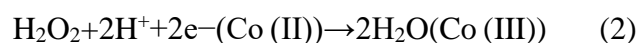
**Figure 3** A. Reflectance spectra of materials; B. UV–visible absorbance spectra of nanozyme; C. UV–visible absorbance spectra of ox-TMB generated by the different nanozymes: (a)  $\text{Co}_3\text{O}_4$  NPs/ITO, (b,c,d) 5, 10, 15 cycles  $\text{MnO}_x$  NPs/ $\text{Co}_3\text{O}_4$  NPs/ITO, respectively, D. Scavengers and activator effect on multiple enzyme-like activities

To determine whether  $\text{H}_2\text{O}_2$  is reduced to hydroxyl radicals, IPA, a hydroxyl radical scavenger, was added, and no absorbance diminishing was observed. Ergo,  $\text{H}_2\text{O}_2$  is probably reduced to water [34]. The mechanism was further validated using KI and EDTA, the

most used hole scavengers, and the oxidation of TMB was fully inhibited [35]. Therefore, the electron vacancies play a pivotal role, and in the oxidase-mimicking activity, the hybrid nanozyme will accept electrons by oxidizing the chromogenic substrate [36].

The effect of oxygen on oxidation was surveyed to reveal the oxidase-mimicking activity. The ox-TMB absorption intensity was reduced to almost zero in the argon-saturated solution, confirming that oxygen takes part in the reaction. In the presence of  $\text{O}_2$ , a substantial increase in absorbance was observed, implying oxygen consumption during catalysis. In line with these findings, the multi-enzyme mimic activities of the hybrid nanozyme were elucidated tentatively, as illustrated in Figure 1. The initial adsorptions of oxygen and TMB are the principal contributing factors to the dual enzyme activity.

The oxygen vacancies of  $\text{MnO}_x$  NPs were beneficial for oxygen adsorption to generate active electrophilic oxygen species [37]. Thus,  $\text{MnO}_x$  NPs serve as a GOx-like nanozyme that oxidizes glucose with the concomitant reduction of  $\text{O}_2$  to  $\text{H}_2\text{O}_2$  (eq. 1). Also, (111) plane of spinel  $\text{Co}_3\text{O}_4$  is the most active facet for the oxygen reduction activities owing to the density of highly exposed  $\text{Co}^{2+}$  active sites in the plane [38]. Therefore,  $\text{Co}_3\text{O}_4$  NPs can reduce oxygen along with  $\text{MnO}_x$ . Simultaneously, Co (III) in  $\text{Co}_3\text{O}_4$  NPs obtains electrons from TMB and then converts to Co (II), thus oxidizing TMB. The catalysts with lower redox potential, such as  $\text{Co}_3\text{O}_4$ , are thermodynamically favorable to transfer electrons to  $\text{H}_2\text{O}_2$  [34]. Therefore, Co (II) can transfer electrons to in situ generated  $\text{H}_2\text{O}_2$  and then convert back to Co (III) (eq. 2), mimicking HRP.



The oxidase-mimicking activity could be attributed to several factors. The NPs with internal voids provide large surface areas and copious catalytically active sites [39]. The accessible surface for the substrate could facilitate concurrent tandem catalysis in NPs [40]. Furthermore, the adsorbent behavior of

nanozyme brings the target molecule of interest close to the nanozyme, which makes the cascade reactions infinitely near each other by preventing the mass transfer process of reactants and intermediates [41]. The remarkable electron transfer occurring on the specific facet is conducive to the escalated nanozyme activity [19].

### 3.3. Colorimetric glucose detection with free-standing nanozyme and steady-state kinetic assay

The nanozyme exhibited a linear dependence for glucose concentrations ranging from 60  $\mu\text{M}$  to 1200  $\mu\text{M}$  ( $y=0.000127x + 0.00342$ ,  $R^2 = 0.9969$ ), implying that detection is likely viable (Figure 4A, B, C). The color of oxidized TMB was visible to the naked eye at glucose concentrations lower than 0.2 mM (Fig. 4A inset). The comparison of the prepared nanozyme with the ones reported in the literature is listed in Table 1.

According to Table 1, a wider measurement range with a lesser operation time was concluded. The large surface area of nanozyme was thought to push the dynamic range to the mM levels. According to the literature, nanozymes with glucose oxidase-like activity are mostly gold-based expensive materials. Herein, a cost-effective nanozyme material containing two metal oxides was proposed. The limit of detection (LOD) was estimated based on  $3(\text{standard deviation of 20 blank measurements/slope of the linear fit})$  and was determined as 18  $\mu\text{M}$ . The limit of quantification was estimated based on  $10(\text{standard deviation of 20 blank measurements/slope of the linear fit})$  and was calculated as 60  $\mu\text{M}$ .

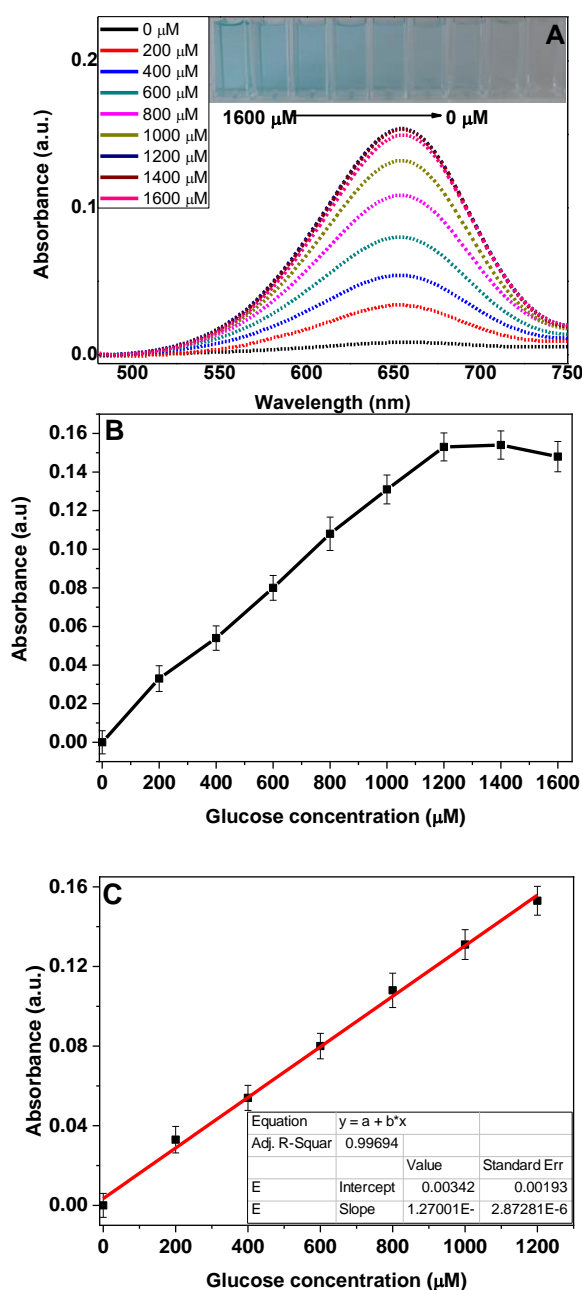


**Figure 4 A.** The absorbance spectra vs. glucose concentration (inset shows the corresponding post-reaction colorizations in various glucose concentrations); **B.** The absorbance vs. glucose concentration plot and **C.** the calibration curve for glucose detection

Typical Michaelis-Menten curves were obtained for glucose oxidation, and kinetic parameters such as the Michaelis-Menten constant ( $K_m$ ) were obtained using the following equation [42]:

$$1/V_o = K_m/V_{max} + (1/[S])(1/K_m) \quad (3)$$

A lower  $K_m$  value is desirable because  $K_m$  represents the substrate's affinity.  $K_m$  values were found to be 0.6 mM, lower than native GOx



(4.1 mM) [42], indicating a high affinity for glucose.

### 3.4. The nanozyme sensor performance

Also, the fabrication process was found to be effective for reproducible sensor production, and the satisfying feasibility was confirmed, outlining the robustness of the nanozyme (Figure 5). The sensor stability was studied for four weeks, and negligible loss in the catalytic activity of less than 3% was found (Figure 6).

The selectivity was assessed by exposing the sensor to 1.2 mM glucose and 1.2 mM glucose analogs, viz. lactose, sucrose, and maltose. The response was not remarkably influenced in the presence of maltose. The absorbance increased to some extent in the presence of lactose and sucrose due to the oxidation of analogs (Figure 7). The plausible reason for this finding is that the nanozyme can lead to the hydrolysis of disaccharides. Some disaccharides may undergo efficient hydrolysis, thus releasing more glucose.

**Table 1.** The performance comparison of the reported nanozyme-based glucose sensors

Material	Method/ temperature	LOD ( $\mu\text{M}$ )	Linear range (mM)	Duration (min)	Ref.
MnO <sub>x</sub> NPs/Co <sub>3</sub> O <sub>4</sub>	spectrophotometric detection/ 35 °C	18	0.06–1.2	8	Current study
NPs/ITO	photoelectrochemical detection/ room temp.	0.46	0.001–1.0	-	[43]
ITO/PbS/SiO <sub>2</sub> /AuNPs	spectrophotometric detection/ room temp.	0.5	2.5–5.0	10	[44]
CS-GO <sup>1</sup>	spectrophotometric detection/ 25 °C	0.8	0.01–1000	0.5	[45]
m-GCN <sup>2</sup>	spectrophotometric detection/ 30 °C	0.055	0.005–1	3	[29]
m-GCN-chitin-acetic acid	spectrophotometric detection/ 37 °C	1	0.005–1.2	15	[46]
MnO <sub>2</sub> nanoflakes	spectrophotometric detection/ n.a. <sup>3</sup>	0.6	0.001–0.3	30	[47]
Au@BSA NPs-GO	spectrophotometric detection/ room temp.	20	0.05–0.4	40	[48]
Au NP@Au NCs					

<sup>1</sup> chitosan-functionalized graphene oxide

<sup>2</sup> modified graphitic carbon nitride

<sup>3</sup> not available

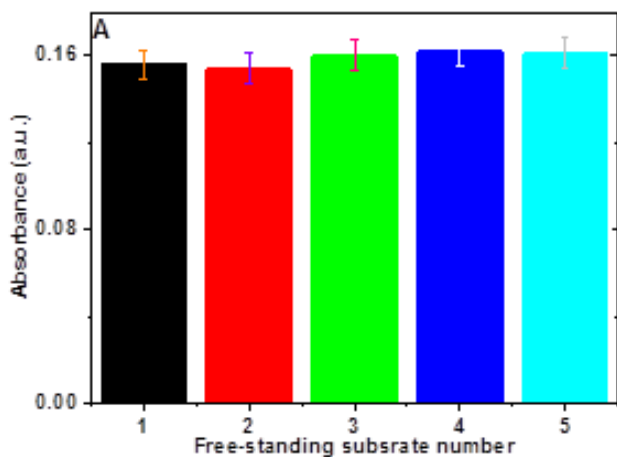


**Figure 5.** The reproducibility of the sensor

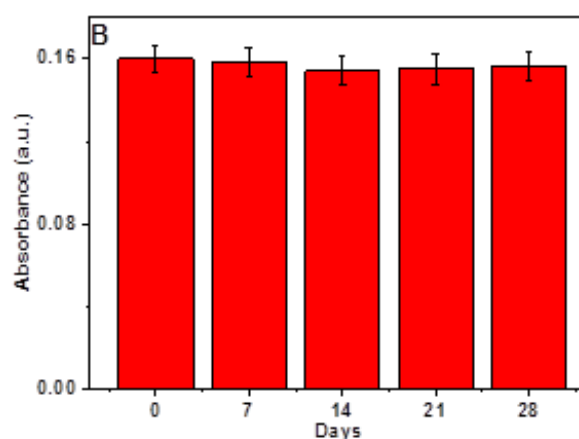


**Figure 6.** The stability study of the sensor

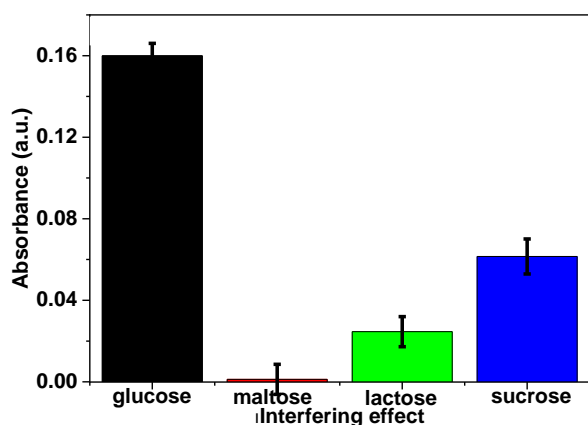


**Figure 7.** The selectivity of the free-standing nanozyme for glucose detection when exposed to glucose and glucose analogs

#### 4. Conclusion

In summary,  $\text{MnO}_x$  NPs/ $\text{Co}_3\text{O}_4$  NPs/ITO was synthesized with favorable morphology for reactants and products, which could catalyze glucose oxidation by molecular oxygen to produce  $\text{H}_2\text{O}_2$ . The coupled oxidase and peroxidase-mimicking activity of  $\text{MnO}_x$  NPs/ $\text{Co}_3\text{O}_4$  NPs/ITO was utilized for colorimetric glucose sensing. Since  $\text{Co}_3\text{O}_4$  NPs and  $\text{MnO}_x$  NPs are mainly peroxidase-like and oxidase-like mimics, respectively, the assembly of these nanozymes exhibited specific and remarkable glucose sensing performance. The rational design of NPs grants access to abundant catalytically active sites and enhances the catalytic activity. This work may find its unique niche as an efficient biomimetic oxidase for glucose monitoring in the sensor area.

#### Article Information Form

##### Acknowledgments

The author would like to thank Prof. Dr. Mehmet Nebioğlu and Assoc. Prof. Dr. Emrah Bulut for their valuable contributions.

##### Funding

The author has not received any financial support for the research, authorship or publication of this study.

##### The Declaration of Ethics Committee Approval

This study does not require ethics committee permission or any special permission.

##### The Declaration of Research and Publication Ethics

The author of the paper declare that he complies with the scientific, ethical and quotation rules of SAUJS in all processes of the paper and that he does not make any falsification on the data collected. In addition, he declares that Sakarya University Journal of Science and its editorial board have no responsibility for any ethical violations that may be encountered, and that this study has not been evaluated in any academic publication environment other than Sakarya University Journal of Science.

##### Copyright Statement

Authors own the copyright of their work published in the journal and their work is published under the CC BY-NC 4.0 license.

##### References

- [1] E. Vargas, H. Teymourian, F. Tehrani, E. Eksin, E. Sánchez-Tirado, P. Warren, A. Erdem, E. Dassau, J. Wang, "Enzymatic/Immunoassay Dual-Biomarker Sensing Chip: Towards Decentralized Insulin/Glucose Detection," *Angewandte Chemie International Edition*, vol. 58, no. 19, pp. 6376–6379, 2019.
- [2] A. J. Gross, M. Holzinger, S. Cosnier, "Buckypaper bioelectrodes: Emerging materials for implantable and wearable biofuel cells," *Energy & Environmental Science journal*, vol. 11, no. 7, pp. 1670–1687, 2018.
- [3] M. Holzinger, P. H. M. Buzzetti, S. Cosnier, "Polymers and nano-objects, a rational combination for developing health monitoring biosensors," *Sensors and Actuators B: Chemical*, vol. 348, p. 130700, 2021.
- [4] B. Çakıroğlu, J. Chauvin, A. Le Goff, K. Gorgy, M. Özacar, M. Holzinger, "Photoelectrochemically-assisted biofuel cell constructed by redox complex and g-C<sub>3</sub>N<sub>4</sub> coated MWCNT bioanode," *Biosensors and Bioelectronics*, vol. 169, p. 112601, Dec. 2020.

- [5] W. Guan, X. Duan, M. A. Reed, "Highly specific and sensitive non-enzymatic determination of uric acid in serum and urine by extended gate field effect transistor sensors," *Biosensors and Bioelectronics*, vol. 51, pp. 225–231, 2014.
- [6] S. Chaiyo, E. Mehmeti, W. Siangproh, T. L. Hoang, H. P. Nguyen, O. Chailapakul, K. Kalcher, "Non-enzymatic electrochemical detection of glucose with a disposable paper-based sensor using a cobalt phthalocyanine–ionic liquid–graphene composite," *Biosensors and Bioelectronics*, vol. 102, pp. 113–120, 2018.
- [7] A. L. Rinaldi, R. Carballo, "Impedimetric non-enzymatic glucose sensor based on nickel hydroxide thin film onto gold electrode," *Sensors and Actuators B: Chemical*, vol. 228, pp. 43–52, 2016.
- [8] L. Gao, J. Zhuang, L. Nie, J. Zhang, Y. Zhang, N. Gu, T. Wang, J. Feng, D. Yang, S. Perrett, X. Yan, "Intrinsic peroxidase-like activity of ferromagnetic nanoparticles," *Nature Nanotechnology*, vol. 2, no. 9, pp. 577–583, 2007.
- [9] D. Jiang, D. Ni, Z. T. Rosenkrans, P. Huang, X. Yan, W. Cai, "Nanozyme: new horizons for responsive biomedical applications," *Chemical Society Reviews*, vol. 48, no. 14, pp. 3683–3704, 2019.
- [10] D. Duan, K. Fan, D. Zhang, S. Tan, M. Liang, Y. Liu, J. Zhang, P. Zhang, Wei Liu, X. Qiu, G. P. Kobinger, G. F. Gao, X. Yan, "Nanozyme-strip for rapid local diagnosis of Ebola," *Biosensors and Bioelectronics*, vol. 74, pp. 134–141, 2015.
- [11] M. N. Karim, S. R. Anderson, S. Singh, R. Ramanathan, V. Bansal, "Nanostructured silver fabric as a free-standing NanoZyme for colorimetric detection of glucose in urine," *Biosensors and Bioelectronics*, vol. 110, pp. 8–15, 2018.
- [12] H. Zhang, X. Liang, L. Han, F. Li, "Non-Naked' Gold with Glucose Oxidase-Like Activity: A Nanozyme for Tandem Catalysis," *Small*, vol. 14, no. 44, p. 1803256, 2018.
- [13] Y. Park, P. K. Gupta, V.-K. Tran, S. E. Son, W. Hur, H. B. Lee, J. Y. Park, S. N. Kim, G. H. Seong, "PVP-stabilized PtRu nanozymes with peroxidase-like activity and its application for colorimetric and fluorometric glucose detection," *Colloids Surfaces B Biointerfaces*, vol. 204, p. 111783, 2021.
- [14] Q. Wang, S. Liu, Z. Tang, "Recent progress in the design of analytical methods based on nanozymes," *Journal of Materials Chemistry B*, vol. 9, no. 39, pp. 8174–8184, 2021.
- [15] B. Gökçal, Ç. Kip, A. Tuncel, "One-pot, direct glucose detection in human whole blood without using a dilution factor by a magnetic nanozyme with dual enzymatic activity," *Journal of Alloys and Compounds*, vol. 843, p. 156012, 2020.
- [16] Q. Chen, S. Li, Y. Liu, X. Zhang, Y. Tang, H. Chai, Y. Huang, "Size-controllable Fe-N/C single-atom nanozyme with exceptional oxidase-like activity for sensitive detection of alkaline phosphatase," *Sensors and Actuators B: Chemical*, vol. 305, p. 127511, 2020.
- [17] Q. Chen, X. Zhang, S. Li, J. Tan, C. Xu, Y. Huang, "MOF-derived Co<sub>3</sub>O<sub>4</sub>@Co-Fe oxide double-shelled nanocages as multi-functional specific peroxidase-like nanozyme catalysts for chemo/biosensing and dye degradation," *Chemical Engineering Journal*, vol. 395, no. March, p. 125130, 2020.
- [18] X. Zhang, Y. Lu, Q. Chen, Y. Huang, "A tunable bifunctional hollow Co<sub>3</sub>O<sub>4</sub>/MO<sub>3</sub> (M = Mo, W) mixed-metal oxide nanozyme for sensing H<sub>2</sub>O<sub>2</sub> and screening acetylcholinesterase activity and its inhibitor," *Journal of Materials Chemistry B*, vol. 8, no. 30, pp. 6459–6468, 2020.


- [19] W. Wu, L. Huang, E. Wang, S. Dong, "Atomic engineering of single-atom nanozymes for enzyme-like catalysis," *Chemical Science*, vol. 11, no. 36, pp. 9741–9756, 2020.
- [20] J. Zhang, Q. Kuang, Y. Jiang, Z. Xie, "Engineering high-energy surfaces of noble metal nanocrystals with enhanced catalytic performances," *Nano Today*, vol. 11, no. 5, pp. 661–677, 2016.
- [21] P. Gallay, M. Eguílaz, G. Rivas, "Designing electrochemical interfaces based on nanohybrids of avidin functionalized-carbon nanotubes and ruthenium nanoparticles as peroxidase-like nanozyme with supramolecular recognition properties for site-specific anchoring of biotinylated residues," *Biosensors and Bioelectronics*, vol. 148, p. 111764, 2020.
- [22] J. Liu, L. Meng, Z. Fei, P. J. Dyson, L. Zhang, "On the origin of the synergy between the Pt nanoparticles and MnO<sub>2</sub> nanosheets in Wonton-like 3D nanozyme oxidase mimics," *Biosensors and Bioelectronics*, vol. 121, pp. 159–165, 2018.
- [23] Q. Chen, S. Li, Y. Liu, X. Zhang, Y. Tang, H. Chai, Y. Huang, "Size-controllable Fe-N/C single-atom nanozyme with exceptional oxidase-like activity for sensitive detection of alkaline phosphatase," *Sensors and Actuators B: Chemical*, vol. 305, p. 127511, 2020.
- [24] J. Xi, C. Zhu, Y. Wang, Q. Zhang, L. Fan, "Mn<sub>3</sub>O<sub>4</sub> microspheres as an oxidase mimic for rapid detection of glutathione," *RSC Advances*, vol. 9, no. 29, pp. 16509–16514, 2019.
- [25] W. Lu, J. Chen, L. Kong, F. Zhu, Z. Feng, J. Zhan, "Oxygen vacancies modulation Mn<sub>3</sub>O<sub>4</sub> nanozyme with enhanced oxidase-mimicking performance for L-cysteine detection," *Sensors and Actuators B: Chemical*, vol. 333, no. January, p. 129560, 2021.
- [26] N. Singh, M. A. Savanur, S. Srivastava, P. D'Silva, G. Mugesh, "A Redox Modulatory Mn<sub>3</sub>O<sub>4</sub> Nanozyme with Multi-Enzyme Activity Provides Efficient Cytoprotection to Human Cells in a Parkinson's Disease Model," *Angewandte Chemie International Edition*, vol. 56, no. 45, pp. 14267–14271, 2017.
- [27] Y. Park, P. K. Gupta, V.-K. Tran, S. E. Son, W. Hur, H. B. Lee, J. Y. Park, S. N. Kim, G. H. Seong, "PVP-stabilized PtRu nanozymes with peroxidase-like activity and its application for colorimetric and fluorometric glucose detection," *Colloids Surfaces B Biointerfaces*, vol. 204, p. 111783, 2021.
- [28] J. Mou, X. Xu, F. Zhang, J. Xia, Z. Wang, "Promoting Nanozyme Cascade Bioplatfrom by ZIF-Derived N-Doped Porous Carbon Nanosheet-based Protein/Bimetallic Nanoparticles for Tandem Catalysis," *ACS Applied Bio Materials*, vol. 3, no. 1, pp. 664–672, Jan. 2020.
- [29] P. Sengupta, K. Pramanik, P. Datta, P. Sarkar, "Chemically modified carbon nitride-chitin-acetic acid hybrid as a metal-free bifunctional nanozyme cascade of glucose oxidase-peroxidase for 'click off' colorimetric detection of peroxide and glucose," *Biosensors and Bioelectronics*, vol. 154, no. February, p. 112072, 2020.
- [30] H. Wang, J. Zhao, C. Liu, Y. Tong, W. He, "Pt Nanoparticles Confined by Zirconium Metal-Organic Frameworks with Enhanced Enzyme-like Activity for Glucose Detection," *ACS Omega*, vol. 6, no. 7, pp. 4807–4815, 2021.
- [31] X. Han, G. He, Y. He, J. Zhang, X. Zheng, L. Li, C. Zhong, W. Hu, Y. Deng, T.-Y. Ma, "Engineering Catalytic Active Sites on Cobalt Oxide Surface for Enhanced Oxygen Electrocatalysis," *Advanced Energy Materials*, vol. 8, no. 10, pp. 1–13, 2018.

- [32] Z.-J. Chen, Z. Huang, Y.-M. Sun, Z.-L. Xu, J. Liu, "The Most Active Oxidase-Mimicking Mn<sub>2</sub>O<sub>3</sub> Nanozyme for Biosensor Signal Generation," *Chemistry – A European Journal*, vol. 27, no. 37, pp. 9597–9604, 2021.
- [33] T. Mahaseth, A. Kuzminov, "Potentiation of hydrogen peroxide toxicity: From catalase inhibition to stable DNA-iron complexes," *Mutation Research*, vol. 773, pp. 274–281, 2017.
- [34] P. Zhang, D. Sun, A. Cho, S. Weon, S. Lee, J. Lee, J. W. Han, D.-P. Kim, W. Choi, "Modified carbon nitride nanozyme as bifunctional glucose oxidase-peroxidase for metal-free bioinspired cascade photocatalysis," *Nature Communications*, vol. 10, no. 1, p. 940, 2019.
- [35] L. Y. Jin, Y. M. Dong, X. M. Wu, G. X. Cao, G. L. Wang, "Versatile and Amplified Biosensing through Enzymatic Cascade Reaction by Coupling Alkaline Phosphatase in Situ Generation of Photoresponsive Nanozyme," *Analytical Chemistry*, vol. 87, p. 10429–10436, 2015.
- [36] X. Tao, X. Wang, B. Liu, J. Liu, "Conjugation of antibodies and aptamers on nanozymes for developing biosensors," *Biosensors and Bioelectronics*, vol. 168, p. 112537, 2020.
- [37] W. Lu, J. Chen, L. Kong, F. Zhu, Z. Feng, J. Zhan, "Oxygen vacancies modulation Mn<sub>3</sub>O<sub>4</sub> nanozyme with enhanced oxidase-mimicking performance for l-cysteine detection," *Sensors and Actuators B: Chemical*, vol. 333, p. 129560, 2021.
- [38] D. Hassen, S. A. El-Safty, K. Tsuchiya, A. Chatterjee, A. Elmarakbi, M. A. Shenashen, M. Sakai, "Longitudinal Hierarchy Co<sub>3</sub>O<sub>4</sub> Mesocrystals with High-dense Exposure Facets and Anisotropic Interfaces for Direct-Ethanol Fuel Cells," *Scientific Reports*, vol. 6, no. December 2015, pp. 1–12, 2016.
- [39] M. Curti, J. Schneider, D. W. Bahnemann, C. B. Mendive, "Inverse Opal Photonic Crystals as a Strategy to Improve Photocatalysis: Underexplored Questions," *The Journal of Physical Chemistry Letters*, vol. 6, no. 19, pp. 3903–3910, Oct. 2015.
- [40] A. Stein, B. E. Wilson, S. G. Rudisill, "Design and functionality of colloidal-crystal-templated materials—chemical applications of inverse opals," *Chemical Society Reviews*, vol. 42, no. 7, pp. 2763–2803, 2013.
- [41] P. Das, P. Borthakur, P. K. Boruah, M. R. Das, "Peroxidase Mimic Activity of Au–Ag/I-Cys-rGO Nanozyme toward Detection of Cr(VI) Ion in Water: Role of 3,3',5,5'-Tetramethylbenzidine Adsorption," *Journal of Chemical & Engineering Data*, vol. 64, no. 11, pp. 4977–4990, Nov. 2019.
- [42] B. Çakıroğlu, A. Çiğil-Beyler, A. Ogan, M. V. Kahraman, S. Demir, "Covalent immobilization of acetylcholinesterase on a novel polyacrylic acid-based nanofiber membrane," *Engineering in Life Sciences*, vol. 18, pp. 254–262, 2018.
- [43] L. Cao, P. Wang, L. Chen, Y. Wu, J. Di, "A photoelectrochemical glucose sensor based on gold nanoparticles as a mimic enzyme of glucose oxidase," *RSC Advances*, vol. 9, no. 27, pp. 15307–15313, 2019.
- [44] G.-L. Wang, X. Xu, X. Wu, G. Cao, Y. Dong, Z. Li, "Visible-Light-Stimulated Enzymelike Activity of Graphene Oxide and Its Application for Facile Glucose Sensing," *The Journal of Physical Chemistry C*, vol. 118, no. 48, pp. 28109–28117, Dec. 2014.
- [45] P. Zhang, D. Sun, A. Cho, S. Weon, S. Lee, J. Lee, J. W. Han, D.-P. Kim, W. Choi, "Modified carbon nitride nanozyme as bifunctional glucose oxidase-peroxidase for metal-free bioinspired cascade photocatalysis," *Nature Communications*, vol. 10, no. 1, p. 940, 2019.

- [46] L. Han, H. Zhang, D. Chen, F. Li, "Protein-Directed Metal Oxide Nanoflakes with Tandem Enzyme-Like Characteristics: Colorimetric Glucose Sensing Based on One-Pot Enzyme-Free Cascade Catalysis," *Advanced Functional Materials*, vol. 28, no. 17, p. 1800018, 2018.
- [47] H. Zhang, X. Liang, L. Han, F. Li, "'Non-Naked' Gold with Glucose Oxidase-Like Activity: A Nanozyme for Tandem Catalysis," *Small*, vol. 14, no. 44, p. 1803256, 2018.
- [48] J. Chen, W. Wu, L. Huang, Q. Ma, S. Dong, "Self-Indicative Gold Nanozyme for H<sub>2</sub>O<sub>2</sub> and Glucose Sensing," *Chemistry – A European Journal*, vol. 25, no. 51, pp. 11940–11944, 2019



## Effect of Signal Features and Model Variables on Energy-Traced Arrival Time Picking of Acoustic Signals Used for Structural Damage Detection

Sena Tayfur 

Ege University, Faculty of Engineering, Department of Civil Engineering, İzmir, Türkiye, [sena.tayfur@ege.edu.tr](mailto:sena.tayfur@ege.edu.tr)

### ARTICLE INFO

### ABSTRACT

#### Keywords:

Crack  
Structural Health Monitoring  
Signal  
Arrival Time  
Akaike Information Criteria  
(AIC)

#### Article History:

Received: 28.12.2022

Accepted: 25.12.2023

Online Available: 22.04.2024

To monitor damage developments in structures, various structural health monitoring methods based on different principles are used. The common aspect of elastic wave-based methods is to place appropriate sensors on the structure, to detect acoustic wave propagation and to analyze these signals the sensors transformed. The arrival time of these recorded signals to the sensors is the most significant parameter used to determine critical information such as the time and location of the damage. Therefore, the accurate calculation of the arrival time affects the accuracy of the damage detection.

In this study, effects of the signal-to-noise ratio (SNR), sampling frequency, length of the signal, and length of the focal window on determining the arrival time of the signals to the sensors were investigated. For this purpose, an energy-traced arrival time picking approach (Akaike Information Criterion, AIC), which is the frequently used method in the literature, has been applied to a typical acoustic signal originated from a concrete cracking. The results of the study suggest the necessity of noise elimination, the optimum level of data logging and the ratios of focal window lengths for accurate time of arrival detection in the field monitoring of the structures using acoustic methods.

## 1. Introduction

The location, size, and time of occurrence of the crack, which is the main damage type in concrete structures, can be determined by acoustic-based nondestructive testing methods. The main principle of these methods is propagation of the energy with frequencies that the human ear cannot hear and detection of them by appropriate sensors [1-3].

When the sound waves reach the sensor, the sensor starts to generate an electrical signal and these signals, which contain information about the damage, can be processed and analyzed to obtain information about the damage status of the structure [4, 5]. Some pulses may be lost as the sensor's signal generation depends on the sampling frequency of the recording system. But

more importantly, arrival time of the signal to the sensor can be lost here. On the other hand, since the recording system is triggered on the basis that the sensor starts to generate a signal as soon as it detects the pulse exceeding the threshold value, a pre-trigger window is also provided to the system in order not to lose the arrival time. Thus, along with the ambient noise, a set of pulses representing arrival time at the very beginning of the signal is added to the signal form.

The arrival time of the signal at the sensor is one of the two main parameters necessary to determine the location of the damage [6-8]. Since the propagation velocity of the wave, which is the other parameter in this problem, is very high (approximately 2500-3500 m/sec) in the concrete material [9], even microsecond errors in the arrival time calculation cause the damage

location to be calculated with high margin errors [10]. For this reason, the problem of accurate picking of this arrival time in the pre-trigger window, which is mixed with noise, has been one of the focal points of signal processing studies for structural damage assessment in the literature. For this purpose, different arrival time capturing methods with various approaches have been proposed [11-14]. Among them, Akaike Information Criteria (AIC), which picks the arrival time by tracing the change of signal energy, is the most preferred because it is used for a long time and it works with high reliability [15, 16].

Numerous studies exist in the literature demonstrating the effectiveness of AIC on the signals. Current studies are generally aimed to improve the method by developing it with different approaches and/or automating it during structural monitoring [17-19]. In this study, instead to search the method that captures the arrival time most accurately, the question of how the improvements that can be made on the signal form affect the arrival time estimation has been investigated. First, the most accurate arrival time obtained by filtering the raw signal exposed to ambient noise was investigated. Accordingly, the effect of noise filters with four different approaches, which are frequently encountered in the literature for damage signals, on arrival time detection was investigated. Then, the arrival time obtained from the most successfully filtered signal was then taken as a reference to reveal the effects of the signal length, sampling frequency and AIC focal window length. In this way, the necessity of noise elimination, optimum data logging level and the ratios of focal window lengths were evaluated to determine the accurate arrival time for monitoring the structures.

## 2. Methodology

Energy released by the damage propagates as acoustic waves with a wide frequency range (kHz-MHz), and these waves can be detected and converted into electrical signals with appropriate sensors placed on or embedded within the structure. Significant information about structural damage can be obtained by statistically evaluating the parameters of these signals and analyzing the signal form with various

techniques [4]. To obtain this information, the experimental setup is of great importance as well as the conditions under which the structure is monitored. The settings such as signal length, sampling frequency, pre-triggering window length to be used in the creation of the signal form should be chosen by an expert who can predict what kind of damage sources and what characteristics the signal will come from. On the other hand, these selections should be kept at an optimum level so as not to miss critical information about the signal and not to slow down the system and increase energy consumption.

### 2.1. Characteristics of acoustic signals

Signals showing the time-dependent voltage values contain important characteristics to determine information as to damage such as its size, type, time of occurrence and location. As seen from Figure 1, which shows a typical acoustic signal recorded from a concrete cracking event, a threshold level is used to highlight the pulses above a certain level. The area of the signal envelope formed by the pulses above the threshold defines the energy of the signal. Parameters such as amplitude, rise time, duration and count are the other characteristics that help determine the size and type of the damage [2].

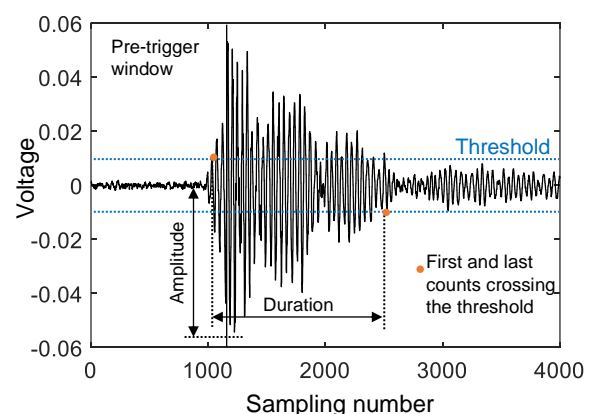


**Figure 1.** Characteristics of an acoustic signal

On the other hand, arrival time differences between the sensors are used to calculate the location of a damage (Figure 2). If the locations of the damage and  $i^{\text{th}}$  sensor's, the origination time of the damage, and the arrival time of the signal are defined as  $(x, y, z)$ ,  $(x_i, y_i, z_i)$ ,  $t_0$  and  $t_i$ ,



respectively, distance between the sensor and the damage ( $D_i$ ) can be calculated using wave velocity of  $V_p$  by Equations 1 and 2 [20]. Solution of the system involving  $i$  equations supplies the intersection point of the hyperbolas, which is the source location.

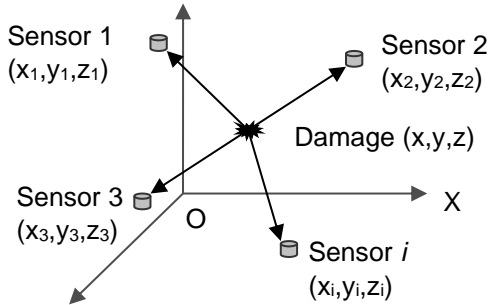


**Figure 2.** Principle of AE source localization

Sample equation;

$$D_i = V_p(t_i - t_0) \quad (1)$$

$$D_i = \sqrt{(x_i - x)^2 + (y_i - y)^2 + (z_i - z)^2} \quad (2)$$

While the system is recording, when the sensor captures the pulse exceeding the threshold, it also creates the pre-trigger window, and the length of this window can be determined depending on the signal length. The arrival time of the signal, which is used to determine the location of the damage, is also included in this window.

## 2.2. Energy-traced picking of signal arrival time

Since the system records data with a certain sampling frequency during the monitoring of the structure, arrival time of the signal can be missed, and it has to be calculated correctly for accurate localization of the damage. Since the propagation velocity of the wave in concrete is very high (~2500-3500 m/sec), even the incorrect calculation of the arrival time in the order of microseconds causes high errors in localization procedure. Akaike Information Criteria (AIC) is a statistical method frequently used for picking the arrival time between the noise and the actual signal data in the time history by tracing the energy changes in the signal [15]. For this, first, the AIC function is calculated using Equation 3 in the region where the average of the values of the voltages in the ten groups of the signal is

more than four times of the previous group. Then a second focal window is opened with reference to the moment when the AIC function reaches the minimum. After the same process is repeated in the second window, the minimum AIC occurrence moment in the second window defines the arrival time of the signal to the sensor [12].

$$AIC\{k\} = k \cdot \log \{G, [1, k]\} + (N - k) \cdot \log \{G, [k + 1, N]\} \quad (3)$$

where  $k$  is the number of the focal signal window,  $G$  is the amplitude of the related time and  $N$  is the total voltage number within the window.

## 2.3. Signal-to-noise ratio (SNR)

Electrical or mechanical background noises, which are clearly visible in the pre-triggering window, also interfere with the damage-related signal form. Signal-to-noise ratio (SNR), is defined as the ratio of signal power to the noise power [21-24] and it can be calculated in dB by Equation 4.

$$SNR(\text{dB}) = 20 \log_{10} \frac{P_s(w_2)}{P_g(w_1)} \quad (4)$$

where  $P_s$  ve  $P_g$  are the mean powers of the damage signal and the noise within the windows  $w_2$  and  $w_1$ , respectively. Windows  $w_1$  and  $w_2$  are selected according to signal and pre-triggering window lengths. Accordingly, the higher SNR of a signal, the better it suppresses noise. Therefore, the intensity of the noise also affects the correct capturing of the arrival time. The SNR of the signal can be increased by various noise filtering techniques [24, 25].

## 3. Processing and Arrival Time Picking of an Acoustic Signal

### 3.1. Details of the tested model

In this study, signal S1 arisen from a crack activity originated in a reinforced concrete beam under flexure test was used to investigate the effects of the signal features and model variables on picking arrival time (Figure 3). The beam was produced from a concrete having cylinder compressive strength of 30 MPa and was in sizes of 235x25x15 cm. It was reinforced with two Ø8

mm longitudinal rebars at the bottom and top of the section and Ø8 mm stirrups with spacing of 10 cm were placed to strengthen shear capacity of the beam. During loading, the beam was monitored using eight piezoelectric sensors having resonance frequency of 150 kHz. The sensors were amplified by preamplifiers with 40 dB gain. Data was recorded using AE system by Mistras.

Threshold of the system was also set as 40 dB level. The specimen was damaged in flexure and 21703 signals were recorded from all sensors. Table 1 shows mean values and standard deviations of AE features of the signals collected from the test. As seen from the signal characteristics, higher standard deviations of average frequency and rise time parameters indicate while some signals represent more tensile-type cracking, some of them are more flexural-shear-type.

**Table 1.** AE features of the data collected

	Mean value	Standard deviation
Energy (aJ)	22.16	231.69
Average frequency (kHz)	156.44	303.70
Rise time ( $\mu$ sec)	135.43	622.84
Amplitude (dB)	46.75	7.69
Peak frequency (kHz)	82.62	52.70
Frequency centroid (kHz)	131.96	32.82

### 3.2.Characteristics of the selected acoustic signal

In order not only to study on a specific crack type, but also to investigate a signal containing high-level noise, signal S1, one of these AE signals recorded during this loading test, was chosen in this study. This signal was selected because it represents a typical concrete cracking signal (Figure 3). Sampling frequency, length and SNR of the signal is 1  $\mu$ sec, 2048 and 3.07 dB, respectively. As can be seen, pre-trigger length is 512. While the system was recording, when the sensor caught the pulse exceeding the

threshold value (40 dB), it added 512 pulses before the trigger and created the whole signal for this reason, arrival time of the signal to the sensor was also included in pre-trigger window with the ambient noise. Thus, using threshold crossing approach causes erroneous results since the arrival time is missed.

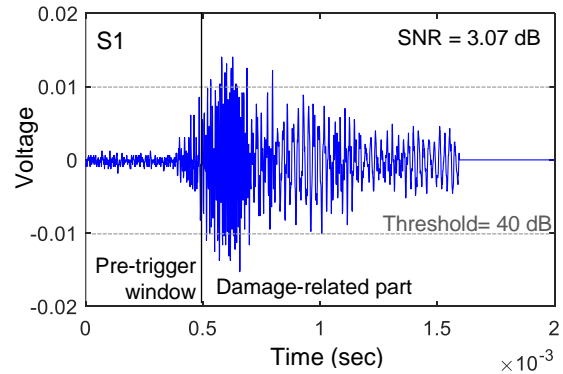


**Figure 3.** A typical acoustic signal caused by concrete cracking used in the study

To determine the effect of the noise on energy-traced picking of the arrival time, first the signal was filtered with different-approach filters. These filters were Band Pass, Wavelet, Wiener and Savitzky-Golay, which are frequently used for acoustic and ultrasonic waves in the literature. A Band Pass filter eliminates frequencies outside a certain band. In this study, the Band Pass filter was designed with 1 kHz of stopband, 2 kHz and 60 kHz of passband frequencies, and 100 kHz of sampling frequency. In Wavelet filtering, the signal was filtered by both scaling and shifting the main function, which acts as a window in the wavelet transform [26-28]. Unlike most other filters with Wiener, the noisy signal was filtered by comparing it with an estimation of the filtered signal [29-31].

Finally, a polynomial was fitted with the Savitzky-Golay filter, which is a low-pass filter, and the value of the polynomial at the midpoint of the window was taken as the filtered pulse [32-34]. To determine the effect of sampling frequency and signal length, the arrival time was calculated by varying the lengths of the signal S1 with different ratios. Thus, the sampling frequency of the signal also changed at these rates. For the effect of the focal window lengths for AIC function, the arrival time was picked according to the ratio of the 1st and 2nd window lengths to the signal length (n).

## 4. Results and Discussion

### 4.1. Effects of the noise

Since the power of the noise decreased after filtering S1 signal, the SNR value increased compared to its raw state (3.07 dB), as expected. Thus, the arrival times according to the five different SNR values of the signal were picked by AIC and the results were given in Figure 4. The arrival times for each signal were captured in the pre-trigger window when the energy-traced AIC function reached its minimum value and the signal energy suddenly increased. However, the point to be considered here is which of the filtered forms of the signal is the most accurate and the appropriate arrival time should be referenced to compare it with others.

When the noise function is filtered from the signal, decreases in the voltage of damage-related part of the signal is expected. But in order not to change the signal behavior and the damage information it represents, it is desirable that the form does not change after triggering. As can be seen, although the highest SNR value (8 dB) was obtained with the Band Pass filter, the voltage level in the damage-related part of the signal was also very low and it did not exhibit the expected behavior from the signal caused by concrete damage. For this reason, the arrival time obtained from S2 was not taken as the reference. When other filters were evaluated from the abovementioned point of view, among the remaining signals the best filtering was obtained from Wiener (S4), which eliminates the pre-triggering noise and did not lose much of the voltage value by not distorting the form in the damage-related part of the signal. In particular, the presence of very low-voltage pulses in the pre-triggering noise window of S4 caused this signal to be chosen as the reference for comparing arrival times.

On the other hand, although the voltage values decreased after filtering, the earliest time of arrival was obtained as 0.000362 sec with using S4. As can be seen from S4, arrival time could be determined earlier than 0.000390 sec obtained from the noisy state of the signal. This shows that filtering without distorting the signal form and voltage values is more effective for accurate

arrival time picking rather than increasing the SNR.

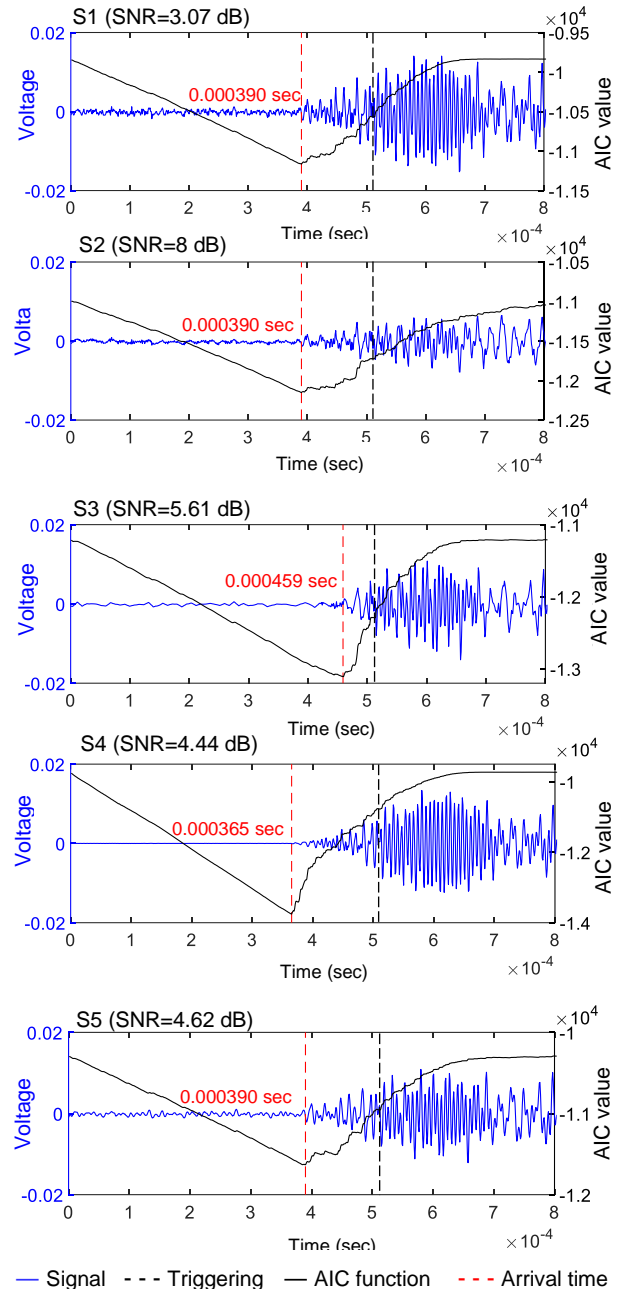


**Figure 4.** Picking the arrival time of the signal according to different SNR values after noise filtering

Since the arrival time of the signal is the most important factor in determining the location of the damage, Table 2 was composed to reveal how the arrival time affects the distance to be calculated between the sensor and the source. Here, the distances were calculated using the propagation velocity of P wave in concrete as 3500 m/sec. As can be seen, although the differences between the arrival times are in the

order of microseconds, they are of great importance in terms of determining the location of the damage, and distance deviations were measured up to 32.9 cm with S3 and 8.75 cm with other filters. These values cause to inaccurate localization results.

**Table 2.** Source-sensor distance errors according to different SNR values after noise filtering

Signal	Arrival time ( $\mu$ sec)	Source-sensor distance (m)	Source-sensor distance error (cm)
S1	390	1.365	8.75
S2	390	1.365	8.75
S3	459	1.606	32.9
S4	365	1.278	-
S5	390	1.365	8.75

**4.2. Effect of the sampling frequency and signal length**

The arrival time was calculated by varying the lengths of the signal S1 (S1N1) with the ratios of 0.5 (S1N05), 2 (S1N2), 3 (S1N3) and 4 (S1N4). Thus, the sampling frequency of the signal also changed at these rates.

Figure 5 shows the arrival time results obtained when the signal length and sampling frequency were changed by these coefficients. As can be seen from the figure, when the signal length and sampling frequency were halved (S1N05), the same arrival time with the noisy state of the signal (S1N1) was picked. However, in the other three cases, the arrival times were delayed by 0.3  $\mu$ sec and 0.5  $\mu$ sec. This shows that as the sampling frequency increases, the sensitivity in picking the arrival time also increases.

However, as can be seen, these changes are not as higher as the changes obtained after noise filtering. In other words, eliminating the noise is a much more effective factor in accurately picking the arrival time, rather than the sampling frequency and length of the signal. For these reasons, Table 3 shows how these small changes affect the distance between the source and the sensor in localization, to determine how necessary it is to upload such data to the recording system by increasing the data frequency in terms of time and energy consumption. As can be seen, the distance difference calculated according to the earliest

and the latest arrival times (0.000390 sec and 0.0003905 sec) is 0.175 cm where the propagation velocity of the P wave in concrete was taken as 3500 m/sec.

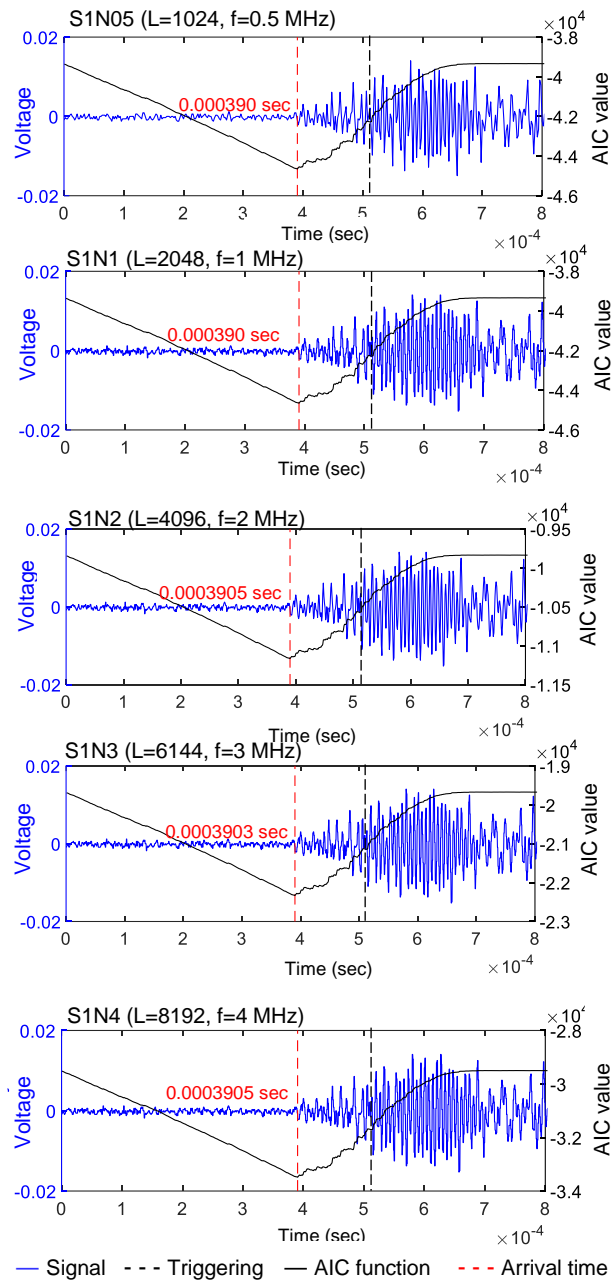


**Figure 5.** Picking the arrival time of the signal according to different sampling frequencies and signal lengths

Although this value is not as much as the noise effect, it will cause incorrect localization of the cracks that occur in the sections of the reinforced concrete beams or columns whose dimensions are much smaller than their lengths. While noise elimination is recommended in this respect; if the filtering has been done sufficiently, the decision whether to change the sampling frequency is left



to the engineer according to the capacity of the recording system used.

**Table 3.** Source-sensor distance errors according to different sampling frequencies and signal lengths

Signal	Arrival time (µsec)	Source-sensor distance (m)	Max. distance error regarding the earliest and the latest two arrival times (cm)
S1N05	3900	1.365	
S1N1	3900	1.365	
S1N2	3905	1.36675	0.175
S1N3	3903	1.36605	
S1N4	3905	1.36675	

#### 4.2. Effect of the focal window length

Arrival times calculated according to the ratio ( $n$ ) of the 1<sup>st</sup> and 2<sup>nd</sup> focal window lengths to the signal length are given in Table 4. As can be seen, by changing the focal window lengths of the unfiltered signal S1, 5 µsec differences occurred in the arrival times. On the other hand, focal window length did not change the arrival time of signal S5, which was references and in which the noise was best filtered as mentioned in title 4.1.

**Table 4.** Arrival times of the filtered signals according to different focal window lengths

Window length			Arrival time (µsec)				
$L_{P1}$	$L_{P2}$	$L_{P2}/L_{P1}$	S1	S2	S3	S4	S5
50	50	1	385	389	459	365	384
100	100	1	390	390	459	365	385
100	50	0.5	385	389	459	365	384
500	500	1	390	390	459	365	390
500	250	0.5	390	390	459	365	390

For this reason, in the absence of noise filtering, especially as the length of the 2<sup>nd</sup> focal window increases, the amount of noise increases the signal energy, and it causes greater differences in picking the arrival time. Especially in these cases, it is recommended to use the 1<sup>st</sup> and 2<sup>nd</sup> focal window lengths with a ratio of 2/1, as it is more successful in picking earlier arrival times.

#### 5. Conclusions

In this study, the effects of SNR, sampling frequency, signal length, and focal window length on the determination of the arrival time of the acoustic signals to the sensors were

investigated. For this purpose, a frequently used energy-traced arrival time picking approach AIC was applied to a typical concrete crack-related acoustic signal that can be recorded while monitoring concrete structures. The results of the study suggest the necessity of noise elimination, the optimum level of data logging and the ratios of focal window lengths for accurate time of arrival picking in the field monitoring of the structures. Accordingly,

1. Among the filters used in the study, Wiener filter was the best to predict the arrival time at earliest by eliminating the noise best and not distorting the damage-related part of the signal.

2. It has been seen that filtering without distorting the signal form and voltage values is more effective for accurate arrival time picking rather than increasing the SNR.

3. It has been revealed that the differences in the order of microseconds between the arrival times cause relatively large distance deviations in the order of centimeters which cannot be ignored.

4. Eliminating the noise is a much more effective factor in accurately picking the arrival time, rather than the sampling frequency and signal length. For this reason, while noise elimination is recommended, it is suggested that the signal sampling frequency can be selected according to the performance of the data recording system if the filtering is done sufficiently.

5. In the absence of noise filtering, especially as the length of the 2<sup>nd</sup> focal window increases, the amount of noise increases the signal energy and larger differences in arrival times occur. Especially in these cases, it is recommended to choose the 1<sup>st</sup> and 2<sup>nd</sup> window lengths with a ratio of 2/1.

6. For future works, development of a statistical analysis can be recommended to prove the results of more and different-type signals.

## Article Information Form

### *The Declaration of Conflict of Interest/ Common Interest*

No conflict of interest or common interest has been declared by the authors.

### *The Declaration of Ethics Committee Approval*

This study does not require ethics committee permission or any special permission.

### *The Declaration of Research and Publication Ethics*

The authors of the paper declare that they comply with the scientific, ethical and quotation rules of SAUJS in all processes of the paper and that they do not make any falsification on the data collected. In addition, they declare that Sakarya University Journal of Science and its editorial board have no responsibility for any ethical violations that may be encountered, and that this study has not been evaluated in any academic publication environment other than Sakarya University Journal of Science.

### *Copyright Statement*

Authors own the copyright of their work published in the journal and their work is published under the CC BY-NC 4.0 license.

## References

- [1] ASTM E 1316, "Standard Terminology for NDT", 2002.
- [2] C. U. Grosse, M. Ohtsu, "Acoustic Emission Testing, Basics for Research-Applications in Civil Engineering, Springer-Verlag, Berlin, Heidelberg, 2008.
- [3] S. Tayfur, N. Alver, "Attenuation and Frequency Characteristics of Acoustic Waves in Steel and Synthetic Fiber-Reinforced Concrete: 3D-PCT and Unsupervised Pattern Recognition", Applied Sciences, Vol. 12, 24, pp. 12976, 2022.
- [4] S. Tayfur, N. Alver, S. Abdi, S. Saatçı, A. Ghiami, "Characterization of concrete matrix/steel fiber de-bonding in an SFRC beam: Principal component analysis and k-mean algorithm for clustering AE data", Engineering Fracture Mechanics, Vol. 194, pp. 73-85, 2018.
- [5] C. Van Steen, EVerstryng, "Signal-Based Acoustic Emission Clustering for Differentiation of Damage Sources in Corroding Reinforced Concrete Beams", Applied Sciences, Vol. 12, 4, pp. 2154, 2022.
- [6] Z. Li, F. Li, X. S. Li, W. Yang, "Determination and AE Characterization of Concrete", Journal of Engineering Mechanics, Vol. 126, 2, pp. 194-200, 2000.
- [7] S. Gollob, G. K. Kocur, T. Schumacher, L. Mhamdi, T. Vogel, "A novel multi-segment path analysis based on a heterogeneous velocity model for the localization of acoustic emission sources in complex propagation media", Ultrasonics, Vol. 74, pp. 48-61, 2017.
- [8] F. Zhang, L. Pahlavan, Y. Yang, "Evaluation of acoustic emission source localization accuracy in concrete structures", Structural Health Monitoring, Volume 19, 6, pp. 2063-2074, 2020.
- [9] Y. H. Lee, T. Oh, "The Measurement of P-, S-, and R-Wave Velocities to Evaluate the Condition of Reinforced and Prestressed Concrete Slabs", Advances in Materials Science and Engineering, Vol. 2016, pp. 1-15, 2016.
- [10] X. Shang, Y. Wang, R. Miao, "Acoustic emission source location from P-wave arrival time corrected data and virtual field optimization method", Mechanical Systems and Signal Processing, Vol. 163, pp. 108129, 2022.
- [11] J. H. Kurz, C. U. Grosse, H. W. Reinhardt, "Strategies for reliable automatic onset time picking of acoustic emissions and of ultrasound signals in concrete", Ultrasonics, Vol. 43, 7, pp. 538-546, 2005.

- [12] A. Carpinteri, J. Xu, G. Lacidogna, A. Manuello, “Reliable onset time determination and source location of acoustic emissions in concrete structures”, *Cement & Concrete Composites*, Vol. 34, pp. 529-537, 2012.
- [13] F. Bai, D. Gagar, P. Foote, Y. Zhao, “Comparison of alternatives to amplitude thresholding for onset detection of acoustic emission signals” *Mechanical Systems and Signal Processing*, Vol. 84, pp. 717-730, 2017.
- [14] M. Zhang, M. Li, H. Li, “Onset detection of ultrasonic signals for the testing of concrete foundation piles by coupled continuous wavelet transform and machine learning algorithms”, *Advanced Engineering Informatics*, Vol. 43, pp. 101034, 2020.
- [15] H. Akaike, “Markovian representation of stochastic processes and its application to the analysis of autoregressive moving average”, *Annals of the Institute of Statistical Mathematics*, Vol. 26, 1, pp. 363–387, 1974.
- [16] G. Kitagawa, H. Akaike, “A procedure for the modeling of non-stationary time series”, *Annals of the Institute of Statistical Mathematics*, Vol. 30, 1, pp. 351-363, 1978.
- [17] R. Madarshahian, P. Ziehl, J. M. Caicedo, “Acoustic emission Bayesian source location: Onset time challenge”, *Mechanical Systems and Signal Processing*, Vol. 23, pp. 483-495, 2019.
- [18] H. Chen, Z. Yang, “Arrival Picking of Acoustic Emission Signals Using a Hybrid Algorithm Based on AIC and Histogram Distance”, *IEEE Transactions on Instrumentation and Measurement*, Vol. 70, pp. 3505808, 2020.
- [19] H. Li, Z. Yang, W. Yan, “An improved AIC onset-time picking method based on regression convolutional neural network”, *Mechanical Systems and Signal Processing*, Vol. 171, pp. 108867, 2022.
- [20] L. Geiger, “Probability method for the determination of earthquake epicentres from the arrival time only”, *Bulletin of St. Louis University*, Vol. 8, pp. 60-71.
- [21] V. Matz, R. Smid, S. Starman, M. Kreidl, “Signal-to-noise ratio enhancement based on wavelet filtering in ultrasonic testing”, *Ultrasonics*, Vol. 49, 8, pp. 752-759, 2009.
- [22] J. Xu, Z. Wang, C. Tan, L. Si, X. Liu, “A Novel Denoising Method for an Acoustic-Based System through Empirical Mode Decomposition and an Improved Fruit Fly Optimization Algorithm”, *Applied Sciences*, Vol. 7, 3, pp. 215, 2017.
- [23] K. Prajna, C. K. Mukhopadhyay, “Fractional Fourier Transform Based Adaptive Filtering Techniques for Acoustic Emission Signal Enhancement”, *Journal of Nondestructive Evaluation*, Vol. 39, 14, pp. 1-15, 2020.
- [24] C. Zhou, Y. Zhang Y, “Particle filter based noise removal method for acoustic mission signals”, *Mechanical Systems and Signal Processing*, Vol. 28, pp. 63-77, 2012.
- [25] M. Sraitih, Y. Jabrane, “A denoising performance comparison based on ECG Signal Decomposition and local means filtering”, *Biomedical Signal Processing and Control*, Vol. 69, pp. 102903, 2021.
- [26] N. Arı, S. Özen, Ö. H. Çolak, “Dalgacık Teorisi”, *Palme Yayıncılık*, Ankara, 2008.
- [27] İ. V. Öner, M. K. Yeşilyurt, E. Ç. Yılmaz, “Wavelet Analiz Tekniği ve Uygulama Alanları”, *Ordu University Journal of Science and Technology*, Vol. 7, 1, pp. 42-56, 2017.
- [28] R. Janeliukstis, “Continuous wavelet transform-based method for enhancing estimation of wind turbine blade natural frequencies and damping for machine

- learning purposes”, Measurement, Vol. 172, pp. 108897, 2021.
- [29] N. Wiener, “The Interpolation, Extrapolation and Smoothing of Stationary Time Series”, Report of the Services 19, Research Project DIC-6037 MIT, 1942.
- [30] M. Jayawardhana, X. Zhu, R. Liyanapathirana, “Damage Detection of Reinforced Concrete Structures Based on the Wiener Filter”, Australian Journal of Structural Engineering, Vol. 14, pp. 57-69, 2013.
- [31] Y. W. Chen, “Noise Reduction by Wiener Filter (<https://github.com/JarvusChen/MATLAB-Noise-Reduction-by-wiener-filter>)”, GitHub. Retrieved April 22, 2022.
- [32] A. Savitzky, M. J. E. Golay, “Smoothing and Differentiation of Data by Simplified Least Squares Procedures”, Analytical Chemistry, Vol. 36, 8, pp. 1627-1639, 1964.
- [33] H. Hassanpour, “A time–frequency approach for noise reduction”, Digital Signal Processing, Vol. 18, 5, pp. 728-738, 2008.
- [34] H. Azami, K. Mohammadiand B. Bozorgtabar, “An Improved Signal Segmentation Using Moving Average and Savitzky-Golay Filter”, Journal of Signal and Information Processing, Vol. 3, 1, pp. 39-44, 2012.





## Bitcoin Price Prediction with Fuzzy Logic

Gulcihan Özdemir 

İstanbul Technical University, Informatics Institute, Department of Applied Informatics, İstanbul, Türkiye, [ozdemirg@itu.edu.tr](mailto:ozdemirg@itu.edu.tr)

### ARTICLE INFO

### ABSTRACT

#### Keywords:

Bitcoin  
Cryptocurrency  
ANFIS  
Price Prediction  
Trend Analysis

Due to cryptocurrencies' rising prices, like bitcoin, more and more people are becoming interested in them. Success in this business depends on a good price prediction. Several methods, including heuristic and machine-learning-based ones, can currently estimate the price with varied degrees of success. This study will use the Adaptive Neuro-Fuzzy Inference Systems (ANFIS) model to predict the price's general direction over the next 10 days. Along with popular traders' indicators, the previous day's price will be used. The findings demonstrated that, despite errors, price direction predictions—an increase, a drop, or a stable price—are typically accurate.

#### Article History:

Received: 12.02.2023

Accepted: 28.12.2023

Online Available: 22.04.2024

## 1. Introduction

The first decentralized cryptocurrency was Bitcoin, which Nakamoto designed and documented [1]. Over the past few years, cryptocurrencies like bitcoin have emerged as a significant new source of investment. The popularity of cryptocurrencies has skyrocketed since the introduction of the bitcoin in 2008 [1], which has resulted in a significant bloom in business opportunities as well as scams [2], on the market. Bitcoin price was around zero in 2009 then reached nearly \$20000 in December 2017 [3]. The highest value it reached in literature so far is about \$64000 in November 2021. The current value is now about \$26000 in Sep 2023 [4]. Cryptocurrencies are an investment that can be profitable as well as risky. It is vital to forecast their future value in order to boost profit while lowering risk. There have already been a number of publications on the subject that attempted to predict future values across various

time periods with varying degrees of success. A Neuro-fuzzy approach is to predict the direction of the change of the daily price of Bitcoin for the next day in [3], and for the stock market trend forecasting with the same methodology again for the next day is studied in [5].

The ability to forecast the four most valuable cryptocurrencies, Bitcoin, Litecoin, Ripple, and Ethereum, using a variety of univariate dynamic linear models and multivariate vector autoregressive model combinations with various types of time horizons ( 1-7 days ahead) is compared in [6]. In all cases, the multivariate models' success rate for directional predictability is over 50%, with higher percentages of around 60% at the two- and three-day-ahead horizons. All of the models produce quite comparable outcomes. The largest returns are obtained for predicting Ripple, with success rates well above 60%, when examining the directional predictability for each currency separately

Ethereum, on the other hand, appears to be the currency whose sign fluctuations are the hardest to forecast. Given the significant gains for log score evaluation, it may be possible to continue examining more sophisticated investment methods that place more emphasis on more powerful instances as opposed to just return direction.

There isn't presently a perfect method to predict the future price or trend of a particular cryptocurrency because of how novel the concept is and how challenging the process is. The research is still fragmented, though; some sought to approach the issue by experimenting with various approaches, while others attempted to use diverse data as variables [7–10]. Others attempt to forecast prices for the upcoming hour or the next day [9, 11].

A study describes how the market will be impacted by the present and future Bitcoin movements concerning seven attributes (variables), and a non-linear autoregressive with external input analysis was done [12]. Levenberg-Marquard (LM), Bayesian Regularization (BR), and Scaled Conjugate Gradient (SCG) algorithms were used as three training algorithms to train a neural network. According to a comparison analysis of these three training methods, the BR approach performed satisfactorily and had a low error rate. The proposed initiative will encourage predicting the market trends that affect the Bitcoin market.

The investigation of a theoretical framework for upcoming cryptocurrency research focuses on developing new, sustainable models for the growth of the cryptocurrency industry forecast [13].

Two statistical and three machine learning algorithms are used to forecast the daily price of Bitcoin [14] in a comparison of statistical and machine learning techniques. The simplest method, moving average analysis, which forecasts future values by averaging previous  $n$  values, has the biggest inaccuracy. However, for time series analysis, a popular method called ARIMA outperforms the simplest neural network approach. Furthermore, even though setting parameters results in multiple analyses, choosing

the optimal ones is not guaranteed. Thus, it is anticipated that nonlinear neural networks outperform ARIMA and other statistical techniques that force data linearization by employing more promising methods for parameter selection from the literature.

The objectives of these studies also tend to differ somewhat. Price fluctuation within a single day or across multiple days may be excessively high. Correctly predicting the price and/or direction could be exceedingly challenging. Before the invention of Bitcoin, a related work about forecasting to model and foresee the realized volatilities for data with very high volatilities was introduced [15].

Several works that use various forms of computational intelligence are available, such as Adaptive Neuro-Fuzzy Inference Systems (ANFIS) and Artificial Neural Networks (ANN) [7, 10-11, 16-18]. Some people also combine several Machine Learning techniques, such as Linear Regression and Autoregressive Integrated Moving Average [8], or even the decomposition-composition approach [19] to achieve their objectives.

Other algorithms are developed utilizing some thoroughly researched external data that is not always related. They include the use of economic indicators including the price of gold and crude oil, as well as the EUR/USD, CNY/USD, and JPY/USD exchange rates [7]. Studies have also been conducted both on the economical and technical aspects of bitcoins, such as the difficulty of mining, hash rate, the volume of transactions, or the overall quantity of bitcoins in existence [20]. Additionally, some people analyze, compare, and parallelize the use of many cryptocurrencies, such as Ethereum or Litecoin [8, 19].

In contrast, we make an effort to predict the price trend of Bitcoin 10 days in advance using only its current and historical prices. As we will go into more detail below, we looked into several trading indicators, including the Bollinger Bands and Moving Average. After that, we experimented with a variety of values, including the price at the start and end of the day, as well as the highest and lowest prices that occurred on that day. Then, we

tested several combinations while utilizing the ANFIS model suggested by Matlab until we got a good outcome. The combination we ultimately chose yielded a respectable outcome for forecasting the direction but is less than ideal for predicting prices.

However, part of the literature makes use of the average between the highest and lowest price, or even all four values at once. Averaging smoothes the peaks that can cause high errors in price forecasting and misleading the trend. We studied some of these indicators before deciding which one to use.

Actually, we are estimating the derivative of the price function by using the relative price fluctuation. That includes positive and negative values, denoting price rises and declines, respectively. Therefore, rather than focusing on the magnitude of the fluctuation, the goal would be to determine its direction. As long as we can predict when the price is rising, declining, stationary, or reaching an extreme, we may say that our outcome is appropriate. Currently, our greatest strength is our ability to predict the ascent and decline of the price 10 days in advance. This will present a significant window of opportunity for planning ahead and give investors enough time to boost their profits even further. Utilizing key stock market directional indicators like the Directional Movement Index, Bollinger bands, Moving Average Convergence/Divergence, and the Ichimoku Cloud is another contribution of our work. Section 2 provides more information.

The estimated and predicted percentages diverge by an average of 7%, highlighting the stark contrast between the outcomes. Given that the forecasted price's permitted  $\pm 10\%$  range lies between 90% and 110%, our 7% precision error is still within this range.

Though the outcome from the error in the price forecasting direction has a higher inaccuracy than the price prediction when considering. Typically, there is only a 12% error in the price's direction.

When forecasting the future, models with a 10% error range offer a strong enough degree of flexibility to account for potential extreme volatility, which is a feature of cryptocurrencies. If not, the prediction would be overfitting, which typically occurs in artificial neural network modeling for the given data set, and it would not be effective for abrupt and volatile price fluctuations. In this regard, ANFIS is advantageous to use for predicting work due to the adaptive and flexible nature of fuzzy logic modeling.

## 2. Modelling

It is possible to find on the internet the daily price value of the bitcoin on the market from 2015 up to today [21]. This data typically includes four values: the price at the beginning and ending of the day, as well as the highest and lowest price reached that day. Typically, when creating additional indicators, the closing price is used. Figure 1 shows the daily closing price of 2500 days of Bitcoin.

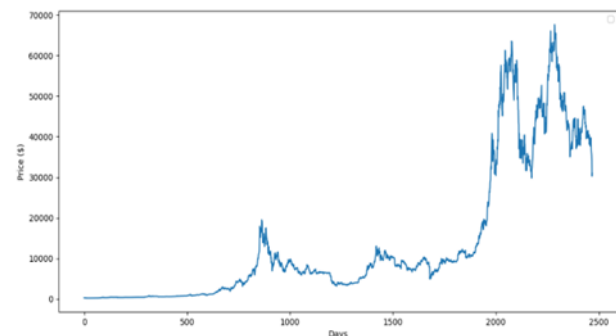


**Figure 1.** Daily closing price of Bitcoin, from 2015-08-07 to 2022-05-10

However, some researchers use the average between the highest and the lowest price, or even all four values at once [14]. We studied some of these indicators before deciding which one to use.

### 2.1 Moving averages

The first, basic, indicator is the Moving Average. Simply said, it smooths the daily value using the prices of previous days. While these are extremely useful for removing noise, they are also used to insert some latency, notably when a change of direction occurs.

The simplest among them is the Simple Moving Average (SMA). It simply averages the daily value on a given time frame, with each price having the same importance. As it is simple to calculate, it is frequently used by other indicators as well. Figure 2 shows the bitcoin daily closing price with the averages (SMA, EMA, DEMA) calculated for a 10-day period.

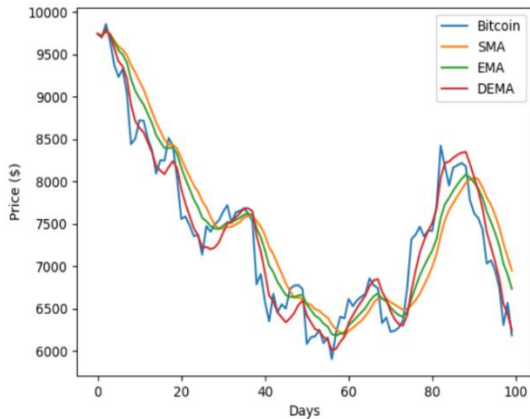


**Figure 2.** Moving average with a 10-day period

The formula used is (1), where  $p$  is the period and  $v$  is an array of daily values, with the 0th entry representing the value for the current day.

$$SMA_p(v) = \sum_{j=0}^p \frac{v_j}{p} \tag{1}$$

The other Moving Average is the Weighted Moving Average (WMA). The daily values are weighted inversely proportionally to their distance from the searched day. Simply said, the values of the given day have the highest weight, while the farther it is, the less weight it becomes (2).

$$MA_p(v) = \frac{\sum_j^p v_j \cdot \frac{p-j}{p}}{\frac{p \cdot (p+1)}{2}} \tag{2}$$

Another common Moving Average is the Exponential Moving Average (EMA) (3) and (4). The daily value is calculated recursively by adding the weighted value of the day with the complementally weighted EMA of the previous day. The important point is to choose an appropriate weight value, which is typically dependent on the desired period. We are using in our case the weight value as  $1 - \sqrt[p]{0.135}$

$$EMA_p^i(v) = v_i \cdot k + EMA_p^{i+1}(v) \cdot (1 - k) \tag{3}$$

$$EMA_p^p(v) = SMA_p(v) \tag{4}$$

There are some other variations of the EMA, such as the Double Exponential Moving Average (DEMA) given in (5), or the Triple Exponential Moving Average (TEMA) given in (6), which use the value of the EMA as input for the EMA formula. However, since the EMA is calculated using an interval, taking the EMA of the EMA requires calculating the EMA of every day on the interval first, which rapidly increases the required calculations. As shown in Figure 2, the EMA gives a value closer to the initial one than the SMA, and the DEMA an even closer one, while still ignoring the smallest disparities.

$$DEMA(v) = 2 \cdot EMA(v) - EMA(EMA(v)) \tag{5}$$

$$TEMA(v) = 3 \cdot EMA(v) - 3 \cdot EMA(EMA(v)) + EMA(EMA(EMA(v))) \tag{6}$$

## 2.2 Relative strength index and bollinger bands

Among the other studied indicators, there are two of them that are quite useful and easy to understand: the Relative Strength Index and the Bollinger Bands.

The Relative Strength Index (RSI) is obtained by summing up the amount of increases and decreases over a given period of time, and then dividing the amount of increase by the sum of the two. This gives us an idea of the general direction of the price. If the value is greater than 0.5—50 in Figure 3 since we are using percent—this means the increases are more important than decreases in the time interval, signifying the price has increased as a whole. Using several RSI of different periods is useful to notice local protuberance on an overall trend. For example, in Figure 3, which uses the same data as Figure 2, we can notice an overall decrease in the price using the RSI 30, but still notice the small lump around days 30 using the RSI 10. We are also using the DEMA of the RSI in order to have a cleaner output, as we can with the RSI 10 around day 50.



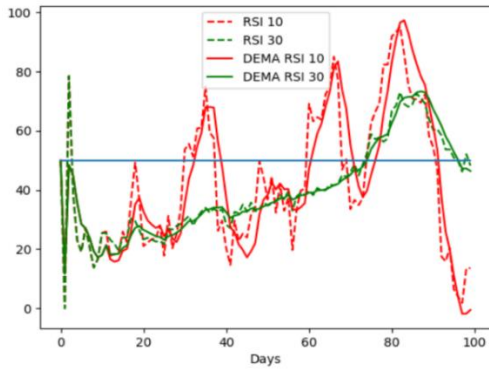


**Figure 3.** RSI of the price of Figure 2

The other really interesting indicator is the Bollinger Bands (BB). They are composed of three bands: a middle one using a traditional SMA, as well as an upper and lower band created by respectively adding and subtracting twice the standard deviation. The main advantage of the Bollinger Bands is that it visually combines several information, such as the average value with its internal band, the strength of the recent variation by looking at the spacing of the external bands, as well as the current trend by comparing the value with all three bands. This can also be used to normalize the price value by encompassing it between the two bands, as shown in Figure 4. In this case, we are using the delay induced by the SMA to get a hold of the price trend.

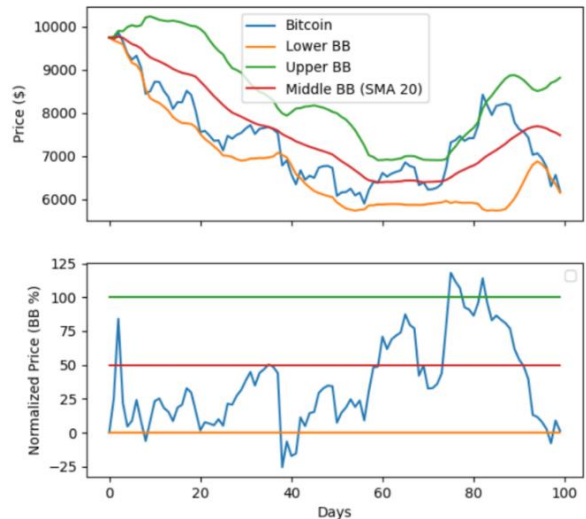


**Figure 4.** Bollinger Bands with a 20-day period

### 2.3. Other indicators

Without entering too much detail, we also studied three other indicators called the Moving Average Convergence/Divergence (MACD), the Directional Movement Index (DMI), and the Ichimoku Cloud.

The MACD is calculated using three periods, typically one small, one medium, and one large. A first line is created using the difference between the medium and large period EMAs, and a second line is obtained with the EMA of the previously created line over the small period. The MACD indicators used the small delay added by the moving average to determine an upper or lower trend, as well as a turning point, by taking the difference between the two previously created lines, as shown in Figure 5.

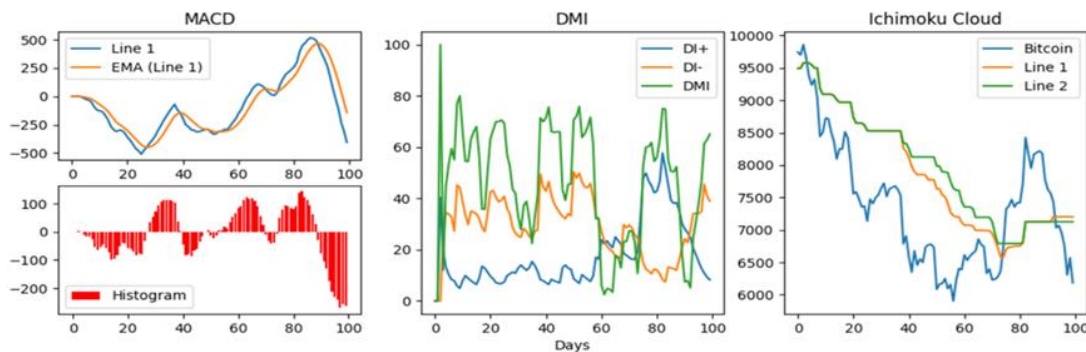


**Figure 5.** Example of MACD (9,12,26), DMI (20) and Ichimoku Cloud, on the same interval

### 3. Formulation

The DMI, much like the RSI, uses the difference in the prices. Unlike the RSI, it will calculate the

increase using the highest daily value and decrease with the lowest daily value. Eventually, the DMI is obtained by dividing the absolute difference of the two by their sum, while adding

some normalization to the process. The DMI focused more on pointing out the strength of a variation rather than its direction, which is an excellent complement to the RSI.

The Ichimoku cloud is without any doubt the most obscure indicator that we studied. The cloud mentioned in the name is the space comprised between two lines obtained using relatively old data. The first line is created by averaging two SMAs of different periods from the past, i.e., a short one, around 1 week, and a longer one, around 1 month, from several days ago, generally another month. The second line uses the current SMA for the longest period covered by the previous curve, so typically around 2 months. Good traders may be able to extract lots of information from the Ichimoku cloud, similarly to how the Bollinger Bands can be used but seems to be more prone to the rule of thumbs than actual logic.

By utilizing all of the aforementioned indicators, we attempted to predict the price in the future. In addition to the codes we prepared, we elected to use the ANFIS technique on the MATLAB platform. Using a few inputs and their anticipated outcomes, ANFIS enables us to automatically create a Neural Network System, which is a compressed form of artificial intelligence.

As the name implies, ANFIS uses a fuzzy approach by assigning a membership function to each input variable and then adaptively creates the model for the provided data set to produce an output. A fuzzy system typically has three steps: first converting a numerical (crisp) input into a fuzzy input, then using the fuzzy inputs to infer with the rules defined and produce a fuzzy output, then converting the fuzzy output into a numerical value.

During the first step, which is called fuzzification, the numerical values are converted depending on their accuracy relative to some vaguer value by choosing an appropriate membership function for each input variable.

The second step, inference, involves applying fuzzy arithmetic to various combinations of the inputs to get an output that complies with certain

rules (if-then rules, reasoning) by utilizing expert knowledge as well.

Following the inference, the ANFIS model has an additional step that assigns weights to each output. Each rule has a particular weight; therefore, the weighting process depends on both the original input and the rule. The formula used for weighting is given in equation (7):

$$weighted = inferred(w_{rule} + \sum_i w_{in_i} in_i) \quad (7)$$

where  $w$  stands for weight and  $in$  for inputs. ANFIS will adjust the weights over multiple iterations of trials and errors until the output is sufficiently near the expected one.

In the third step, defuzzification, we aggregate the results of every rule output and then perform the rules of defuzzification. The fuzzy system, as shown in Figure 6, converts them to a single numerical value, crisp output.

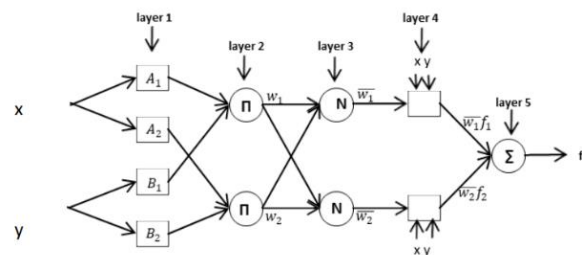


Figure 6. ANFIS structure [22]

The ANFIS plugin can be found on MATLAB's applications under the name Neuro-Fuzzy Designer. The input data file is prepared as follows to get the data ready for ANFIS to train the data and then build a model: the first to  $(n-1)^{th}$  columns of the array will be input variables, and the last column of the array  $n^{th}$  will be output variables. Once the data are loaded, the number of inputs are inferred with the rules defined, and it becomes possible to generate the Fuzzy Inference System (FIS). By selecting Grid Partition for the generation, we can specify for each input the number of fuzzy membership functions we want, as well as their shape. In our case, we are using four Generalized Bell (gbell) function as inputs, with a linear output. Once the FIS is generated, the last step is to train it using the inputted data. We trained our FIS a total of 13 iterations since we noticed it to be the optimal number of iterations in error-wise.

One thing must be noted. One rule will be generated for every combination of the membership functions of every input. This means that four inputs with three membership functions generate  $3^4=81$  rules in total, but with six inputs, we already reach  $3^6=729$  rules. With that much, we need a huge amount of data for training, as well as a lot of time for it to be performed. For that reason, we have decided to limit ourselves to a maximum of four inputs, greatly reducing our possibilities of input.

Moreover, because of the high fluctuation of the bitcoin price, our data are very heterogeneous, as seen in Figure 1. Our initial price is of the order  $10^2$ , which was around  $10^3$  after a few years and reached  $10^4$  a few years ago. For that reason, it is not possible to train our algorithm using actual

values; the difference in the order of the price would forbid us to effectively train our FIS. We need to transform them into something that is stable—or at least consistent—over time. We did try to use the added value compared to the previous day, but the resulting data was as fluctuating as with the initial one, as seen in Figure 7. Therefore, we moved to the use of relative value. That is, instead of using the flat difference in the price compared to the previous day, we use the added percentage of it. This gives us new data way more consistent, varying between plus and minus twenty with some isolated peaks throughout the whole dataset. An equivalent method needs to be applied to some indicators as well in order to normalize them and obtain once again consistent data.

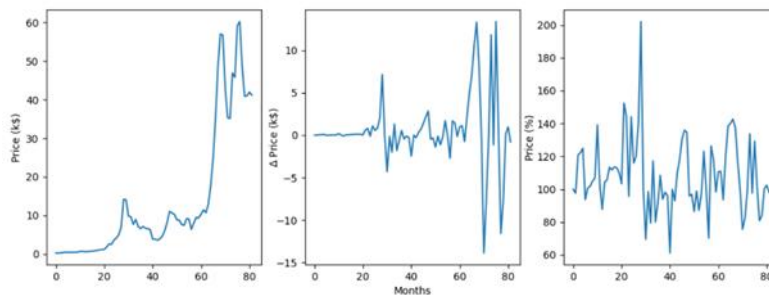


**Figure 7.** Difference of interpretation of monthly Bitcoin value

### 3. Results and Discussion

After several combinations of the previously described indicators, we set our minds over the combination of the three following indicators: the daily closing price relative to the average closing price over 10 days ( $v_0/SMA_{10}(v)$ ), the position of the daily closing price relative to the Bollinger Bands of 20 days (BB20 normalized price), as well as the ratio between the upper and lower Bollinger Bands. As for the output, we decided to use the average closing price for the upcoming 10 days over the average closing price covering the past 10 days ( $SMA_p(v_{-p})/SMA_p(v)$ ).

We tested it over three samples of data, as shown in Figure 8. The first dataset includes data from 2022-01-31 to 2022-05-10, both included.

The second dataset is from 2022-05-10 to 2020-12-27 again, while the third one is also part of the training datasets, located between 2018-05-03 and 2018-08-10.

The percentages estimated and expected differ by an average of 7%, which highlights the results' significant disparity. Given that the allowable  $\pm 10\%$  range for the predicted price falls between 90 and 110%, our 7% precision error remains within this range.

However, when looking at the error in the direction of the price, the result is not as good as the price forecasting. If we exclude the 98-102% range since we can consider it the stagnation price range, and count the number of times the calculated and expected values are on different sides of the 100% line, there is on average only a

**Table 1.** Comparison of existing techniques for cryptocurrency and stock market price forecasting.

Paper	Year	Objective	Methodology	Data type	Forecast duration	Cryptocurrency	Results
3	2019	Forecasting direction in the change of the daily price of Bitcoin	Hybrid neuro-fuzzy controller, two ANFIS sub-systems, PATSOS, buy-and-hold	Closing price	Next day (1 day ahead)	Bitcoin, Ethereum, Litecoin, Ripple	Accuracy: %71,21
5	2009	Prediction of stock market short-term trend	Hybrid neuro-fuzzy controller, two ANFIS sub-systems, PATSOS, buy-and-hold	Closing price	Next day (1 day ahead)	Stock market	Accuracy: %68.33
6	2019	Comparison of univariate and multivariate models for point and density forecasting	Univariate and multivariate models, density forecasting, dynamic model averaging	Closing price	1 to 7 days ahead	Bitcoin, Ethereum, Litecoin, Ripple	Accuracy: %60
7	2021	Forecasting price of Bitcoin	ANFIS	Closing price		Bitcoin	RMSE: %8.4
8	2020	Forecasting price of Bitcoin	Machine learning, time series analysis	Closing price		Bitcoin, Ethereum, Litecoin, Zcash	
9	2021	Predict short-term price movement of Bitcoin market	Machine learning		5-min, 15-min, 60-min	Bitcoin	Accuracy: above %50
11	2017	Predict the next day the direction of the price of Bitcoin	ANN ensemble approach called Genetic Algorithm-based Selective NN Ensemble		Next day	Bitcoin	Accuracy: %58-%63
12	2021	Attribute selection and Trend analysis of Bitcoin	Non-linear Autoregressive with External Input analysis with seven attributes, NN-based LM, BR, and SCG algorithms	Price, Volume, Market cap, Social dominance, Development activity, Market value to realized value, Realized cap	Next value	Bitcoin	LM R:0.65751 BR R:0.59395 SCG R:0.65589
13	2020	Analysis and prediction of the growth of the cryptocurrency market	Pool complexity approach to choose the optimal technology, EOS network structure	social activity on the internet, trading parameters		Bitcoin, Ethereum	
14	2021	Forecasting price of Bitcoin	Statistical analysis, MVA, ARIMA, and Machine Learning, DNN, RNN, CNN,	Closing price, Average (previous n-values)	Next day	Bitcoin	MAPE: 1-layer, ANN:4.05 3-layer, ANN:3.84 CNN:3.75 RNN:2.70
18	2020	Forecasting price of Bitcoin and Ethereum	NN analysis, Backpropagation, Radial bases function, Extreme learning machine, Long-short term memory	Opening price		Bitcoin, Ethereum	Bitcoin RMSE ELM:25.8 RBF:31.31 ANFIS:31.3 BP:18.52 LSTM:17.8
19	2020	Develop a novel approach for modeling and analysis of the cryptocurrency prices	Two-stage decomposition and composition method (2SDC)	Daily closing		Bitcoin, Bitcoin cash, Ethereum, Litecoin, Monero, Dash	

12% error of direction of the price. It can be noticed that the findings are better when compared to the data in Table 1 than the literature review.



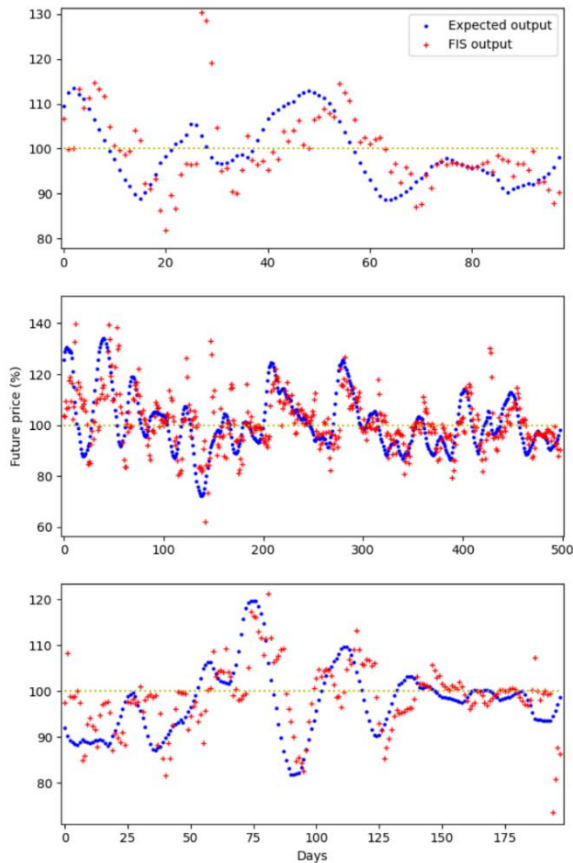


**Figure 8.** The expected result compared to the obtained result, ANFIS simulation results.

By utilizing the relative price variation, we are in fact estimating the derivative of the price function. Positive values are produced by price increases, while negative values are produced by price decreases. Therefore, determining the direction of the fluctuation rather than its magnitude would be the key factor. We can consider our outcome to be appropriate as long as we can anticipate when the price is rising, falling, stagnant, or reaching an extreme. The ability to identify rise and decline is currently our greatest strength. However, the current version is unable to detect an extremum accurately, which is discovered while the price is already declining.

#### 4. Conclusion

Eventually, we were able to create a prediction algorithm that was only based on the price of bitcoin. We successfully developed a model that ANFIS can use since we are able to adjust our data.

As a result, it has successfully created a system capable of making predictions. Even though the

results are far from perfect, accuracy is still a respectable 88% percent with a 12% error, which is better than the findings of the literature review displayed in Table 1.

We did have a few issues even though we were able to forecast the price. First of all, the enormous data disparity makes the entire prediction process challenging. Predicting the future price while considering the current value is difficult, both computationally and from a human perspective. In fact, there appears to be no pattern as the price fluctuates sharply from time to time. The major reason is that the price is determined by external circumstances, in this case, excessive purchases and/or sales, rather than adhering to a straightforward or even complex formula.

The ANFIS input limit was another issue that we did run across. The capabilities of ANFIS limited us. The number of rules is greatly increased by expanding the dataset, adding more input variables, and using more membership functions. This barrier could be removed or at least decreased, but not entirely, leading to an increase in computing complexity or longer processing times. We could only use four variables at once or three of them due to the limited amount of data we could gather simultaneously. Of course, we could have used more variables if we had manually set the requirements and the required signs. The testing and planning stages, however, would have taken a very long period. As a result, we may say that ANFIS is not the greatest instrument for making these kinds of forecasts.

However, when forecasting, models should provide some degree of error freedom and enough degree of flexibility to account for potential extreme volatility, which is a feature and nature of cryptocurrencies. If not, the prediction would be overfitting, which typically occurs in artificial neural network modeling for the given data set, sometimes measured data and predicted data fitted one-to-one and it would not be effective for abrupt and volatile price fluctuations. In this regard, ANFIS is advantageous to use for predicting work due to the adaptive and flexible nature of fuzzy logic modeling.

## Article Information Form

### Acknowledgments

The author would like to thank Valentin L'Homel for his contributions.

### Funding

The author (s) has not received any financial support for the research, authorship, or publication of this study.

### The Declaration of Conflict of Interest/ Common Interest

No conflict of interest or common interest has been declared by the authors.

### The Declaration of Ethics Committee Approval

This study does not require ethics committee permission or any special permission.

### The Declaration of Research and Publication Ethics

The authors of the paper declare that they comply with the scientific, ethical, and quotation rules of SAUJS in all processes of the paper and that they do not make any falsification of the data collected. In addition, they declare that Sakarya University Journal of Science and its editorial board have no responsibility for any ethical violations that may be encountered, and that this study has not been evaluated in any academic publication environment other than Sakarya University Journal of Science.

### Copyright Statement

Authors own the copyright of their work published in the journal and their work is published under the CC BY-NC 4.0 license.

## References

- [1] S. Nakamoto, "Bitcoin: A Peer-to-Peer Electronic Cash System," 2008. [Online]. Available: [www.bitcoin.org](http://www.bitcoin.org).
- [2] M. Bartoletti, S. Lande, A. Loddo, L. Pompianu, S. Serusi, "Cryptocurrency scams: Analysis and perspectives," *IEEE Access*, vol. 9, pp. 148353–148373, 2021.
- [3] G. S. Atsalakis, I. G. Atsalaki, F. Pasiouras, C. Zopounidis, "Bitcoin price forecasting with neuro-fuzzy techniques," *European Journal of Operational Research*, vol. 276, no. 2, pp. 770–780, Jul. 2019.
- [4] "Coin Market Cap." Accessed: Sep. 19, 2023. [Online]. Available: <https://coinmarketcap.com/currencies/bitcoin/>
- [5] G. S. Atsalakis, K. P. Valavanis, "Forecasting stock market short-term trends using a neuro-fuzzy based methodology," *Expert Systems with Applications*, vol. 36, no. 7, pp. 10696–10707, Sep. 2009.
- [6] L. Catania, S. Grassi, F. Ravazzolo, "Forecasting cryptocurrencies under model and parameter instability," *International Journal of Forecasting*, vol. 35, no. 2, pp. 485–501, Apr. 2019.
- [7] B. Kutlu Karabıyık and Z. Can Ergün, "Forecasting Bitcoin Prices with the ANFIS Model," 2021.
- [8] N. Maleki, A. Nikoubin, M. Rabbani, Y. Zeinali, "Bitcoin Price Prediction Based on Other Cryptocurrencies Using Machine Learning and Time Series Analysis," *Sharif University of Technology, Scientia Iranica, Transactions E: Industrial Engineering*, Vol. 30, no. 1, 285-301, 2023.
- [9] P. Jaquart, D. Dann, C. Weinhardt, "Short-term bitcoin market prediction via machine learning," *Journal of Finance and Data Science*, vol. 7, pp. 45–66, Nov. 2021.
- [10] S. E. Charandabi and K. Kamyar, "Prediction of Cryptocurrency Price Index Using Artificial Neural Networks: A Survey of the Literature," *European Journal of Business and Management Research*, vol. 6, no. 6, pp. 17–20, Nov. 2021.
- [11] Y. Liu, Institute of Electrical and Electronics Engineers, and IEEE Circuits and Systems Society, "Bitcoin price prediction using ensembles of neural networks," in *ICNC-FSKD 2017: 13th*

- International Conference on Natural Computation, Fuzzy Systems, and Knowledge Discovery: Guilin, Guangxi, China, 29-31 Jul, 2017, 2018.
- [12] R. Sujatha, V. Mareeswari, J. M. Chatterjee, A. A. A. Mousa, A. E. Hassanien, “A Bayesian regularized neural network for analyzing bitcoin trends,” *IEEE Access*, vol. 9, pp. 37989–38000, 2021.
- [13] A. Mikhaylov, “Cryptocurrency market analysis from the open innovation perspective,” *Journal of Open Innovation: Technology, Market, and Complexity*, vol. 6, no. 4, pp. 1–19, Dec. 2020.
- [14] B. Aygun, E. Kabakci Gunay, “Comparison of Statistical and Machine Learning Algorithms for Forecasting Daily Bitcoin Returns,” *European Journal of Science and Technology*, Jan. 2021.
- [15] T. G. Andersen, T. Bollerslev, F. X. Diebold, “w8160\_ModellingandForecastingRealizedVolatility\_2003,” 2001.
- [16] O. Liashenko, T. Kravets, Y. Repetskyi, “Neural Networks in Application to Cryptocurrency Exchange Modeling,” 2021.
- [17] C. H. Su, C. H. Cheng, “A hybrid fuzzy time series model based on ANFIS and integrated nonlinear feature selection method for forecasting stock,” *Neurocomputing*, vol. 205, pp. 264–273, Sep. 2016.
- [18] O. Liashenko, T. Kravets, Y. Repetskyi, “Neural Networks in Application to Cryptocurrency Exchange Modeling,” 2020.
- [19] B. Yang, Y. Sun, S. Wang, “A novel two-stage approach for cryptocurrency analysis,” *International Review of Financial Analysis*, vol. 72, Nov. 2020.
- [20] İ. Daş, “Bitcoin Price Forecasting Under the Influences of Network Metrics and Other Financial Assets, M.Sc. Dissertation, Middle East Technical University of Applied Mathematics, Ankara,” 2022.
- [21] “Historical Data.” Accessed: Feb. 08, 2023. [Online]. Available: [https://web-api.coinmarketcap.com/v1/cryptocurrency/ohlcv/historical?convert=USD&slug=bitcoin&time\\_end=1589946400&time\\_start=1589000000](https://web-api.coinmarketcap.com/v1/cryptocurrency/ohlcv/historical?convert=USD&slug=bitcoin&time_end=1589946400&time_start=1589000000)
- [22] J. S. R. Jang, “ANFIS: Adaptive-Network-Based Fuzzy Inference System,” *IEEE Transactions on Systems, Man, and Cybernetics*, vol. 23, no. 3, pp. 665–685, 1993.

## Machine Learning Based Classification for Spam Detection

Serkan Keskin<sup>1\*</sup>, Onur Sevli<sup>2</sup>

<sup>1</sup> Burdur Mehmet Akif Ersoy University, Institute of Science and Technology, Department of Computer Engineering, Burdur, Türkiye, [serkankeskin@isparta.edu.tr](mailto:serkankeskin@isparta.edu.tr)

<sup>2</sup> Burdur Mehmet Akif Ersoy University, Faculty of Engineering and Architecture, Department of Computer Engineering, Burdur, Türkiye, [onursevli@mehmetakif.edu.tr](mailto:onursevli@mehmetakif.edu.tr)

\* Corresponding author

### ARTICLE INFO

### ABSTRACT

#### Keywords:

Artificial Intelligence  
Email Classification  
Machine Learning  
Spam Detection



#### Article History:

Received: 13.03.2023

Accepted: 08.12.2023

Online Available: 22.04.2024

Electronic Electronic messages, i.e. e-mails, are a communication tool frequently used by individuals or organizations. While e-mail is extremely practical to use, it is necessary to consider its vulnerabilities. Spam e-mails are unsolicited messages created to promote a product or service, often sent frequently. It is very important to classify incoming e-mails in order to protect against malware that can be transmitted via e-mail and to reduce possible unwanted consequences. Spam email classification is the process of identifying and distinguishing spam emails from legitimate emails. This classification can be done through various methods such as keyword filtering, machine learning algorithms and image recognition. The goal of spam email classification is to prevent unwanted and potentially harmful emails from reaching the user's inbox. In this study, Random Forest (RF), Logistic Regression (LR), Naive Bayes (NB), Support Vector Machine (SVM) and Artificial Neural Network (ANN) algorithms are used to classify spam emails and the results are compared. Algorithms with different approaches were used to determine the best solution for the problem. 5558 spam and non-spam e-mails were analyzed and the performance of the algorithms was reported in terms of accuracy, precision, sensitivity and F1-Score metrics. The most successful result was obtained with the RF algorithm with an accuracy of 98.83%. In this study, high success was achieved by classifying spam emails with machine learning algorithms. In addition, it has been proved by experimental studies that better results are obtained than similar studies in the literature.

## 1. Introduction

With the widespread use of the Internet, electronic communication has become more preferred. One of the most important tools of electronic communication is electronic messages, which we call e-mail. Today, individuals or organizations have one or more e-mail accounts. Instant delivery of messages, no cost and ease of use increase the importance and prevalence of e-mail [1]. According to Statista Research Department data, the number of actively used e-mail accounts in 2020 is more

than 4 billion. This number is estimated to increase to 4.6 billion in 2025. In 2020, 306 billion e-mails are sent and received every day, and this number is expected to exceed 376 billion in 2025 [2].

The use of e-mail is not only practical but also has various vulnerabilities. The e-mail account to be hijacked in various ways, for e-mails containing advertisements etc. to hijack your computer by installing a software on your computer when you click on the advertisement, and for the installed software to disrupt communication by sometimes filling the



bandwidth. Such unsolicited e-mails are characterized as "spam". Between October 2020 and September 2021, the global daily spam volume peaked in July 2021 with approximately 283 billion spam emails out of a total of 336.41 billion emails. By August 2021, this number had fallen to 65.50 billion. By September, the average spam volume had again increased by 36 percent, reaching 88.88 billion out of a total of 105.67 billion emails sent worldwide [3].

Email providers are expected to stop spam emails before they reach users. Many email providers include mechanisms that attempt to filter spam by comparing the sender address of emails against so-called blacklists of known spammers. However, since spammers frequently change their sender addresses, the success of these programs has not reached the desired level [4]. At this point, a more effective and flexible solution is needed. Generally, spam e-mails contain messages such as "easy money", "adult entertainment", etc. in their headers or content, which can deceive individuals. The process of classifying emails by interpreting messages is based on the keyword detection rule. This method has made the inadequacy of address-based filtering of spam e-mails more successful with keyword detection algorithms. Machine learning techniques, which have recently gained popularity and are used in many different fields, provide alternative solutions for filtering spam e-mails much more successfully.

## 1.1. Methods used to detect spam emails

Unsolicited emails (spam) are usually fake emails sent for advertising or fraudulent purposes and often contain content that users do not want or are not interested in. Such emails can put users in difficult situations or reduce work efficiency. Therefore, it is important to detect and filter spam emails.

### 1.1.1. Traditional spam detection systems

Such spam detection systems, which are not based on artificial intelligence, usually use simple algorithms that distinguish spam based on the content of the message, the sender's address or the content of its links. The effectiveness and accuracy of these systems is lower than that of AI-based systems. They are less flexible and

adaptive than AI-based systems. The main methods used in traditional spam detection systems are as follows:

- **Email authentication:** This method is used to verify who the sender of an email is. It verifies the authenticity of the sender using standards such as DomainKeys Identified Mail (DKIM) and Sender Policy Framework (SPF). This makes it possible to detect fake emails or spam emails sent from fake accounts [5].
- **List of email addresses:** This method enables the detection of spam emails using a predefined list of email addresses. This list may include email addresses with a high probability of spam [6]. This method can be effective in preventing spam emails, but it also involves the risk of false positives, i.e., correct email addresses being falsely flagged as spam.
- **Content filtering:** This method is used to detect spam emails based on the content in the emails. For example, words and phrases such as advertisements, product sales or illegal content can be detected in emails and these emails can be marked as spam. This method can be effective in preventing spam emails, but it also involves the risk of false positives [7].
- **Sharing a list of email addresses:** This method enables the detection of spam emails by sharing a list of spam email addresses between different users and organizations. In this way, it enables the detection of spam emails by sharing a list of spam email addresses between different users and organizations [7].

### 1.1.2. Artificial intelligence-based spam detection systems

Artificial intelligence-based spam detection systems are software used to detect spam messages that are common in electronic communication networks. These systems use various artificial intelligence techniques to search for and detect specific characteristics of spam messages. Spam messages are usually marketing messages with a high content of advertisements and promotions. These messages are often sent to many people and are often unsolicited or unnecessary. Sending too many

spam messages wastes the time and effort of email users. Artificial intelligence-based spam detection systems are designed to reduce these problems. These systems examine the content, headers and other features of e-mail messages and classify spam messages according to certain criteria [8].

- **Systems based on biological intelligence:** Systems based on biological intelligence are artificial intelligence systems that mimic the structure and functioning of the human brain. Such systems have a high degree of adaptive and learning capabilities, mimicking the learning, remembering and problem-solving abilities of the human brain. In particular, they have a network structure that transmits signals from inputs to outputs using structures called neural networks. These neural networks can have learning and adaptive properties, much like the human brain. By mimicking the natural structure and functioning of the human brain, such systems can have a very high degree of adaptive and learning capabilities [9].

- **Machine learning-based systems:** Machine learning-based spam systems are systems that help to automatically detect spam emails. These systems usually identify spam emails using features such as keywords and phrases found in the content of the emails. They also take into account that spam emails are usually sent regularly and that they fit a certain profile of email addresses and domains used. Spam systems developed using machine learning learn from pre-labeled datasets and discover which features in these datasets are more effective in identifying spam emails [10].

- These features may include keywords and phrases in the content of the emails, the sender's email address and domain, the email header, and the format of the email. The learned features are used to detect spam emails and new incoming emails are evaluated according to these features. The advantages of machine learning-based spam systems are that they have high detection rates as they learn from pre-labeled datasets [11]. Furthermore, these systems can improve themselves through dynamic learning processes and become more accurate classifiers over time. However, the disadvantages of machine

learning-based spam systems include errors such as decreasing correct detection rates if the datasets are not large and diverse enough, or mistakenly identifying non-spam emails as spam [12].

## 2. Literature Review

When we examine the studies conducted in the literature using artificial intelligence techniques for the detection of spam e-mails, it is seen that e-porta classification processes are performed with different algorithms. Some of these studies used traditional machine learning algorithms, while others used algorithms inspired by biological systems such as Artificial Neural Networks (ANN).

In a study classifying comments in different languages obtained from social media, an accuracy of 96% was achieved using the Naive Bayes (NB) algorithm [13]. In another study to classify e-mails, a dataset containing 5574 English messages was classified with 95.48% accuracy using the NB algorithm and 97.83% accuracy using the Support Vector Machine (SVM) algorithm [14]. In another study for filtering short messages (SMS), unwanted advertisements were tried to be distinguished. The highest scores obtained in the classification process were reported as 98.61% with SVM and 97.55% with NB [15].

In some studies, classification is performed with messages sent via social media. In the result obtained by classifying 1383 tweets, the accuracy rate of RF was 92.95% [16]. The same algorithm may not always be more successful in the results found. This is because different data sets are used. For example, in another spam e-mail detection study, 600 e-mails were classified. As a result of this classification, Naive Bayes was 95.5% and SVM was 93.5% [17]. In another study, 6000 emails were classified and Naive Bayes was 94.6% and SVM was 98.5% successful [18]. Another of the algorithms examined is LR. In this study, LR was used to classify incoming emails as raw and spam. Dedekurt et al. presented a new spam approach by combining LR and artificial bee colony [19].

In another study, the ABC-LR algorithm was more successful than the classical LR algorithm [20]. Janez-Martino used the LR algorithm on a spam dataset to evaluate the combination of LR with a bag of words [21]. Apart from this, it has been observed that certain algorithms such as Naive Bayes-based and SVM have been used more than other machine learning algorithms [22].

It was revealed that the NB algorithm was 96.31% successful in the classification of 310 e-mails using the similar word suggestion feature of the Zemberek library [23]. In a study conducted on 4327 mail data sets with simulated neural networks (SNN), the success rate was found to be 95.82 [24]. In a study with the nearest neighbor (KNN) algorithm, the highest success rate of the KNN algorithm was 97.50% on a dataset of 4601 e-mails taken from the UCI machine learning repository website [25]. In another study on the same data set, the SVM algorithm was 93.07% successful.

In the study conducted by Jain et al. they used a data set consisting of 5572 messages labelled as raw and spam. As a result of the classification, they achieved a success rate of 98.79% with the SVM algorithm [26]. On the same data set, Gadde et al. used the LSTM model and achieved a success rate of 98.5%. TF-IDF and Hashing Vectoriser were used in the model [27]. Reddy and Reddy achieved 95.32% success rate by using SVM algorithm on 5572 spam sms dataset [28]. In another study, 98.56% success rate was achieved by using NB algorithm [29]. In the study conducted by Abayomi et al. on the same data set, a 98.6% success rate was obtained with the BILSTM model using deep learning method. [30].

### 3. Material and Method

In this study, a classification study was carried out on a data set consisting of 5558 samples for distinguishing spam e-mails. After natural language processing, the results of the classifications performed with 5 different machine learning algorithms consisting of Random Forest, Logistic Regression, Naive Bayes, Support Vector Machine and Artificial Neural Network are reported in terms of different metrics.

### 3.1. Data set

In this study, a dataset consisting of 5558 samples and two attributes was used to detect spam e-mails. The first attribute is the English content text of the email message and the second attribute is the target label that indicates whether the email is spam or not. This csv file (spam.csv, 480.13 kB) prepared by Faisal Qureshi, contains 5558 unique instances of ham (87%) and spam (13%) messages. [31].

Of the instances in the dataset, 747 are marked as spam and 4811 are marked as non-spam. The graph showing the class distribution rates in the dataset is given in Figure 1.

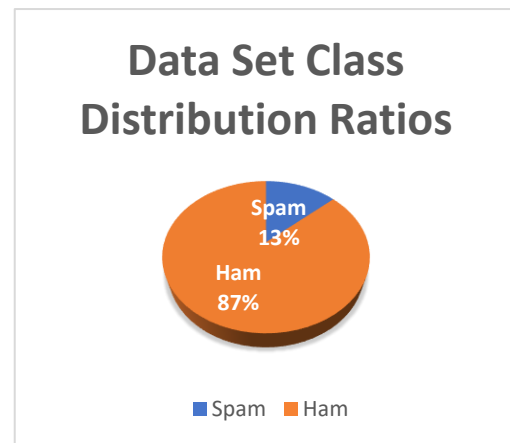


**Figure 1.** Class distribution rates

When the class distribution rates are analyzed, it is seen that the data set is not balanced. For this reason, cross-validation was applied in classification processes and detailed measurement metrics obtained through complexity matrices are reported.

### 3.2. Natural language processing (NLP)

Natural Language Processing (NLP) enables computers to communicate and process data using natural language. It is a sub-branch that uses technologies such as artificial intelligence and machine learning and typically works with text and audio data. NLP is artificial intelligence technologies that give humans the ability to understand and use natural language. NLP is divided into two main parts: text processing and audio processing.

Text processing works with text data and performs operations such as reading,



understanding and summarizing texts. Voice processing, on the other hand, works with voice data and performs operations such as recognizing voices, generating text from voices and translating texts into voice. In recent years, there has been a rapid development of NLP in phenomena such as question answering, machine translation and machine reading comprehension. NLP can be divided into three parts: modeling, learning and reasoning [32]. TF-IDF (Term Frequency-Inverse Document Frequency) is a natural language processing technique used to measure word importance in texts. TF-IDF calculates how often a word occurs in a text (Term Frequency, TF) and how few texts containing that word occur in total texts (Inverse Document Frequency, IDF). The product of these two values indicates the importance of the word. TF-IDF is used to better understand the meaning of texts. TF-IDF is widely used for measuring word distributions in texts and can be used in applications such as determining the similarity of texts, classifying texts or making connections between texts [33].

Each word in the dataset used in this study is associated with a numerical index value and those that carry spam flags are labeled. During the model training, the textual expressions in the dataset were separated word by word and subjected to numerical transformations, making it a completely numerical dataset. The dataset was classified with 5 different machine learning algorithms. In the study carried out with algorithms written in Python programming language in a spyder environment, tests were carried out using various library structures. With the algorithms applied to the dataset, performance evaluations were made according to precision, sensitivity, accuracy and F1 scores. All algorithms were subjected to 5-fold cross-validation.

### 3.3. Classification algorithms used

The data set used in the study was classified using 5 different machine learning algorithms: Support Vector Machine, Logistic Regression, Naive Bayes, Random Forest and Artificial Neural Network.

#### 3.3.1. Support vector machine (SVM)

SVM is widely used in many studies because it produces significant accuracy with less computational power. SVM is one of the most popular supervised learning algorithms used to solve regression and classification problems. The goal of the SVM algorithm is to construct the best line or decision boundary that can classify data points in a multidimensional space that classifies them distinctly [34]. This boundary is called the hyperplane. The SVM selects endpoints or vectors to form the hyperplane. This selected state is called the support vectors [35]. The SVM algorithm is used in many different fields such as image classification, text classification and face detection.

#### 3.3.2. Logistic regression (LR)

LR, like SVM, is one of the important machine learning algorithms among the algorithms that use supervised learning techniques. It is used to predict a categorical dependent variable using a set of independently given variables. LR predicts the output of a categorical dependent variable. It should give a discrete or categorical value as a result. The result can be true or false, 0 or 1. Instead of giving an exact value, it gives a probabilistic value between 0 and 1. Instead of a linear line, LR draws an "S" shaped function to cover two maximum values. This function curve gives the probability of whether a state exists or not [36]. LR is a highly successful machine learning algorithm that calculates probabilities using discrete and continuous data and classifies newly entered data.

#### 3.3.3. Naive bayes (NB)

It is the first filtering algorithm used as a probabilistic classifier [37]. The NB algorithm is a supervised learning algorithm for solving classification problems based on Bayes theory. It is used for text classification with a high-dimensional training data set. The NB algorithm can make predictions quickly. It makes predictions by calculating the probability of the object. Due to their simplicity and high performance, these approaches are the most widely used in open-source systems proposed for spam filtering [38]. This algorithm is also used in

areas such as article classification and sentiment analysis.

### 3.3.4. Random forest (RF)

The RF algorithm is a machine learning algorithm created by combining many decision trees. This algorithm can be used for classification and regression problems. The RF algorithm is a combination of many decision tree models, each trained with different subsets of data. Each decision tree makes decisions on specific features and data points using a set of decision tree nodes. Decision trees work by dividing the data into small subsets and classifying the data points in these subsets with a set of decision nodes. [39].

This algorithm allows each decision tree to make predictions individually and eventually produces a result by combining all the predictions. This improves accuracy and consistency, giving better results than a single decision tree. A large number of trees in the forest provides higher accuracy [40]. Training time is less compared to other algorithms. It can maintain accuracy even if a certain part of the data is missing. It is generally used in banking, medicine, land use and marketing sectors.

### 3.3.5. Artificial neural network (ANN)

An Artificial Neural Network (ANN) is a machine learning model that works like the brain. Like a network of nerve cells in the brain, an ANN is made up of many nerve cells (neurons). Neurons are connected and process information by sending signals to each other. The ANN learns by using the connections between neurons and adjusting their weights [41]. Information is transmitted to the network from the input layer. It is then processed in the intermediate layer and sent to the output layer. The information coming into the network is converted into output using the weight value of the network. To produce the correct outputs, the evaluation of the weights must be done correctly. The process in ANN is to calculate the parameters  $w$  (weight) and  $b$  (bias) that will give the model the best score. [42]. ANN is a method that offers successful solutions to many problems we encounter in daily life such as classification, prediction and modeling.

## 3.4. Model performance measurement

A confusion matrix was used to express the performance of the classifier used. The confusion matrix is a table used to evaluate how well a class is distinguished from each other. It allows us to see how well the algorithm can predict the correct class. The rows of the matrix represent the predicted class and the columns represent the true class [43]. For a binary classification problem where the classes are "positive" and "negative", the general structure of the complexity matrix looks like Figure 2.

		Predicted Class	
		+	-
Actual Class	+	TP True Positives	FN False Negatives
	-	FP False Positives	TN True Negatives

Figure 2. Complexity matrix

In machine learning, true positive refers to the number of correct positive predictions made by a model out of all positive predictions. In other words, it is the number of instances where the model correctly identifies a positive instance as positive. True negative refers to the number of correct negative predictions made by a model out of all negative predictions. It is the number of instances where the model correctly identifies a negative instance as negative. False positive refers to the number of false positive predictions made by a model out of all negative predictions. In other words, it is the number of instances where the model predicts a positive instance when it is negative. In machine learning, false negative refers to the number of false negative predictions made by a model out of all positive predictions. It is the number of instances where the model predicts a negative pattern when it is positive.

Different evaluation metrics can be calculated from a complexity matrix. These metrics are useful for understanding the performance of a classification algorithm and comparing the performance of different models. The formulas for deriving these measures from the complexity matrix are given in Table 1.

**Table 1.** Formulation of measurements

Measure	Description	Formula
<b>Accuracy</b>	Overall	$\frac{TP + TN}{TP + TN + FP + FN}$
	performance of model	
<b>Precision</b>	How accurate the positive predictions are	$\frac{TP}{TP + FP}$
<b>Sensitivity</b>	Coverage of actual positive sample	$\frac{TP}{TP + FN}$
<b>F1 Score</b>	Hybrid metric useful for unbalanced classes	$\frac{2TP}{2TP + FP + FN}$

**Accuracy:** The proportion of correct predictions. It is calculated as the number of true positives divided by the total number of true negatives divided by the number of predictions.

**Precision:** The proportion of correct positive predictions. It is calculated by dividing the number of true positives by the total number of true positives and false positives.

**Sensitivity:** The proportion of true positive cases that are correctly predicted. It is calculated by dividing the number of true positives by the total number of true positives and false negatives.

**F1 Score:** The harmonic mean of the precision and recall values. The F1 score takes values between 0 and 1, with higher values indicating better classification performance.

#### 4. Experimental Study and Findings

In the study conducted for spam detection, the dataset consisting of 5558 samples was classified using 5 different machine learning algorithms: SVM, LR, NB, RF and ANN. Before the classification process, the e-mail message texts in the dataset were subjected to natural language processing. The texts were first parsed into sentences and then segmented into words according to the determined brackets. Word vectors were created and Term Frequency / Inverse Document Frequency was calculated. The mathematically transformed e-mail messages were classified with the specified algorithms using 5-fold cross-validation. The

averages of the measurements obtained with each algorithm are reported.

The complexity matrix obtained as a result of the classification process performed with the SVM algorithm is given in Figure 3.

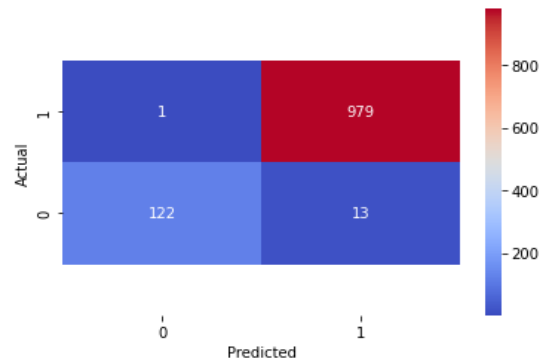


**Figure 3.** SVM results

In the complexity matrix of the DVM algorithm, it is understood that the model distinguishes between spam and non-spam emails with overall success. The values of the metrics calculated over the complexity matrix of the model are given in Table 2.

**Table 2.** Calculated metrics for SVM

SVM Metrics	Ratios
Accuracy	98.74
Precision	98.86
Sensitivity	99.89
F1 Score	99.29

In Table 2, the accuracy value showing the overall success of the model is 98.74%. The precision and sensitivity values showing the discrimination of the classes were obtained as 98.86% and 99.89%. The F1 Score value, which expresses the balance of these two values, was obtained as 99.29%.

The complexity matrix obtained as a result of the classification process performed with the LR algorithm is given in Figure 4.

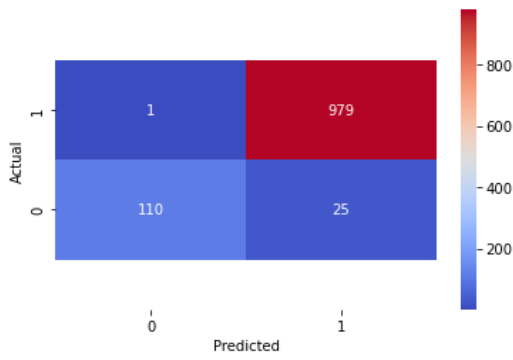


Figure 4. LR results

In the complexity matrix of the LR algorithm, it turns out that the model distinguishes spam and non-spam emails with general success. The values of the metrics calculated over the complexity matrix of the model are given in Table 3.

Table 3. Calculated metrics for LR

LR Metrics	Ratios
Accuracy	97.66
Precision	97.75
Sensitivity	99.89
F1 Score	98.68

In Table 3, the accuracy value showing the overall success of the model is 97.66%. The precision and sensitivity values showing the discrimination of the classes were obtained as 97.75% and 99.89%. The F1 Score value, which expresses the balance of these two values, was obtained as 98.68%.

The complexity matrix obtained as a result of the classification process performed with the NB algorithm is given in Figure 5.

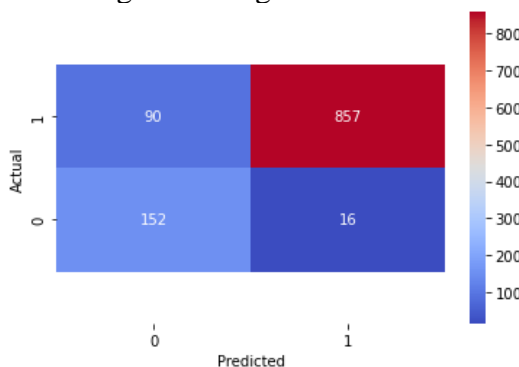


Figure 5. NB results

In the complexity matrix of the NB algorithm, it is understood that the model mixes TN and TP values with FN. This affects the success of the model. The values of the metrics calculated over

the complexity matrix of the model are given in Table 4.

Table 4. Calculated metrics for NB

NB Metrics	Ratios
Accuracy	90.49
Precision	98.16
Sensitivity	90.49
F1 Score	94.17

In Table 4, the accuracy value showing the overall success of the model is 90.49%. The precision and sensitivity values showing the discrimination of the classes were obtained as 98.16% and 90.49%. The F1 Score value, which expresses the balance of these two values, was obtained as 94.17%.

The complexity matrix obtained as a result of the classification process performed with the RF algorithm is given in Figure 6.

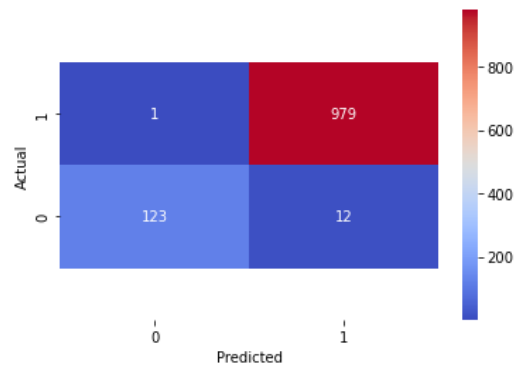


Figure 6. RF results

In the complexity matrix of the RF algorithm, it appears that the model distinguishes spam and non-spam emails with overall success. The values of the metrics calculated over the complexity matrix of the model are given in Table 5.

Table 5. Calculated metrics for RF

RF Metrics	Ratios
Accuracy	98.83
Precision	98.78
Sensitivity	99.89
F1 Score	99.34

In Table 5, the accuracy value showing the overall success of the model is 98.83%. The precision and sensitivity values showing the discrimination of the classes were obtained as 98.78% and 99.89%. The F1 Score value, which

expresses the balance of these two values, was obtained as 99.34%.

The complexity matrix obtained as a result of the classification process performed with the ANN algorithm is given in Figure 7.

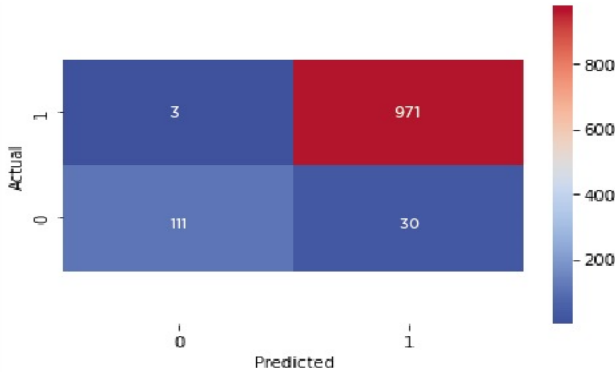


Figure 7. ANN results

In the Complexity matrix of the ANN algorithm, it is understood that the model successfully distinguishes between spam and non-spam emails in general. The values of the metrics calculated over the complexity matrix of the model are given in Table 6.

Table 6. Calculated metrics for ANN

ANN Metrics	Ratios
Accuracy	97.04
Precision	97.00
Sensitivity	99.69
F1 Score	98.32

In Table 6, the accuracy value showing the overall success of the model is 97.04%. The precision and sensitivity values showing the discrimination of the classes were obtained as 97.00% and 99.69%. The F1 Score value, which expresses the balance of these two values, was obtained as 98.32%.

The measurements obtained as a result of the classification processes performed with 5 different algorithms are summarized in Table 7.

Table 7. Calculated measurements of the algorithms used

Machine Learning Algorithm	Accuracy	Precision	Sensitivity	F1 Score
SVM	98.74	98.86	99.89	99.29
LR	97.66	97.75	99.89	98.68
NB	90.49	98.16	90.49	94.17
RF	98.83	98.78	99.89	99.34
ANN	97.04	97.00	99.69	98.32

When Table 7, which shows the classification performance of the algorithms, is analysed, it is revealed that the RO algorithm ranks first with 98.83% accuracy in terms of overall success. The NB algorithm showed the lowest performance with 90.49% accuracy. In terms of F1 score, which expresses the balance in distinguishing the classes, the most successful algorithm was RO with 99.34%, while the lowest success was NB algorithm with 94.17%. It is understood that RO>DVM>LR> ANN> in the general success ranking.

The comparison of the findings obtained in the classification process performed in this study with other similar studies in the literature is given in Table 8. In this table, the most successful algorithm and accuracy rates are given.

The last row in Table 8 is the result of this study. The reason why the accuracy rates in some studies in this table are close to the accuracy rates of our study is that the data set sizes and data sets are close to each other. As it can be understood, it has been experimentally demonstrated that this study is more successful than other studies. This is due to the fact that the natural language processing processes of the study are more successful than other similar studies.

### 5. Conclusion

E-mail is one of the most widely used communication tools and one of the biggest problems in the use of this tool is spam messages. Spam messages are e-mails that are intended to advertise or deceive and their detection is of great importance. Various techniques and algorithms have been proposed to detect spam e-mails.



In the present study, 5 different machine learning algorithms were used to classify spam e-mails using a dataset of 5558 samples consisting of spam and non-spam e-mail messages. With 5-fold cross-validation, the results of the classification processes are reported with accuracy, precision, sensitivity and f1 score metrics.

In the study, the rf algorithm produced the most successful result with 98.83% accuracy. In this

study, unlike other studies, the use of natural language processing made the success different and high. It is concluded that this score is higher than similar studies in the literature. This study sets an example for a machine learning-based infrastructure that will consistently filter spam content in e-mail servers. In future studies, it is aimed to obtain higher performance results with different algorithms on datasets to be prepared for different natural languages.

**Table 8.** Comparison table of the most successful accuracy rates on the same and different data sets

Study Name	Data Set Used	Most Successful Algorithm	Highest Accuracy (%)
Kumar and al., 2023 [29]	Spam Dataset	NB	98.56
Jain and al., 2022 [26]	Spam Dataset	SVM	98.79
Abayomi and al., 2022 [30]	Spam Dataset	BILSTM	98.60
Reddy and Reddy, 2021 [28]	Spam Dataset	SVM	95.32
Gadde and al., 2021 [27]	Spam Dataset	LSTM	98.50
Junnarkar and al., 2021 [4]	Data set containing 5574 e-mails	SVM	97.83
Ma and al., 2020 [21]	6000 data sets containing e-mails	SVM	95.5
Salihi, 2019 [16]	1183 units obtained from Twitter the resulting data set	RF	92.95
Karamollaoglu and Dogru, 2018 [6]	TurkishMail dataset consisting of 600 e-mails	NB	95.5
Nazlı, 2018 [44].	Data set consisting of 300 e-mails	SVM	98.33
Kale, 2018 [45]	Data set of 4,709 e-mails	Gradient Boosted Tree (GBT)	94.97
Yıldız, 2017 [31]	Data set of 310 Turkish e-mails	NB	96.31
Alkaht and al., 2016 [28]	CSDMC 2010, SpamAssassin, Tarassul	SNN	95.82
Sharma and Suryawanshi, 2016 [29]	Spambase	KNN	97.50
Zavvar al., 2016. [46]	Spambase	SVM	93.07
<b>This study</b>	<b>Spam Dataset</b>	<b>SVM 98.74</b> <b>LR 97.66</b> <b>NB 90.49</b> <b>RF 98.83</b> <b>ANN 97.04</b>	<b>98.83</b>

## Article Information Form

### Funding

The author (s) has no received any financial support for the research, authorship or publication of this study.

### Authors' Contribution

All authors have contributed in experimental study and writing of the manuscript equally.

***The Declaration of Conflict of Interest/ Common Interest***

No conflict of interest or common interest has been declared by the authors.

***The Declaration of Ethics Committee Approval***

This study does not require ethics committee permission or any special permission.

***The Declaration of Research and Publication Ethics***

The authors of the paper declare that they comply with the scientific, ethical and quotation rules of sauks in all processes of the paper and that they do not make any falsification on the data collected. In addition, they declare that sakarya university journal of science and its editorial board have no responsibility for any ethical violations that may be encountered, and that this study has not been evaluated in any academic publication environment other than sakarya university journal of science.

***Copyright Statement***

Authors own the copyright of their work published in the journal and their work is published under the CC BY-NC 4.0 license.

**References**

[1] E. G. Dada, J. S. Bassi, H. Chiroma, A. O. Adetunmbi, & O. E. Ajibuwa, "Machine learning for email spam filtering: review, approaches and open research problems." *Heliyon*, 5(6), e01802, 2019.

[2] L.Ceci (2022, Nov. 14). Number of e-mail users worldwide [online]. Available:<https://www.statista.com/statistics/255080/number-of-e-mail-users-worldwide/>

[3] S. Dixon (2022, Apr. 28) Daily spam volume worldwide Available: <https://www.statista.com/statistics/1270424/daily-spam-volume-global/>

[4] P.Pantel, D. L. Spamcop, "A Spam Classification and Organization Program." *Learning for Text Categorization*, 2006.

[5] S. Zeadally, E. Adi, Z. Baig, & I. A. Khan, "Harnessing artificial intelligence capabilities to improve cybersecurity." *Ieee Access* 8, 23817-23837, 2020.

[6] A. Karim, S. Azam, B. Shanmugam, K. Kannoopatti, & M. Alazab, "A comprehensive survey for intelligent spam email detection." *IEEE Access* 7, 168261-168295, 2019.

[7] T. Dogan, "On Term Weighting for Spam SMS Filtering." *Sakarya University Journal of Computer and Information Sciences* 3.3, 239-249, 2020.

[8] S. Douzi, F. A. AlShahwan, M. Lemoudden, & B. El Ouahidi, "Hybrid email spam detection model using artificial intelligence." *International Journal of Machine Learning and Computing* 10.2 2020.

[9] E. M. Onyema, S. Dalal, C. A. T. Romero, B. Seth, P. Young, & M. A. Wajid, "Design of intrusion detection system based on cyborg intelligence for security of cloud network traffic of smart cities." *Journal of Cloud Computing* 11.1, 1-20, 2022.

[10] A. Bhowmick, S. M. Hazarika, "E-mail spam filtering: a review of techniques and trends." *Advances in Electronics, Communication and Computing: ETAEERE-2016*, 583-590, 2018.

[11] D. Abidin, The Effect of Derived Features on Art Genre Classification with Machine Learning. *Sakarya University Journal of Science*, 25(6), 1275-1286, 2021

[12] P. Sharma, U. Bhardwaj. "Machine learning based spam e-mail detection." *International Journal of Intelligent Engineering and Systems* 11.3, 1-10, 2018

[13] Ö. Şahinaslan, H. Dalyan, E. Şahinaslan, "Naive bayes sınıflandırıcısı kullanılarak youtube verileri üzerinden çok dilli duygu analizi." *"Bilişim Teknolojileri Dergisi* 15.2, 221-229, 2022



- [14] A. Junnarkar, S. Adhikari, J. Fagania, P. Chimurkar, D. Karia "E-mail spam classification via machine learning and natural language processing." 2021 Third International Conference on Intelligent Communication Technologies and Virtual Mobile Networks (ICICV). IEEE, 2021.
- [15] Y. S. Bozan, Ö. Çoban, G. T. Özyer, & B. Özyer, "SMS spam filtering based on text classification and expert system." 2015 23rd Signal Processing and Communications Applications Conference (SIU). IEEE, 2015.
- [16] A. K. A. Salihi, Spam detection by using word-vector learning algorithm in online social networks. MS thesis. Fen Bilimleri Enstitüsü, 2019.
- [17] H. Karamollaoglu, İ. A. Dogru, M. Dörterler, "Detection of Spam E-mails with Machine Learning Methods." 2018 Innovations in Intelligent Systems and Applications Conference (ASYU). IEEE, 2018.
- [18] M. T. Ma, K. Yamamori, A. Thida, "A comparative approach to Naïve Bayes classifier and support vector machine for email spam classification." 2020 IEEE 9th Global Conference on Consumer Electronics (GCCE). IEEE, 2020.
- [19] B. K. Dedeturk, B. Akay. "Spam filtering using a logistic regression model trained by an artificial bee colony algorithm." *Applied Soft Computing* 91 106229, 2020.
- [20] N. Baktır, A. Yılmaz, "Makine Öğrenmesi Yaklaşımlarının Spam-Mail Sınıflandırma Probleminde Karşılaştırmalı Analizi." *Bilişim Teknolojileri Dergisi* 15.3: 349-364, 2022.
- [21] F. Jánez-Martino, E. Fidalgo, S. González-Martínez, J. Velasco-Mata, "Classification of spam emails through hierarchical clustering and supervised learning." *arXiv preprint arXiv: 2005.08773*, 2020.
- [22] R. Mansoor, N. D. Jayasinghe, M. M. A. Muslam. "A comprehensive review on email spam classification using machine learning algorithms." 2021 International Conference on Information Networking (ICOIN). IEEE, 2021.
- [23] A. Yıldız, M. Demirci, Kurumsal e-posta sınıflandırma sistemi. Diss. Yüksek Lisans Tezi, Gazi Üniversitesi Fen Bilimleri Enstitüsü, 82, Ankara, 2017.
- [24] I. J. Alkaht, B. Al-Khatib. "Filtering spam using several stages neural networks." *Int. Rev. Comp. Softw* 11.2, 2016.
- [25] A. Sharma, A. Suryawanshi. "A novel method for detecting spam email using KNN classification with spearman correlation as distance measure." *International Journal of Computer Applications* 136.6, 28-35, 2016
- [26] Jain, T., Garg, P., Chalil, N., Sinha, A., Verma, V. K., & Gupta, R. SMS spam classification using machine learning techniques. In 2022 12th international conference on cloud computing, data science & engineering (confluence) (pp. 273-279). IEEE, 2022.
- [27] Gadde, S., Lakshmanarao, A., & Satyanarayana, S. SMS spam detection using machine learning and deep learning techniques. In 2021 7th International Conference on Advanced Computing and Communication Systems (ICACCS) (Vol. 1, pp. 358-362). IEEE, 2021.
- [28] Reddy, G. A., & Reddy, B. I. Classification of Spam Text using SVM. *Journal of University of Shanghai for Science and Technology*, 23(8), 616-624, 2021
- [29] Kumar, R., Murthy, K. S. R., Ramesh Babu, J., & Shaik, A. Live Text Analyzer to Detect Unsolicited Messages Using Count Vectorizer. *Journal of Engineering Sciences*, 14(06), 2023.
- [30] Abayomi-Alli, O., Misra, S., & Abayomi-Alli, A. A deep learning method for

- automatic SMS spam classification: Performance of learning algorithms on indigenous dataset. *Concurrency and Computation: Practice and Experience*, 34 (17), e6989, 2022.
- [31] 'Email Spam Detection 98% Accuracy | Kaggle'. <https://www.kaggle.com/code/mfaisalqureshi/email-spam-detection-98-accuracy/data> (accessed Aug. 21, 2023).
- [32] M. Zhou, N. Duan, S. Liu, H. Y. Shum, "Progress in neural NLP: modeling, learning, and reasoning." *Engineering* 6.3, 275-290, 2020.
- [33] I. Yahav, O. Shehory, D. Schwartz, "Comments mining with TF-IDF: the inherent bias and its removal." *IEEE Transactions on Knowledge and Data Engineering* 31.3, 437-450, 2018
- [34] Y. Altuntaş, A. F. Kocamaz, A. M. Ülkün, "Determination of Individual Investors' Financial Risk Tolerance by Machine Learning Methods." *2020 28th Signal Processing and Communications Applications Conference (SIU)*. IEEE, 2020.
- [35] R. Gürfidan, M. Ersoy, "Classification of death related to heart failure by machine learning algorithms." *Advances in Artificial Intelligence Research* 1.1, 13-18, 2021
- [36] S. Şenel, B. Alatlı. "Lojistik regresyon analizinin kullanıldığı makaleler üzerine bir inceleme." *Journal of Measurement and Evaluation in Education and Psychology* 5.1, 35-52, 2014.
- [37] A. McCallum, K. Nigam. "A comparison of event models for naive bayes text classification." *AAAI-98 workshop on learning for text categorization*. Vol. 752. No. 1. 1998.
- [38] V. Metsis, I. Androutsopoulos, G. Paliouras. "Spam filtering with naive bayes-which naive bayes?", *CEAS*. Vol. 17. 2006.
- [39] F. M. Avcu, "Az Veri Setli Çalışmalarında Derin Öğrenme Ve Diğer Sınıflandırma Algoritmalarının Karşılaştırılması: Agonist Ve Antagonist Ligand Örneği "İnönü Üniversitesi Sağlık Hizmetleri Meslek Yüksek Okulu Dergisi 10.1, 356-371, 2022
- [40] Ö. Akar, O. Güngör, "Rastgele orman algoritması kullanılarak çok bantlı görüntülerin sınıflandırılması." *Jeodezi ve Jeoinformasyon Dergisi* 106, 139-146, 2012.
- [41] A. Arı, M. E. Berberler, "Yapay sinir ağları ile tahmin ve sınıflandırma problemlerinin çözümü için arayüz tasarımı." *Acta Infologica* 1.2, 55-73, 2017
- [42] O. I. Abiodun, A. Jantan, A. E. Omolara, K. V. Dada, A. M. Umar, O. U. Linus, M. U. Kiru, "Comprehensive review of artificial neural network applications to pattern recognition." *IEEE Access* 7, 158820-158846, 2019
- [43] Z. K. Şentürk, "Artificial neural networks based decision support system for the detection of diabetic retinopathy." *Sakarya Üniversitesi Fen Bilimleri Enstitüsü Dergisi* 24.2, 424-431, 2020.
- [44] N. Nazlı, Analysis of machine learning-based spam filtering techniques. MS thesis. 2018.
- [45] B. Kale, Veri madenciliği sınıflandırma algoritmaları ile e-posta önemliliğinin belirlenmesi. MS thesis. Fen Bilimleri Enstitüsü, 2018.
- [46] M. Zavvar, M. Rezaei, S. Garavand. "Email spam detection using combination of particle swarm optimization and artificial neural network and support vector machine." *International Journal of Modern Education and Computer Science* 8.7, 68, 2016.

## Morphological and Structural Characterization of Low-Cost Graphene Produced by Electrochemical Exfoliation Method

Tamer Güzel<sup>1\*</sup>, Yasemin İşlek<sup>1</sup>, Oğuzhan Yıldız<sup>2</sup>

<sup>1</sup> Niğde Ömer Halisdemir University, Mechatronic Department, Niğde, Türkiye, tamerguzel7840@gmail.com, ymeric@ohu.edu.tr

<sup>2</sup> Niğde Ömer Halisdemir University, Electrical and Energy Department, Niğde, Türkiye, oguzhan.yildiz@ohu.edu.tr

\* Corresponding Author

### ARTICLE INFO

### ABSTRACT

#### Keywords:

Exfoliation Graphene  
Electrochemical Exfoliation  
Graphene Nanosheet  
Graphene Layer  
Raman  
XRD

#### Article History:

Received: 26.03.2023

Accepted: 26.12.2023

Online Available: 22.04.2024

The low-cost and mass production of graphene has gained importance in recent years. The electrochemical exfoliation method, one of the graphene production methods, is an efficient technique used to obtain low-cost-effective and large quantities of graphene nanosheets. Exfoliation parameters affect the properties of exfoliated graphene nanosheets. In this study, graphene production is fabricated by the method of exfoliation using electrolyte and voltage parameters. For this, a pen tip was used instead of pure platinum, which is very expensive, at the cathode. The structural research was done by X-ray diffraction spectroscopy (XRD), Raman spectroscopy and Fourier Transform Infrared Spectrometer (F-TIR). Morphological analyses were carried out by Scanning Electron Microscopy (SEM). The number of layers and crystallite of graphene layers were estimated. The obtained results were compared with the results of the other similar studies. Analysis results show that low-cost multilayer graphene can be produced by the electrochemical exfoliation method with the electrical parameters.

## 1.Introduction

Graphene is defined as two-dimensional (2D) honeycomb lattice,  $sp^2$ -hybridized carbon atoms with only ultra-thin sheet layer of carbon atoms (one-atom-thick) [1]. This material has many properties such as high conductivity and transparency [2-11]. Because of these unique properties, graphene has the potential to apply in many fields including nano electronics, space, nuclear, automotive, medicine and biomedical industrial areas [10, 12-14]. Also, it can be used in transparent conductive films, electronic circuits, sensors (chemical and biosensors), transparent and flexible electrodes for screens, and carbon-based materials such as energy storage devices [15-19]. Because of its widely application area of this material, the production of high amounts of graphene at low costs has gained significant importance.

Many techniques have been improved for graphene fabrication, some of these are micromechanical method, chemical vapor deposition (CVD), liquid-phase exfoliation, electrochemical exfoliation, chemical synthesis (Hummers Method), chemical reduction of graphene oxide and epitaxial growth on Silicon Carbide[20-25]. These techniques often require clean room, vacuum environments and high temperatures. On the other hand, some of these techniques required poisonous molecules(gases). So they are not suitable for serial production. The electrochemical exfoliation method, one of these production techniques that could be used at different temperatures, does not necessarily a special ambiance (such as a vacuum), is environment-friendly, and can be made for superior quality products.

This method is also appropriate for production in large quantities [26-28]. Because of these

advantages, high quantities of graphene could be manufactured at a lower price using this technique. On the other hand, the electrochemical exfoliation system has two electrodes and an ionic liquid. Generally, one of these electrodes is a graphite used as a carbon source and the other is conductive material that is not affected by acidic ambience [28].

Exfoliation parameters affect the features of exfoliated graphene nano sheets. In the literature; many researchers have carried out extensive work on lower-price and superior-quality graphene fabricated by electrochemical exfoliation of graphite. Coros showed a low-cost and simple way to produce graphene nano sheet by exfoliation of graphite rods. They explained that this method has many advantages, such as being able to control the oxidation degree of graphene with the applied voltage [28]. Petrovski et al obtained graphene using with electrolysis in sulfuric acid electrolytes. They developed a low cost method for high-yield production of graphene [29].

Wang et al investigated that highly efficient and a large amount synthesis of graphene by electrolytic exfoliation. They explained that the current preparation method can be scaled up for the mass production of graphene materials [30]. Sahoo et al reported that simple, fast and cost-effective graphene nanosheets can be obtained using electrochemical synthesis method. They also reported ionic liquid is a significant key factor in reducing imperfection and oxidation [30]. Munuera et al showed that pre-treatment with concentrated sulfuric acid is a powerful strategy to increase the anodic exfoliation efficiency of graphite foil in an aqueous electrolyte media. They announced that this easy way should help to make anodic exfoliation a more vying method for the mass production of graphene [31].

Zhou et al studied a large amount production of high-quality graphene by innovator electrochemical exfoliation at air-electrolyte interface. They reported that a novel electrochemical exfoliation method at the air-electrolyte interface to obtain the high-quality graphene with excellent yield from the graphite foil in  $(\text{NH}_4)_2\text{SO}_4$  electrolyte [32]. Chen et al

reported that nano clay helped the exfoliation of graphite for converting to superior-conducting graphene. They also reported that a sophisticated and cost-effective approach for manufacturing high-conductive graphene products was approved by nano clay-helped exfoliation of graphite rod in liquid electrolyte ambience [33].

In recent years, interest in the synthesis methods of graphene production has been increased. Therefore, the characterization of graphene nanosheets produced using electrochemical electrolysis method has gained importance because of some advantages such as economic and environmentally friendly.

In this study, pristine graphene was produced using the electrochemical exfoliation method. This method is a very practical, environmentally friendly approach that does not require special rooms. Structural analysis was performed using X-Ray Diffraction Diffractometer, Raman Spectrometer and Fourier Transform Infrared Spectrometer. Morphology examination of the produced graphene was done using Scanning Electron Microscope. The obtained results were discussed in comparison with each other and similar other studies.

## 2. Experimental

### 2.1. Production of graphene nanosheets

In this study graphite rods and sulfuric acid ( $\text{H}_2\text{SO}_4$ ) were mainly used. A commercially available 0.7mm (HB) pen tip was located as the counter electrode. The electrochemical exfoliation operations were done in (2)-electrode system. The graphite rod and pen tip were placed in 1M  $\text{H}_2\text{SO}_4$  solution as shown in Figure 1A.

The electrochemical exfoliation process was started by applying voltage by DC power supply (+10 V) on the graphite electrode. The process was completed in about 4 minutes. After the exfoliation process, the deposited layers on the surface part of the electrolyte were gathered (Figure 1D). After 30 min of sonication, vacuum filtration was implemented with a 0.22 mm porous polyvinyl membrane filter. Finally, the sample was washed several times with deionized water to clean acid salts from the surface and



desiccated at 80°C. According to the experimental observations, when the exfoliation process was finished (about 4 minutes), the layer expansion and the structural change were observed in the graphite in the form of pure rods (Figure 1B).

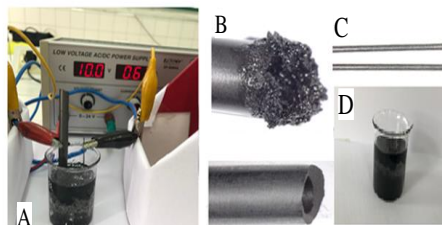


**Figure 1.** A- Experiment setup B- Image of the graphite rod before and after exfoliation C- Image of the pen tip before and after exfoliation D- The exfoliate products in suspension

Besides, any change in the structure of the pen tip used as counter electrode was not observed. (Figure 1C). The exfoliation product was analyzed in Niğde Ömer Halisdemir University Central Research Laboratory. Structural examination of the produced samples was done with the help of X-ray Diffraction Analyses (XRD), Raman Spectroscopy, and Fourier Transform Infrared Spectroscopy (F-TIR). In addition, the morphological research of the samples was done by Scanning Electron Microscope (SEM).

### 3. Results and Discussion

#### 3.1 X-Ray diffraction

The XRD technique was used to examine the crystal structure of the product formed as a result of exfoliation with graphite. The XRD patterns of graphite and exfoliation products are shown in Figure 2. As shown in Figure 2A, there are four peaks in the graphite diffraction pattern ( $2\theta$ ) 26.57, 42.50, 44.57 and 54.57. These peaks are compatible with the reflection planes (h k l) 0 0 2, 1 0 0, 1 0 1 and 0 0 4 respectively. The graphite shows peaks centered at 26.52° corresponding to the 0 0 2 plane. On the other hand, the exfoliation product indicates peaks centered at 26.40° corresponding to the 0 0 2 plane but its peak is shorter and wider than the graphite peak.

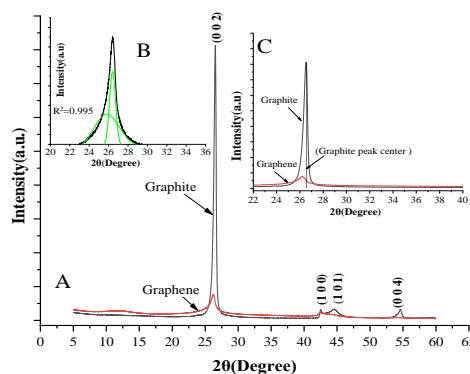


**Figure 2.** A- X-ray diffraction patterns of graphite and graphene B- Deconvoluted of the peak of the 2 0 0 plane of the graphene C- Comparison of graphite and graphene peak centers of the 0 0 2 plane

The reason for the shorter peak may be due to a reduction in the number of layers or a mixture of nanosheets having different number of layers [34]. It is clearly seen the situation at Figure 2B. According to that, when the 2 0 0 plane reflection angle is deconvoluted, it can be seen that it actually consists of different nested peaks.

On the other hand, this indicates layers of stacked and corrugated graphene sheets [35]. These diffraction patterns are also indicative of the formation of multi-layer graphene nanosheets [36, 37]. In addition, it can be seen that the reflection angles relative to plane 0 0 2 shift at a lower angle after exfoliation. This shows an increase in the d space value and consequently a decrease in the number of layers (Figure 2C).

The reason of that is formation of CO<sub>2</sub> and CO gases between the layers of graphite due to the formation of oxygen gas with SO<sub>4</sub><sup>2-</sup> ions and hydroxylation to the surface and edges of the graphene nanosheets. This may be another reason for increasing the interlayer spacing [36]. These results are compatible with the literature [29, 33, 38, 39]. According to these results, the product obtained by exfoliation was understood to be graphene. This demonstrates the success of the exfoliation process. On the other hand, to find the graphene layer, Debye-Scherrer (Eq. 1,2) and Bragg equations (Eq. 3) can be used [40].

$$L_a = \frac{k\lambda}{\beta \cos\theta} \quad (1)$$

$$n = \frac{L_a}{d} \quad (2)$$

$$d = \frac{n\lambda}{2\sin\theta} \quad (3)$$

where  $L_a$  is the crystallite size,  $\lambda$  is the wavelength of the laser,  $\beta$  is the width of the measured peak in half of the maximum (FWHM) in radians,  $k$  is shape factor ( $k=0.89$ ), the angle  $\theta$  is the angle of reflection of the plane 0 0 2 and  $n$  is the number of layers.

**Table 1.** The analysis results of XRD spectra

Sample	$2\theta$ (°)	d-spacing (Å)	$L_a$ (nm)	Layers of number (n)
Graphite	26.52	3.35	14.71	66.47
Graphene	26.40	3.38	2.79	9

According to the Equation 1; the crystallite value of graphene were calculated as 2.79 nm [29]. In addition, the number of layers was found about 9 layers with the angle of  $26.40^\circ$  of the graphene, from Equation 2. Some parameters and calculated layers number for graphite and graphene are shown in Table 1. Since the shortening and expansion of the sharp peak decreases the crystallite value according to the Debye-Scherrer equation, this can be interpreted as graphene formation.

When examined in Figure 3B, it can be seen the peak of graphite at 44.57 degrees disappears after graphene formation. However, it can be seen the peak of graphite at 55.47 degrees is shortened and expanded after exfoliation in Figure 3A. It can be also observed that the peak center shifts to smaller angles. The state can be suggested that the plane 0 0 4 of the graphite is due to the decrease in the number of layers. Indeed, other researchers have found similar diffraction patterns for this plane [29, 35].

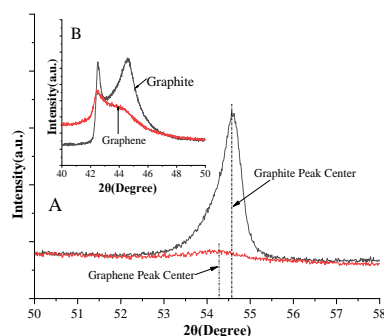


**Figure 3.** Graphite and graphene diffraction patterns in other planes A The pattern of peaks of the 1 0 0 and 1 0 1 planes B The pattern of peak of the 0 0 4 plane

### 3.2. Raman spectroscopy

Raman spectroscopy is a powerful method used to analyze the structure of crystalline materials. This technique is a non-destructive, fast and accurate technique estimated the defect density and the number and quality of graphene layers [29]. Carbon structures have 3 base peaks, named D peak (around  $1350\text{ cm}^{-1}$ ), G peak (around  $1580\text{ cm}^{-1}$ ) and 2D peak (around  $2700\text{ cm}^{-1}$ ) [34]. The D peak shows the defects in the crystal structure, while the G band shows the vibrations of the carbon atoms between the layers and the crystallized structures. The 2D band is related to the stacking of the structure [39].

Raman spectra of the sample produced exfoliation method are shown in Figure 4. According to Figure 4B, the D band of graphite has a very low intensity at  $1333\text{ cm}^{-1}$ , D' band at  $1621\text{ cm}^{-1}$  and the G band is a very strong peak at  $1582\text{ cm}^{-1}$ . While the presence of the G peak signs the crystal structure of the graphite, the presence of the weak D peak indicates that the graphite contains partial defects in its structure [41]. D' peak is also related to the disorder of edge carbons [42, 43].

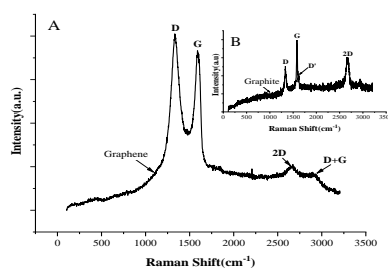


**Figure 4.** A Raman spectrum of graphene B Raman spectrum of graphite

The intense 2D peak at  $2661\text{ cm}^{-1}$  originates from two-phonon double resonance. These similar results were also reported by other researchers [41, 42, 44]. After the exfoliation, the structure, D and G peaks are seen at  $1330\text{ cm}^{-1}$  and  $1594\text{ cm}^{-1}$  respectively (Figure 4A). Especially the increase in the density of the D peak is remarkable.

**Table 2.** Raman analysis of studied graphene samples

Sample	D Peak Position ( $\text{cm}^{-1}$ ) Intensity (a.u.)	G Peak Position ( $\text{cm}^{-1}$ ) Intensity (a.u.)	2D Peak Position ( $\text{cm}^{-1}$ ) Intensity (a.u.)	$I_D/I_G$	$I_{2D}/I_G$
Graphite	1333 683	1582 994	2660 793	0,68	0.79
Graphene	1333 10007	1590 9200	2650 4010	1.08	0.44

It can be the result of an increase in defects in the crystal structure due to the oxygen-containing functional groups attached to the graphite layers during the exfoliation process [45]. The G peak can be seen to be over  $1590\text{cm}^{-1}$ . Chamoli showed that this is an indicator of the standoff of oxygen functional groups from exfoliated nano sheets [46].

On the other hand, it is observed that the 2D peak of the exfoliated graphene is smaller and wider compared to the graphite [29, 34, 45, 47]. This result proves that the number of stacks and the number of layers is reduced. In addition that the result shows that transform from graphite to multilayer graphene [29, 41, 48]. Petrovski reported that 2D peak which is less pronounced and broad is indicated the asset of multilayered graphene ( $>8$ -layers) [29]. Ferrari explained that the broad 2D peak suggests the presence of multilayer graphene [41]. Beside that the D+G peak at  $2910\text{ cm}^{-1}$  is related disorder of graphene structure [26, 34]. These results have also been reported in previous studies [41, 45, 47, 49].

According to Firdhouse, the shift of G peak around  $20\text{-}30\text{cm}^{-1}$  indicates 5-20 graphene layer. Accordingly, the shift of the G peak in this study indicates the 5-20 layer number of the graphene layer [50-52]. This result is compatible with the number of layers obtained from the XRD results analysis. On the other hand, the  $I_D/I_G$  ratio gives information about the graphene quality while

$I_{2D}/I_G$  gives information about the number of layers of graphene [29, 53].

$I_D/I_G$  and  $I_{2D}/I_G$  ratios calculated using Figure 4 are given in Table 2. Accordingly, the  $I_D/I_G$  ratio of 1.25 shows that there are some defects in the graphene structure caused by the edge plane of the graphene sheets [41, 54]. This result has also been reported in previous studies [43, 53, 55]. The  $I_{2D}/I_G$  value of the exfoliated graphene is shown in Table 2. Gupta reported that when the number of graphene layers decreased, the value of  $I_{2D}/I_G$  increased. The relatively low  $I_{2D}/I_G$  ratio indicates mostly multilayer graphene [56].

Nguyen calculated the graphene  $I_{2D}/I_G$  ratio as 0.44 and reported that the graphene produced was multilayer [57]. Other researchers have obtained similar results.[53, 58]. According to the results, it has been understood that multilayer graphene was formed from graphite. Moreover, the crystallite size of graphene has calculated according to the Tuinstra and Koenig Equation 4 and 5:

$$\frac{I_D}{I_G} = \frac{C(\lambda)}{L_a} \quad (4)$$

$$L_a = C(\lambda) \frac{I_G}{I_D} \quad (5)$$

where the pre-factor  $C(\lambda)$  is equal to 4.95 for  $532\text{nm}$ . The  $L_a$  value was calculated as  $4.52\text{ nm}$  according to the equation. The result is compatible with the literature [29, 53]. In addition, there is a difference between the  $L_a$  value calculated from the Tuinstra and Koenig equation and the value calculated from the Debye Sheerer equation. The reason of the difference the result of the spectroscopy technique. While first technique is based on X-ray reflections, the other is based on changes in the Raman spectrum such as frequency shifts.

### 3.3. Fourier transform infrared spectroscopy

Infrared Spectroscopy (IR) provides a fast and reliable technique for identifying and characterizing the chemical structures of many substances, from biomaterials to composite materials, liquids and gases [59, 60]. F-TIR spectra of graphene nanosheets produced by exfoliation method are presented in Figure 5.



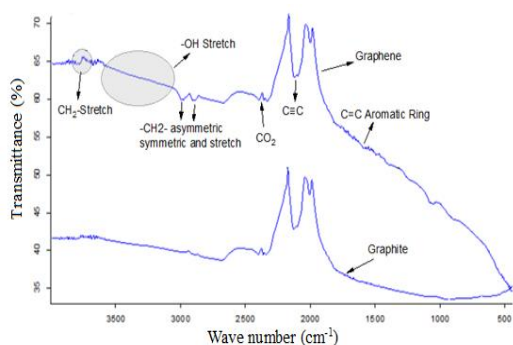


**Figure 5.** F-TIR spectra of graphite and graphene nanosheets

It can be seen that the vibrations of the functional groups are reasonably weak in the Figure 5. This shows that there are no functional groups in the nanosheets. It can be suggested that high heat generated during exfoliation leads to that. Due to the high temperature, the oxygen groups formed between the layers may be removed again. Therefore, the graphene nanosheets produced have a structure known in the literature as pristine graphene [61]. On the other hand, the F-TIR spectra of the graphene nano sheets synthesized is consistent with the literature [62-64]. Furthermore, in the F-TIR spectrum, the peak of CO<sub>2</sub> gas absorbed from the environment or formed between layers can be seen around 2350 cm<sup>-1</sup>. In addition, the difference between graphene and graphite transmittance values is quite evident in figure 5. This may be interpreted as a decrease in the number of layers. F-TIR results also confirm the conversion from graphite to graphene nanosheets.

### 3.4. Scanning electron microscope

Scanning electron microscopy (SEM) is one of the best techniques used to study surface morphologies among modern image analysis methods.

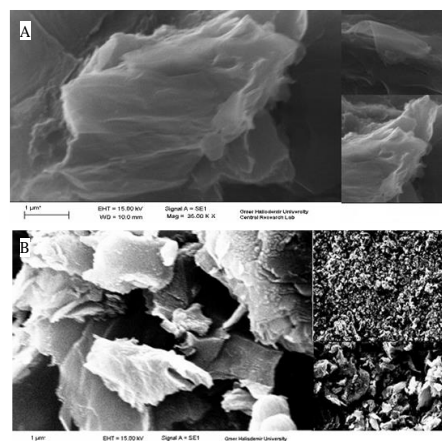


**Figure 6.** A- SEM images of graphene B- SEM images of graphite

SEM images of graphene and exfoliation graphite are shown in Figure 6. It can be seen that from Figure 6 while the graphite structure is shown a flat, thick structure consisting of layers, the structure of the exfoliation graphene is seen wrinkled and thin membrane-like structure [27-29, 38, 65]. This is due to the bending and buckling caused by the thermal stability of graphene during exfoliation. This may be regarded as an indication of the conversion from graphite to graphene as a result of an electrochemical process. The very thin and transparent structure (small picture) formed as a result of exfoliation confirms the previously calculated number of layers.

## 4. Conclusion

To produce graphene by electrochemical exfoliation technique, a graphite rod as a carbon source, a pencil tip as a cathode, and sulfuric acid as an electrolyte was used. Multilayer graphene nanosheets were produced by this method. Morphological and thermal characteristic of graphene nanosheets were performed by XRD, Raman Spectroscopy, F-TIR Spectroscopy and SEM measurements. According to the XRD results, it was found that the graphene nano sheet structure is multi-layer (about 9-10 layers). The Raman Spectroscopy results shown that there are some structural defects in the graphene nanosheets. F-TIR results confirmed that the products are pristine graphene structures. SEM results showed that graphene layers were observed in thin layers. The results showed that low-cost multilayer graphene can be produced with the electrochemical exfoliation method.

The produced graphene can be used as a cathode material instead of the rather expensive pure platinum in the pen tip. The materials used in the experiment can be obtained from more cost-effective materials has further reduced the cost of the produced graphene. The electrochemical method is a very easy and useful method in graphene production. However, further investigation of the effect of changes in experimental inputs on graphene may provide the production of graphene with more controllable properties for future studies.

### **Article Information Form**

#### ***Acknowledgments***

We would like to thank the staff of Niğde University Central Research Laboratory

#### ***Funding***

This work was funded by Niğde University Research Projects Unit under the grant no. FEB 2018/19.

#### ***The Declaration of Conflict of Interest/ Common Interest***

No conflict of interest or common interest has been declared by the authors

#### ***Author Contributions***

The authors declare their equal contribution to this publication. All authors have read and agreed to the published version of the manuscript.

#### ***The Declaration of Ethics Committee Approval***

The author declares that this document does not require an ethics committee approval or any special permission.

#### ***The Declaration of Research and Publication Ethics***

The author of the paper declares that he complies with the scientific, ethical, and quotation rules of SAUJS in all processes of the paper and that he does not make any falsification on the data collected. In addition, he declares that Sakarya University Journal of Science and its editorial board have no responsibility for any ethical violations that may be encountered and that this study has not been evaluated in any academic publication environment other than Sakarya University Journal of Science.

### ***Copyright Statement***

Authors own the copyright of their work published in the journal and their work is published under the CC BY-NC 4.0 license.

### **References**

- [1] A. K. Geim, K. S. Novoselov, "The rise of graphene", *Nature Mater*, 6, p. 183-191, 2007
- [2] K. S. Novoselov, A. K. Geim, S. V. Morozov, D. Jiang, Y. Zhang, S. V. Dubonos, I. V. Grigorieva, A. A. Firsov, "Electric field effect in atomically thin carbon films", *Science*, 306, p. 666-669, 2004
- [3] K. S. Novoselov, A. K. Geim, S. Morozov, D. Jiang, M. I. Katsnelson, I. Grigorieva, S. Dubonos, Firsov, A A, "Two-dimensional gas of massless Dirac fermions in graphene", *Nature*, 438, p. 197, 2005
- [4] Y. Zhang, Y.-W. Tan, H. L. Stormer, P. Kim, "Experimental observation of the quantum Hall effect and Berry's phase in graphene", *Nature*, 438, p. 201, 2005
- [5] C. Lee, X. Wei, J. W. Kysar, J. Hone, "Measurement of the elastic properties and intrinsic strength of monolayer graphene", *Science*, 321, p. 385-388, 2008
- [6] A. A. Balandin, S. Ghosh, W. Bao, I. Calizo, D. Teweldebrhan, F. Miao, C. N. Lau, "Superior thermal conductivity of single-layer graphene", *Nano Letters*, 8, p. 902-907, 2008
- [7] K. I. Bolotin, K. J. Sikes, Z. Jiang, M. Klima, G. Fudenberg, J. Hone, P. Kim, H. Stormer, "Ultrahigh electron mobility in suspended graphene", *Solid State Communications*, 146, p. 351-355, 2008
- [8] A. A. Balandin, "Thermal properties of graphene and nanostructured carbon materials", *Nature Materials*, 10, p. 569, 2011

- [9] V. B. Mohan, K.-t. Lau, D. Hui, D. Bhattacharyya, "Graphene-based materials and their composites: a review on production, applications and product limitations", *Composites Part B: Engineering*, 142, p. 200-220, 2018
- [10] J. Lu, J.-x. Yang, J. Wang, A. Lim, S. Wang, K. P. Loh, "One-pot synthesis of fluorescent carbon nanoribbons, nanoparticles, and graphene by the exfoliation of graphite in ionic liquids", *ACS Nano*, 3, p. 2367-2375, 2009
- [11] H. B. Heersche, P. Jarillo-Herrero, J. B. Oostinga, L. M. Vandersypen, A. F. Morpurgo, "Bipolar supercurrent in graphene", *Nature*, 446, p. 56, 2007
- [12] L. Vicarelli, M. Vitiello, D. Coquillat, A. Lombardo, A. C. Ferrari, W. Knap, M. Polini, V. Pellegrini, A. Tredicucci, "Graphene field-effect transistors as room-temperature terahertz detectors", *Nature Materials*, 11, p. 865, 2012
- [13] M. D. Mukherjee, C. Dhand, N. Dwivedi, B. P. Singh, G. Sumana, V. V. Agarwal, J. S. Tawale, B. D. Malhotra, "Facile synthesis of 2-dimensional transparent graphene flakes for nucleic acid detection", *Sensors and Actuators B: Chemical*, 210, p. 281-289, 2015
- [14] S. J. Wang, Y. Geng, Q. Zheng, J.-K. Kim, "Fabrication of highly conducting and transparent graphene films", *Carbon*, 48, p. 1815-1823, 2010
- [15] X. Song, Z. Shi, X. Tan, S. Zhang, G. Liu, K. Wu, "One-step solvent exfoliation of graphite to produce a highly-sensitive electrochemical sensor for tartrazine", *Sensors and Actuators B: Chemical*, 197, p. 104-108, 2014
- [16] S. Kim, H. S. Lee, J. M. Kim, S. W. Seo, J. H. Kim, C. W. Jang, S.-H. Choi, "Effect of layer number on flexible perovskite solar cells employing multiple layers of graphene as transparent conductive electrodes", *Journal of Alloys and Compounds*, 744, p. 404-411, 2018
- [17] K. Parvez, R. Li, S. R. Puniredd, Y. Hernandez, F. Hinkel, S. Wang, X. Feng, K. Müllen, "Electrochemically exfoliated graphene as solution-processable, highly conductive electrodes for organic electronics", *ACS Nano*, 7, p. 3598-3606, 2013
- [18] Z. Y. Xia, G. Giambastiani, C. Christodoulou, M. V. Nardi, N. Koch, E. Treossi, V. Bellani, S. Pezzini, F. Corticelli, V. Morandi, "Synergic exfoliation of graphene with organic molecules and inorganic ions for the electrochemical production of flexible electrodes", *ChemPlusChem*, 79, p. 439-446, 2014
- [19] Y. L. Zhong, Z. Tian, G. P. Simon, D. Li, "Scalable production of graphene via wet chemistry: progress and challenges", *Materials Today*, 18, p. 73-78, 2015
- [20] Z. Chen, W. Ren, L. Gao, B. Liu, S. Pei, H. - M. Cheng, "Three-dimensional flexible and conductive interconnected graphene networks grown by chemical vapour deposition", *Nature Materials*, 10, p. 424, 2011
- [21] R. Singh, C. C. Tripathi, "Synthesis of Colloidal Graphene by Electrochemical Exfoliation of Graphite in Lithium Sulphate", *Materials Today: Proceedings*, 5, p. 973-979, 2018
- [22] J. Chen, B. Yao, C. Li, G. Shi, "An improved Hummers method for eco-friendly synthesis of graphene oxide", *Carbon*, 64, p. 225-229, 2013
- [23] Z. Yang, S. Xu, L. Zhao, J. Zhang, Z. Wang, X. Chen, X. Cheng, F. Yu, X. Zhao, "A new direct growth method of graphene on Si-face of 6H-SiC by synergy of the inner and external carbon sources", *Applied Surface Science*, 436, p. 511-518, 2018

- [24] A. T. Najafabadi, E. Gyenge, "High-yield graphene production by electrochemical exfoliation of graphite: Novel ionic liquid (IL)-acetonitrile electrolyte with low IL content", *Carbon*, 71, p. 58-69, 2014
- [25] T. Güzel, "Investigation of the usability of nitric acid electrolyte in graphene production by electrochemical method", *Fullerenes, Nanotubes and Carbon Nanostructures*, 1-8, 2020
- [26] R. I. Jibrael, M. K. Mohammed, "Production of graphene powder by electrochemical exfoliation of graphite electrodes immersed in aqueous solution", *Optik*, 127, p. 6384-6389, 2016
- [27] S. Yang, S. Brüller, Z.-S. Wu, Z. Liu, K. Parvez, R. Dong, F. Richard, P. Samori, X. Feng, K. Müllen, "Organic radical-assisted electrochemical exfoliation for the scalable production of high-quality graphene", *Journal of the American Chemical Society*, 137, p. 13927-13932, 2015
- [28] M. Coroş, F. Pogăcean, M.-C. Roşu, C. Socaci, G. Borodi, L. Mageruşan, A. R. Biriş, S. Pruneanu, "Simple and cost-effective synthesis of graphene by electrochemical exfoliation of graphite rods", *RSC Advances*, 6, p. 2651-2661, 2016
- [29] A. Petrovski, A. T. Dimitrov, A. Grozdanov, P. Paunović, B. Andonović, G. Gentile, M. Avella, B. Rangelov, "Study of Graphene Obtained by Electrolysis in Sulfuric Acid Electrolytes", *SciFed Nanotech Research Letters*, 2017
- [30] G. Wang, B. Wang, J. Park, Y. Wang, B. Sun, J. Yao, "Highly efficient and large-scale synthesis of graphene by electrolytic exfoliation", *Carbon*, 47, p. 3242-3246, 2009
- [31] J. Munuera, J. Paredes, S. Villar-Rodil, A. Martínez-Alonso, J. Tascón, "A simple strategy to improve the yield of graphene nanosheets in the anodic exfoliation of graphite foil", *Carbon*, 115, p. 625-628, 2017
- [32] Q. Zhou, Y. Lu, H. Xu, "High-yield production of high-quality graphene by novel electrochemical exfoliation at air-electrolyte interface", *Materials Letters*, 235, p. 153-156, 2019
- [33] K. Chen, D. Xue, "From graphite-clay composites to graphene electrode materials: in-situ electrochemical oxidation and functionalization", *Materials Research Bulletin*, 96, p. 281-285, 2017
- [34] M. Alanyalıoğlu, J. J. Segura, J. Oró-Solè, N. Casañ-Pastor, "The synthesis of graphene sheets with controlled thickness and order using surfactant-assisted electrochemical processes", *Carbon*, 50, p. 142-152, 2012
- [35] K. Chen, D. Xue, "Preparation of colloidal graphene in quantity by electrochemical exfoliation", *Journal of Colloid and Interface Science*, 436, p. 41-46, 2014
- [36] S. K. Sahoo, A. Mallik, "Simple, fast and cost-effective electrochemical synthesis of few layer graphene nanosheets", *Nano*, 10, p. 1550019, 2015
- [37] I. Afanasov, O. Shornikova, D. Kirilenko, I. Vlasov, L. Zhang, J. Verbeeck, V. Avdeev, G. Van Tendeloo, "Graphite structural transformations during intercalation by HNO<sub>3</sub> and exfoliation", *Carbon*, 48, p. 1862-1865, 2010
- [38] K. Chen, D. Xue, S. Komarneni, "Nanoclay assisted electrochemical exfoliation of pencil core to high conductive graphene thin-film electrode", *Journal of Colloid and Interface Science*, 487, p. 156-161, 2017
- [39] F. T. Johra, J.-W. Lee, W.-G. Jung, "Facile and safe graphene preparation on solution based platform", *Journal of Industrial and Engineering Chemistry*, 20, p. 2883-2887, 2014

- [40] B. E. Warren, *X-ray Diffraction*. 1990: Courier Corporation.
- [41] A. C. Ferrari, J. Meyer, V. Scardaci, C. Casiraghi, M. Lazzeri, F. Mauri, S. Piscanec, D. Jiang, K. Novoselov, S. Roth, "Raman spectrum of graphene and graphene layers", *Physical Review Letters*, 97, p. 187401, 2006
- [42] K. S. Rao, J. Senthilnathan, Y.-F. Liu, M. Yoshimura, "Role of peroxide ions in formation of graphene nanosheets by electrochemical exfoliation of graphite", *Scientific Reports*, 4, p. 4237, 2014
- [43] A. Radoń, P. Włodarczyk, D. Łukowiec, "Structure, temperature and frequency dependent electrical conductivity of oxidized and reduced electrochemically exfoliated graphite", *Physica E: Low-dimensional Systems and Nanostructures*, 99, p. 82-90, 2018
- [44] M. Pimenta, G. Dresselhaus, M. S. Dresselhaus, L. Cancado, A. Jorio, R. Saito, "Studying disorder in graphite-based systems by Raman spectroscopy", *Physical Chemistry Chemical Physics*, 9, p. 1276-1290, 2007
- [45] R. Singh, C. C. Tripathi, "Electrochemical exfoliation of graphite into graphene for flexible supercapacitor application", *Materials Today: Proceedings*, 5, p. 1125-1130, 2018
- [46] P. Chamoli, M. K. Das, K. K. Kar, "Green synthesis of less defect density bilayer graphene", *Graphene*, 3, p. 56-60, 2015
- [47] S.-H. Lee, S.-D. Seo, K.-S. Park, H.-W. Shim, D.-W. Kim, "Synthesis of graphene nanosheets by the electrolytic exfoliation of graphite and their direct assembly for lithium ion battery anodes", *Materials Chemistry and Physics*, 135, p. 309-316, 2012
- [48] L. Malard, M. Pimenta, G. Dresselhaus, M. Dresselhaus, "Raman spectroscopy in graphene", *Physics Reports*, 473, p. 51-87, 2009
- [49] C.-Y. Su, A.-Y. Lu, Y. Xu, F.-R. Chen, A. N. Khlobystov, L.-J. Li, "High-quality thin graphene films from fast electrochemical exfoliation", *ACS Nano*, 5, p. 2332-2339, 2011
- [50] M. J. Firdhouse, P. Lalitha, "Eco-friendly synthesis of graphene using the aqueous extract of *Amaranthus dubius*", *Carbon: Science and Technology*, 5, p. 253-259, 2013
- [51] V. Singh, D. Joung, L. Zhai, S. Das, S. I. Khondaker, S. Seal, "Graphene based materials: past, present and future", *Progress in Materials Science*, 56, p. 1178-1271, 2011
- [52] V. Chabot, B. Kim, B. Sloper, C. Tzoganakis, A. Yu, "High yield production and purification of few layer graphene by Gum Arabic assisted physical sonication", *Scientific Reports*, 3, p. 1378, 2013
- [53] H. S. Wahab, S. H. Ali, A. A. Hussein, "Synthesis and characterization of graphene by Raman spectroscopy", *Journal of Materials Sciences and Applications*, 1, p. 130-135, 2015
- [54] R. Navik, Y. Gai, W. Wang, Y. Zhao, "Curcumin-assisted ultrasound exfoliation of graphite to graphene in ethanol", *Ultrasonics Sonochemistry*, 48, p. 96-102, 2018
- [55] A. Ambrosi, M. Pumera, "Electrochemically exfoliated graphene and graphene oxide for energy storage and electrochemistry applications", *Chemistry—A European Journal*, 22, p. 153-159, 2016
- [56] A. Gupta, G. Chen, P. Joshi, S. Tadigadapa, P. Eklund, "Raman scattering from high-frequency phonons in supported n-graphene layer films", *Nano Letters*, 6, p. 2667-2673, 2006



- [57] H. D. Le, T. T. T. Ngo, D. Q. Le, X. N. Nguyen, N. M. Phan, "Synthesis of multi-layer graphene films on copper tape by atmospheric pressure chemical vapor deposition method", *Advances in Natural Sciences: Nanoscience and Nanotechnology*, 4, p. 035012, 2013
- [58] A. Hamra, H. Lim, W. Chee, N. Huang, "Electro-exfoliating graphene from graphite for direct fabrication of supercapacitor", *Applied Surface Science*, 360, p. 213-223, 2016
- [59] Y.-H. Son, W.-C. Jung, J.-I. Jeong, N.-G. Park, I.-S. Kim, I.-H. Bae, "FTIR characteristics of hydrogenated amorphous carbon films prepared by Ecr-Pecvd", *Journal-Korean Physical Society*, 39, p. 713-717, 2001
- [60] E. Vaghri, Z. Khalaj, M. Ghoranneviss, "Preparation and characterization of diamond-like carbon films on various substrates by PECVD system", *Studia Univ Babes-Bolyai Chemia*, 57, p. 143-150, 2012
- [61] M. Hayyan, A. Abo-Hamad, M. A. AlSaadi, M. A. Hashim, "Functionalization of graphene using deep eutectic solvents", *Nanoscale Research Letters*, 10, p. 324, 2015
- [62] A. Mir, A. Shukla, "Bilayer-rich graphene suspension from electrochemical exfoliation of graphite", *Materials & Design*, 156, p. 62-70, 2018
- [63] O. Sadak, A. K. Sundramoorthy, S. Gunasekaran, "Facile and green synthesis of highly conductive graphene paper", *Carbon*, 138, p. 108-117, 2018
- [64] Z. M. Marković, B. M. Babić, M. Dramićanin, I. H. Antunović, V. B. Pavlović, D. Peruško, B. T. Marković, "Preparation of highly conductive carbon cryogel based on pristine graphene", *Synthetic Metals*, 162, p. 743-747, 2012
- [65] F. Tavakoli, M. Salavati-Niasari, F. Mohandes, "Green synthesis and characterization of graphene nanosheets", *Materials Research Bulletin*, 63, p. 51-57, 2015





## Potential Anti-SARS-CoV-2 Effects of Gossypol and AT-101: Molecular Docking Study Against Angiotensin Converting Enzyme 2

Süleyman İlhan<sup>1</sup> , Harika Atmaca<sup>1\*</sup> 

<sup>1</sup> Manisa Celal Bayar University, Faculty of Engineering and Natural Science, Department of Biology, Manisa, Türkiye, [suleyman.ilhan@cbu.edu.tr](mailto:suleyman.ilhan@cbu.edu.tr), [harika.atmaca@cbu.edu.tr](mailto:harika.atmaca@cbu.edu.tr)

\*Corresponding Author

### ARTICLE INFO

### ABSTRACT

#### Keywords:

AT-101

Gossypol

COVID-19

Anti-SARS-CoV-2

Molecular Docking



#### Article History:

Received: 11.06.2023

Accepted: 16.01.2024

Online Available: 22.04.2024

This study explores the potential anti-SARS-CoV-2 effects of gossypol (GP) and its AT-101 derivative through *in silico* molecular docking simulations. GP and AT-101 are natural and modified compounds, respectively, with promising biological activities. Using Autodock Vina software, molecular docking simulations were performed to assess the binding interactions between GP, AT-101, and the receptor binding domain of angiotensin-converting enzyme 2 (ACE2) which plays a vital role in facilitating viral entry into host cells. The docking results revealed that GP and AT-101 exhibited favorable interactions with ACE2, suggesting their potential as anti-SARS-CoV-2 agents. GP formed seven hydrogen bonds with ACE2, while AT-101 formed eight, indicating more stable binding and superior interaction. However, it is important to acknowledge that these findings are based on *in silico* modeling and further research is required to validate the antiviral properties of GP and AT-101 *in vitro* and *in vivo*. Moreover, the long-term safety and efficacy of these compounds for COVID-19 treatment warrant further investigation through clinical trials. In conclusion, this *in silico* study provides preliminary evidence of the potential anti-SARS-CoV-2 effects of GP and AT-101 by demonstrating their ability to interact with ACE2. However, it is important to acknowledge that these findings are based on *in silico* modeling and further research is required to validate the antiviral properties of GP and AT-101 *in vitro* and *in vivo*.

## 1. Introduction

Gossypol (GP) is a natural polyphenol compound found in cottonseeds and the tropical tree *Thespesia populnea* L. [1]. GP has several biological activities including anti-oxidant, anti-viral, anti-parasitic, and anti-bacterial. It has been studied for its potential anticancer properties due to its ability to inhibit the activity of several enzymes involved in cell growth and survival [2]. Despite all its potential activities GP has been found to have toxic side effects, including male infertility and cardiac toxicity, which have limited its clinical use [3]. As a result, researchers have developed a modified form of GP called *-/-* GP (AT-101) that has reduced toxicity while enhancing its biological activities.

AT-101 is a Bcl-2 family inhibitor that has been investigated for its potential use in the treatment of various types of cancer. It works by inhibiting the activity of Bcl-2 protein and other anti-apoptotic proteins, which can lead to apoptosis in cancer cells [4]. Several clinical trials have been conducted to evaluate the safety and efficacy of AT-101 in the treatment of various cancers, including prostate, bladder, ovarian, lung, glioblastoma, leukemia, and multiple myeloma cells with promising results [5–11]. Currently, it is undergoing phase II/III clinical trials for further evaluation [12]. Although its anticancer properties have been widely studied, there is limited research on the antiviral effects of GP. GP is effective in inhibiting other ssRNA viruses, including plant viruses like tobacco

mosaic virus [13], as well as zoonotic viruses such as avian influenza virus [14], West Nile virus [15], and Hendra virus [16]. One study showed that the GP derivative could be a safe and effective broad-spectrum therapeutic agent to treat diseases caused by Zika and dengue virus infection without toxicity [17]. In a study, authors shed light on the underlying mechanism of GP's action by demonstrating that it likely targets the RNA-dependent RNA polymerase of ssRNA viruses across a broad range of hosts, including plants and animals, which was previously not fully understood [18]. Overall, while there is some preliminary evidence suggesting that GP and its derivatives may have antiviral properties, more research is needed to confirm these findings and to determine whether they could be useful in the treatment of viral infections.

The emergence of SARS-CoV-2 has led to an unprecedented global health crisis, with the virus spreading rapidly across the world and causing significant social and economic disruptions [19]. While vaccines have proven effective in preventing COVID-19, the virus's ability to mutate and the emergence of new variants of concern have raised concerns about the long-term effectiveness of current vaccines. Researchers and healthcare professionals are therefore working tirelessly to develop new treatments and broad-spectrum inhibitors that can effectively combat various SARS-CoV-2 variants [20]. Additionally, as the virus has been found to cause serious damage to both humans and animals [21], there is a pressing need to understand its pathogenic mechanisms and identify potential therapeutic targets to mitigate the effects of COVID-19. Despite the challenges presented by the ongoing pandemic, the scientific community remains committed to developing effective strategies to control the spread of SARS-CoV-2 and protect public health.

The SARS-CoV-2 spike protein is the key protein that enables the virus to enter host cells. The spike protein comprises two subunits, S1 and S2, with the receptor-binding domain (RBD) located on the S1 subunit. The RBD is responsible for binding to the host cell receptor

angiotensin-converting enzyme 2 (ACE2), which is present on the surface of human cells [22].

In the present work, to identify possible antiviral effects to target SARS-CoV-2, the interactions of AT-101 or GP with ACE2 were screened. This methodical computer-aided drug-designing methodology not only helped to learn more about the potential putative targets of the compounds but also revealed structural characteristics of the compounds that are responsible for their bioactivity on the selected target.

## 2. General Methods

### 2.1. Receptor preparation

Receptor preparation is an essential step in molecular docking, which involves preparing the three-dimensional structure of the target receptor protein for the docking simulation. The main objective is to ensure that the receptor is in an optimal conformation to interact with ligands. The SARS-CoV-2 main protease ACE2 (PDB ID: 1R42) was selected as the receptor proteins. The three-dimensional (3D) structure of ACE2 was obtained from a reliable source the Protein Data Bank (PDB) in PDB format (<https://www.rcsb.org/>). The PDB provides experimentally determined structures of proteins, including X-ray crystallography and NMR-derived structures. Autodock Vina 4.2.5.1 software was employed for eliminating water molecules, hydrogenating the proteins, and adjusting the load distribution. Water molecules and other heteroatoms that are not directly involved in the binding site or relevant interactions are typically removed from the receptor structure.

This simplifies the docking process and focuses on the key interactions between the receptor and ligands. By following these steps, the receptor structure is prepared in a state that optimizes its binding site and overall conformation for the subsequent docking simulation with ligands. The prepared receptor is then ready to be used in molecular docking experiments to investigate ligand-receptor interactions and predict binding affinities. A maximum of five cavities were

found using default parameters in order to acquire better potential binding sites.

## 2.2.Ligand preparation

Ligand preparation is a crucial step in molecular docking, where the three-dimensional structure of the ligand molecule is prepared to ensure its compatibility with the docking software and accurate representation of its chemical properties. The three-dimensional structures of GP and AT-101 were downloaded from Pubchem database as “sdf” format and converted to PDB format. Autodock Vina software was utilized to remove water molecules and adjust the load distribution. By following these steps, the ligand structure is prepared in a suitable form for molecular docking simulations. Proper ligand preparation ensures that the ligand's chemical properties are accurately represented and facilitates the exploration of ligand-receptor interactions, binding modes, and affinity predictions during the docking process.

## 2.3.Docking

High-throughput molecular docking was performed using Autodock Vina, a widely used software for predicting ligand-receptor interactions. The docking simulations were carried out to investigate the binding of GP or AT-101 to ACE2 receptor. To define the search space for docking, the grid center coordinates and dimensions of the grid box were set. For ACE2, the grid center was set at X=19.81, Y=-5.57, and Z=14.73, with the same grid box dimension. These parameters were determined after careful calibration and optimization.

By utilizing the standardized grid box size and other docking parameters, consistent conditions were maintained for the docking experiments with GP and AT-101. The Autodock Vina software performed an exhaustive sampling of the ligand conformational space within the defined search space, generating a range of possible ligand-receptor binding conformations.

To gain insights into the molecular interactions, the resulting docked conformations were analyzed and visualized using PyMOL software. The docking approach employed in this study

enables the exploration of ligand-receptor interactions at the atomic level, providing valuable information for understanding the potential interactions between GP derivatives and ACE2.

## 2.4.Molecular dynamics (MD) simulations

The docked ligand targets were merged in Discovery Studio Visualizer (DSV) software as a complex. The system was configured to simulate water TIP4P in a 10 Å orthorhombic box. The docked complex, comprising merged ligand targets, was neutralized by the automatic addition of ions calculated by DSV software. Subsequently, the simulation was equilibrated for 1 ns, with trajectory recording at 4.2 ps intervals, using the NPT ensemble class and a temperature of 310 K. The parameters obtained for analysis included root mean square displacement (RMSD) and root mean square fluctuation (RMSF). Docking results were also verified via DSV software.

## 3. Results and Discussion

The process of testing the pharmacokinetic and pharmacodynamic properties of components for the discovery or design of new drugs is a time-consuming endeavor spanning several years. However, well-established ingredients that have undergone extensive research and development over time possess clearly defined profiles, thereby reducing the need for prolonged preclinical studies [23]. These properties render them highly promising candidates for novel applications.

In recent times, the advent of *in silico* studies, which involve computational methods and simulations, has opened up new possibilities for investigating SARS-CoV-2. Notably, the elucidation of the crystal structure of ACE2 (the cellular receptor for the virus) has provided a valuable perspective for theoretical exploration and analysis of the virus [24]. *In silico* studies have been instrumental in studying the interactions between potential drug candidates and viral targets, aiding in the identification and optimization of compounds with therapeutic potential against SARS-CoV-2 [25]. These computational approaches enable the rapid screening and evaluation of large libraries of

molecules, accelerating the drug discovery process and offering valuable insights for the design of new treatments [26, 27].

Natural products, such as those derived from plants, have historically been a source of potential drugs. They often contain diverse chemical compounds that may exhibit biological activities [28]. Some natural products, such as certain plant extracts or herbal remedies, have been investigated for their antiviral properties in general [29, 30], but their effectiveness against COVID-19 specifically is still being studied. It's worth mentioning that while natural products may have potential therapeutic properties, rigorous scientific investigation, including clinical trials, is necessary to establish their safety and efficacy for COVID-19 treatment.

The findings highlight the diverse capabilities of numerous medicinal plants in employing a multimodal approach, encompassing anti-viral effects for the management of COVID-19 [31]. Previous studies have reported the potential virucidal effects of GP against the influenza virus, indicating that extracts derived from *Gossypium* leaves demonstrated inhibitory effects on viral adsorption and replication within host cells [32, 33]. Although there are many herbs with reported anti-viral effects, and GP and AT-101 (Figure 1) show a wide range of biological effects, there is no information about their potential anti-COVID effects.

The biological properties of a drug molecule at a specific therapeutic target receptor are shaped by its spatial structure. This structure, influenced by the connectivity of the constituent atoms, determines the molecule's geometry. When this spatial arrangement introduces asymmetry, the molecule exhibits optical activity, resulting in the existence of enantiomeric pairs. It is known that enantiomers have different binding pockets due to their different conformations, thus exhibiting differences in binding energies, leading to different conformations within chiral selective structures.

**Table 1.** Interaction of the ACE2 receptor with GP or AT-101

Protein name	Docking Score (Binding Energy, Kcal/mol)	H Bond	Amino acid Residue
AT-101/ACE2	-118.086	-13.425	Tyr199, Lys187, Asp 509, Trp203, Ser511, Ala99, Leu100, Ser77, Leu73, Gln102, Asn103
Gossypol/ACE2	-96.996	-23.605	Asp382, Glu375, Ala348, Glu402, Asn397, His401, Phe400, Glu398, Gly395, Asp206

Molecular docking studies could identify highly active compounds, based on binding energy scores. The compounds with the lowest binding energy of the docking scores are usually the most effective in inhibiting the target receptor because lower binding energy equates to higher binding affinity [34].

Amino acid residues, H bond, and docking scores corresponding to the binding energies of the screened compounds with ACE2 are presented in Table 1. Each of the compounds effectively docked with ACE2 receptor (Figure 2). Both of them had negative ACE2 binding energy values, indicating positive interactions with the ACE2 active sites. The binding energy of the GP was -96.996 indicating a good binding affinity. Active site residues were Glu375, Ala348, Asn397, His401, Phe400, Gly395, Asp206 (Figure 3A). AT-101 had the impressive binding energy value, which was -118.086 kcal/mol showing effectively docked against ACE2. It established steric contacts with Trp203, Ser77, Gln102, Asn103, hydrogen interactions with Tyr199, Lys187, Asp509, Ser511, Ala99,



Ser77, Leu73 (Figure 3B). It also formed steric interactions with Ala348, Glu402, Asn397, His401.

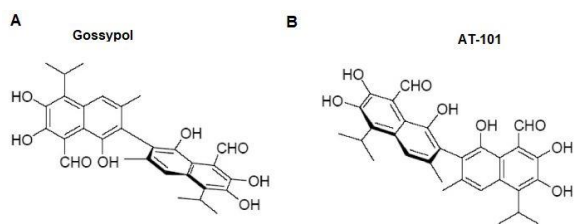


**Figure 1.** Chemical structures of (A) GP and (B) AT-101

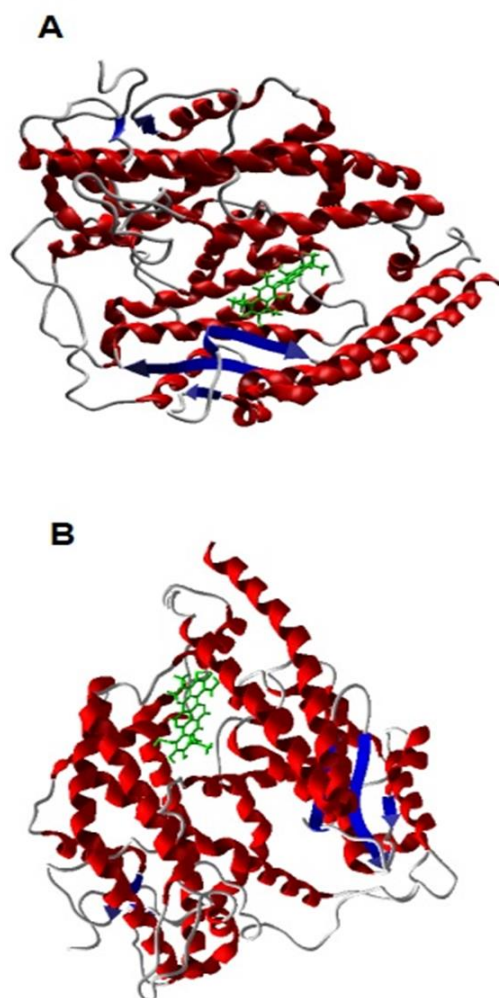


**Figure 2.** Molecular docking of ACE2 receptor with (A) GP and (B) AT-101

The results clearly show that AT-101 has better binding values. GP was described as an anti-HIV drug in 1989 [35], but no data on its effectiveness in any assays were provided. Novel GP compounds were created and their anti-HIV-1 and anti-H5N1 properties were tested *in vitro* [36]. The virus entrance stage of cell infection may be compromised by these novel GP

compounds describing them as a new type of antiviral agent. However, there is no study investigating the anti-viral effect of AT-101.

The stability of protein-ligand interactions relies on the presence of hydrogen bonds (H-bonds), which are intermolecular forces responsible for keeping two or more molecules bound together [37]. H-bond interactions were shown in Figure 3, Based on this analysis, GP has 7 H-bonds with ACE2 and AT-101 has 8 H-bonds with ACE2. The presence of six phenolic hydroxyl groups and two aldehydic groups makes GP chemically reactive. GP, due to the limited rotation of its internaphthyl bond, is classified as a chiral compound. The atropisomeric (-)-gossypol form of GP is AT-101 and formed more H-bonds than GP. Since the two molecules have different binding pockets, their binding affinities and therefore their activities were determined to be different from each other. As our findings are supported, many previous studies have shown that AT-101 is more active and effective than GP in biological systems. The critical role of the interaction between potential antiviral compounds and ACE2 in facilitating virus entry into host cells makes it an important target for therapeutic and vaccine development. Obtaining a comprehensive understanding of the intricate structure of this interaction offers valuable insights into the virus's mechanism of cell entry and potential strategies for prevention. However, further research is necessary to assess its long-term safety and effectiveness.

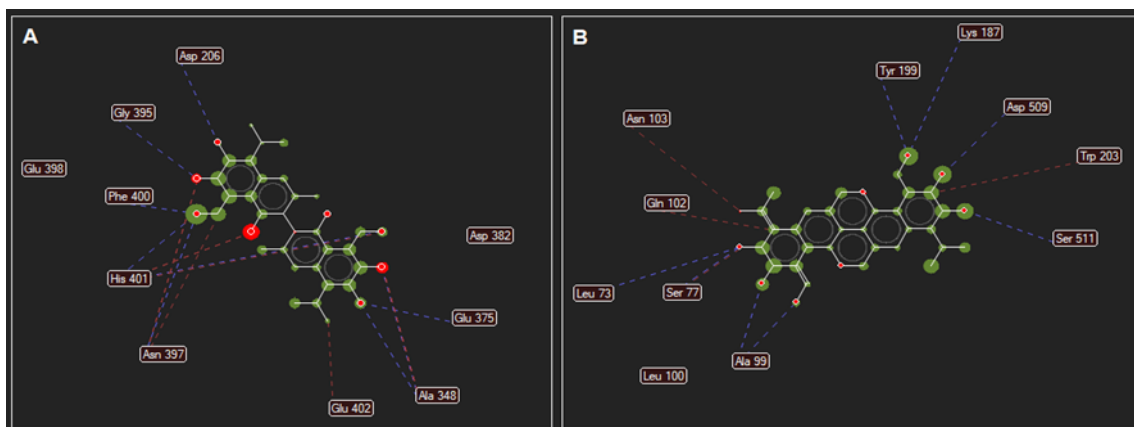


**Figure 3.** Molecular docking of ACE2 receptor and (A) GP or (B) AT-101 and interactions with key residues

The stability of the docked complex was evaluated by calculating the root mean square deviation (RMSD) of each trajectory record throughout 4.2 picoseconds during the 1.0 nanosecond MD simulation, with respect to the initial position of the docked complex. The plot demonstrates that the RMSD values of GP (A) and AT-101 (B) have a steep increase due to the initial binding to the substrate in the period of approximately 0.01 ns (Figure 4). GP takes 0.2 ns and AT-101 takes 0.15 ns to reach a stabilized

conformation. To further confirm the stability of the protein-ligand complex, we also monitored the RMSF of specific residues involved in interactions. RMSF depends on the RMSD graph, where more fluctuations in the RMSF graph generally provide a less stable RMSD graph. An RMSF value exceeding 2.5 Å suggests instability in these particular sites. Based on the results, it is evident that AT-101 exhibits the lowest degree of fluctuation (Figure 5).

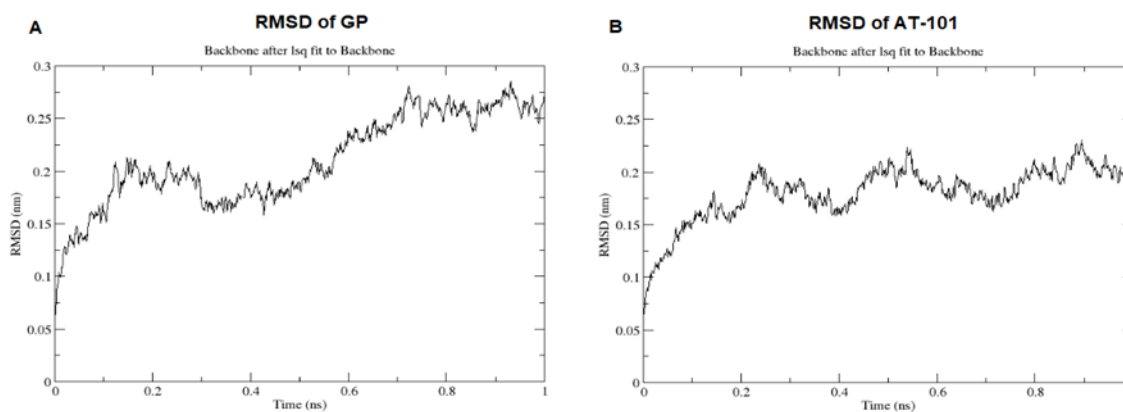


**Figure 4.** Root mean square deviation (RMSD) for a 1 ns period of MD simulation studies for (A) GP and (B) AT-101



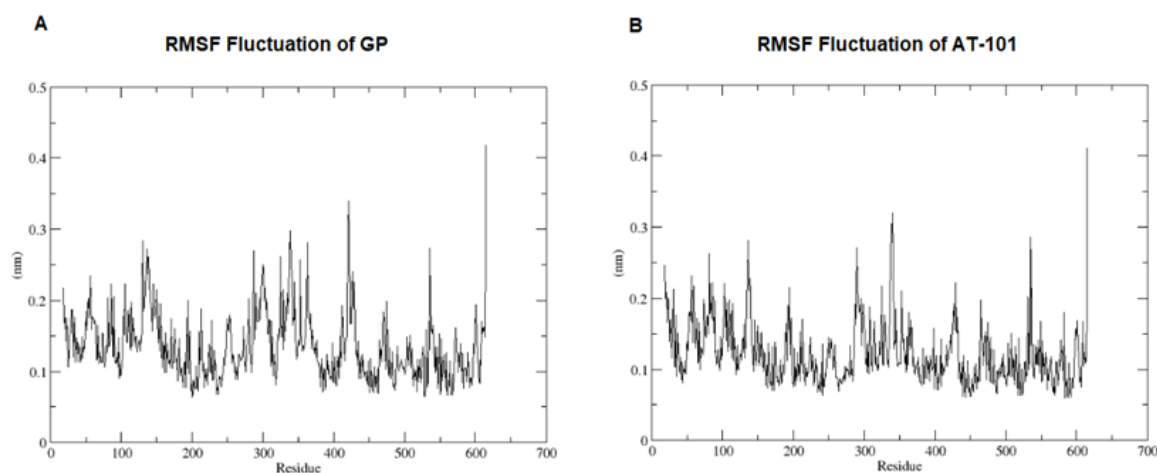


**Figure 5.** Root mean square fluctuation (RMSF) for (A) GP and (B) AT-101

Moreover, we have investigated the protein-ligand contact simulation results to verify docking scores. For GP, the dominant contribution to the interaction arises from the Asn397 residue where hydrogen bond and water bridge interactions collectively constitute an interaction fraction of 0.6 (equivalent to 60% of the total interaction). The other interactions are given by other residues that help the protein-ligand interaction His401 and Ala348 where the combination of H-bonds and water bridges with interaction fractions of approximately 0.5 and 0.65, respectively. For AT-101, Ala99 residue has the highest interaction overall, with an interaction value of 1.2, and the other contributing residues were Ser77 and Leu73.

#### 4. Conclusion

The anti-viral property of GP has been demonstrated *in silico* and confirmed *in vitro*. However, there are neither *in silico* nor *in vitro* anti-viral studies on AT-101. The anti-COVID effects of both GP derivatives are not available in the literature. In this study, the anti-COVID capacity of GP and AT-101 was demonstrated for the first time by *in silico* methods.

#### Article Information Form

##### **Funding**

The author (s) has no received any financial support for the research, authorship or publication of this study.

##### **Authors' Contribution**

The authors contributed equally to the study.

##### **The Declaration of Conflict of Interest/ Common Interest**

No conflict of interest or common interest has been declared by the authors.

##### **The Declaration of Ethics Committee Approval**

This study does not require ethics committee permission or any special permission.

##### **The Declaration of Research and Publication Ethics**

The authors of the paper declare that they comply with the scientific, ethical and quotation rules of SAUJS in all processes of the paper and that they do not make any falsification on the data collected. In addition, they declare that Sakarya University Journal of Science and its editorial board have no responsibility for any ethical violations that may be encountered, and that this study has not been evaluated in any academic publication environment other than Sakarya University Journal of Science.

##### **Copyright Statement**

Authors own the copyright of their work published in the journal and their work is published under the CC BY-NC 4.0 license.

#### References

- [1] D. Pal, P. Sahu, G. Sethi, C. E. Wallace, A. Bishayee, "Gossypol and Its Natural Derivatives: Multitargeted Phytochemicals as Potential Drug

- Candidates for Oncologic Diseases,” *Pharmaceutics*, vol. 14, no. 12. 2022.
- [2] J. A. Kenar, “Reaction chemistry of gossypol and its derivatives,” *JAACS, Journal of the American Oil Chemists’ Society*, vol. 83, no. 4. 2006.
- [3] I. C. N. Gadelha, N. B. S. Fonseca, S. C. S. Oloris, M. M. Melo, B. Soto-Blanco, “Gossypol toxicity from cottonseed products,” *Scientific World Journal*, vol. 2014. 2014.
- [4] I. Marzo J. Naval, “Bcl-2 family members as molecular targets in cancer therapy,” *Biochemical Pharmacology*, vol. 76, no. 8. 2008.
- [5] K. Balakrishnan, W. G. Wierda, M. J. Keating, V. Gandhi, “Gossypol, a BH3 mimetic, induces apoptosis in chronic lymphocytic leukemia cells,” *Blood*, vol. 112, no. 5, 2008.
- [6] D. Caylioglu, R. J. Meyer, D. Hellmold, C. Kubelt, M. Synowitz, J. Held-Feindt, “Effects of the anti-tumorigenic agent at101 on human glioblastoma cells in the microenvironmental glioma stem cell niche,” *International Journal of Molecular Science*, vol. 22, no. 7, 2021.
- [7] X. Pang, Wu, Y., Wu, Y., Lu, B., Chen, J., Wang, J., M., Liu, “(-)-Gossypol suppresses the growth of human prostate cancer xenografts via modulating VEGF signaling-mediated angiogenesis,” *Molecular Cancer Therapeutics*, vol. 10, no. 5, 2011.
- [8] M. P. Kline, Rajkumar, S. V., Timm, M. M., Kimlinger, T. K., Haug, J. L., Lust, J. A., S. Kumar, “R(-)-gossypol (AT-101) activates programmed cell death in multiple myeloma cells,” *Experimental Hematology*, vol. 36, no. 5, 2008.
- [9] J. A. Macoska, S. Adsule, K. Tantivejkul, S. Wang, K. J. Pienta, C. T. Lee, “(-)-Gossypol promotes the apoptosis of bladder cancer cells in vitro,” *Pharmacological research*, vol. 58, no. 5–6, 2008.
- [10] T. Ren Shan, J., Qing, Y., Qian, C., Li, Q., Lu, G., S. F., Zhou, “Sequential treatment with AT-101 enhances cisplatin chemosensitivity in human non-small cell lung cancer cells through inhibition of apurinic/aprimidinic endonuclease I-activated IL-6/STAT3 signaling pathway,” *Drug design, development and therapy*, vol. 8, 2014.
- [11] G. B. Patil, D. M. Borse, M. P. More, D. A. Patil, “Gossypol-Embedded Casein Nanoparticles for Potential Targeting of Ovarian Cancer: Formulation, Characterization, and Anticancer Activity,” *Journal of Pharmaceutical Innovation*, vol. 12, no.1, 2022.
- [12] O. Renner, Mayer, M., Leischner, C., Burkard, M., Berger, A., Lauer, U. M., S. C. Bischoff, “Systematic Review of Gossypol/AT-101 in Cancer Clinical Trials,” *Pharmaceutics*, vol. 15, no. 2, 2022.
- [13] L. Li, Li, Z., Wang, K., Zhao, S., Feng, J., Li, J., Q. Wang, “Design, synthesis, and biological activities of aromatic gossypol schiff base derivatives,” *Journal of agricultural and food chemistry*, vol. 62, no. 46, 2014.
- [14] J. Yang Chen, G., Li, L. L., Pan, W., Zhang, F., Yang, J., P. Tien, “Synthesis and anti-H5N1 activity of chiral gossypol derivatives and its analogs implicated by a viral entry blocking mechanism,” *Bioorganic and medicinal chemistry letters*, vol. 23, no. 9, 2013.
- [15] A. J. Lopez-Denman, A. Russo, K. M. Wagstaff, P. A. White, D. A. Jans, J. M. Mackenzie, “Nucleocytoplasmic shuttling of the West Nile virus RNA-dependent RNA polymerase NS5 is critical to infection,” *Cellular Microbiology*, vol. 20, no. 8, 2018.

- [16] S. C. Atkinson, Audsley, M. D., Lieu, K. G., Marsh, G. A., Thomas, D. R., Heaton, S. M., N. A., Borg, "Recognition by host nuclear transport proteins drives disorder-to-order transition in Hendra virus v," *Scientific Reports*, vol. 8, no. 1, 2018.
- [17] Y. Gao, Tai, W., Wang, X., Jiang, S., Debnath, A. K., Du, L., S. Chen, "A gossypol derivative effectively protects against Zika and dengue virus infection without toxicity," *BMC Biology*, vol. 20, no. 1, 2022.
- [18] W. Wang, Li, W., Wen, Z., Wang, C., Liu, W., Zhang, Y., Li, "Gossypol Broadly Inhibits Coronaviruses by Targeting RNA-Dependent RNA Polymerases," *Advanced Science*, vol. 9, no. 35, 2022.
- [19] Q. Wang, Zhang, Y., Wu, L., Niu, S., Song, C., Zhang, Z., J. Qi, "Structural and Functional Basis of SARS-CoV-2 Entry by Using Human ACE2," *Cell*, vol. 181, no. 4, 2020.
- [20] R. Wang, Zhang, Q., Ge, J., Ren, W., Zhang, R., Lan, J., Zhang, L. "Analysis of SARS-CoV-2 variant mutations reveals neutralization escape mechanisms and the ability to use ACE2 receptors from additional species," *Immunity*, vol. 54, no. 7, 2021.
- [21] E. Song, Zhang, C., Israelow, B., Lu-Culligan, A., Prado, A. V., Skriabine, S., A., Iwasaki, "Neuroinvasion of SARS-CoV-2 in human and mouse brain," *Journal of Experimental Medicine*, vol. 218, no. 3, 2021.
- [22] C. G. K. Ziegler, Allon, S. J., Nyquist, S. K., Mbano, I. M., Miao, V. N., Tzouanas, C. N., K. Zhang, "SARS-CoV-2 Receptor ACE2 Is an Interferon-Stimulated Gene in Human Airway Epithelial Cells and Is Detected in Specific Cell Subsets across Tissues," *Cell*, vol. 181, no. 5, 2020.
- [23] A. Basu, A. Sarkar, U. Maulik, "Molecular docking study of potential phytochemicals and their effects on the complex of SARS-CoV2 spike protein and human ACE2," *Scientific Reports*, vol. 10, no. 1, 2020.
- [24] Z. Jin, Du, X., Xu, Y., Deng, Y., Liu, M., Zhao, Y., H. Yang, "Structure of Mpro from SARS-CoV-2 and discovery of its inhibitors," *Nature*, vol. 582, no. 7811, 2020.
- [25] A. G. Junior, S. E. L. Tolouei, F. A. dos Reis Lívero, F. Gasparotto, T. Boeing, and P. de Souza, "Natural Agents Modulating ACE-2: A Review of Compounds with Potential against SARS-CoV-2 Infections," *Current Pharmaceutical Design*, vol. 27, no. 13, 2021.
- [26] S. Barage, Karthic, A., Bavi, R., Desai, N., Kumar, R., Kumar, V., K. W., Lee, "Identification and characterization of novel RdRp and Nsp15 inhibitors for SARS-COV2 using computational approach," *Journal of Biomolecular Structure and Dynamics*, vol. 40, no. 6, 2022.
- [27] J. O. Ogidigo, E. A. Iwuchukwu, C. U. Ibeji, O. Okpalefe, M. E. S. Soliman, "Natural phyto, compounds as possible noncovalent inhibitors against SARS-CoV2 protease: computational approach," *Journal of Biomolecular Structure and Dynamics*, vol. 40, no. 5, 2022.
- [28] F. Zhu, Qin, C., Tao, L., Liu, X., Shi, Z., Ma, X., Y. Chen, "Clustered patterns of species origins of nature-derived drugs and clues for future bioprospecting," *Proceedings of the National Academy of Sciences*, vol. 108, no. 31, 2011.
- [29] V. S. L. Goh, C. K. Mok, J. J. H. Chu, "Antiviral natural products for arbovirus infections," *Molecules*, vol. 25, no. 12, 2020.
- [30] M. F. Montenegro-Landívar, Tapiá-Quirós, P., Vecino, X., Reig, M., Valderrama, C., Granados, M., J. Saurina, "Polyphenols and their potential role to fight viral diseases: An overview," *Science of the Total Environment*, vol. 801, 2021.

- [31] X. Y. Lim, B. P. Teh, T. Y. C. Tan, "Medicinal Plants in COVID-19: Potential and Limitations," *Frontiers in pharmacology*, vol. 12, 2021.
- [32] L. Li, Z. Li, K. Wang, Y. Liu, Y. Li, Q. Wang, "Synthesis and antiviral, insecticidal, and fungicidal activities of gossypol derivatives containing alkyimine, oxime or hydrazine moiety," *Bioorganic Medicinal Chemistry*, vol. 24, no. 3, 2016.
- [33] L. F. de Lima, J. O. de Oliveira, J. N. P. Carneiro, C. N. F. Lima, H. D. M. Coutinho, M. F. B. Morais-Braga, "Ethnobotanical and antimicrobial activities of the *Gossypium* (Cotton) genus: A review," *Journal of Ethnopharmacology*, vol. 279, 2021.
- [34] L. Simon, A. Imane, K. K. Srinivasan, L. Pathak, I. Daoud, "In Silico Drug-Designing Studies on Flavanoids as Anticancer Agents: Pharmacophore Mapping, Molecular Docking, and Monte Carlo Method-Based QSAR Modeling," *Interdisciplinary Sciences: Computational Life Sciences*, vol. 9, no. 3, 2017.
- [35] T. S. Lin, Schinazi, R., Griffith, B. P., August, E. M., Eriksson, B. F., Zheng, D. K., W. H. Prusoff, "Selective inhibition of human immunodeficiency virus type 1 replication by the (-) but not the (+) enantiomer of gossypol," *Antimicrobial agents and chemotherapy*, vol. 33, no. 12, 1989.
- [36] Y. Liu, L. Wang, L. Zhao, Y. Zhang, "Structure, properties of gossypol and its derivatives from physiological activities to drug discovery and drug design," *Natural Product Reports*, vol. 39, no. 6, 2022.
- [37] S. A. Gouhar Z. A. Elshahid, "Molecular docking and simulation studies of synthetic protease inhibitors against COVID-19: a computational study," *Journal of Biomolecular Structure and Dynamics*, vol. 40, no. 24, 2022.

## The Effect of Peptizing Agent Concentration on Processing and Properties of Alumina Based Catalyst Support

Servet Turan<sup>1\*</sup> , Irmak Su Ökten<sup>1</sup> , Cem Açıkşarı<sup>2</sup> , Serdar Çelebi<sup>2</sup> , Umut Savacı<sup>1</sup> , Erhan Ayas<sup>1</sup> 

<sup>1</sup> Eskişehir Technical University, Department of Materials Science and Engineering, Eskişehir, Türkiye, [irmaksuokten@ogr.eskisehir.edu.tr](mailto:irmaksuokten@ogr.eskisehir.edu.tr), [umutsavaci@eskisehir.edu.tr](mailto:umutsavaci@eskisehir.edu.tr), [erayas@eskisehir.edu.tr](mailto:erayas@eskisehir.edu.tr), [sturan@eskisehir.edu.tr](mailto:sturan@eskisehir.edu.tr)

<sup>2</sup> Türkiye Turkish Petroleum Refineries Co. (TUPRAS) R&D Center, Kocaeli, Türkiye, [cem.aciksari@tupras.com.tr](mailto:cem.aciksari@tupras.com.tr), [serdar.celebi@tupras.com.tr](mailto:serdar.celebi@tupras.com.tr)

\*Corresponding Author

### ARTICLE INFO

### ABSTRACT

#### Keywords:

Catalyst Support  
Gamma Alumina  
Peptizing  
Extrusion



#### Article History:

Received: 06.07.2023

Accepted: 23.12.2023

Online Available: 22.04.2024

Gamma alumina ( $\gamma$ -Al<sub>2</sub>O<sub>3</sub>) has drawn attention as a support material for heterogeneous catalysts extensively used in the oil and gas industry due to its superior properties. Boehmite (AlOOH) is an industrially accepted and well-known precursor to produce gamma alumina-based support. The process additions such as nitric acid (HNO<sub>3</sub>) are commonly used in shaping process of alumina to control textural, mechanical and structural properties of final catalyst support. In this work, gamma alumina precursor boehmite was peptized by nitric acid at molar ratio of HNO<sub>3</sub>/AlOOH ranging from 0 to 0.054. With addition of nitric acid, extrusion paste showed higher plasticity up to 0.017 mole of HNO<sub>3</sub>/AlOOH. The addition of more than this point led to an inhomogeneity of extrusion paste caused by hard and brittle structure caused by the formation of aluminum nitrate salts. Also, higher mechanical strength was observed for samples peptized with lower nitric acid concentration because of effective deagglomeration by peptization. The pore size of catalyst support pellets increased up to an acid/ boehmite molar ratio of 0.017 by peptizing of boehmite. However, beyond this point pore size decreased due to dissolution of boehmite.

## 1. Introduction

In modern industry, more than 90% of processes are catalytic [1]. Many important processes require heterogeneous catalysts in which the reactant phase and catalyst phases are different. Heterogeneous catalysts are among the main solutions for sustainable industrial applications [2]. Catalysts basically consist of two parts: a support material and micro or nano-sized active metals positioned on this support material [3]. The primary function of the catalyst support material is to create a surface to site to the active metal parts and to increase the area of the active parts [4]. Among all the catalyst support materials,  $\gamma$ -Al<sub>2</sub>O<sub>3</sub> is in the class of transition alumina and is widely used in the oil and gas industry thanks to its superior properties such as

cheapness and abundance, chemical and mechanical inertness, and controllable acid-base characteristics [5]. Boehmite (AlOOH) is an important precursor for the preparation of  $\gamma$ -Al<sub>2</sub>O<sub>3</sub> catalysts because the heat treatment of boehmite produces a series of transition alumina from  $\gamma$ -Al<sub>2</sub>O<sub>3</sub> and  $\eta$ -Al<sub>2</sub>O<sub>3</sub> to  $\delta$ -Al<sub>2</sub>O<sub>3</sub>, and  $\theta$ -Al<sub>2</sub>O<sub>3</sub>, which exhibit high surface areas (200–500 m<sup>2</sup>/g) [6]. Thus, boehmite is the most frequently used precursor to  $\gamma$ -Al<sub>2</sub>O<sub>3</sub> support. Understanding and optimizing the properties of the support material is crucial for current and future studies and one of the ways to improve the final performance of the catalyst is to improve the properties of the support material. One of the most important factors for optimizing the catalyst material is the shape of the catalyst. The shape of the catalyst has a great influence on the process



(flow regime, pressure drop, etc.) and performance [7]. Extrusion is the most widely used shaping technique for forming fixed bed catalytic support materials [8].

To achieve extrusion successfully, process additions influence the extrusion process and final product properties [9]. One of these process additives is the peptizing agent in alumina systems and is necessary to prevent agglomeration of powders by dispersion of boehmite [10]. Boehmite particles used as starting material of  $\gamma$ -Al<sub>2</sub>O<sub>3</sub> support are usually supplied in agglomerated form. The agglomerated particles provide easier and cleaner handling, a more manageable production environment, and improved storage qualities. However, it is necessary to break agglomerates to shape and tune the properties of catalyst. Alumina based catalysts are commonly formed by peptization of boehmite agglomerates by dilute monoprotic acids (e.g., HNO<sub>3</sub>) [11].

The acid as peptizing agent helps break agglomerates into smaller particles as much as possible. This leads to favorable extrusion by improving the plastic behavior of the paste [12, 13]. Although several patents and publications deal with extrusion of alumina with nitric acid as a peptizing agent, this detailed study based on the effect of wide range of HNO<sub>3</sub> concentration on the final properties of  $\gamma$ -Al<sub>2</sub>O<sub>3</sub> that is used as a catalyst support in oil& gas refinery [14, 15].  $\gamma$ -Al<sub>2</sub>O<sub>3</sub> catalysts are also shaped to optimize mechanical requirements and peptizing agents help to increase to a certain point [16, 17]. Furthermore, design of tailored textural properties (surface area, pore size and pore distribution) requires a good knowledge of the effect of the peptization process [18].

The detailed analyses were related to the deagglomeration phenomena of boehmite particles by using nitric acid solution. The aim of this work was to investigate the effect of a wide range of peptizing agent concentration on extrudability and properties of  $\gamma$ -Al<sub>2</sub>O<sub>3</sub> catalyst support.

## 2. Methods

### 2.1. Materials

Boehmite powder (Sasol GmbH, Germany) having BET surface area of 280 m<sup>2</sup>/g and the average particle size of 40  $\mu$ m, nitric acid (HNO<sub>3</sub>,  $\geq$  65%, Sigma-Aldrich) as peptizing agent and deionized water were used in the present investigation.

### 2.2. Catalyst support shaping

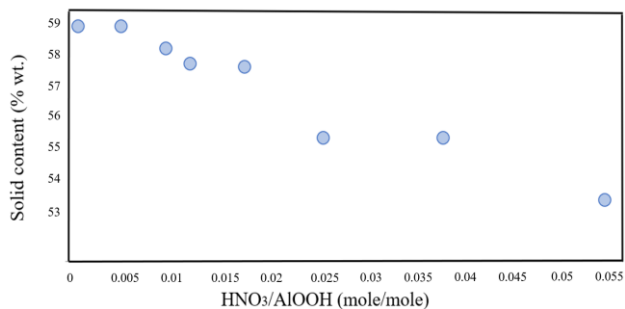
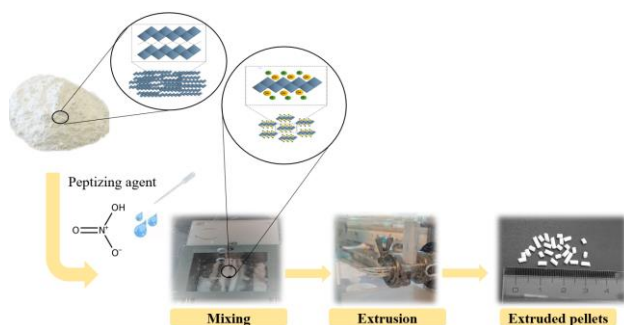
Catalyst support pellet for the extrusion was carried out by the following procedure. First, boehmite powder was mixed with optimum amount of nitric acid at various concentrations and only deionized water until having a homogeneous mixture prior to extrusion for 16 min at 40 rpm by means of a mixer (Caleva Multi Lab, UK) with Z-shaped mixing arm. The nitric acid with different concentrations was added slowly to the boehmite particles to obtain a plastic dough for extrusion. The molar concentrations of nitric acid and its corresponding HNO<sub>3</sub>/ AlOOH by mole and HNO<sub>3</sub>/ total composition by wt. were calculated and given in Table 1. The solid content for each batch was adjusted to the level resulting in the highest torque.

The solid content by wt. percent for each batch was given in Figure 1. The optimum solid content decreased with increasing HNO<sub>3</sub> concentration due to effect of gelation caused by the deagglomeration of boehmite particles. Then, paste was transferred to a single screw extruder (Caleva Multi Lab, UK) for shaping through a 2 mm diameter die at an extrusion speed of 30 rpm. The green extrudates were dried at 80 °C for overnight in an oven and cut into the length of 2-4 mm sized pellets. Schematic flow chart for pellet preparation was summarized in Figure 2. After, they fed into the the box furnace where they were calcined at 600 °C for 5 h with a heating rate of 3 °C/ min to obtain gamma alumina.



**Table 1.** HNO<sub>3</sub>/ AlOOH and HNO<sub>3</sub>/ total composition by wt. of various HNO<sub>3</sub> molar concentrations

Molar concentration of HNO <sub>3</sub> solution (M)	HNO <sub>3</sub> / AlOOH (mole/mole)	HNO <sub>3</sub> / total composition (% wt.)
0.00	0.000	0.00
0.10	0.004	0.44
0.20	0.009	0.90
0.25	0.011	1.14
0.37	0.017	1.69
0.50	0.025	2.47
0.75	0.037	3.63
1.00	0.054	5.15

**Figure 1.** The solid content (wt. %) versus HNO<sub>3</sub>/AlOOH (mole/mole) of each batch**Figure 2.** Schematic flow chart for pellet preparation by extrusion of the dough consisting of boehmite and nitric acid

### 2.3. Characterization

Rheological characterization of the paste was determined by using a mixer torque rheometer-MTR (Caleva, MTR-3, UK). The optimum solid content of mixture and mix time of paste for extrusion were analyzed for each batch.

The morphology of as-received boehmite particles was carried out via scanning electron

microscopy (SEM- Zeiss Supra 50VP, Germany).

The thermal behavior of the green extrudates was conducted on a thermogravimetric analyzer (Perkin-Elmer, TGA 4000, USA) at a heating rate of 5 °C/min under air atmosphere.

The crystal phases of boehmite powder and the extrudates were determined at  $2\theta = 10^\circ - 80^\circ$  with a scanning speed of 1°/min by using an X-Ray diffractometer (XRD- Bruker, D8 Advance, Germany) with Cu K $\alpha$  X-ray source.

The strength of extrudates was determined by crushing test method (VINCI Technologies, France). Single pellet strength was determined by uniaxial compression between two parallel rigid platens. The diameter of every pellet was measured with a caliper before the pellet was placed on the bottom plate of a press. The crushing strength is calculated by dividing the maximum recorded load by diameter. At least 25 pellets are tested and then all tested samples are averaged and calculated standard deviation.

Brunauer-Emmett-Teller- BET (Micromeritics, ASAP 2020, USA) gas sorption measurement was performed to investigate the specific surface area and porous structure of the extrudates. After 6 hours of degassing at 300 °C, multi-point BET analysis was performed based on the N<sub>2</sub> gas adsorption technique in a liquid N<sub>2</sub> at 77.3 K. The pore size distribution and pore diameters were obtained by a Barrett-Joyner-Halenda- BJH model from the desorption branches of the isotherms.

## 3. Results and Discussion

### 3.1. Identification of the starting powder

The boehmite powder was used as precursor; its properties were summarized in Table 2. It is a member of the alumina hydrate family and was supplied as a spray-dried particle. The final crystalline phase and physical properties of calcined gamma alumina depend on the initial crystalline properties of the starting precursor as well as the calcination temperature [19]. Boehmite transforms into  $\gamma$ -Al<sub>2</sub>O<sub>3</sub> transition alumina under a temperature range of 450–650 °C with a departure of structural water [20]. The

sequence of phase transitions was given in Figure 3 [21].

**Table 2.** Properties of Boehmite- $\text{AlOOH}$  powder

Properties	Boehmite powder
$\text{Al}_2\text{O}_3$ (wt. %)	74
$\text{Na}_2\text{O}$ (wt. %)	0.002
Particle size $d_{10}$ ( $\mu\text{m}$ )	10
Particle size $d_{50}$ ( $\mu\text{m}$ )	40
Particle size $d_{90}$ ( $\mu\text{m}$ )	85
Packed bulk density (g/l)	800-1100
Surface area (BET) ( $\text{m}^2/\text{g}$ )	280
Pore volume (BET) ( $\text{cm}^3/\text{g}$ )	0.43
Pore diameter (BET) (nm)	5
Crystallite size (120)* (nm)	5
Loss on ignition (LOI) (wt. %)	26

\*The size is calculated by Scherrer equation for (120) plane

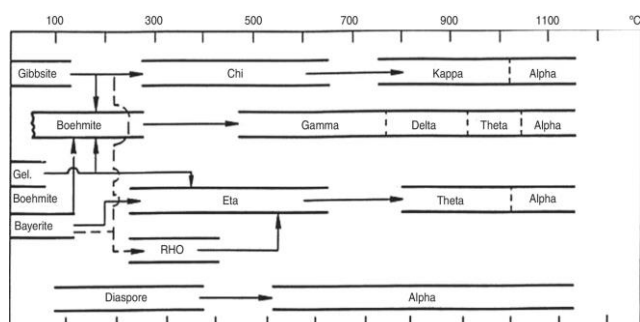


**Figure 3.** Transformation sequences of precursors to  $\alpha\text{-Al}_2\text{O}_3$

The variation of zeta potential of boehmite vs pH in aqueous media was demonstrated in Figure 4 [22]. As it can be seen, the zeta potential and repulsive force between the boehmite particles are high at  $\text{pH} < 8$  due to surface charge effect. Furthermore, stable region in acidic zone is wider than basic. This is the reason for both nitric acid and water are able to peptize the boehmite particles.

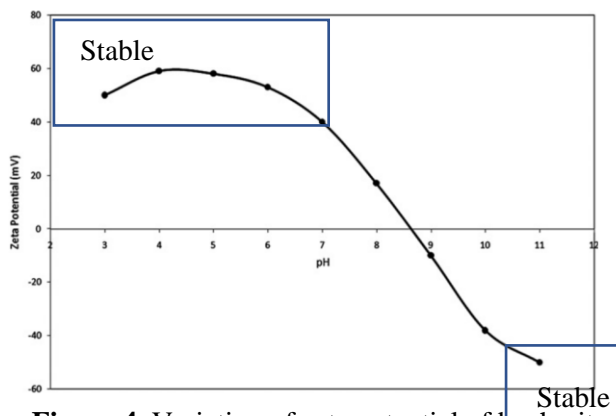


**Figure 4.** Variation of zeta potential of boehmite versus pH in aqueous media

As already mentioned, supplied boehmite is a spray-dried and the presence of large particles and agglomerates were detected by using SEM images in Figure 5.

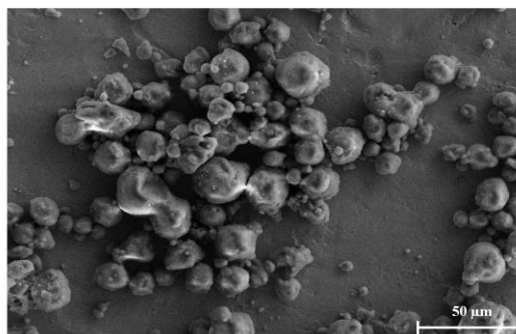


**Figure 5.** SEM images of as received boehmite

### 3.2. Rheological characterization

Mixer torque rheometer (MTR) has been widely used to determine the optimum amount of liquid in formulations intended for extrusion and spheronisation [23]. MTR was used to characterize the rheological properties of batches containing varying amounts of  $\text{HNO}_3$  and water. The result of mean line torque (Nm) vs binder ratio (ml/g) of the boehmite powder peptized with only water was given in Figure 6. According to Figure 6., 40 rpm mixing rate was chosen for extrusion for all mixtures due to its highest torque value. Also, optimum binder ratio 0.533 ml/g was used while solid content of mixtures was studied.

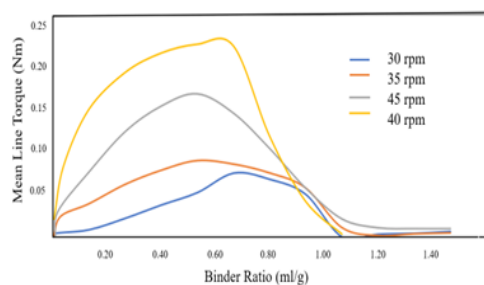


**Figure 6.** The mean line torque (Nm) versus binder ratio (ml/g) of the boehmite powder peptized with only water

The effect of peptizing agent concentrations on torque of wet mixtures was given in Figure 7. It results in the maximum torque value increased with increased peptizing agent molar ratio. However, the mixtures were not favorable after a certain point for extrusion. In Figure 7, the mixture below was favorable for extrusion and the mixture above was not. Although the torque was high, extrudability of the mixture was quite low at high concentrations of acid.

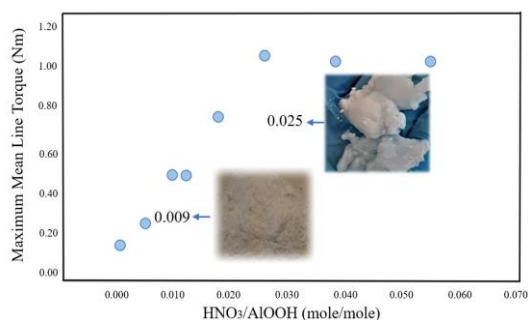


**Figure 7.** The maximum mean line torque (Nm) versus  $\text{HNO}_3/\text{AlOOH}$  (mol/mol) values of each batch

The  $\text{HNO}_3/\text{AlOOH}$  ratio is critical for extrusion of alumina. If the extrusion paste does not have sufficient consistency, the shape of extrudates differs. The extrudates stuck with each other at low ratios of the  $\text{HNO}_3/\text{AlOOH}$  and they were very glassy and brittle at high ratios of the  $\text{HNO}_3/\text{AlOOH}$ . The pictures of stuck, ideal, glassy extrudates were given in Figure 8.



**Figure 8.** Images of the extrudates peptized with (a) 0  $\text{HNO}_3/\text{AlOOH}$ , (b) 0.017  $\text{HNO}_3/\text{AlOOH}$ , (c) 0.054  $\text{HNO}_3/\text{AlOOH}$  molar ratios

### 3.3. Thermal analysis

TG graph of shaped green sample peptized with various  $\text{HNO}_3/\text{AlOOH}$  molar ratio was seen in Figure 9. The all green extrudates showed similar thermal behavior. The large mass change corresponds to the conversion step from boehmite to  $\gamma$ -alumina, and it is also attributed to the removal of chemically adsorbed water from the structure. In the last step, although no thermal event occurs for mixture. There is a continuous mass loss starting at about 600 °C. Here, residual hydroxyls are removed from the structure and the mass loss is 1.85 wt. % [7]. Although the amount of the acid concentration increases, it is not observed a significant change in the temperature of boehmite to gamma alumina transition. However, it is stated in the literature that high amount of nitric acid leads to the formation of basic aluminum salts between primary particles of boehmite [24, 25]. Consequently, the weight loss in TGA analysis corresponds to the removal of as formed aluminum salts at the samples that were prepared by adding a higher amount of  $\text{HNO}_3$ .

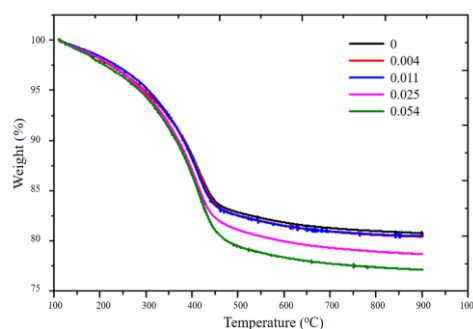


**Figure 9.** TG graph of the green sample peptized with various  $\text{HNO}_3/\text{AlOOH}$  molar ratios

### 3.4. XRD analysis

XRD graph of boehmite powder not peptized at room temperature and after peptization with  $\text{HNO}_3/\text{AlOOH}$  ratio and calcined at 600 °C was given in Figure 10. It was seen that the obtained diffraction pattern for boehmite powder at room temperature belongs to regular orthorhombic boehmite (JCPDS file of 21–1307). After calcination at 600 °C for 5 h, all green extrudates transformed to gamma alumina phase. Gamma alumina crystals have been conventionally described as a defect spinel (cubic spinel

structure with presence of tetragonal distortion along one of the axes of the spinel cell) (JCPDS file of 10-0425) [6]. According to the literature, it is known that a significant change in crystallite shape and size cannot be made with the addition of acid, but only in their spatial arrangement [15]. This is in agreement with XRD results showing that there were no significant changes in characteristic peaks of gamma alumina which produce at different nitric acid concentrations.

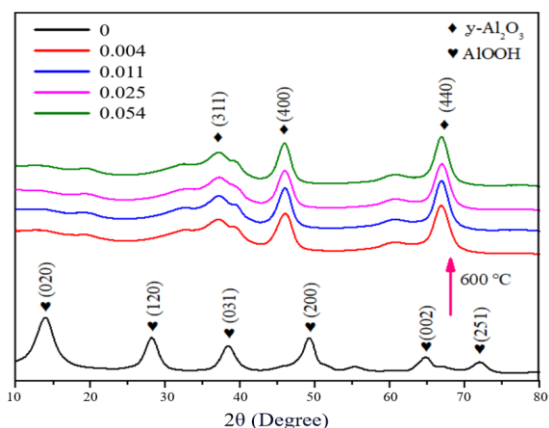


**Figure 10.** XRD patterns of boehmite powder not peptized at room temperature and after peptization with HNO<sub>3</sub>/ AIOOH ratio and calcined at 600 °C

### 3.5. SEM images

Secondary scanning electron microscopy images (showed in Figure 11) were taken from the cross-section of extrudates supports produced by 0.00, 0.017 and 0.054 HNO<sub>3</sub>/AIOOH mole ratio and calcined at 600 °C in air atmosphere. A large agglomerate of Alumina particles in micron size was seen in Figure 11a due to the absence of peptizing agent. In Figure 11b, it was seen that increase in acid content leads to a breaking of boehmite agglomerates by chemical attack. A denser packing microstructure is clearly observed on a sample prepared with 0.054 HNO<sub>3</sub>/AIOOH mole ratio. This result is also in good agreement with the pore size distribution results calculated from N<sub>2</sub> adsorption/desorption isotherm in Table 3. It can be explained by the peptization process involving a partial dissolution of boehmite particles starting from particle surface [24, 25].

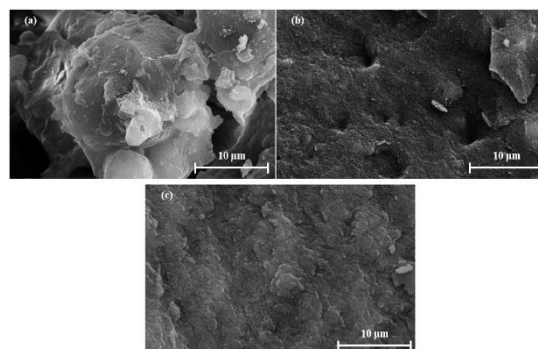


**Figure 11.** SEM images of calcined samples peptized with different HNO<sub>3</sub>/AIOOH (mole/mole) ratios: (a) 0; (b) 0.017; (c) 0.054

### 3.6. Mechanical properties

The graph of crushing strength versus HNO<sub>3</sub>/AIOOH (mole/mole) of the extrudates was given in Figure 12. The extrudates with highest strength were around 26 N/mm at the HNO<sub>3</sub>/AIOOH ratio of 0.009. It was followed by 25 N/mm at the HNO<sub>3</sub>/AIOOH ratio of 0.012 and 22 N/mm at 0.017. The peptization of boehmite by nitric acid up to 0.017 HNO<sub>3</sub>/AIOOH mole ratio, breaks down the coarse soft agglomerates of primary particles and increase plasticity of pastes, which enhances mechanical strength of the final catalyst support.

However, it is known that an excess amount of nitric acid leads to dissolution of primary pseudoboehmite particles more and resulting in low paste consistency during extrusion process [24]. Therefore, the nitric acid molar ratios greater than 0.017 were not found to be suitable due to having insufficient compression strength. Samples that were produced by HNO<sub>3</sub>/AIOOH molar ratios between 0.009 and 0.017 were a good stability and stiffness under mechanical loads for a high-performance catalyst support especially when compared to the samples that were peptized with the distilled water (10.78 N/mm) and highest amount of HNO<sub>3</sub> (6.54 N/mm).



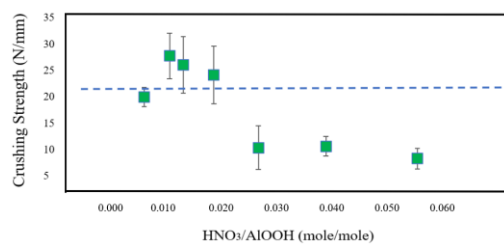


**Figure 12.** The crushing strength vs  $\text{HNO}_3/\text{AlOOH}$  (mole/mole) of the extrudates

### 3.7. Textural properties

The adsorption-desorption isotherms of extrudates peptized with different  $\text{HNO}_3/\text{AlOOH}$  molar ratios were given in Figure 13. The type IV hysteresis on the adsorption and desorption behavior of all samples peptized with different molar ratios confirmed the mesoporous structure.

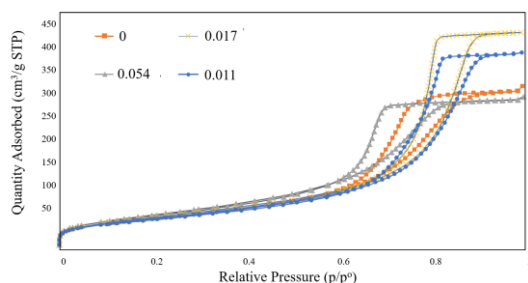


**Figure 13.** Nitrogen adsorption-desorption isotherm (Langmuir Type IV) of calcined samples peptized with various  $\text{HNO}_3/\text{AlOOH}$  (mole/mole) ratios

The pore diameter ( $\text{\AA}$ ) and pore volume ( $\text{cm}^3/\text{g}$ ) of extrudates versus  $\text{HNO}_3/\text{AlOOH}$  (mole/mole) was presented in Figure 14. According to the figure, with increasing molar ratio  $\text{HNO}_3/\text{AlOOH}$  up to 0.017, pore diameter and pore volume increased due to peptizing effect. Then, they decreased dramatically when acid/alumina ratio of extrudates exceeded 0.017. For calcined samples prepared with relatively higher nitric acid content ( $\text{HNO}_3/\text{AlOOH} = 0.025, 0.037$  and  $0.054$ ), the small pore diameter and pore volume are consistent with their corresponding close-packed morphology (Figure 11c) and partial dissolution of the initial aluminum hydroxide would lead to smaller porosity.

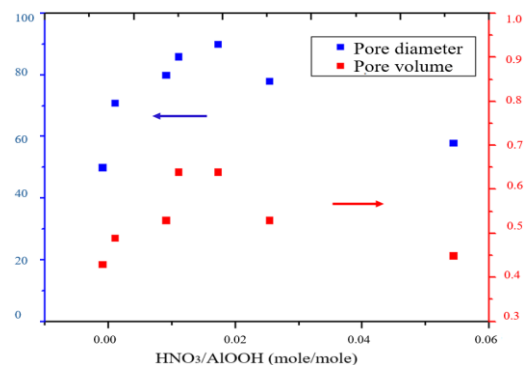


**Figure 14.** Pore diameter ( $\text{\AA}$ ) and pore volume ( $\text{cm}^3/\text{g}$ ) of extrudates versus  $\text{HNO}_3/\text{AlOOH}$  (mole/mole)

Pore size distribution of calcined samples peptized with different  $\text{HNO}_3/\text{AlOOH}$  (mole/mole) ratios were given in Figure 15. Even if the pore diameters change with nitric acid molarity, the pore size distribution of all prepared samples showed a uniform pore size in the range of 5–9 nm.

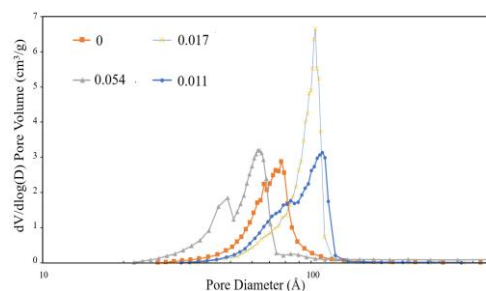


**Figure 15.** Pore size distribution of calcined samples peptized with various  $\text{HNO}_3/\text{AlOOH}$  (mole/mole) ratios

The textural properties of the extrudates at various  $\text{HNO}_3/\text{AlOOH}$  molar ratio were given in Table 3. BET surface area of as received boehmite exhibited the highest value. It was expected to reduce BET surface area value with the calcination process.

**Table 3.** Textural properties of the selected extrudates

HNO <sub>3</sub> / AlOOH (mole/mole)	BET surface Area, m <sup>2</sup> /g	Average Pore Diameter, Å	Total Pore Volume, cm <sup>3</sup> /g
Boehmite	280	50	0.43
0	217	71	0.49
0.009	216	80	0.53
0.011	215	86	0.58
0.017	220	90	0.64
0.025	220	78	0.53
0.054	240	58	0.45

#### 4. Conclusion

This study provided fundamental understanding of the effect of wide range of HNO<sub>3</sub> concentration where HNO<sub>3</sub> is used as a peptizing agent for boehmite deagglomeration, extrusion processing and properties of  $\gamma$ -Al<sub>2</sub>O<sub>3</sub> catalyst support.

Optimum nitric acid/ boehmite molar ratio range was determined as 0-0.017. The paste became glassy and heterogenous at higher molar ratios due to over-gelation. The solid content by weight decreased with increasing HNO<sub>3</sub> concentration for forming in extrusion. The crushing strength values were greater than 20 N/mm when nitric acid/boehmite molar ratio is in between 0.009-0.017. Pore size and pore volume of catalyst increased until 0.017 nitric acid/boehmite molar ratio and decreased after the point of 0.017.

#### Article Information Form

##### Acknowledgments

The authors would like to thank TUPRAS (Türkiye Petrol Rafinerileri A.Ş.) with a project number P1.20AP.03 for laboratory infrastructure.

##### Funding

The authors would like to thank TÜBİTAK (119C161- 2244 industrial Ph.D. program) for financial support.

##### Authors' Contribution

The authors contributed equally to the study.

##### The Declaration of Conflict of Interest/ Common Interest

No conflict of interest or common interest has been declared by the authors.

##### The Declaration of Ethics Committee Approval

This study does not require ethics committee permission or any special permission.

##### The Declaration of Research and Publication Ethics

The authors of the paper declare that they comply with the scientific, ethical and quotation rules of SAUJS in all processes of the paper and that they do not make any falsification on the data collected. In addition, they declare that Sakarya University Journal of Science and its editorial board have no responsibility for any ethical violations that may be encountered, and that this study has not been evaluated in any academic publication environment other than Sakarya University Journal of Science.

##### Copyright Statement

Authors own the copyright of their work published in the journal and their work is published under the CC BY-NC 4.0 license.

#### References

- [1] A. Glotov, E. Karakhanov, "Heterogeneous Catalysts for Petrochemical Synthesis and Oil Refining," *Catalysts*, vol. 11, no. 5, pp.602, 2021.
- [2] E. Vitz. (2022, Dec. 11). Heterogeneous Catalysis [Online]. Available: 18.12: Heterogeneous Catalysis- Chemistry LibreTexts
- [3] Y. Pan, X. Shen, L. Yao, A. Bentalib, Z. Peng, "Active sites in heterogeneous catalytic reaction on metal and metal oxide: theory and practice," *Catalysts*, vol. 8, no. 10, pp. 78, 2018.



- [4] A. Hagemeyer, A.F. Volpe, *Encyclopedia of Condensed Matter Physics*. Academic Press, 2005.
- [5] K. Y. Paranjpe, "Alpha, Beta and Gamma alumina as catalyst," *Pharma Innov*, vol. 6, no. 11, pp. 236-238, 2017.
- [6] P. Alphonse, M. Courty, "Structure and thermal behavior of nanocrystalline boehmite," *Thermochimica acta*, vol. 425, no. 1-2, pp. 75-89, 2005.
- [7] C. Kozicki, C. Carlson. (2022, Dec. 11). Why Agglomerate Powder? [Online]. Available: Why Agglomerate Powder? (feeco.com)
- [8] M. Al-Ani, M. Al-Dahhan, "Effect of catalyst shape on pressure drop and liquid holdup in a pilot plant trickle bed reactor," *Fuel*, vol. 284, pp. 118860, 2021.
- [9] K. P. de Jong, *Synthesis of solid catalysts*. John Wiley & Sons, 2009.
- [10] S. Devyatkov, N. V. Kuzichkin, D. Murzin, "On comprehensive understanding of catalyst shaping by Extrusion," *Chemistry Today*, vol. 33, no. 6, pp. 57-64, 2015
- [11] J. A. Schwarz, C. I. Contescu, *Surfaces of nanoparticles and porous materials*. CRC press, 1999.
- [12] M. Dronova, "Study of concentrated boehmite suspensions containing anisotropic colloidal particles: phase diagram, structure and rheology-Application to membrane separation processes," Ph.D. dissertation, Sorbonne Université, 2021.
- [13] N. van Garderen, F. J. Clemens, C. G. Aneziris, T. Graule, "Improved  $\gamma$ -alumina support based pseudo-boehmite shaped by micro-extrusion process for oxygen carrier support application," *Ceramics International*, vol. 38, no. 7, pp. 5481-5492, 2012.
- [14] G. T. Whiting, S. Chung, D. Stosic, A. D. Chowdhury, L. van der Wal, D. Fu, J. Zecevic, A. Travert, K. Houben, M. Baldus, B. M. Weckhuysen, "Multiscale mechanistic insights of shaped catalyst body formulations and their impact on catalytic properties," *ACS Catalysis*, vol. 9, no. 6, pp. 4792-4803, 2019.
- [15] W. C. Cheng, R. G. Donnelly, "Surfactants in acid-peptized catalyst compositions," U.S. Patent 4705767, November 10 1987.
- [16] K. W. Jun, Y. J. Lee, S. M. Kim, J. Y. Kim, "Method of preparing boehmite and gamma-alumina with high surface area," U. S. 11886367, September 5 2012.
- [17] F. Karouia, M. Boualleg, M. Digne, P. Alphonse, "The impact of nanocrystallite size and shape on phase transformation: Application to the boehmite/alumina transformation," *Advanced Powder Technology*, vol. 27, no. 4, pp. 1814-1820, 2016.
- [18] S. Lowell, J. E. Shields, *Powder Surface Area and Porosity: Second Edition*. Chapman and Hall, 1984.
- [19] J. M. Drouin, T. Chopin, P. Nortier, H. Van Damme, "Rheology and structure of peptized boehmite pastes," *Journal of colloid and interface science*, vol. 125, no. 1, pp. 314-326, 1988.
- [20] Sasol. (2022, Dec. 11). High Purity Aluminas [Online]. Available: <https://products.sasol.com/pic/products/home/categories/high-purity-aluminas/index.html>
- [21] S. Lamouri, M. Hamidouche, N. Bouaouadja, H. Belhouchet, V. Garnier, G. Fantozzi, J. F. Trelkat, "Control of the  $\gamma$ -alumina to  $\alpha$ -alumina phase transformation for an optimized alumina densification," *Boletín de la Sociedad Española de cerámica y vidrio*, vol. 56, no. 2, pp. 47-54, 2017.

- [22] K. Wefers, C. Misra, "Oxides and hydroxides of aluminum," Alcoa Technical Paper, no. 19, 1987.
- [23] L. Sharifi, M. Beyhaghi, T. Ebadzadeh, E. Ghasemi, "Microwave-assisted sol-gel synthesis of alpha alumina nanopowder and study of the rheological behavior," *Ceramics International*, vol. 39, no. 2, pp. 1227-1232, 2013.
- [24] Y. V. Vatutina, K. A. Nadeina, O. V. Klimov, M. O. Kazakov, I. G. Danilova, S. V. Cherepanova, A. S. Noskov, "Peptization of alumina by ammonia to adjust catalytic properties of NiMo/B-Al<sub>2</sub>O<sub>3</sub> hydrotreating catalysts," *Catalysis Today*, no. 375, pp. 377-392, 2021.
- [25] V. Y. Tregubenko, I. E. Udras, V. A. Drozdov, A. S. Belyi, "Effect of pseudoboehmite peptization by organic acids on texture characteristics of obtained aluminum oxides," *Russian journal of applied chemistry*, vol. 84, pp. 9-16, 2011.

## DFT Calculations, Molecular Docking, and Pharmacological Properties Investigation for 5-Benzoxazolecarboxylic Acid as a Target Anti-Cancer Agent

Ceyhun Küçük Zonguldak Bülent Ecevit University, Ahmet Erdogan Vocational School of Health Services, Zonguldak, Türkiye, [ceyhun.kucuk@beun.edu.tr](mailto:ceyhun.kucuk@beun.edu.tr)

### ARTICLE INFO

### ABSTRACT

#### Keywords:

5-benzoxazolecarboxylic Acid  
DFT  
Toxicity  
ELF  
Molecular Docking

#### Article History:

Received: 27.07.2023

Accepted: 28.12.2023

Online Available: 22.04.2024

In this study, the electronic properties of the 5-Benzoxazolecarboxylic acid molecule, a benzoxazole derivative, were calculated at the DFT/B3LYP/6-311++G(d,p) level of theory. Electronic properties and chemical reactivity of the optimized structure, such as Frontier molecular orbital (FMO), global and chemical reactivity descriptors, molecular electrostatic potential (MEP), and charge analyses (APT, Hirshfeld, and NBO), were investigated. Also, electronic properties are supported by electron localization function (ELF) and localized orbital locator (LOL) analyses. Toxicity effects such as mutagenic, tumorigenic, irritant, reproductive effect, and physicochemical properties such as druglikeness and drugscore were investigated. Molecular docking studies were conducted with the vascular endothelial growth factor receptor VEGFR-2 and the PARP-2 inhibitor, which is involved in many critical cellular processes, including DNA single-stranded fracture repair and cell death control, and its effectiveness in cancer treatment was investigated.

## 1. Introduction

Benzoxazole is an organic heterocyclic molecule formed as a result of the fusion of the oxazole ring along the 4 and 5 positions of the benzene ring. Benzoxazole and its derivatives show a wide range of activities, such as anticancer (multidrug resistance cancer cell activities) [1, 2], antimicrobial [3], antifungal [4], antiviral [5], antiallergic [6], anti-inflammatory [7], anti-Alzheimer [8], and anti-HIV-1 [9]. Also, the benzoaxazole ring is structurally similar to the adenine and guanine bases in the structure of nucleic acids. For all these reasons, benzoxazole is seen as one of the most important core structures in drug design [10].

With the changing lifestyle, a rapid growth in the diagnosis of cancer has erupted, and cancer affects the lives of millions of people all over the world [11, 12]. The most common types of cancer are lung, mouth, and breast cancers [13].

Chemotherapy is used in almost all stages of cancer treatment. However, the increasing incidence of drug resistance against chemotherapeutic agents causes serious problems in treatments and the death of cancer cells and healthy surrounding tissues [14, 15].

Therefore, there is a great need to research new cancer drugs [16]. In the literature, there are many studies investigating the anticancer activities of benzoaxazole derivatives. Some examples of these studies could be the following: In one study, benzoxazole-1,3,4 oxadiazole derivatives were synthesized and their anticancer activities were investigated against four human cancer cell lines, including A549 (lung cancer), MCF-7 (breast cancer), A-375 (melanoma cancer), and HT-29 (colon cancer). It has been reported that some of these synthesized compounds give better results against the HT-29 cancer cell line than the standard drug (CA-4) [17]. In another study, benzoxazole fused with

benzofuran and 1,2,4-oxadiazole were synthesized. The cytotoxicity activities of these compounds against human breast cancer (MCF-7), lung (A549), melanoma (A375), and colon (HT-29) cell lines were evaluated. According to the results obtained, some of the synthesized compounds showed stronger activity than the control group [18].

Molecular docking is a computer-aided drug design method that simulates molecular interaction and satisfies the binding mode and affinity between ligands and receptors. Moreover, this method greatly increases the productivity of pharmacological researchers and reduces research costs [19]. There are also many molecular docking studies for cancer research with benzoxazole derivatives in the literature. Carcinogenesis is accompanied by the overactivation of receptor tyrosine kinase (RTK) signaling pathways.

Therefore, it is very important to identify inhibitors that will inhibit these receptors in cancer treatment. In the study on the Synthesis, Synthesis, Anti-Breast Cancer Activity, and Molecular Modeling of Some Benzothiazole and Benzoxazole Derivatives, molecular docking studies were performed on the RTK receptor, and it was reported that docking with appropriate affinities and modes was determined [20]. In another study, benzoxazole and benzothiazole derivative compounds were synthesized as potential vascular endothelial growth factor receptor-2 (VEGF-2) inhibitors and supported by molecular docking studies for all synthesized compounds to evaluate their affinity towards the active site of VEGFR-2 [21].

In the first stage of this study, conformation analysis was performed using the Spartan software package. And then optimization calculations were carried out for the conformer structure with the highest Boltzman distribution and the lowest value using the Gaussian 09 program. In the second step, DFT calculations were made to determine the electronic properties of the title molecule. The chemical reactivity of the 5-Benzoxazolecarboxylic acid molecule was determined according to the energy of the HOMO-LUMO orbitals. In addition, a molecular electrostatic potential surface (MEP) map was

designed to identify negative (electrophilic) and positive (nucleophilic) regions of the title molecule that could react with biological targets and was supported by APT, Hirshfeld, and NBO charge analyses. Finally, electron localization function (ELF) and localized orbital locator (LOL) analysis were performed to determine the reactive sites. In the third and final stage, molecular docking studies on a cancer disease-related protein were performed, along with toxicological and physicochemical property analyses.

## 2. Computational Details

The conformer structure analysis was performed using MMFF theory by Spartan software [22]. Using the Gaussian 09 and GaussView 5.0 package programs, geometric optimization and electronic properties were calculated at the DFT/B3LYP/6-311++G(d,p) level of theory [23-25]. The Multiwfn program was used for ELF and LOL analyses [26]. Molecular docking studies were performed in the Autodock Vina software. Binding sites of ligand and protein were visualized in Discover Studio software. [27]. Toxicological and physicochemical properties were determined with the Ossiris Property Explorer program [28].

## 3. Results and Discussion

### 3.1. Conformational analysis

Before determining the optimized geometric structure of the molecule at the lowest energy (in the most stable state), conformation analysis was performed for the title molecule. Therefore, in the first part of this study, using the Spartan software program [22], two conformational structures (see Figure 1) were determined by the MMFF theory (molecular mechanic) for the 5-Benzoxazolecarboxylic acid molecule according to the Boltzman distribution [29]. Optimization calculations were performed on the Conformer I structure, which has the lowest energy and the highest Boltzmann distribution from these two conformer structures. The optimized geometric structure for 5-Benzoxazolecarboxylic acid molecule, which was calculated at the DFT/B3LYP/ 6-311++G(d,p) level of theory, is presented in Figure 2.





**Table 1.** The energy values of the global reactivity parameters of the 5-Benzoxazolecarboxylic acid molecule

Parameters	Energy Values (eV)
$E_{HOMO}$	-7.29
$E_{LUMO}$	-1.84
Energy band gap ( $\Delta E = E_{LUMO} - E_{HOMO}$ )	5.44
Ionization potential ( $I = -E_{HOMO}$ )	7.29
Electron affinity ( $A = -E_{LUMO}$ )	1.84
Chemical hardness ( $\eta = (-E_{HOMO} + E_{LUMO})/2$ )	2.72
Chemical softness ( $\sigma = 1/2\eta$ )	0.37
Electronegativity ( $\chi = -\mu_c$ )	4.57
Chemical potential ( $\mu_c = (E_{HOMO} + E_{LUMO})/2$ )	-4.57
Global electrophilicity ( $\omega = (\mu_c^2)/2\eta$ )	3.83

### 3.4. ELF and LOL analyses

ELF and LOL maps are important tools to help identify molecular space regions with a high probability of finding an electron pair and to perform covalent bond analysis, and the maps created in both methods depend on the kinetic energy density of the electrons. The ELF map scale is in the range of 0.0–1.0, and delocalized electrons are found in the range below 0.5, whereas bound and unbound localized electrons are over the range of 0.5 [26, 40]. ELF and LOL maps for the 5-Benzoxazolecarboxylic acid molecule were designed using the Multiwfn software program and are presented in Figure 5. According to Figure 5, the red color on the H atoms is indicative of bound and unbound localized electrons. In addition, localized and delocalized electrons are concentrated in the region where the C, N, and O atoms in the benzene and oxazole rings bond with each other. The blue circular regions around the C, N, and O atoms in the structure of the 5-Benzoxazolecarboxylic acid molecule are indicative of a delocalized electron density. On the other hand, LOL has large values in regions

where the electron density is dominated by electron localization, and the LOL map presented in Figure 5 gives similar results to the ELF maps.

### 3.5. Charge analyses

Charge analysis was also performed to obtain information about the binding potential and reactivity of the title molecule [41]. Atomic polar tensor (APT), Hirshfeld, and natural bond orbital (NBO) charge values were calculated using the B3LYP functional with 6-311++G(d,p) basis set in the DFT method and are presented in Table 2. In three different charge analyses, the atom with the most negative (electrophilic) value of the 5-Benzoxazolecarboxylic acid molecule was found to be the O<sub>3</sub> atom. O<sub>2</sub>, O<sub>1</sub>, and N<sub>4</sub> atoms were found in other highly negative atoms, respectively. Also, the C<sub>7</sub>, C<sub>9</sub>, and C<sub>10</sub> atoms of the benzene ring have a negative value. Apart from the atoms discussed above, other atoms in the molecule were found positive in all three charge analysis methods.

**Table 2.** Atomic charge values of the 5-Benzoxazolecarboxylic acid molecule

Atoms	APT	Hirshfeld	NBO
O <sub>1</sub>	-0.594	-0.104	-0.471
O <sub>2</sub>	-0.763	-0.174	-0.689
O <sub>3</sub>	-0.847	-0.286	-0.601
N <sub>4</sub>	-0.414	-0.187	-0.463
C <sub>5</sub>	0.077	0.022	0.070
C <sub>6</sub>	0.325	0.067	0.295
C <sub>7</sub>	-0.292	-0.025	-0.173
C <sub>8</sub>	0.087	-0.022	-0.145
C <sub>9</sub>	-0.064	-0.038	-0.236
C <sub>10</sub>	-0.021	-0.022	-0.146
C <sub>11</sub>	0.433	0.131	0.390
C <sub>12</sub>	1.412	0.209	0.790
H <sub>13</sub>	0.097	0.058	0.240
H <sub>14</sub>	0.066	0.059	0.226
H <sub>15</sub>	0.091	0.053	0.234
H <sub>16</sub>	0.098	0.078	0.192
H <sub>17</sub>	0.308	0.181	0.486

These results are in good agreement when compared with the MEP, ELF, and LOL maps. We determined that the electrophilic (i.e., the most negative) regions are distributed over the O<sub>3</sub> atom and N<sub>4</sub> atom in the MEP map, and there is a delocalized electron cloud around these atoms in the ELF and LOL maps.



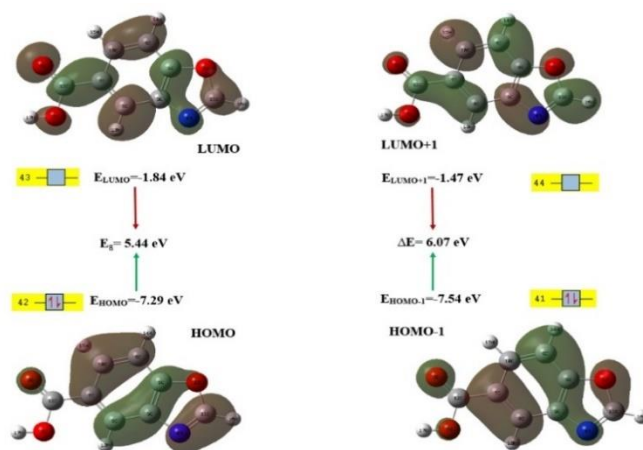


**Figure 3.** Frontier molecular orbital distribution of the 5-Benzoxazolecarboxylic acid molecule

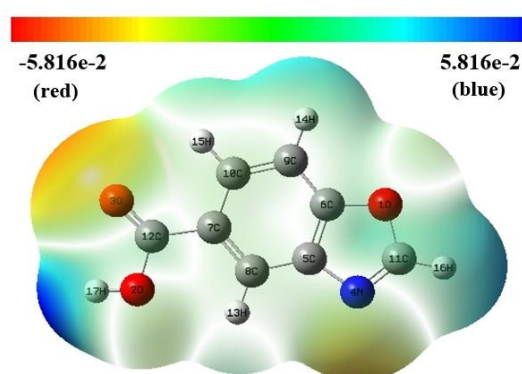


**Figure 4.** Molecular electrostatic potential surface map of the 5-Benzoxazolecarboxylic acid molecule

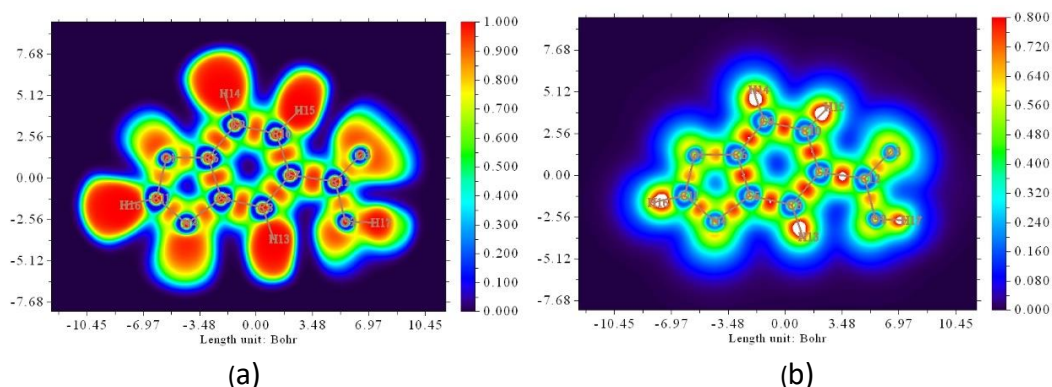


**Figure 5.** Color-filled ELF (a) and LOL (b) map of the 5-Benzoxazolecarboxylic acid molecule

### 3.6. Pharmacological property analysis

The toxic risk assessment and psychochemical properties of the title molecule were evaluated using the Ossiris Property Explorer program and the results are listed in Table 3. After a drug is taken orally, it first passes through the intestinal lining and enters the aqueous blood. It then passes through the lipid-based cell membrane to reach the cell. Therefore, the water solubility of a molecule that is thought to be used as a potential drug is very important. The cLogP

value is used to estimate the water solubility, and if this value is below 5.00, it is interpreted that the molecule is well soluble in water. In addition, the solubility of the molecule in water significantly affects its absorption and distribution properties. Good solubility results in good absorption, and the aim is to avoid the use of poorly soluble compounds [42].

The logS value is another measure of water solubility, and the larger this value, the better the solubility. For more than 80% of drugs on the

market, the logS value is greater than -4 [43]. The TPSA value is related to the passage of the structure through the cell membrane and should be less than 140Å<sup>2</sup>. Molecules with a TPSA value higher than this value make passing through the cell membrane more difficult [44, 45]. In addition, if the molecular weight of a molecule is above 450, intestinal absorption begins to be restricted, and absorption from the cell membrane becomes difficult [46]. If the drug score of a molecule is close to 1, it is concluded that that molecule can be used as a drug, and if it is close to 0, its use as a drug carries a great risk [47]. When the results obtained are evaluated, the 5-Benzoxazolecarboxylic acid molecule does not carry a toxic risk. In addition, the values obtained for the psychochemical properties are within the limits of the above-mentioned values, and this molecule has the potential to be used as a drug.

### 3.7. Molecular docking

In this study, molecular docking studies were carried out for the vascular endothelial growth factor receptor VEGFR-2 (PDB ID: 4ASD) [48], which plays a key role in tumor angiogenesis and the formation of new blood vessel networks necessary to provide nutrition and oxygen for tumor growth, and PARP-2 inhibitor (PDB ID: 4TVJ) [48] involved in many critical cellular processes, including DNA single-strand break repair and cell death control, using the Autodock Vina program [49].

**Table 3.** Toxicological and physicochemical properties of the 5-Benzoxazolecarboxylic acid molecule

Toxicity risks	Mutagenic	-
	Tumorigenic	-
	Irritant	-
	Reproductive effect	-
Physicochemical properties	ClogP	1.16
	Solubility	-2.47
	MW	163.13
	TPSA	63.33
	Druglikeness	0.48
	Drugscore	0.76

The resulting binding modes and affinity values are listed in Tables 4-5, while the molecular docking between ligand and protein is presented

in Figures 6-7. The energy value of the minimum binding affinity of the 5-Benzoxazolecarboxylic acid molecule with 4ASD and 4TVJ proteins was -6.60 kcal/mol and 7.2 kcal/mol for mode 1, which contains a pose with optimal binding on the basis of RMSD~0.00 Å. As a result of the ligand interaction of the 4ASD protein, it was determined that the O<sub>2</sub> atom of the title molecule is located at a distance of 2.31 Å from the H atom of CYS919. Also, the O atom of GLU917 was found at a distance of 2.09 Å from the H<sub>17</sub> atom of the ligand. In the ligand interaction of the 4TVJ protein, it was found that the O<sub>3</sub> atom of the title molecule is located at a distance of 2.11 Å from the H atom of GLY429. Also, the O atoms of SER 470 and TRP427 were found at a distance of 2.06 and 2.84 Å from the H<sub>17</sub> atom of the ligand. The general assumption in the literature is that for good docking, the distance between the ligand and the receptor should be close to 2.00 Å [50]. The results obtained from molecular docking studies provide information that the 5-Benzoxazolecarboxylic acid molecule can exhibit biological activity for the treatment of cancer disease, and this molecule can be used in the synthesis of new drugs.

**Table 4.** The binding affinity values of different poses of 4ASD protein interaction with the 5-Benzoxazolecarboxylic acid molecule

Mode	Affinity (kcal/mol)	Distance from best mode	
		RMSD l.b.	RMSD u.b.
1	-6.6	0.000	0.000
2	-6.6	1.800	4.357
3	-6.4	2.171	4.917
4	-6.2	1.483	2.349
5	-5.9	8.692	10.233
6	-5.9	12.546	14.792
7	-5.7	1.854	4.750
8	-5.7	18.170	19.529
9	-5.6	13.337	15.238

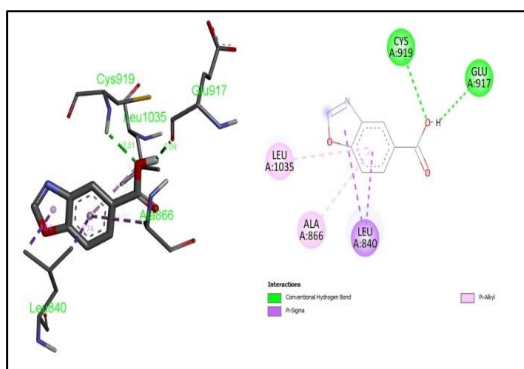


**Figure 6.** 3D bonding and 2D interaction between the 5-Benzoxazolecarboxylic acid molecule and the 4ASD protein

**Table 5.** The binding affinity values of different poses of 4TVJ protein interaction with the 5-Benzoxazolecarboxylic acid molecule

Mode	Affinity (kcal/mol)	Distance from best mode	
		RMSD l.b.	RMSD u.b.
1	-7.2	0.000	0.000
2	-7.0	1.194	2.072
3	-6.9	1.754	4.368
4	-6.7	2.181	3.136
5	-6.2	11.762	13.248
6	-6.1	9.623	10.682
7	-6.1	8.217	9.200
8	-5.9	2.781	3.973
9	-5.9	10.928	12.046

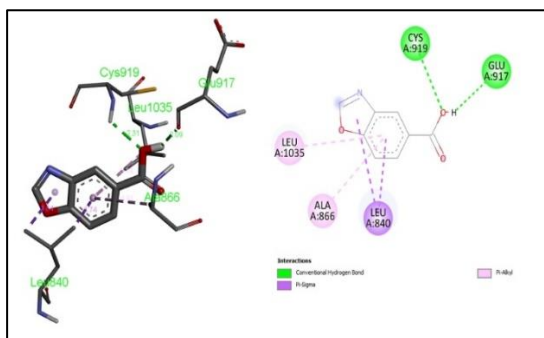


**Figure 7.** 3D bonding and 2D interaction between the 5-Benzoxazolecarboxylic acid molecule and the 4TVJ protein

#### 4. Conclusion

In this study, conformation analysis, electronic, toxicity, and pharmacological properties of the 5-Benzoxazolecarboxylic acid molecule were investigated. Two stable conformer structures were obtained for the title molecule. The conformer structure with the lowest energy and the highest Boltzman distribution was selected, and all other calculations were performed for this

structure. The energy values of the HOMO-LUMO orbitals were calculated to determine and interpret various global reactivity parameters.

The energy gap, global hardness, and global softness values of the 5-Benzoxazolecarboxylic acid molecule between the HOMO and LUMO orbitals are 5.44, 2.77, and 0.37 eV, respectively. The MEP map shows that the O<sub>3</sub> atom of the carboxyl group is dark red, and the N<sub>4</sub> atom in the oxazole ring has the most negative value. In addition, ELF and LOL maps were also used to determine the density of localized and delocalized electrons and gave results consistent with the MEP map. APT, Hirshfeld, and NBO charge analyses of the 5-benzoxazolecarboxylic acid molecule were performed. O<sub>3</sub>, O<sub>2</sub>, O<sub>1</sub>, and N<sub>4</sub> atoms were found to have the most negative values in the calculations for the three charge analyses.

It was determined that the 5-Benzoxazolecarboxylic acid molecule, whose toxicity and pharmacological properties were investigated, did not have any mutagenic, tumorigenic, irritant, or reproductive effects and had a very good drug score. Molecular docking studies were performed with the vascular endothelial growth factor receptor VEGFR-2 and the PARP-2 inhibitor, which is involved in many critical cellular processes, including DNA single-stranded fracture repair and cell death control. The conventional hydrogen bonding of the title molecule with these protein structures, which have important roles in cancer, gives the idea that this molecule can be evaluated as an anti-cancer drug.

#### Article Information Form

##### Acknowledgments

The authors would like to thank Prof. Dr. Şenay YURDAKUL for her contributions.

##### Funding

The author (s) has no received any financial support for the research, authorship or publication of this study.

***The Declaration of Conflict of Interest/ Common Interest***

No conflict of interest or common interest has been declared by the authors.

***The Declaration of Ethics Committee Approval***

This study does not require ethics committee permission or any special permission.

***The Declaration of Research and Publication Ethics***

The authors of the paper declare that they comply with the scientific, ethical and quotation rules of SAUJS in all processes of the paper and that they do not make any falsification on the data collected. In addition, they declare that Sakarya University Journal of Science and its editorial board have no responsibility for any ethical violations that may be encountered, and that this study has not been evaluated in any academic publication environment other than Sakarya University Journal of Science.

***Copyright Statement***

Authors own the copyright of their work published in the journal and their work is published under the CC BY-NC 4.0 license.

**References**

- [1] Kamal, K. S. Reddy, M. Naseer, M. J. Ramaiah, "Synthesis, DNA binding ability and anticancer activity of benzthiazole/benzoxazolepyrrolo[2,1-c][1,4]benzodiazepine conjugates," *Bioorganic & Medicinal Chemistry Letters*, vol.18, pp. 4747-4761, 2010.
- [2] H. Lage, E. Aki-Sener, I. Yalcin, "High antineoplastic activity of new heterocyclic compounds in cancer cells with resistance against classical DNA topoisomerase II-targeting drugs," *International Journal of Cancer*, vol. 119, no.1, pp. 213-220, 2006.
- [3] M. Arisoy, O. T. Arpaci, F. K. Onurdag, S. Ozgen, "Synthesis and antimicrobial activity of novel benzoxazoles," *Zeitschrift für Naturforschung C*, vol. 67, no. 9-10, pp. 466-472, 2012.
- [4] L. Srikanth, R. Jadha, K. Manohar, "Synthesis and evaluation of new phenylamino-thiadiazolo-oxadiazolo-1,3-benzoxazoles for their antifungal and anti-inflammatory activity," *Der Pharma Chemica*, vol. 2, pp.231-243, 2010.
- [5] D. N. Ward, D. C. Talley, M. Tavag, S. Menji, P. Schaughency, A. Baier, P. J. Smith, "UK-1 and structural analogs are potent inhibitors of hepatitis C virus replication," *Bioorganic & Medicinal Chemistry Letters*, vol. 24, no. 2, pp. 609-612, 2014.
- [6] A. Srinivas, J. Vidyasagar, M. Sarangapani, "Design, synthesis and biological evaluation of benzoxazole derivatives as new antiinflammatory agents," *Journal of Chemical and Pharmaceutical Research*, vol. 2 pp. 319-326, 2010.
- [7] M. Sham, S. N. Singh, A. Kumar, L. Meijer, "Synthesis, antiinflammatory, analgesic and kinase (CDK-1, CDK-5 and GSK-3) inhibition activity evaluation of benzimidazole/benzoxazole derivatives and some schiff's bases," *Bioorganic & Medicinal Chemistry Letters* vol. 14, pp. 3758-3765, 2006.
- [8] Celik, M. Erol, O. T. Arpaci, F. S. Senol, I. E. Orhan, "Evaluation of activity of some 2,5-disubstituted benzoxazole derivatives against acetylcholinesterase, butyrylcholinesterase and tyrosinase: ADME prediction, DFT and comparative molecular docking studies," *Polycyclic Aromatic Compounds*, vol. 42, no. 2, pp. 412-423, 2020.
- [9] S. M. Rida, F. A. Ashour, A. M. Soad, E. Hawash, M. Mona, H. B. Mona. "Synthesis of some novel benzoxazole derivatives as anticancer, antiHIV1 and antimicrobial agents," *European Journal of Medicinal Chemistry* vol. 40, pp. 949-959, 2005.
- [10] T. Zeyrek, B. Boyacioglu, Ö. T. Arpaci, H. Ünver, A. Elmali, "Spectroscopic, quantum mechanical and molecular



- docking studies of a new benzoxazole compound with an oxidoreductase enzyme and DNA,” *Journal of Molecular Structure*, vol. 1136, pp. 112-126, 2017.
- [11] P. Anand, A. B. Kunnumakkara, C. Sundaram, K. B. Harikumar, S. T. Tharakan, O. S. Lai, B. Sung, B. B. Aggarwal, “Cancer is preventable disease that requires major lifestyle changes,” *Pharmaceutical Research*, vol. 25, pp. 2097-2116, 2008.
- [12] H. Lage, E. A. Sener, I. Yalcin, “High anti-neoplastic activity of new heterocyclic compounds in cancer cells with resistance against classical DNA topoisomerase-II targeting drugs,” *International Journal of Cancer*, vol. 119, no. 1, pp. 213-220, 2006.
- [13] S. Vijayan, D. S. Janardhanam, M. Karthikeyan, J. Sunitha, R. J. Raghunatham, “Laison between microorganisms and oral cancer,” *Journal of Pharmacy & Bioallied Sciences*, vol. 7, pp. 354-360, 2015.
- [14] S. Grivennikov, F. R. Greten, M. Karin, “Immunity, Inflammation, and Cancer,” *Cell*, vol. 140 no. 6, pp. 883-899, 2010.
- [15] Kuzu, C. Hepokur, M. A. Alagoz, S. Burmaoglu, O. Algul, “Synthesis, Biological Evaluation and *In Silico* Studies of Some 2-Substituted Benzoxazole Derivatives as Potential Anticancer Agents to Breast Cancer,” *ChemistrySelect*, vol. 7, no. 1, pp. e202103559, 2022.
- [16] S. Desai, V. Desai, S. Shingade, “In-vitro Anti-cancer assay and apoptotic cell pathway of newly synthesized benzoxazole-N-heterocyclic hybrids as potent tyrosine kinase inhibitors,” *Bioorganic Chemistry*, vol. 94, pp.103382, 2020.
- [17] B. Ravinaik, D. Ramachandran, M. V. B. Rao, “Synthesis and Anticancer evaluation of Amide Derivatives of 1,3,4 –oxadiazole linked with Benzoxazole,” *Russian Journal of General Chemistry* vol. 89, no. 5, pp. 1003–1008, 2019.
- [18] S. Pervaram, D. Ashok, M. Sarasija, C. V. R. Reddy, G. Sridhar, “Synthesis and Anticancer Activity of 1,2,4-Oxadiazole Fused Benzofuran Derivatives,” *Russian Journal of General Chemistry*, vol. 88, pp. 1219-1223, 2018.
- [19] Fan, A. Fu, L. Zhang, “Progress in molecular docking,” *Quantitative Biology*, vol. 7 pp. 83-89, 2019.
- [20] M. A. Abdelgawad, A. Belal, H. A. Omar, L. Hegazy, M. E. Rateb, “Synthesis, Anti-Breast Cancer Activity, and Molecular Modeling of Some Benzothiazole and Benzoxazole Derivatives,” *Arch Pharm Chemistry in Life Sciences*, vol. 346, no. 7, pp. 534-541, 2013.
- [21] A. G. A. El-Helby, H. Sakr, İ. H. İsa, A. A. Al-Karmalawy, K. El-Adl, “Benzoxazole / benzothiazole-derived VEGFR - 2 inhibitors: Design, synthesis, molecular docking, and anticancer evaluations,” *Archiv der Pharmazie-Chemistry in Life Sciences*, vol. 352, no. 12, pp. 1900178, 2019.
- [22] Y. Shao, L. F. Molnar, Y. Jung, J. Kussmann, C. Ochsenfeld, S. T. Brown, A. T. B. Gilbert, L. V. Slipchenko, S. V. Levchenko, D. P. O’Neill, R. A. DiStasio Jr, R. C. Lochan, T. Wang, G. J. O. Beran, N. A. Besley, J. M. Herbert, C. Y. Lin, T.V. Voorhis, S. H. Chien, A. Sodt, R. P. Steele, V. A. Rassolov, P. E. Maslen, P. P. Korambath, R. D. Adamson, B. Austin, J. Baker, E. F. C. Byrd, H. Dachsel, R. J. Doerksen, A. Dreuw, B. D. Dunietz, A. D. Dutoi, T. R. Furlani, S. R. Gwaltney, A. Heyden, S. Hirata, C. P. Hsu, G. Kedziora, R. Z. Khalliulin, P. Klunzinger, A. M. Lee, M. S. Lee, W. Liang, I. Lotan, N. Nair, B. Peters, E. I. Proynov, P. A. Pieniazek, Y. M. Rhee, J. Ritchie, E. Rosta, C. D. Sherrill, A. C. Simmonett, J. E. Subotnik, H. L. Woodcock III, W. Zhang, A. T. Bell, A. K. Chakraborty, D. M. Chipman, F. J. Keil, A. Warshel, W. J. Hehre, H. F.



- Schaefer III, J. Kong, A. I. Krylov, P. M. W. Gill, M. H. Gordon, "Advances in methods and algorithms in a modern quantum chemistry program package," *Physical Chemistry Chemical Physics*, vol. 8, pp. 3172-3191, 2016.
- [23] S. Çelik, "Conformational Analysis and DFT Investigations of 1-(4-Fluorophenyl) Piperazine by ELF and LOL, Inhibitory Activity Against Alzheimer's Disease, and ADME Prediction," *Sakarya Üniversitesi Fen Bilimleri Enstitüsü Dergisi*, vol. 26, no. 5, pp. 931-941, 2022.
- [24] M. J. Frisch, G. W. Trucks, H. B. Schlegel, G. E. Scuseria, M. A. Robb, J. R. Cheeseman, G. Scalmani, V. Barone, B. Mennucci, G. A. Petersson, H. Nakatsuji, M. Caricato, X. Li, H. P. Hratchian, A. F. Izmaylov, J. Bloino, G. Zheng, J. L. Sonnenberg, M. Hada, M. Ehara, K. Toyota, R. Fukuda, J. Hasegawa, M. Ishida, T. Nakajima, Y. Honda, O. Kitao, H. Nakai, T. Vreven, J. A. Montgomery, Jr., J. E. Peralta, F. Ogliaro, M. Bearpark, J. J. Heyd, E. Brothers, K. N. Kudin, V. N. Staroverov, R. Kobayashi, J. Normand, K. Raghavachari, A. Rendell, J. C. Burant, S. S. Iyengar, J. Tomasi, M. Cossi, N. Rega, J. M. Millam, M. Klene, J. E. Knox, J. B. Cross, V. Bakken, C. Adamo, J. Jaramillo, R. Gomperts, R. E. Stratmann, O. Yazyev, A. J. Austin, R. Cammi, C. Pomelli, J. W. Ochterski, R. L. Martin, K. Morokuma, V.G. Zakrzewski, G. A. Voth, P. Salvador, J. J. Dannenberg, S. Dapprich, A. D. Daniels, O. Farkas, J. B. Foresman, J. V. Ortiz, J. Cioslowski, D. J. Fox., "Gaussian Inc," Wallingford CT, 2009
- [25] R. Dennington, T. Keith, J. Millam, "GaussView Version 5," Semichem Inc., Shawnee Mission KS., 2009.
- [26] B. Silvi, A. Savin, "Classification of chemical bonds based on topological analysis of electron localization functions," *Nature*, 371, pp. 683-686, 1994.
- [27] Dassault Systemes BIOVIA, Discovery Studio Visualizer v17.2.0.16349, 2016. San Diego
- [28] Organic Chemistry Portal OSIRIS Property Explorer, (2023, Jul. 20.) Available: <http://www.organic-chemistry.org/prog/peo/>
- [29] Kucuk, S. Yurdakul, B. Erdem. "Combined Experimental and Theoretical Spectroscopic Properties (FT-IR, FT-Ra, Uv-Vis, and NMR), DFT Studies, Biological Activity, Molecular Docking, and Toxicity Investigations of 3-methoxy-1-piperazinylbenzene," *Letters in Organic Chemistry*, vol. 20, no. 5, pp. 457-480, 2023.
- [30] M. N. Ahmed, K. A. Yasin, K. Ayub, T. Mahmood, M. N. Tahir, B. A. Khan, M. Hafeez, M. Ahmed, I. ul-Haq, "Click one pot synthesis, spectral analyses, crystal structures, DFT studies and brine shrimp cytotoxicity assay of two newly synthesized 1,4,5-trisubstituted 1,2,3-triazoles," *Journal of Molecular Structure*, vol. 1106, pp. 430-439, 2016.
- [31] M. Arshad, A. Bibi, T. Mahmood, A. Asiri, K. Ayub, "Synthesis, crystal structures and spectroscopic properties of triazine-based hydrazone derivatives; a comparative experimental-theoretical study," *Molecules*, vol. 20, pp. 5851-5874, 2015.
- [32] M. Evecen, "Structural, Conformational and Spectroscopic Properties of C16H16BrNO3 SchiffBase Molecule: A Theoretical Investigation," *Sakarya Üniversitesi Fen Bilimleri Enstitüsü Dergisi*, vol. 22, pp. 1591-1600, 2018.
- [33] M. Noreen, N. Rasool, Y. Gull, M. Zubair, T. Mahmood, K. Ayub, F.-H. Nasim, A. Yaqoob, M. Zia-Ul-Haq, V. Feo, "Synthesis, density functional theory (DFT), urease inhibition and antimicrobial activities of 5-aryl thiophenes bearing sulphonylacetamide moieties," *Molecules*, vol. 20, pp. 19914-19928, 2015.

- [34] S. D. Oladipo, G. F. Tolufashe, C. Mocktar, B. Omondi, "Ag(I) symmetrical N,N' -diarylformamidine dithiocarbamate PPh<sub>3</sub> complexes: Synthesis, structural characterization, quantum chemical calculations and in vitro biological studies," *Inorganica Chimica Acta*, vol. 520, pp. 120316, 2021.
- [35] S. J. Basha, S. P. V. Chamundeeswari, S. Muthu, B. R. Raajaraman, "Quantum computational, spectroscopic investigations on 6- aminobenzimidazole by DFT/TD-DFT with different solvents and molecular docking studies," *Journal of Molecular Liquids*, vol. 296, pp. 11178, 2019.
- [36] T. Chaudharya, M. K. Chaudharya, B. D. Joshi, M. S. A. de Santana, A. P. Ayala, "Spectroscopic (FT-IR, Raman) analysis and computational study on conformational geometry, AIM and biological activity of cephalixin from DFT and molecular docking approach," *Journal of Molecular Structure*, vol. 1240, pp. 130594, 2021.
- [37] H. P. Gümüş, Ö. Tamer, Y. Atalay, "4-(Metoksümetil)-1,6-dimetil-2-okso-1,2-dihidropiridin-3-karbonitril molekülünün teorik olarak incelenmesi," *Sakarya Üniversitesi Fen Bilimleri Enstitüsü Dergisi*, vol. 19 no 3, pp. 303 -311, 2015.
- [38] N. Okulik, A. H. Jubert "Theoretical study on the structure and reactive sites of nonsteroidal anti-inflammatory drugs," *Journal of Molecular Structure: THEOCHEM*, vol. 682, pp. 55-62, 2004.
- [39] B. Şaş, S. Çiftçi, M. KURT, "Spectroscopic Characterization and DFT Calculations on 1H-benzimidazole-2-carboxylic acid monohydrate Molecule," *Sakarya Üniversitesi Fen Bilimleri Enstitüsü Dergisi*, vol. 26, no. 5, pp. 879-891, 2022.
- [40] B. F. Rizwana, J. C. Prasana, S. Muthu, C. S. Abrahama, "Molecular docking studies, charge transfer excitation and wave function analyses (ESP, ELF, LOL) on valacyclovir: a potential antiviral drug," *Computational Biological Chemistry*, vol. 78, pp. 9 -17, 2019.
- [41] A. Atilgan, Ş. Yurdakul, Y. Erdoğan, M. T. Güllüoğlu, "DFT simulation, quantum chemical electronic structure, spectroscopic and structure-activity investigations of 4-acetylpyridine," *Journal of Molecular Structure*, vol. 1161, pp. 55-65, 2018.
- [42] Utrecht, "Prediction of a new drug's potential to cause idiosyncratic reactions," *Current Opinion in Drug Discovery and Development*, vol. 4, no. 1, pp. 55-59, 2001.
- [43] M. Ishikawa, Y. J. Hashimoto, "Improvement in aqueous solubility in small molecule drug discovery programs by disruption of molecular planarity and symmetry," *Journal of medicinal Chemistry*, vol. 54, no. 6, pp. 1539-1554, 2011.
- [44] T. P. Begley, "Wiley Encyclopedia of Chemical Biology, Volume 1," Wiley, New York, 2009.
- [45] Di, E. H. Kerns, "Blood-Brain Barrier in Drug Discovery: Optimizing Brain Exposure of CNS Drugs and Minimizing Brain Side Effects for Peripheral Drugs," John Wiley & Sons, 2015.
- [46] M.A. de Brito, "Pharmacokinetic study with computational tools in the medicinal chemistry course," *Brazilian Journal of Pharmaceutical Sciences*, vol. 47, no. 4, pp. 797-805, 2011.
- [47] Guan, H. Yang, Y. Cai L. Sun, P. Di, W. Li, Y. Tang, "ADMET-score – a comprehensive scoring function for evaluation of chemical drug-likeness," *Medicinal Chemistry Communication*, vol. 10, no. 1, pp. 148-157, 2019.
- [48] RCSB PDB Protein Data Bank, (2023, Jul. 20.) Available:<https://www.rcsb.org/>

- [49] K. Haruna, V. S. Kumar, Y. S. Maray, S. A. Popoola, R. Thomas, M. S. Roxy, A. A. Al-Saadi, “Conformational profile, vibrational assignments, NLO properties and molecular docking of biologically active herbicide 1,1-dimethyl-3-phenylurea,” *Heliyon*, vol. 5, pp. e01987, 2019.
- [50] J. L. Stigliani, V. B. Genisson, J. Bernadou, G. Pratviel, “Cross-docking study on InhA inhibitors: a combination of Autodock Vina and PM6-DH2 simulations to retrieve bio-active conformations,” *Organic & Biomolecular Chemistry*, vol. 10, pp. 6341–6349, 2012.

## Semiconducting Characteristic of Antiferromagnetic $Al_4X_3Mn$ ( $X = P, As$ and $Sb$ ) Compounds with Ab Initio Simulation Methods

Buğra Yıldız<sup>1\*</sup> , Aytaç Erkişi<sup>2</sup> 

<sup>1</sup> Hacettepe University, Faculty of Engineering, Department of Physics, Ankara, Türkiye, [bugrayildiz@hacettepe.edu.tr](mailto:bugrayildiz@hacettepe.edu.tr)

<sup>2</sup> Pamukkale University, Faculty of Science, Department of Physics, Denizli, Türkiye, [aerkisi@pau.edu.tr](mailto:aerkisi@pau.edu.tr)

\*Corresponding Author

### ARTICLE INFO

### ABSTRACT

Keywords:  
Density Functional Theory  
Ab-initio Simulation Methods  
Semiconductor  
Antiferromagnetism

#### Article History:

Received: 08.08.2023

Accepted: 25.12.2023

Online Available: 22.04.2024

This research reports the electronic characteristics of ternary aluminium-based  $Al_4X_3Mn$  ( $X=P, As$  and  $Sb$ ) compounds for the most stable magnetic order which is A-type antiferromagnetic. The related systems are conforming 215 space number with P-43m space group which is simple cubic crystal structure. The computations in this research have been done within the framework of Density Functional Theory. The calculations utilized Perdew-Burke-Ernzerhof type correlation functionals within the meta-generalized gradient approximation. For considered four different type magnetic orders, the visualized volume-energy plots and the calculated formation energy values imply that the magnetic nature of these compositions is A-type antiferromagnetic. Besides, the investigated electronic natures in the detected stable magnetic phase of these systems are semiconductor since the band gaps were observed in their electronic band structures and density of states ( $E_g = 0.36$  eV for  $Al_4P_3Mn$ ,  $E_g = 0.33$  eV for  $Al_4As_3Mn$ , and  $E_g = 0.18$  eV for  $Al_4Sb_3Mn$ ).

## 1. Introduction

The compounds which belong to Group III and V elements in periodic table, are highly preferred for electronic devices due to having some intriguing physical properties. High heat conduction, wide electronic bandgap and strong resistance to radiation are just some of the interesting features [1-6]. The materials containing the mentioned elements having wide application fields in the electronic device industry could be used in communication area and high-speed rail transportation [7-11]. In this regard, the material scientists have focused on the gallium- and aluminium-based compounds which are among these type materials, for a long time.

In a theoretical research, the thermal conductivity and some mechanical properties of GaAs, AlAs, and  $Al_xGa_{1-x}As$  alloys were discussed [7]. In another study, the vibrational properties and

dynamic stability of  $Ti_xGa_nAs_m$  and  $Ti_xGa_nP_m$  compounds were studied by using ab initio calculations within GGA and LDA approximations [12]. Also, the half-metallic nature of  $Ti_xGa_{1-x}P$  was presented by some other researchers [13-15].

Furthermore, recently, the magnetic nature and electronic characteristic of  $Ga_4P_3Mn$  and  $Ga_4As_3Mn$  compounds were investigated with ab initio simulation methods [16]. In particular, the obtained observations and results in the mentioned studies in references [7, 12-16] formed the main motivation of this study.

For decades, material scientists have investigated many physical properties such as electronic behavior, magnetic nature, thermodynamic or thermoelastic properties, of solid crystalline materials theoretically, by using ab-initio simulation approaches grounded density functional theory (DFT). These type of

computations are very useful to understand material and encourage related experimental and theoretical studies [17-22].

In this regard, for this research, ab-initio simulation methods have been employed by using appropriately normed and strongly constrained semilocal density functional, (METAGGA-SCAN) meta-generalized gradient approximation. Also, it has been found that ternary aluminum-based  $\text{Al}_4\text{X}_3\text{Mn}$  (X=P, As, and Sb) systems have A-Type antiferromagnetic nature and semiconducting characteristic. Despite having a small band gap, these types of materials may find applications in optoelectronics [23]. Therefore, these new ternary aluminium-based materials, due to having well physical properties such as semiconducting behavior could have large usage in some technological and industrial applications.

## 2. The Computational Details

The structural and electronic characteristics of  $\text{Al}_4\text{X}_3\text{Mn}$  (X: P, As, Sb) compounds have been investigated applying Vienna Ab-initio Simulation Package (VASP) [24, 25] with projector augmented wave (PAW) approach [26] based on Density Functional Theory (DFT) [27, 28]. The Kohn-Sham equations have been solved constantly until every pressures and forces on each atom reached zero.

The calculations utilized PBE (Perdew-Burke-Ernzerhof) type correlation functionals and employed structure was META-GGA (Meta Generalized Gradient Approximations) [29]. In order to express interactions among electrons and ion cores, PAW (projector-augmented) method has been considered. The valence electron configurations for Aluminum (Al) and Manganese (Mn) atoms are given  $3s^2 3p^1$  and  $4s^2 3d^5$ . Also, for the Phosphorus (P), Arsenic (As) and Antimony (Sb) atoms are  $3s^2 3p^3$ ,  $4s^2 3d^{10} 4p^3$  and finally  $5s^2 4d^{10} 5p^3$  with respectively.

To ensure accuracy, a  $12 \times 12 \times 12$  Monkhorst and Pack (MP) scheme k-point mesh has been employed [30]. The Methfessel–Paxton smearing method with a 0.01 eV smearing parameter has been adopted and the iterations

have been continued as far as all the forces on each ion become lower than  $10^{-8}$  eV/Å. Further, the convergence criteria for the iteration steps has been set at  $10^{-9}$  eV. The cut-off energy has been set at 900 eV. In addition, the three dimensional visualization an X-ray diffraction pattern have been achieved by using VESTA [31].

With the aim of picking most convenient magnetic phase  $2 \times 2 \times 2$  super-cells have been created and ground state energies have been determined. And finally structural parameters, electronic band structures and density of states have been inspected in most suitable magnetic order. Furthermore, for the electronic part,  $6 \times 6 \times 6$  MP (Monkhorst-Pack) k-point mesh has been used for sampling reciprocal space. Also, for the calculation  $\text{IBRION} = -1$ ,  $\text{EDIFF} = 1.E-9$ ,  $\text{EDIFFG} = -1.E-8$  and finally cut-off energy has been chosen as 600 eV

## 3. Results

### 3.1. Structural properties

Ternary aluminum-based a of  $\text{Al}_4\text{X}_3\text{Mn}$  compounds, where X represents P, As or Sb atoms, possess a simple cubic structure with 215 space number with  $P\bar{4}3m$  space group. The 3d (three-dimensional) primitive cell of  $\text{Al}_4\text{X}_3\text{Mn}$  (X: P, As, Sb) materials consists of 8 atoms have been given in Figure 1 with X-ray diffraction pattern (XRD). Also, it has been revealed that the  $2\theta$  values of the maximum peak is 27.64 degrees for  $\text{Al}_4\text{P}_3\text{Mn}$ , 26.81 degree for  $\text{Al}_4\text{As}_3\text{Mn}$  and finally 25.07 degree for  $\text{Al}_4\text{Sb}_3\text{Mn}$  in figure 1. As can be clearly seen from the figure, it has been observed that the maximum peak value decreased as the atomic radius increased.

In this research concerning to determine most convenient magnetic phase, three types of antiferromagnetic orders as A-type, C-type, and G-type and ferromagnetic phases has been considered [32]. Figure 2 presents the total energies-volume plots for these magnetic phases which have been plotted by using Vinet equation [33]. The results suggest that the A-type antiferromagnetic order is the most appropriate for all three materials, as the ground state energies have been very closely grouped.



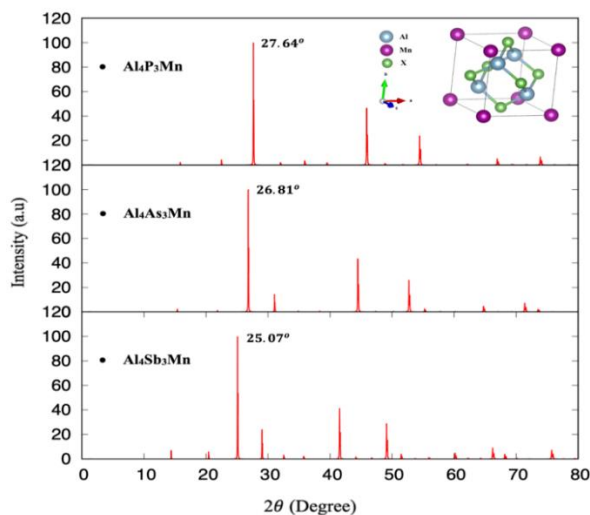


**Figure 1.** The three-dimensional (3d) crystallographic arrangement and X-Ray diffraction pattern (XRD) of  $\text{Al}_4\text{X}_3\text{Mn}$  (X: P, As, Sb). Where abbreviation of arbitrary unit is a.u.

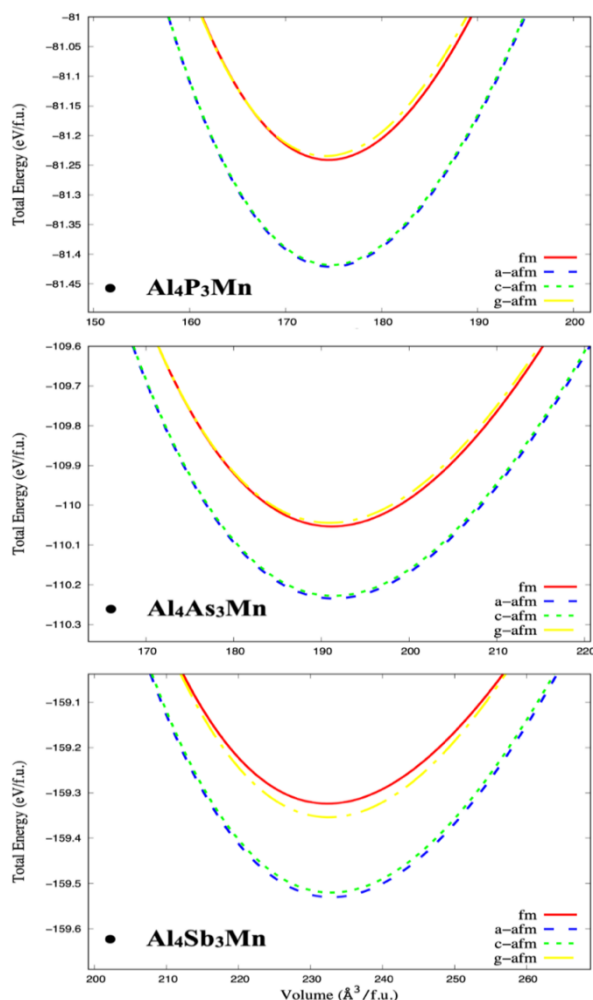


**Figure 2.** The total energy-volume plots for three types of A, C and G type antiferromagnetic order and for the ferromagnetic order; a)  $\text{Al}_4\text{X}_3\text{Mn}$  (X: P, As, Sb).

**Table 1.** The determined bond lengths (d), lattice parameters (a), and the formation enthalpies ( $\Delta E_f$ ) for the  $\text{Al}_4\text{X}_3\text{Mn}$  (X: P, As, Sb) compounds.

Compounds	a (Å)	$d_{\text{Al-X}}$ (Å)	$d_{\text{Al-Mn}}$ (Å)	$\Delta E_f$ (eV/f.u.)
$\text{Al}_4\text{P}_3\text{Mn}$	5.58601	2.38621	2.52264	-2.5387500
				-2.5384375
				-2.5443750
				-2.5446875
$\text{Al}_4\text{As}_3\text{Mn}$	5.75533	2.47240	2.55336	-3.4393750
				-3.4390625
				-3.4443750
				-3.4446875
$\text{Al}_4\text{Sb}_3\text{Mn}$	6.14708	2.67203	2.63142	-4.9787500
				-4.9796875
				-4.9850000
				-4.9856250

In the Equation 1,  $E_{\text{Al}_3\text{X}_3\text{Mn}}$  represents the total energies where X denotes P, As or Sb elements. Also, the other terms represent ground state energies of each element. Table 1 provides information on the bond lengths (d) and lattice parameters (a), showing that both quantities increased with the radius of X atoms as expected. Notably, the determined formation energies of all three compounds are negative for all magnetic orders. It indicates that, their energetic feasibility and stability for structural synthesis. In addition the most suitable magnetic arrangements for all three materials are the A-type antiferromagnetic order, as it exhibits lowest formation energies. These findings align with the trends observed in the volume-energy plots in Figure 2. Therefore, our materials structurally stable and thermodynamically synthesizable.

$$\Delta E_f = E_{\text{Al}_4\text{X}_3\text{Mn}} - (4E_{\text{Al}}^{\text{bulk}} + 3E_{\text{X}}^{\text{bulk}} + E_{\text{Mn}}^{\text{bulk}}) \quad (1)$$

### 3.2. The observations about the electronic characteristics

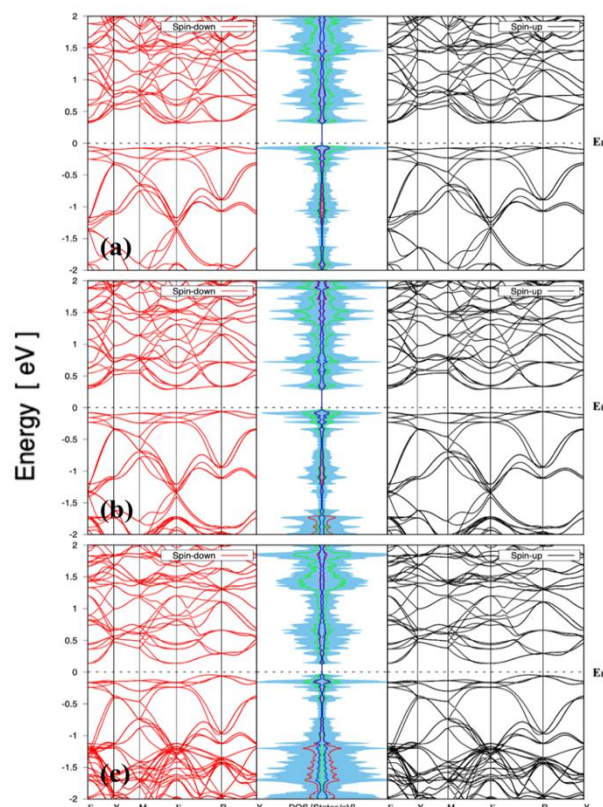


**Figure 3.** The determined electronic band structures for spin majority orientation (right) and spin minority orientation (left) with Density of States for (a)  $\text{Al}_4\text{P}_3\text{Mn}$  (b)  $\text{Al}_4\text{As}_3\text{Mn}$  and (c)  $\text{Al}_4\text{Sb}_3\text{Mn}$ . Also, the Fermi energy level ( $E_F$ ) is set to zero and it is represented with the black dashed line.

The electronic features of the materials have been analyzed using the calculated partial and total density of states with the electronic band structures, depicted in Figure 3. The electronic band structures for three compounds have been visualized onward the high symmetry points and META-GGA has been applied to both spin majority and spin minority states. The results show that all three ternary aluminium-based materials in this study, exhibit semiconductor behavior, with an indirect band gap (R to  $\Gamma$  point) of  $E_g = 0.36$  eV for  $\text{Al}_4\text{P}_3\text{Mn}$ ,  $E_g = 0.33$  eV for  $\text{Al}_4\text{As}_3\text{Mn}$ , and  $E_g = 0.18$  eV for  $\text{Al}_4\text{Sb}_3\text{Mn}$ . Additionally, these band gaps are inversely proportional to the atomic radius of P, As, and Sb atoms, which are 98, 114, and 133 pm, respectively.

Also, Figure 4, illustrates the partial (PDOS) and total (TDOS) orbital projected density of states for each atom in the  $\text{Al}_4\text{X}_3\text{Mn}$  (X: P, As, Sb)

compounds. For all three crystal systems, transition metal Manganese (Mn) atom contribute significantly to the total density of states, particularly for the energy range from -0.5 eV up to Fermi energy level. The dominant orbital in this range are 3d states of Mn atoms. One notable difference between the materials, is that hybridizations of Antimony (Sb) atoms p-orbitals around Fermi energy levels. Therefore, the band gap ( $E_g = 0.18$  eV) for the  $\text{Al}_4\text{Sb}_3\text{Mn}$  compound is smaller than the others.

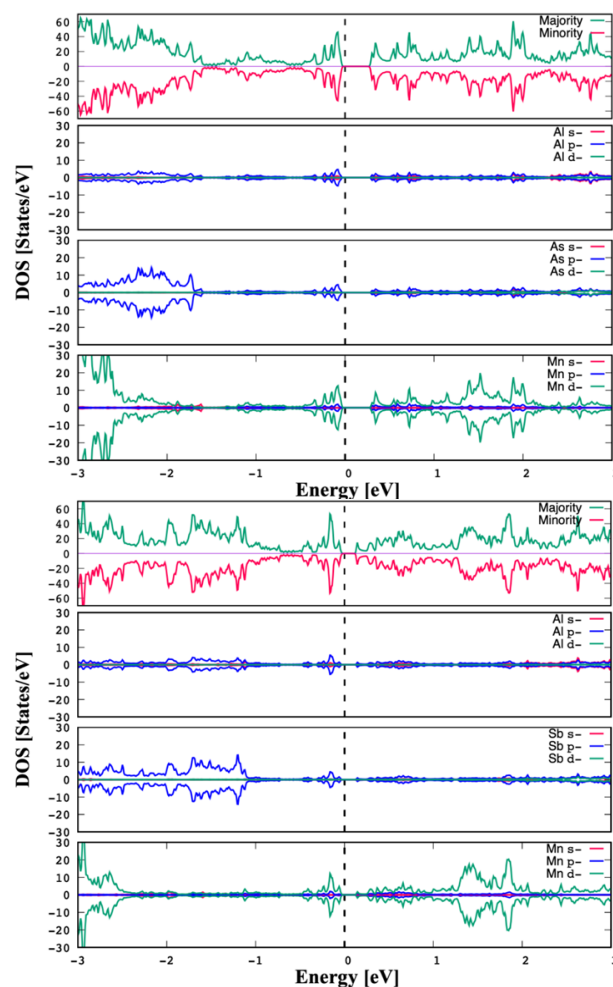


**Figure 4.** The orbital projected Density of states (DOS) for the elements in  $\text{Al}_4\text{X}_3\text{Mn}$  (X: P, As, Sb) compounds for both spin up and down case respectively.

## 4. Conclusion

For this computational research, the structural and electronic features of  $\text{Al}_4\text{X}_3\text{Mn}$  (X: P, As, Sb) compounds have been examined in detail. These compounds, denoted as simple cubic structure in accordance having a space number of 215 and its space group is  $P\bar{4}3m$ . Despite of the ground state energies for all three compounds are

quite close, it becomes evident that the firmly the most suitable magnetic phases are the A-type antiferromagnetic order for all three materials. The almost same behavior observed in the spin majority and spin minority states of the plotted electronic band structures also shows antiferromagnetic tendency.

Moreover, the determined formation energies of all three compounds are negative for all considered magnetic orders. It indicates that, the materials energetically feasible and stable for structural synthesis. The partial and total density of states and the electronic band structures reveal that our materials exhibit semiconductor behavior with an indirect band gap of 0.36 eV for  $\text{Al}_4\text{P}_3\text{Mn}$ , 0.33 eV for  $\text{Al}_4\text{As}_3\text{Mn}$ , and finally 0.18 eV for  $\text{Al}_4\text{Sb}_3\text{Mn}$  compounds. The observed their semiconducting characters and the calculated negative formation energies may suggest that the mentioned materials are good candidates for use in particularly semiconductor device technology.

#### Article Information Form

##### *Funding*

The author (s) has no received any financial support for the research, authorship or publication of this study.

##### *Authors' Contribution*

The authors contributed equally to the study.

##### *The Declaration of Conflict of Interest/ Common Interest*

No conflict of interest or common interest has been declared by the authors.

##### *The Declaration of Ethics Committee Approval*

This study does not require ethics committee permission or any special permission.

##### *The Declaration of Research and Publication Ethics*

The authors of the paper declare that they comply with the scientific, ethical and quotation rules of SAUJS in all processes of the paper and that they do not make any falsification on the data collected. In addition, they declare that Sakarya University Journal of Science and its editorial board have no responsibility for any ethical violations that may be encountered, and that this

study has not been evaluated in any academic publication environment other than Sakarya University Journal of Science.

##### *Copyright Statement*

Authors own the copyright of their work published in the journal and their work is published under the CC BY-NC 4.0 license.

#### References

- [1] M. Durandurdu, "Pressure-induced phase transition of zinc-blende AlN: An ab initio molecular dynamics study," *Journal of Physics and Chemistry of Solids*, vol. 69, pp. 2894–2897, 2008.
- [2] H. Gomez, T. R. Taylor, D. M. Neumark, "Anion photoelectron spectroscopy of aluminum phosphide clusters," *The Journal of Physical Chemistry A*, vol. 105, 6886–6893, 2001.
- [3] P. Bowen, J. G. Highfield, A. Mocellin, T. A. Ring, "Degradation of aluminum nitride powder in an aqueous environment," *Journal of American Ceramic Society*, vol. 73, pp. 724–728, 1990.
- [4] N. Takahashi, Y. Matsumoto, T. Nakamura, "Investigations of structure and morphology of the AlN nano-pillar crystal films prepared by halide chemical vapor deposition under atmospheric pressure," *Journal of Physics and Chemistry of Solids*, vol. 67, pp. 665–668, 2006.
- [5] O. A. Golikova, "Boron and Boron-based semiconductors," *Physica Status Solidi A*, vol. 51, pp. 31–40, 1979.
- [6] Q. Y. Fan, C. C. Chai, Q. Wei, Y. T. Yang, "Thermodynamic, elastic, elastic anisotropy and minimum thermal conductivity of  $\beta$ -GaN under high temperature," *Chinese Journal of Physics*, vol. 55, pp. 400–411, 2017.
- [7] S. Adachi, "GaAs, AlAs, and  $\text{Al}_x\text{Ga}_{1-x}\text{As}$ : Material parameters for use in research and device applications," *Journal of Applied Physics*, vol. 58, pp. R1–R29, 1985.






- [8] L. Guo, "Structural, energetic, and electronic properties of hydrogenated aluminum arsenide clusters," *Journal of Nanoparticle Research*, vol. 13, pp. 2029–2039, 2011.
- [9] L. Y. Shen, X. S. Xu, W. Lu, B. Shi, "Aluminum nitride shaping by non-aqueous gelcasting of low-viscosity and high solid-loading slurry," *Ceramics International*, vol. 42, pp. 5569–5574, 2016.
- [10] B. C. Chen, C. Y. Ho, M. Y. Wen, C. S. Chen, C. Ma, Y. H. Tsai, "Ultrashort-laser-pulse machining characteristics of aluminum nitride and aluminum oxide," *Ceramics International*, vol. 41, pp. S191–S196, 2015.
- [11] L. E. McNeil, M. Grimsditch, R. H. French, "Vibrational spectroscopy of aluminum nitride," *Journal of American Ceramic Society*, vol. 76, pp. 1132–1136, 1993.
- [12] P. Palacios, P. Wahnnon, C. Tablero, "Ab initio phonon dispersion calculations for  $Ti_xGa_{1-x}As_m$  and  $Ti_xGa_{1-x}P_m$  compounds," *Computational Materials Science*, vol. 33, pp. 118–124, 2005.
- [13] P. Palacios, J. J. Fernandez, K. Sanchez, J. C. Conesa, P. Wahnnon, "First-principles investigation of isolated band formation in half-metallic  $Ti_xGa_{1-x}P$  ( $x = 0.3125–0.25$ )," *Physical Review B*, vol. 73, pp. 085206, 2006.
- [14] J. J. Fernandez, C. Tablero, P. Wahnnon, "Application of the exact exchange potential method for half metallic intermediate band alloy semiconductor," *The Journal of Chemical Physics*, vol. 120, pp. 10780–10785, 2004.
- [15] C. Tablero, A. Garcia, J. J. Fernandez, P. Palacios, P. Wahnnon, "First principles characterization of direct transitions for high efficiency new photovoltaic materials," *Computational Materials Science*, vol. 27, pp. 58–64, 2003.
- [16] A. Erkişi, "The First-principles study on the investigation of magnetic and electronic properties of  $Ga_4X_3Mn$  ( $X = P$  and  $As$ )", *Süleyman Demirel Üniversitesi Fen Edebiyat Fakültesi Fen Dergisi*, vol. 17(2), pp. 371–381, 2022.
- [17] R. Masrour, "Study of magnetic properties of Ising nanowires with core–shell structure.", *The European Physical Journal B*. vol. 96, pp. 100, 2023.
- [18] S. Belhamra, R. Masrour, E. K. Hlil, "Dynamic Phase Transitions, Electronic, and Magnetic Properties of  $Ba_2NiWO_6$  and  $Sr_2NiWO_6$  Double Perovskites." *Journal of Superconductivity and Novel Magnetism*. vol. 35, pp. 3613–3622, 2022.
- [19] R. Masrour, G. Kadim, A. Jabar, E. Mohamed Emerging opportunities for  $Sr_2FeReO_6$  and  $Sr_2CrWO_6$  double perovskites in potential magnetic refrigerants and spintronics in room temperature regime. " *Applied Physics A*. vol. 128, pp. 1023, 2022.
- [20] M. Y. Raïâ, R. Masrour, M. Hamedoun, J. Kharbach, A. Rezzouk, A. Hourmatallah, N. Benzakour, K. Bouslykhane, "Effect of L21 and XA ordering on structural, martensitic, electronic, magnetic, elastic, thermal and thermoelectric properties of  $Co_2FeGe$  Heusler alloys" *Solid State Communications*, vol. 35, pp. 114932, 2022.
- [21] I. A. Elkoua, R. Masrour, "Structural, thermodynamics, optical, electronic, magnetic and thermoelectric properties of Heusler  $Ni_2MnGa$ : An ab initio calculations." *Optical and Quantum Electronics*, vol. 54, pp. 667, 2022.
- [22] A. Abjaou, R. Masrour, A. Jabar, E. K. Hlil, "Magnetocaloric Effect, Structural, Magnetic and Electronic Properties of High Entropy Alloys  $AlCo_xCr_{1-x}FeNi$ : First-Principle Calculations and Monte Carlo Simulations", *Spin*, vol. 12, pp. 2250017, 2022.



- [23] S. Kumar, N. Kumar, K. Yadav, A. Kumar, “DFT investigations on optoelectronic spectra and thermoelectric properties of barium cadmium disulphide (BaCdS<sub>2</sub>)”, *Optik*, vol. 207, pp. 163797, 2020.
- [24] G. Kresse, J. Hafner, “Ab initio molecular dynamics for liquid metals,” *Physical Review B*, vol. 47, pp. 558–561, 1993.
- [25] G. Kresse, J. Furthmuller, “Efficiency of ab initio total energy calculations for metals and semiconductors using a plane-wave basis set,” *Computational Materials Science*, vol. 6, pp. 15–50, 1996.
- [26] P. E. Blöchl, “Projector augmented-wave method,” *Physical Review B*, vol. 50, pp. 17953-17979, 1994.
- [27] W. Kohn, L. J. Sham, “Self-Consistent Equations Including Exchange and Correlation Effects,” *Physical Review A*, vol. 140, pp. A1133-A1138, 1965.
- [28] P. Hohenberg, W. Kohn, “Inhomogeneous Electron Gas,” *Physical Review*, vol. 136, pp. B864-B871, 1964.
- [29] J. P. Perdew, K. Burke, M. Ernzerhof, “Generalized Gradient Approximation Made Simple,” *Physical Review Letters*, vol. 77, pp. 3865-3868, 1996.
- [30] H. J. Monkhorst, J. D. Pack, “Special points for Brillouin-zone integrations,” *Physical Review B*, vol. 13, pp. 5188-5192, 1976.
- [31] K. Momma, F. Izumi F, “VESTA: a three-dimensional visualization system for electronic and structural analysis,” *Journal of Applied Crystallography*, vol. 41, pp. 653: 658, 2008.
- [32] F. Han, “A Modern Course in the Quantum Theory of Solids.” Singapore World Scientific Publishing, pp. 378-379, 2013.
- [33] P. Vinet, J. H. Rose, J. Ferrante, J. R. Smith, “Universal Features of the Equation of State of Solids,” *Journal of Physics: Condensed Matter*, vol. 1, pp. 1941, 1969.



## Repair Analysis of Overlay Woven Fabric CFRP Laminates

Osman Çağlar Baysallı<sup>1</sup> , Alihan Cambaz<sup>1</sup> , Yasin Furkan Görgülü<sup>2\*</sup> , Arman Uluoğlu<sup>1</sup> , Umur Ulaş Harman<sup>1</sup> 

<sup>1</sup> Turkish Aerospace Industries Incorporation, Ankara, Türkiye, osmanbysll@hotmail.com, cambazalihan7@gmail.com, armanuluoglu@gmail.com, uuharman@gmail.com

<sup>2</sup> Isparta University of Applied Sciences, Keciborlu Vocational School, Department of Machinery and Metal Technologies, Isparta, Türkiye, yasingorgulu@isparta.edu.tr

\*Corresponding Author

### ARTICLE INFO

### ABSTRACT

#### Keywords:

CFRP Overlay Repair  
Composite Repair  
Prepreg Repair  
Repair Analysis  
Wet Lay-up



#### Article History:

Received: 20.08.2023

Accepted: 09.12.2023

Online Available: 22.04.2024

The increase in aerospace composites usage for structural components demands advanced repair analysis. Overlay repairs of carbon fiber-reinforced polymer laminates offer an alternative that is easier to perform and less time-consuming to produce than the widely used tapered scarf repair and stepped lap. Composite specimen manufacturing was based on both twill carbon/epoxy prepreg and wet lay-up. The repair was performed with both prepreg and wet extra plies to the parent prepreg structure. However, the design of overlay joints must be carefully investigated to avoid generating stress concentration regions at free edges. This study examined specific extra ply terminations' impact on peak stresses in the adhesive bond line. Linear finite element analysis was performed to conduct a maximum principal stress study with a focus on three joint design parameters: ply material, overply effect, and stacking sequence. FEA accurately predicted experimentally observed responses and provided further insight into the failure behavior of the structure. Results showed that overlay joints have a strong sensitivity to ply material type, the number of overply, and stacking sequence. The introduction of overplies provided protection and stiffness at joint tips, and an overply material behavior was identified. The location of  $\sigma$  plies in the composite laminates was highlighted as an important factor. The analysis was then extended to three-dimensional FE models for verification. In conclusion, results showed that high-stress concentration in overlay joints can be mitigated with the introduction of overplies and appropriate changes in joint design parameters to reduce stress peaks at joint tips and corners.

## 1. Introduction

With advancements in technology, the aviation industry has witnessed a significant increase in the use of composite materials. These materials offer exceptional strength-to-weight ratios and corrosion resistance, making them ideal for aerospace applications. The demand for lightweight aircraft structures has driven the adoption of composites in various components, including fuselages, wings, and interior parts. The progress in fiber-reinforced polymer composite materials has led to notable

improvements in the construction of lightweight structures [1].

In recent times, there has been a growing utilization of CFRP (Carbon Fiber-Reinforced Polymer) in airframes and engine components to decrease aircraft fuel usage. CFRP, possessing a minimum yield strength of 550 MPa, exhibits a density that is one-fifth that of steel and three-fifths that of aluminum-based alloys [2]. Despite considerable advancements in aerospace materials, certain obstacles remain, notably the insufficient strength to meet the rising need for lightweight materials [3].

While composites offer numerous benefits, composite structures are prone to various defects that can occur during manufacturing or while in use. These defects have the potential to impact the overall structural integrity, leading to a significant decrease in the strength and stiffness of the composite structure [4–7]. The repair of composite materials plays a crucial role in maintaining structural integrity, ensuring operational safety, and extending the service life of aircraft. However, repairing composites poses unique challenges due to their complex structures, anisotropic behavior, and the need to maintain material performance.

There is a study that evaluates the mechanical performance of damaged steel pipelines repaired with CFRP composites using finite element analysis. Two repair strategies, wrap and patch repair, are analyzed under Maximum Allowable Operating Pressure (MAOP) conditions. Findings suggest that thicker CFRP reduces stress in both the pipe wall and CFRP, and enhancing CFRP reinforcement can be achieved with higher elastic modulus infill materials [8].

Another aim of this research is to perform Finite Element Analysis (FEA) validation of mechanically tested and overlay-repaired aviation composites. The study focuses on evaluating the effectiveness and reliability of overlay repair techniques through numerical simulations. The key goals include assessing the structural performance, load-carrying capacity, and long-term durability of the repaired composite components.

FEA is an important tool in providing consistent data in the analysis and design of composite structures [9]. It enables engineers to simulate and predict the mechanical behavior of repaired composites, aiding in the optimization of repair processes and enhancing repair reliability.

This study also aims to provide a comprehensive analysis of the repair techniques for overlay woven fabric CFRP laminates. It will review the existing literature, highlighting the key findings and advancements in this field. Furthermore, it will present experimental results from the research, focusing on the evaluation of different

repair approaches and their impact on the laminates' performance.

This analysis is intended to contribute to the ongoing efforts to enhance the repair capabilities of overlay woven fabric CFRP laminates and provide insights for the design and implementation of more reliable and efficient repair methods.

## 2. Experimental Work

The manufacturing and repair process of composite laminates was carried out by standard repair procedures for the manufacture and repair of aircraft composite laminates. Made of M21/AS4C/ 40RC/T2/285/6K 2 × 2 twill carbon/epoxy fabric with cure coat thickness 0.285 mm 45/0/45/0/45/0/45 orientations 20 composite samples of 250x25x2 mm dimensions were produced at 180° and 7 bar pressure for 9 hours according to the specifications provided by the manufacturer [10].

The size and geometry of the test specimens were prepared according to the requirements of the ASTM Tensile Test Standard for Polymer Matrix Composites (D3039/3039 M) [11]. 20 mm x 20mm x 1.7 mm laminated part from the center of each sample was removed with 120° or finer sandpaper. The last ply of the sample was left and Hysol EA 9396 resin was injected into it. After the resin injection process was completed, HYSOL 9396 was cured at 66 +/- 2 degrees for 1 hour. Curing procedures were performed per the resin manufacturer's instructions.

After the curing process, 4 different sample types were created with different numbers of extra plies and wet with 12,5 mm overlapping, prepreg methods on the bag side and tool side. The first sample type was cured with 2 extra bag sides and 1 extra from the tool sides with the carbon prepreg method at 180 +/-5 degrees according to the autoclave manufacturer's requirements.

In the second sample type, additional carbons were laid by 2 bag sides and 2 tool sides by prepreg-applied and cured in an autoclave. The third sample type was created by laying extra carbons by the wet lay-up method by 2 bag sides and 1 tool side. The fourth sample type was

created by laying extra ply by 2 bag sides and 2 tool sides. The samples produced with the third and fourth type wet method were cured with HEATCON (heat blanket) in a 650 mmHg vacuum. For the wet method, Hexforce G0904 D 1070 TCT plain weave dry carbon fabric was laid using Hysol EA 9396 resin [10].

The properties of the carbon and resin laid with the wet method are given in Tables 1 and 2 [12]. All extra plies are laid at 45 degrees, and plies with the same orientation as the top ply have been selected. In the first and second sample types, the extra plies were laid with 12,5 mm overlapping using FM-300K film adhesive. FM-300K material properties are given in the table and cured according to the manufacturer's requirements.

After the repair and curing cycle of the prepared samples, they were examined with the help of Manual Ultrasonic Pulse Echo Inspection (MUPE), and defects such as delamination and debond were evaluated. In addition, the porosity values in the samples were observed by the MATEC ultrasonic tester (MA, USA) using the Automatic Ultrasonic Transition Method (AUTT).

Keeping the Porosity values at a 6 dB attenuation difference ( $\Delta$ dB) allows the samples to be accepted for testing. While 6 dB attenuation difference values were observed in the laminated non-resinous regions of the samples, a 15-20 dB attenuation difference was observed in the resin-filled region due to the nature of the resin.

Since the main purpose of the Nondestructive Inspection application is to see the porosity and defects in the laminate, the porosity value observed in the resin does not interfere with the test.

After the samples were inspected, plain tension tests of the samples were carried out according to ASTM 3039 with the Instron 8852 Tensile Testing Machine (MA, USA). The test setup can be seen in Figure 1. a clip-on extensometer was used to get more accurate results in stress and strain measurements.

**Table 1.** Mechanical properties of Hexforce G0904 plain weave dry carbon fabric impregnated with Hysol EA 9396 adhesive, with a 1/3 weight ratio and M21 / AS4C impregnated material [10, 13–15].

Property	Symbol	Hexforce G0904	M21 / AS4C
Elastic Modulus (GPa)	$E_{11}$	49.6	61.0
	$E_{22}$	49.6	61.0
	$E_{33}$	8.0	8.9
Shear Modulus (GPa)	$G_{12}$	3.3	4.2
	$G_{13}, G_{23}$	2.8	3.8
Tensile Strength (MPa)	$X_t$	517	930
	$Y_t$	517	940
Shear Strength (MPa)	$S_{12}$	60	96
	$S_{13}, S_{23}$	34	64
Poisson's Ratio	$\nu_{12}$	0.045	0.05
	$\nu_{13}, \nu_{23}$	0.28	0.3

**Table 2.** Mechanical Properties of the adhesives [13, 15–18].

Property	Symbol	FM-300K	HYSOL EA 996
Tensile Modulus (GPa)	E	3.12	2.7
Shear Modulus (GPa)	G	0.9	0.7
Tensile Strength (MPa)	$t_n^0$	72	55
Shear Strength (MPa)	$t_s^0, t_t^0$	42	26
Tensile Stiffness ( $N/mm^3$ )	$K_n$	15,600	$10^6$
Shear Stiffness ( $N/mm^3$ )	$K_s, K_t$	4500	$10^6$
Toughness in Tension (N/mm)	$G_{IC}$	1.1	0.3
Toughness in Shear (N/mm)	$G_{IIC}, G_{IIIC}$	4.8	0.5

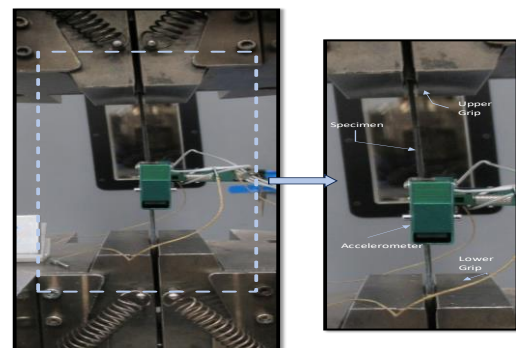


**Figure 1.** Test configuration.

### 3. Finite Element Model and Analysis

A three-dimensional finite element method for the overlay repairs was performed in ANSYS 2021 R1.

Fig 2 presents a schematic two-dimensional view of the model and its boundary conditions including the force of direction and fixed point (fixed joint). Specified material properties, geometry, and dimensions of the 3D model consisting of seven-layered composite laminates bonded by Hysol EA 9396 adhesive are kept the same as in experimental work. Individual plies with  $[45/0/45/0]_s$  pattern were discretely modeled. ply-by-ply surface contact is applied with a multipoint constraint (MPC) algorithm to obtain a perfect bonding between interfaces [19].

Discretized layers meshed with hexahedral 8-node elements were used. Four model fibers are aligned parallel to the loading direction along the x-axis, with overply lap length set at 0.5 inches  $[-45/+45]$  stacking sequence. The 3D finite element model consists of about 750,000 elements, the total number of elements is higher than about 550,000 elements done by Hamza and others [12]. Repair types are different from Hamza's work but the total area of geometry and discretized layers are very consistent with the model.

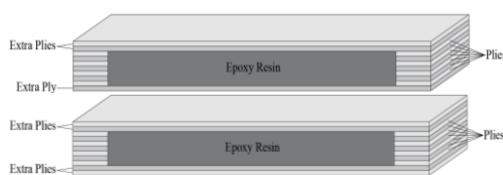


**Figure 2.** Schematic views of the repair configurations.

Linear static analysis was performed to investigate local peak stress. Primary stress includes peel stress, shear stress, and max principal stress to verify analysis with the help of test results. Peel (Normal) stress is considered along the Z-axis and shear stress was taken for both XY and XZ, but XY shear stress values are neglected as their values are smaller.

Failure load values of four specimens were investigated considering peak stress as given load from the test result. The gathered test results

agree with the observation made in the 3D finite element model. The addition of extra plies and different overply materials provided added stiffness and protection from local stress at adhesive tips.

#### 3.1. Maximum stress theory

Maximum Stress Theory states that failure happens if any stress along the material loading direction exceeds the allowable strength of the material. Five independent strength constants are important for a single ply [17, 20, , 21–28, 29–34]:

- $S_{Lc}$  – Longitudinal Compressive Strength
- $S_{Lt}$  – Longitudinal Tension Strength
- $S_{Tc}$  – Transverse Compressive Strength
- $S_{Tt}$  – Transverse Tension Strength
- $S_S$  – In-plane Shear Strength

To avoid failure, stress values along the loading direction have to be:

$$\begin{aligned} -S_{Lc} < \sigma_{11} < S_{Lt} \\ -S_{Tc} < \sigma_{22} < S_{Tt} \\ -S_S < \tau_{12} < S_S \end{aligned} \quad (1)$$

If it is the case that the material is loaded with simple tension which means  $\sigma_{xx}$  is present while,  $\sigma_{yy}$  and  $\sigma_{xy}$  values are negligible; three failure scenarios can be taken into account as follows:

1. Longitudinal to fiber direction, failure is primarily caused by fiber fracture:

$$\sigma_{xx} = \frac{S_{Lt}}{\cos^2 \theta} \quad (2)$$

2. Transverse to the fiber direction, failure is primarily caused by matrix or fiber-matrix composition:

$$\sigma_{xx} = \frac{S_{Tt}}{\sin^2 \theta} \quad (3)$$

3. Shear forces cause failure by matrix or fiber-matrix interface, or both at the same time:

$$\sigma_{xx} = \frac{S_S}{\sin \theta \cos \theta} \quad (4)$$



This theory falls short when one would like to interpret the interaction of stresses through all directions and their corresponding mixed failure modes, but it ensures a solid ground if the material is loaded with simple tension.

#### 4. Modeling Results and Discussion

The stress distributions of the four models are initially simulated and presented. Fig 3 demonstrates a comparison of experimental and numerical displacement curves for each overlay model. The results show that the finite element model can closely predict the actual load–displacement behavior.

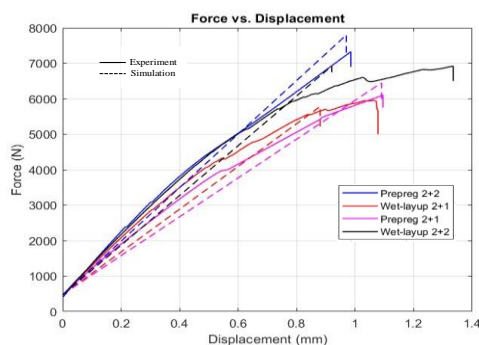


**Figure 3.** Comparison of experimental and numerical load-displacement curves for specimens with the wet lay-up and impregnated extra plies.

An adjustment to the excess of the experimental displacements may result from the positioning of the extensometer in the center of the sample and the subsequent integration of the displacement data. While scarf and step-lap repairs do not exhibit this change, overlapping fixes do [35]. Different stiffness leads to local peak stress variations through the thickness. Fig 4 depicts the 3D finite element peak shear and peel stress in the stress field in four models.

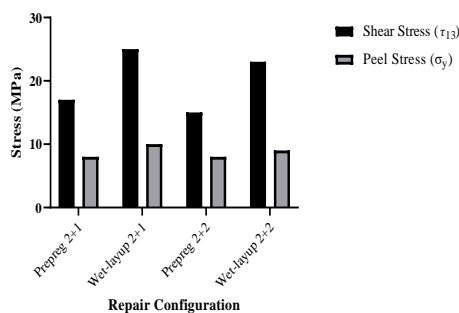


**Figure 4.** Failure peel and shear stress values for all models predicted by simulations.

For the four models, the main differences between wet-layup and prepreg repair stiffness consist of local peak stress along thickness and width which are highest near the free edges of the adhesive-filled area. Average stresses along with approximately constant but we focused on local peak stresses as local peak stresses reach allowable stress limits contributing to failure before average stresses. The stress variation of the four repair models is shown in Fig 4.

The finite element model provides investigation with stress concentration regions. High-stress concentration was observed at the corners contacting the adhesive in all 4 models. High peel and shear stresses were observed in 4 models since the 3-12° taper angle was not observed as in classical scarf repairs. Failure mode changed from cohesive to adhesive failure as the adhesive surface area was greatly reduced.

The adhesive zone creates a load path between the  $[45/0/45/0]_s$  parent structure. Since the adhesive cannot carry a sufficient load due to its low hardness value, shear, and peel stress peaks at the adhesive ends.

Thanks to the nature of the Continuum mechanic approach, stress-strain values are compared with allowable values which are obtained from test results. The singularity values observed in the adhesive-filled corners were eliminated by fine meshing. The absence of a progressive bonding surface such as step-wise or taper between the parent structure and the adhesive causes adhesive failure. Adhesive failure resistance values are much lower than cohesive failure, so it is not a desired failure.

##### 4.1. Maximum stress theory

Since Hysol EA9396 resin is a brittle material, it was also modeled above the thickness limits preferred in aviation, so the extra plies directly affected the strength. The maximum stress values observed at the points where the plies were in contact with the adhesive caused the failure.

The crack that started in the adhesive corners advanced in the 45° direction and exceeded the maximum shear strength of Hysol ea 9396. Since the overlap distances of the extra-laid carbons



were to be fixed above a certain limit, overplies of 12.5 mm were set. Extra-laid prepreg carbon plies were adhered using FM-300K film adhesive, causing potential porosity areas. Lower dB losses were observed in the carbons laid by hand layup in clean room conditions, compared to the models applied with the prepreg method.

Since the defects in the material directly affect its characterization, the differences in strength values in the models with extra laying vary between 15-20%. Since the stiffness values of the prepreg models are higher than the wet method, higher strength values were observed compared to the wet method.

#### 4.1. Effect of overply

Since the lap length is set to 12.5 mm, the main purpose of this article is to investigate the lacquer peak stresses that cause failure. In prepreg models, the effect of one extra individual 1 per 45° layer is about 15% power. The effect of the extra 45° layer is around 15% in the models laid with the wet method.

Peak stress fields observed at the tip of the adhesive cause the adhesive to deteriorate. Peel stress values are symmetrical along the x-axis from the center of the adhesive-filled area.

While shear stress values were found to be maximum at the adhesive ends, higher stress values were observed compared to the shear stress values. Shear stress values reach a maximum along the x-axis from the area filled with the adhesive to the ends.

The reason for limiting the number of extra plies in the building to 3-4 ply is to eliminate factors such as the human factor during the preparation of the prepreg model that will affect the behavior of the material, such as the porosity effect.

Since the symmetry is broken in the overlay models due to extra ply, bending occurred in the model, and local compressive stresses were observed. In the unsymmetrical extra plies, the highest stress values were obtained by making a finer mesh on the load path. These results are in good agreement with the test results.

## 5. Results and Discussion

M21 / AS4C composite material is produced in 4 models as its main structure. While an extra layer was laid on the area filled with the adhesive in the parent structure with the prepreg method, FM-300K was used while the extra layer was laid with the wet laying method, while Hysol EA9396 was used. Models laid with M21 / AS4C laminate showed higher strength thanks to its stiffness. However, the potential for porosity in the extra layers laid with FM-300k changes the failure mode. In this study, it was observed that the extra plies laid with the prepreg method caused the cohesive failure.

As can be seen in Figure 5, the extra-laid carbons did not cause undesired adhesive failure with good adhesion.

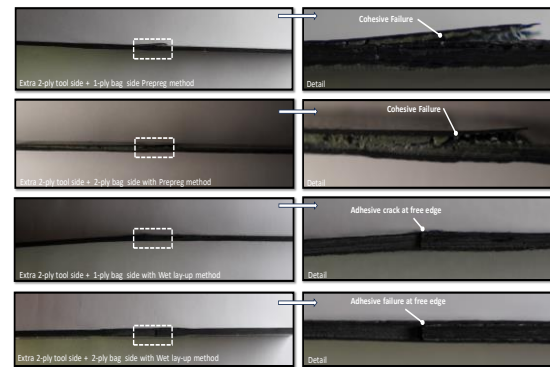


**Figure 5.** Failure cross-section of four models.

However, the failure loads in the Wet-layup method are satisfactory compared to the Prepreg method. Although wet lay-up repair stiffness values are low, HYSOL EA 9396 bonded adhered well to the adhesive-filled area.

Because lower  $\Delta$ dB were observed in the wet lay-up method, it prevented the expected failure load differences between repair models produced by the prepreg and the wet lay-up.

While 90-degree cracks were investigated in the adhesive-filled area in the samples with extra laying with the wet method, 45-degree cracks were observed in the adhesive-filled area in the samples that were extra-laid with the prepreg method.

The additional prepreg carbon-laid samples had higher local peak stresses, which sped up fracture

propagation. The load inputs and failure loads of the test samples from the extensometer were examined in the analyses. The extensometer adhesive was above the filled zone, which led to oscillation in the curve, which resulted in bearing damage and fractures.

While the adhesive was filled in the middle of the unrepaired samples, sandpaper caused buckling at the ply ends and the discontinuity in the structure caused heavy bearing damage at the edges of the adhesive-filled region.

It is produced as the parent structure of M21 / AS4C composite material in 4 models. FM-300K was used when laying extra ply on the shadow filled with the adhesive in the main structure with the prepreg method, and Hysol EA9396 was used when laying the extra ply with the wet lay-up method. Models laid with M21 / AS4C laminated showed higher strength due to its rigidity.

However, the porosity potential in the extra lays laid with FM-300k changes the failure mode. In this study, it was observed that the extra plies laid with the prepreg method caused the cohesive failure.

As can be seen in Figure 5, the extra-laid carbons did not cause undesired adhesive failure with good adhesion.

CFRP laminate specimens are modeled ply-by-ply and discretized because the composite structure is not homogeneous and is anisotropic. Lamina or ply analysis addressed and determined properties of plies which are oriented at an angle to the loading axis. Composite laminates are normally thin compared to their length and width and are loaded in plane stress conditions. This paper emphasized in-plane loading.

As shown in Fig 4., for positive shear stress, the maximum tensile stress is parallel to the fiber direction and is supported by strong fibers, if shear stress is negative, maximum tensile stress is perpendicular to the fiber direction and the matrix supports the load. Thus, a positive shear stress leads to higher load-carrying capability than a negative shear stress. Elastic constants of both on-axis and off-axis plies are obtained and used to predict overall laminate response using

maximum stress theory. Laminate theory estimates laminate behavior fairly accurately in the interior of the laminate.

However, within about one laminate thickness of free edges, lamination theory breaks down and fails to predict large interlaminar stresses that can develop. Large interlaminar stresses developed leading to bearing damage and adhesive cracking at the edges. Edge effects arise as a result of the requirement for strain compatibility between plies in laminate and adhesive-filled areas. Interlaminar shear and through-the-thickness peel stress develop near the free edges of laminate contact with the adhesive-filled area.

The principal reason for the development of these interlaminar stresses is a mismatch of Poisson's Ratio ( $\nu_{xy}$ ) and coefficients of mutual influence between adjacent plies. The difference in Poisson's ratios leads to different transverse contractions. This leads to interlaminar shear stresses between plies and the Hysol EA 9396 filled area. The adhesive-filled area created a free edge that led to the discontinuous middle of specimens. Interlaminar shear stresses between plies, forcing zero-degree ply to expand in the transverse direction and the 45-degree ply to contract.

The shear force is confined to the edge because once the required tension ( $\sigma_{yy}$ ) is established in zero-degree ply, compatibility is ensured across the middle of the laminate part. Shear stress obtained maximum at free edges,  $\sigma_{yy}$  a turning moment is produced thus to balance this moment, peel stresses develop in laminate with distribution indicated in figure 6. The strain observed in the specimens is shown in Figure 7. The tensile test results of the experiments obtained according to different layouts are given in table 3.

**Table 3.** Summary of the tensile testing results.

Specimen Type	# of Specimens Tested	Average Tensile Strength	Max Tensile Strength	CoV (%)	Recovery Rate
Extra Wet laid 2+1	5	119	128	7.0	22.8
Extra Wet laid 2+2	5	146	150	2.6	28.1
Extra Prepreg laid 2+1	5	132	141	6.3	25.3
Extra Prepreg laid 2+2	5	154	164	6.0	29.6
Intact	5	520	560	7.1	-

In the analysis of the 2+1 sample of the Extra Prepreg, it is observed that the top ply, having a higher stiffness than the resin, bears the load, leading to the initiation of delamination from the top ply. As only a single extra ply laid on the bag side is incapable of transferring the load, it separates and subsequently transfers the load to the resin, resulting in cracking at the free edge of the resin. As indicated in the analyses, maximum stress and strain values are observed in the free edge regions.

In the examination of stress and strain values in the 2+2 sample of Extra Prepreg, it exhibited a behavior similar to the 2+1 sample of Extra Prepreg, but due to the additional 1 ply effect, it failed at higher stress and strain levels. As illustrated in Figure 5, ply delamination was followed by film adhesive separation. The film adhesive separation causing cohesive failure continued along the resin free edges. Stress and strain values causing cohesive failure are observed in the resin free edges.

Upon examining the failure of the Extra Wet laid 2+1 sample, the reason for its differing appearance from the Extra Prepreg Laid 2+1 and Extra Prepreg Laid 2+2 samples lies in the inherent nature of the wet method, which does not necessitate the use of film adhesive. Similar to prepreg methods, the region filled with resin after the top ply delamination in the wet method failed as it could not transfer shear flow.

The wet approach's credibility for on-site repairs is increased when it exhibits behavior similar to the prepreg method. As evident in the analysis results, there is an approximate reasonable difference of about 3%.

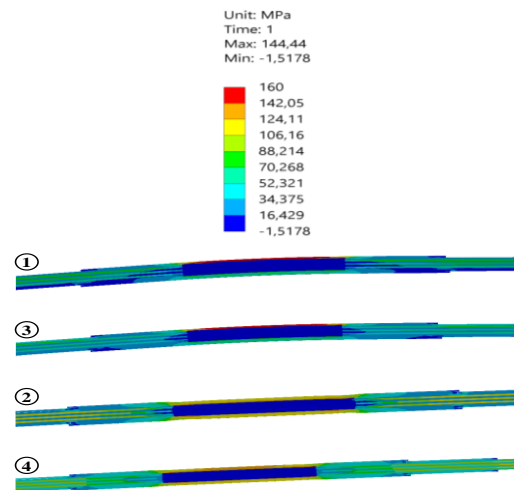


**Figure 6.** Stress results of CFRP laminate repaired: (1) extra wet laid 2+1, (2) extra wet laid 2+2, (3) extra prepreg laid 2+1, (4) extra prepreg laid 2+2.

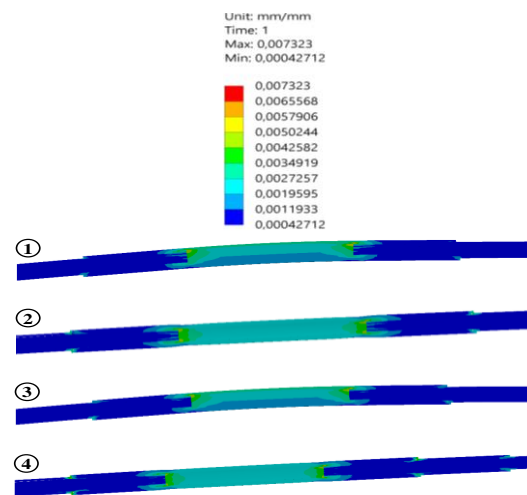


**Figure 7.** Strain results of CFRP laminate repaired: (1) extra wet laid 2+1, (2) extra wet laid 2+2, (3) extra prepreg laid 2+1, (4) extra prepreg laid 2+2.

In both the Extra Wet Lay-up 2+2 and Extra Prepreg Lay-up 2+2 samples, a symmetrical condition was achieved by adding two extra plies, resulting in both analysis and test outcomes showing no bending and being subjected to pure tension loading. In repairs using wet methods, the absence of film adhesive led to higher shear stress values, causing the structure to fail. As observed in the analysis results, failures were evident at 0.7% tension strain values.

When compared to the manufacturer-supplied strain value of 1.62% tension strain in the intact laminate structure, it was observed that separation occurred from the region in contact with the resin due to shear effects, without adherent failure.

## 6. Conclusion

In this study, both the number of extra plies and the repair technique (prepreg or wet lay-up) significantly influence the durability of the overlay + resin potted repair have been demonstrated. From the experimental findings, it is evident that as the number of additional plies approaches the thickness of the initial laminate stack-up, the strength of the repair increases. Specifically, prepreg repair techniques exhibited marginally higher tensile strength compared to wet lay-up overlay repair.

Comparatively, the FEA corroborated these experimental results, illustrating a similar trend in strength enhancement with increased ply numbers and favoring the prepreg method. The FEA also provided deeper insights into the stress distribution and potential failure points, which were observed to align with the experimental outcomes. Notably, cohesive failure was predominantly observed in prepreg repairs, a finding that was mirrored in the FEA through stress concentration analyses. Conversely, adhesive failures near the free edges of the resin-potted region, primarily seen in wet lay overlay repairs experimentally, were also predicted by the FEA models.

The congruence between the FEA and experimental results strengthens the validity of our findings. Further investigations, as highlighted by both methodologies, will focus on exploring the effects of varying overlap amounts and the impact of symmetric laminates with greater thickness than the tested laminate. This future research aims to refine our understanding of the repair mechanics and optimize repair methodologies for enhanced durability.

### Article Information Form

#### *Funding*

The authors have not received any financial support for the research, authorship or publication of this study.

#### *Authors' Contribution*

The authors contributed equally to the study.

#### *The Declaration of Conflict of Interest/ Common Interest*

No conflict of interest or common interest has been declared by the authors.

#### *The Declaration of Ethics Committee Approval*

This study does not require ethics committee permission or any special permission.

#### *The Declaration of Research and Publication Ethics*

The authors of the paper declare that they comply with the scientific, ethical and quotation rules of SAUJS in all processes of the paper and that they do not make any falsification on the data collected. In addition, they declare that Sakarya University Journal of Science and its editorial board have no responsibility for any ethical violations that may be encountered, and that this study has not been evaluated in any academic publication environment other than Sakarya University Journal of Science.

#### *Copyright Statement*

Authors own the copyright of their work published in the journal and their work is published under the CC BY-NC 4.0 license.

### References

- [1] P. Balakrishnan, M. J. John, L. Pothan, M. S. Sreekala, S. Thomas, "Natural Fibre Composites and their Applications in Aerospace Engineering," 2014.
- [2] D. K. Rajak, D. D. Pagar, P. L. Menezes, E. Linul, "Fiber-reinforced polymer composites: Manufacturing, properties, and applications," *Polymers*, vol. 11, no. 10, 2019.
- [3] B. Parveez, M. I. Kittur, I. A. Badruddin, S. Kamangar, M. Hussien, M. A. Umarfarooq, "Scientific Advancements in Composite Materials for Aircraft Applications: A Review," *Polymers*, vol. 14, no. 22, 2022.
- [4] R. F. El-Hajjar, D. R. Petersen, "Gaussian function characterization of unnotched tension behavior in a carbon/epoxy composite containing localized fiber



- waviness,” *Composite Structures*, vol. 93, no. 9, pp. 2400–2408, 2011.
- [5] H. M. Hsiao, I. M. Daniel, “Elastic properties of composites with fiber waviness,” *Composites Part A: Applied Science and Manufacturing*, vol. 27, no. 10, pp. 931–941, 1996.
- [6] C. Soutis, J. Lee, “Scaling effects in notched carbon fibre/epoxy composites loaded in compression,” *Journal of Materials Science*, vol. 43, no. 20, pp. 6593–6598, 2008.
- [7] H. Huang, R. Talreja, “Effects of void geometry on elastic properties of unidirectional fiber reinforced composites,” *Composites Science and Technology*, vol. 65, no. 13, pp. 1964–1981, 2005.
- [8] J. Chen, H. Wang, M. Salemi, P. N. Balaguru, “Finite element analysis of composite repair for damaged steel pipeline,” *Coatings*, vol. 11, no. 3, 2021.
- [9] E. Sonat, M. Bakır, S. Özerinç, “Failure behavior of on-site repaired CFRP laminates,” *Composite Structures*, vol. 311, no. June 2022, 2023.
- [10] Hexcel, “Composite Materials and Structures,” 2023. <https://www.hexcel.com/> (accessed Jun. 07, 2023).
- [11] ASTM, “D3039/D3039M Standard Test Method for Tensile Properties of Polymer Matrix Composite Materials.” [https://www.astm.org/d3039\\_d3039m-00.html](https://www.astm.org/d3039_d3039m-00.html) (accessed Jul. 27, 2023).
- [12] H. Bendemra, P. Compston, P. J. Crothers, “Optimisation study of tapered scarf and stepped-lap joints in composite repair patches,” *COMPOSITE STRUCTURE*, vol. 130, pp. 1–8, 2015.
- [13] E. Sonat, “Mechanical Properties of Repaired Carbon Fiber Reinforced Polymer Composites,” Middle East Technical University, 2021.
- [14] S.-H. Ahn, G. S. Springer, “Repair of Composite Laminates-II: Models,” *Journal of Composite Materials*, vol. 32, no. 11, pp. 1076–1114, Jun. 1998. [Online].
- [15] E. Sonat, S. Özerinç, “Failure behavior of scarf-bonded woven fabric CFRP laminates,” *Composite Structures*, vol. 258, no. September 2020, p. 113205, 2021.
- [16] Henkel, “LOCTITE® EA 9396 AERO,” 2023. [https://www.henkel-adhesives.com/vn/en/product/industrial-adhesives/loctite\\_ea\\_9396\\_aero0.html](https://www.henkel-adhesives.com/vn/en/product/industrial-adhesives/loctite_ea_9396_aero0.html) (accessed Jun. 07, 2023).
- [17] T. J, S. W, E. P, Y.-K. Y, “Shear Stress-Strain Data for Structural Adhesives,” 1997.
- [18] Solvay, “FM 300,” 2023. <https://www.solvay.com/en/product/fm-300> (accessed Jun. 07, 2023).
- [19] M. Kashfuddoja, M. Ramji, “Assessment of local strain field in adhesive layer of an unsymmetrically repaired CFRP panel using digital image correlation,” *International Journal of Adhesion and Adhesives*, vol. 57, pp. 57–69, 2015.
- [20] B. D. Agarwal, L. J. Broutman, *Analysis and Performance of Fiber Composites*, 3rd ed. Wiley Blackwell, 1980.
- [21] V. K. S. Choo, *Fundamentals of Composite Materials*. Knowen Academic Press, 1990.
- [22] R. M. Christensen, *Mechanics of Composite Materials*. Dover Publications, 2005.
- [23] I. M. Daniel, O. Ishai, *Engineering Mechanics of Composite Materials*, 2nd ed. Oxford University Press, 2005.
- [24] D. Gay, *Composite Materials: Design and Applications*. CRC Press, 2014.
- [25] Z. Hashin, B. W. Rosen, E. A. Humphreys,



- C. Newton, S. Chatterjee, “Fiber Composite Analysis and Design: Composite Materials and Laminates, Volume 1,” 1997.
- [26] L. P. Kollar, G. S. Springer, *Mechanics of Composite Structures*. Cambridge University Press, 2002.
- [27] M. Piggott, *Load Bearing Fibre Composites*. Kluwer Academic Publishers, 2002.
- [28] G. H. Stabb, *Laminar Composites*. Butterworth-Heinemann, 2015.
- [29] S. W. Tsai, H. T. Hahn, *Introduction to Composite Materials*. Technomic Publishing, 1980.
- [30] M. E. Tuttle, *Structural Analysis of Polymeric Composite Materials*. Marcel Dekker Inc., 2004.
- [31] V. V. Vasiliev, E. V. Morozov, *Mechanics and Analysis of Composite Materials*. Elsevier Ltd., 2001.
- [32] J. R. Vinson, R. L. Sierakowski, *The Behavior of Structures Composed of Composite Materials*, 2nd ed. Kluwer Academic Publishers, 2004.
- [33] L. J. Hart-Smith, D. Brown, S. Wong, “Surface Preparations for Ensuring that the Glue Will Stick in Bonded Composite Structures,” in *Handbook of Composites*, Boston, MA: Springer US, 1998, pp. 667–685.
- [34] F. C. Campbell, “Secondary Adhesive Bonding of Polymer-Matrix Composites,” in *Composites*, ASM International, 2001, pp. 620–632.
- [35] J. P. A. Valente, R. D. S. G. Campilho, E. A. S. Marques, J. J. M. Machado, L. F. M. da Silva, “Adhesive joint analysis under tensile impact loads by cohesive zone modelling,” *Composite Structures*, vol. 222, no. January, p. 110894, 2019.

## Optical Signal Investigation of Monolayer MoS<sub>2</sub> Grown Via Glass-Assisted CVD On Patterned Surfaces

Aydan Yeltik TOBB University of Economics and Technology, Faculty of Engineering, Department of Material Science and Nanotechnology Engineering, Ankara, Türkiye, [ayeltik@etu.edu.tr](mailto:ayeltik@etu.edu.tr)

### ARTICLE INFO

### ABSTRACT

Keywords:  
2D Material  
Transition Metal  
Dichalcogenide  
Photoluminescence  
Chemical Vapor Deposition  
Patterned Surface



Article History:  
Received: 27.08.2023  
Accepted: 05.01.2024  
Online Available: 24.04.2024

Enhancing photoluminescence (PL) in single-layer transition metal dichalcogenides has garnered significant interest, particularly for advancing high-performance 2D electronics and optoelectronics. The combination of surface engineering and contemporary growth methods has provided a platform for investigating optical signals. In this study, we present variations in PL and Raman signals of single-layer MoS<sub>2</sub> flakes grown conformally using the glass-assisted CVD method on square-patterned surfaces with varying well depths. PL spectroscopy revealed a systematic and pronounced enhancement in intensities as the valley thickness decreased from 285 nm to 225 nm. Conversely, for the hill regions of the samples, the PL intensity initially increased with decreasing valley thickness and then decreased, despite the hill regions having a constant thickness of 300 nm. On the other hand, PL maps did not exhibit a systematic dependence of intensities on the hill-valley thickness distinction, contrary to expected results based on literature data for similar materials on flat surfaces. The origin of the intensity oscillations was attributed to possible mechanisms, including thickness-dependent interference and strain-related exciton funneling effects. Additionally, Raman measurements revealed irregular variations in intensity in hill regions, dependent on the thicknesses of the underlying SiO<sub>2</sub> layers. Furthermore, we observed that the sizes of the flakes increased as the well depths of the underlying patterned surface decreased. This phenomenon might be attributed to alterations in the carrier gas flow pattern and varying temperature gradients between the hills and valleys. These results hold substantial potential to open new avenues for the integration of 2D transition metal dichalcogenides into on-chip electronic and optoelectronic devices.

## 1. Introduction

Transition metal dichalcogenide (TMD) materials have attracted considerable attention due to their advantageous properties, such as a tunable direct bandgap, high carrier mobility, and stability, crucial for future electronic and optoelectronic applications [1–6].

Previous studies have demonstrated enhanced photoluminescence (PL) in suspended graphene and MoS<sub>2</sub>, attributing it to the reduction of detrimental interactions with underlying substrates. These interactions include

nonradiative recombination, charge transfer, and various excitonic transitions [7–10]. Moreover, the dielectric surroundings around 2D materials were reported to regulate the in- and out-coupling of light, resulting in significant variations in PL and Raman intensities [11–15].

Zhang et al. examined the impact of multilayer film interference on the optical signal of single-layer MoS<sub>2</sub> on a flat SiO<sub>2</sub>/Si substrate, determining that the correct SiO<sub>2</sub> layer thickness is crucial for improving PL and Raman intensities [16]. Similarly, Lien et al. investigated thickness-dependent interference effects for

single-layer WSe<sub>2</sub>. They observed that the outcoupling mechanism, involving numerous reflections, leads to variations in PL signal depending on the thickness of the underlying SiO<sub>2</sub> surface [17]. Additionally, the dependence of the Raman signal of monolayer MoS<sub>2</sub> and WSe<sub>2</sub> on the thickness of the flat SiO<sub>2</sub> layer was revealed in previous studies [16, 17].

However, despite being a promising candidate among 2D TMDs with optoelectronic properties surpassing graphene and other 2D materials [18], the impact of surroundings on the optical signals of monolayer MoS<sub>2</sub> on patterned surfaces has not been thoroughly explored. Therefore, it remains both significant and challenging to examine the optical signal of monolayer MoS<sub>2</sub> based on the well depths of patterned surfaces in order to uncover the underlying mechanisms.

In this study, the impact of surface patterning on the PL and Raman signals of monolayer MoS<sub>2</sub> was investigated, correlating these effects with the depth of patterned wells. This variation in well depth induces changes in the surrounding dielectric environment and potentially other parameters. Patterned surfaces, featuring square arrays with varying well depths, were employed to elucidate the optical characteristics of monolayer crystals grown conformally on hill and valley regions. The properties of these flakes were predominantly investigated through atomic force microscopy (AFM),  $\mu$ -PL spectroscopy, and  $\mu$ -Raman spectroscopy.

By adjusting well depths, we achieved tunable and distinctive PL intensities specific to the thickness of the underlying substrate. Raman signals were also scrutinized, revealing negligible oscillatory behaviors. Furthermore, the lateral sizes of monolayer MoS<sub>2</sub> exhibited changes corresponding to the well depth of the patterned surfaces. The findings presented in this study demonstrate the substantial effects of patterned substrate features on the optical emission outcoupling of conformally grown monolayer MoS<sub>2</sub>.

## 2. Experimental Section

### 2.1. Surface patterning

SiO<sub>2</sub> surfaces on p-type Si substrates were patterned through a photolithography process followed by plasma etching. The Karl Suss MJB4 mask aligner facilitated the photolithography, while an inductively coupled plasma (Advanced Vacuum ICP) system was utilized for SiO<sub>2</sub> surface patterning. Initially, after substrate cleaning, samples were spin-coated with positive photoresist AZ5214E at 4000 rpm for 40 s and subsequently annealed at 110 °C for 50 s. Following alignment with the mask, the samples were exposed to UV for 50 s. UV-exposed areas were then developed using AZ 351B developer, and residual components were removed by washing with DI water. A protective layer was formed by waiting for 10 min at 110 °C. Patterning was achieved through an ICP etching process under the conditions of 40 sccm CF<sub>4</sub> gas flow, 700 mW power, and 100 mTorr pressure. Etching times were set at 5 s, 10 s, and 20 s to achieve SiO<sub>2</sub> layer thicknesses of 285 nm (15 nm depth), 270 nm (30 nm depth), and 225 nm (75 nm depth), respectively, at the valleys.

### 2.2. Growth precursors and wafers

Sulphur (S) (Sigma-Aldrich 99.98%) and molybdenum (MoO<sub>3</sub>) (SigmaAldrich 99.995%) precursors, both in powder form, were employed in amounts of 300 mg and 0.5 mg, respectively. Commercially obtained SiO<sub>2</sub>/Si substrates with lateral dimensions of 2 cm x 2 cm and lamellas measuring 2 cm x 2 cm x 0.15 mm were used. Energy dispersive X-ray (EDX) spectroscopy analysis revealed glass atomic concentrations of 9.42% sodium, 2.45% magnesium, and 2.28% calcium.

### 2.3. Crystal growth

A horizontal CVD system, featuring a quartz tube with a 7 cm diameter, was utilized for the growth of monolayer MoS<sub>2</sub> crystals (Figure 1). The system underwent pre-cleaning by raising the temperature to 1100 °C (with a rate of increase of 12 °C/min) under a 500 sccm N<sub>2</sub> gas

flow at atmospheric pressure, followed by a 20-minute waiting period. Soda-lime glass lamellas were positioned on the plate inside the system, with a graphite foil placed between them to prevent cracking. The SiO<sub>2</sub>/Si substrates were located near the lamellas, as depicted in the figure. Sulphur was placed in a quartz container, and MoO<sub>3</sub> was positioned on a SiO<sub>2</sub>/Si substrate. The distance between MoO<sub>3</sub>-S and MoO<sub>3</sub>-the beginning point of SiO<sub>2</sub>/Si substrates were determined as 4x and x, respectively, where x equals 4 cm. The growth conditions were maintained at 750 °C (with a rate of increase of 12 °C/min), 5 min duration, 150 sccm carrier gas flow rate, and 760 Torr pressure.

## 2.4. Material characterization

The Witec Alpha 300R  $\mu$ -Raman and  $\mu$ -PL spectroscopy system, equipped with a Zeiss objective, was employed for structural and optical analyses at room temperature. A continuous-wave laser with a 532 nm wavelength, 0.5 mW power, 1 s integration time, and a 300 nm spot size was used. Nanomagnetic Instruments AFM (tapping mode) was utilized for examining flake thickness, and 2D material morphologies were observed using the Nikon Eclipse LV100NDA microscopy system.

## 3. Results and Discussions

Figure 1 illustrates a schematic representation of the glass-assisted CVD MoS<sub>2</sub> configuration.

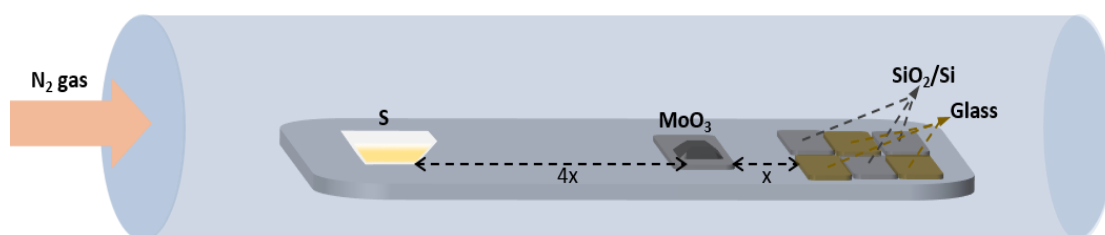


**Figure 1.** Schematic representation of the glass-assisted CVD configuration

In Figure 3(a-c), AFM images and corresponding thickness profiles of the flakes grown on the surfaces with three distinct valley thicknesses are presented. These profiles reveal that the thickness of the flakes is  $\sim 0.7$  nm, a value consistent with literature results for monolayer MoS<sub>2</sub> [22]. Moreover, measurements on the valley pattern regions indicated similar

The growth process was optimized for a three of which are SiO<sub>2</sub>/Si (with one patterned surface and two flat surfaces) and the remaining three are soda-lime glasses. Monolayer MoS<sub>2</sub> structures were grown on square-patterned silica surfaces with varying valley thicknesses, as depicted in Figure 2(a-c). The surfaces featured square patterns spaced approximately 20  $\mu$ m apart, with varying valley SiO<sub>2</sub> thicknesses (i.e., 285 nm, 270 nm, and 225 nm) serving as the growth substrates. To enhance the crystal growth rate, soda-lime glasses with a high sodium concentration were employed as growth promoters, aligning with findings from previous studies [19, 20]. The presence of sodium ions in the lamellas produces an intermediate product that is highly volatile compared to the melting point of MoO<sub>3</sub>. This, in turn, lowers the growth temperature, accelerating the MoS<sub>2</sub> growth process [18].

The size of the triangular-shaped MoS<sub>2</sub> flakes increased proportionally with the rise in valley thickness, as illustrated from (c) to (a) in Figure 2. While the primary cause for this difference may be attributed to alterations in the carrier gas flow pattern, sophisticated simulations are required to validate this argument. Additionally, the formation of larger flakes could be traced back to an elevated growth rate, potentially influenced by the varying temperature gradients between the hills and valleys [21].

thicknesses of around 0.7 nm, pointing towards conformal growth on the studied surfaces. The heightened surface wettability resulting from sodium content in the growth process aligns with the anticipated outcome of conformal growth in these samples [23]. Particles located at the edge of the crystal are often responsible for a sharp peak in the AFM line profiles, which is a

common phenomenon for CVD-grown MoS<sub>2</sub> without H<sub>2</sub> gas [24, 25]. At the edges of a MoS<sub>2</sub> flake, atoms experience a different environment compared to the interior of the crystal. The

coordination and bonding of atoms at the edge are altered, resulting in a modified electronic structure and, consequently, an increase in thickness at the edge.



**Figure 2.** Monolayer MoS<sub>2</sub> flakes on patterned surfaces with valley thicknesses of (a) 285 nm (15 nm depth), (b) 270 nm (30 nm depth), and (c) 225 nm (75 nm depth)

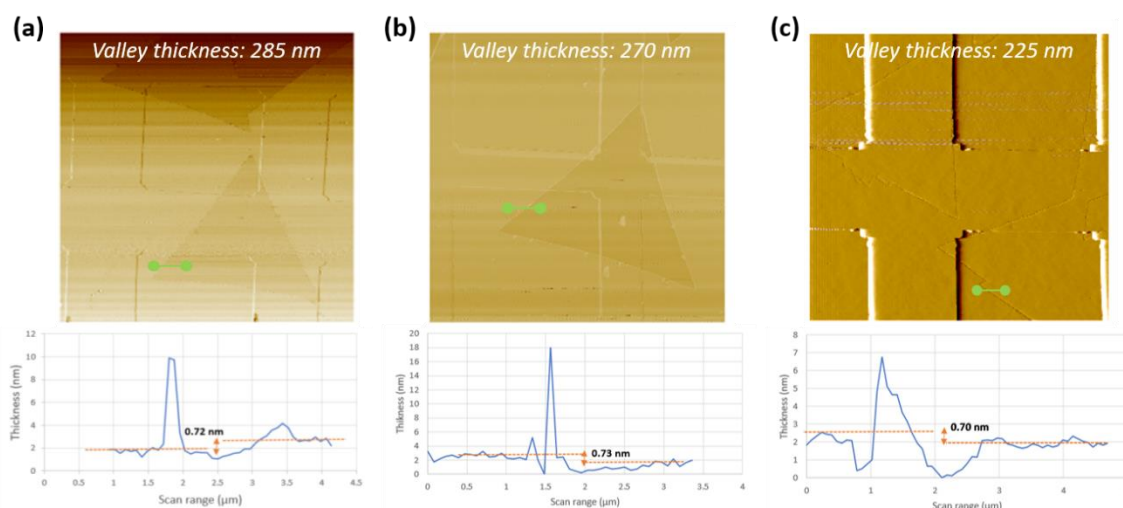


**Figure 3.** AFM images of MoS<sub>2</sub> materials on patterned surfaces with valley thicknesses of (a) 285 nm, (b) 270 nm, and (c) 225 nm, accompanied by the corresponding thickness profiles

Monolayer MoS<sub>2</sub> materials were further examined through  $\mu$ -PL and  $\mu$ -Raman spectroscopy. Figure 4(a-c) present PL intensity maps obtained with a 532-nm excitation wavelength from the flakes grown on the patterns with decreasing valley thicknesses (increasing well depths). The corresponding optical microscopy (OM) images of the flakes are inset in the figures. The PL intensities did not exhibit a systematic dependence on the hill-valley thickness distinction, which is not an expected result considering literature data for similar materials on flat surfaces [16, 17].

Zhang et al. previously explored the influence of multilayer film interference on the optical signal

of monolayer MoS<sub>2</sub> on SiO<sub>2</sub>/Si substrate and revealed that the proper SiO<sub>2</sub> layer thickness is important to enhance the PL and Raman intensities [16]. However, contrary to the presented results here at the 532-nm excitation wavelength, they observed PL enhancement with increasing thickness of flat SiO<sub>2</sub> in the spectral region we focused on (225 to 285 nm).

Similarly, Lien et al. investigated thickness-dependent interference effects for single-layer WSe<sub>2</sub>, revealing that the PL signal exhibited almost unvarying behavior between 225 and 285 nm thickness of the underlying SiO<sub>2</sub> layer. This behaviour was attributed to the outcoupling mechanism with multiple reflections [17].



Figure 5 presents separate PL intensity curves from the valley and hill regions. A systematic and pronounced enhancement in PL intensities was observed with decreasing valley thickness. Conversely, for the hill regions of the samples, the PL intensity initially increased with decreasing valley thickness and then decreased, despite the hill regions having the same thicknesses in these samples. The PL peak positions were determined to be 1.793, 1.818,

and 1.815 eV for SiO<sub>2</sub> valley thicknesses of 285 nm, 270 nm, and 225 nm, respectively (Figure 5(a)). Similarly, in the same order, the PL peak positions were found to be 1.794, 1.819, and 1.817 eV (Figure 5(b)) for SiO<sub>2</sub> hill regions with a constant thickness of 300 nm. The deconvoluted data and peak positions for each PL curve in Figure 5 are also presented in the supplementary file (Figure S1).

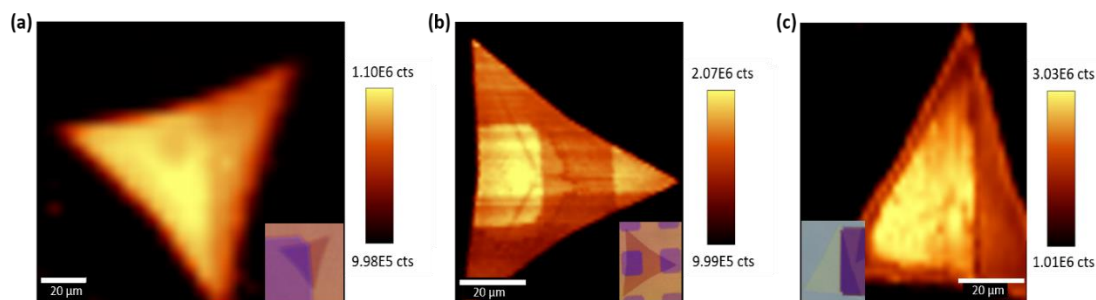


**Figure 4.** PL intensity maps of single-layer flakes on patterned surfaces with valley thicknesses of (a) 285 nm, (b) 270 nm, and (c) 225 nm. The insets show OM images of the flakes

In related literature, Wang et al. explored 2D materials on zero and non-zero Gaussian structures, such as trench and donut-like geometries [26]. They noted significant PL peak intensity changes between the valley and hill areas on both zero and non-zero Gaussian structures, attributing these variations to thickness-dependent interference. While over non-zero Gaussian regions, 2D materials grew under strain, resulting in a significant redshift at the PL peak wavelength, only minor meV shifts were observed in the PLs of our study obtained from the valley-hill regions of each sample.

Though exciton funneling effects were not expected to be evident in this study, strain-induced exciton funneling still might be the underlying mechanism for these nonuniform PL variations, yet there need to be more investigation including high resolution data on these findings especially from the vicinity of the pattern edges. Additionally, the location of the flakes on the patterns and the carrier gas flow pattern, as noted earlier for size distribution

variations, should be subjects of continued investigation for a more comprehensive understanding of these interesting optical results.

Raman spectral peaks corresponding to the E<sub>2g</sub><sup>1</sup> in-plane and A<sub>g</sub><sup>1</sup> out-of-plane modes at valley points were observed at around 384 and 404 cm<sup>-1</sup>, 381 and 400 cm<sup>-1</sup>, 383 and 402 cm<sup>-1</sup> for SiO<sub>2</sub> valley thicknesses of 285 nm, 270 nm, and 225 nm, respectively (Figure 6(a)). The change in the Raman modes, measured as  $\Delta=19-20$  cm<sup>-1</sup>, indicated the growth of monolayer MoS<sub>2</sub> on the studied patterned surfaces [27]. Similarly, Raman peaks at hill points were obtained at around 383 and 402 cm<sup>-1</sup>, 382 and 402 cm<sup>-1</sup>, 383 and 402 cm<sup>-1</sup> for SiO<sub>2</sub> valley thicknesses of 285 nm, 270 nm, and 225 nm, respectively (Figure 6(b)). The mode difference was measured as  $\Delta=19-20$  cm<sup>-1</sup>, indicating monolayer growth of MoS<sub>2</sub>. The Raman peak intensities remained approximately constant without a systematic variation particularly at the hill points.

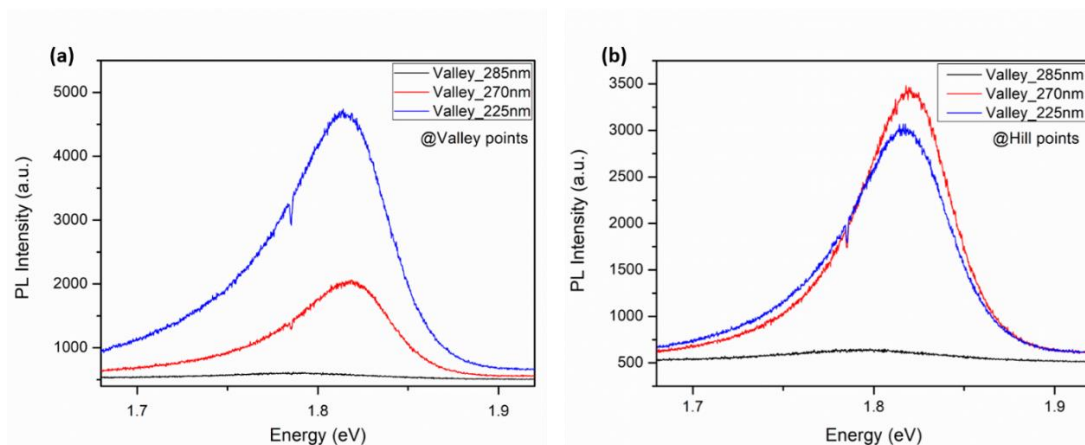


**Figure 5.** PL spectra from both the (a) valley and (b) hill regions of the samples with varying SiO<sub>2</sub> layer thicknesses at valleys. The hills correspond to 300 nm thick SiO<sub>2</sub> layer on Si for all the samples

Notably, there was no considerable spectral difference observed between the valley and hill regions with changes in underlying SiO<sub>2</sub> thickness. The 2LA mode observed at around 450 cm<sup>-1</sup> in the second-order Raman resonance, which involves longitudinal acoustic phonons, is attributed to the in-plane collective motions of atoms within the MoS<sub>2</sub> lattice [28]. The absence of additional Raman peaks suggests that glass components are not responsible for the varying intensity of PLs. As the study's parameters were consistently maintained, any potential doping effect is anticipated to be uniform across both hills and valleys. On the other hand, Zhang et al. reported enhanced modes of monolayer MoS<sub>2</sub> Raman signal from 225 nm to both 270 nm and 285 nm thicknesses of flat SiO<sub>2</sub> capping layers [16]. In addition, Lien et al. observed oscillatory behaviour in the Raman signal of single-layer WSe<sub>2</sub> between 225 and 285 nm thicknesses of underlying SiO<sub>2</sub>, attributed to multiple-reflection light outcoupling [17]. The optical signals of monolayer MoS<sub>2</sub> on the patterned surfaces in this study displayed distinct variation profiles with underlying SiO<sub>2</sub> thickness, contrary to literature values that typically use flat surfaces. These results suggest characteristic features specific to the studied patterned platform for monolayer MoS<sub>2</sub>.

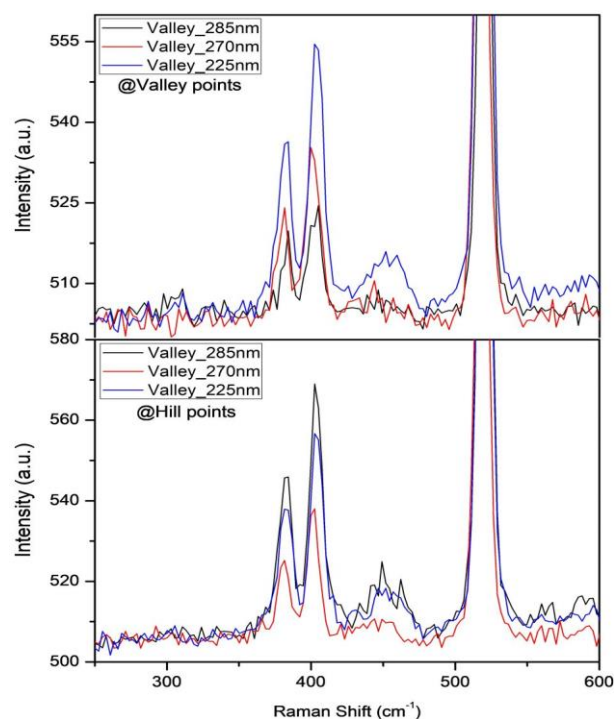


**Figure 6.** Raman spectra from both the (a) valley and (b) hill regions of the samples with varying SiO<sub>2</sub> layer thicknesses at valley

#### 4. Conclusions and Discussion

In conclusion, this study demonstrates that the optical signals of single-layer MoS<sub>2</sub>, grown conformally on square-patterned surfaces via glass-assisted CVD, exhibit distinct characteristics compared to those on flat platforms. Specifically, in samples with valley thicknesses of 285 nm and 270 nm, the PL intensity in square hills appeared higher than in valleys, whereas the opposite result was obtained in structures with a valley thickness of 225 nm.

Furthermore, the PL from the valley points enhanced as the valley thickness decreased from 285 nm to 225 nm, while the PL intensity initially increased for the hill regions with decreasing valley thickness and then diminished, despite the hill regions having a constant thickness of 300 nm. The oscillations in PL might be attributed to potential mechanisms, including thickness-dependent interference and strain-related exciton funneling effects.

Notably, the Raman signals of the samples did not exhibit a systematic behaviour at the hill points. Additionally, the lateral dimensions of the monolayer MoS<sub>2</sub> flakes showed varying behavior on the patterned surfaces with changes in well depth. This variability is likely a result of alterations in the carrier gas flow pattern and varying temperature gradients between the hills and valleys. These findings may pave the way for novel strategies in the effective integration of 2D TMDs into nanoelectronic and optoelectronic devices. Consequently, follow-up studies are of high significance to reveal the underlying mechanisms of the results presented in this study.

### Article Information Form

#### Acknowledgments

The author would like to thank Prof. Nihan Kosku Perkgoz and Prof. Feridun Ay for their valuable support.

#### Funding

The study was supported by The Scientific and Technological Research Council of Turkey Project Number: 121M601.

#### Authors' Contribution

Conceptualization, A.Y.; methodology, A.Y.; data curation, A.Y.; writing—original draft preparation, A.Y.; writing—review and editing, A.Y. All authors have read and agreed to the published version of the manuscript.

#### The Declaration of Conflict of Interest/ Common Interest

No conflict of interest or common interest has been declared by the author.

#### The Declaration of Ethics Committee Approval

This study does not require ethics committee permission or any special permission.

#### The Declaration of Research and Publication Ethics

The authors of the paper declare that they comply with the scientific, ethical and quotation rules of SAUJS in all processes of the paper and that they do not make any falsification on the data collected. In addition, they declare that Sakarya University Journal of Science and its editorial board have no responsibility for any ethical violations that may be encountered, and that this study has not been evaluated in any academic publication environment other than Sakarya University Journal of Science.

#### Copyright Statement

Authors own the copyright of their work published in the journal and their work is published under the CC BY-NC 4.0 license.

### References


- [1] W. Zhu, T. Low, H. Wang, P. Ye, X. Duan, "Nanoscale electronic devices based on transition metal dichalcogenides", *2D Materials*, vol. 6, no. 3, pp. 1–18, 2019.
- [2] T. J. Ko, M. Wang, C. Yoo, E. Okogbue, M. A. Islam, H. Li, M. S. Shawkat, S. S. Han, K. H. Oh, Y. Jung, "Large-area 2D TMD layers for mechanically reconfigurable electronic devices", *Journal of Physics D: Applied Physics*, vol. 53, no. 31, pp. 1–27, 2020.
- [3] E. Singh, P. Singh, K. S. Kim, G. Y. Yeom, H. S. Nalwa, "Flexible molybdenum disulfide (MoS<sub>2</sub>) atomic layers for wearable electronics and optoelectronics", *ACS Applied Materials & Interfaces*, vol. 11, no. 12, pp. 11061–11105, 2019.
- [4] J. Cheng, C. Wang, X. Zou, L. Liao, "Recent advances in optoelectronic devices based on 2D materials and their heterostructures", *Advanced Optical Materials*, vol. 7, no. 1, pp. 1–15, 2019.

- [5] S. Aftab, M. Z. Iqbal, S. Hussain, H. H. Hegazy, M. A. Saeed, "Transition metal dichalcogenides solar cells and integration with perovskites: A review", *Nano Energy*, vol. 108, no. 108249, pp. 1–17, 2023.
- [6] R. Sharma, R. Laishram, B. K. Gupta, "A Review on MX<sub>2</sub> (M = Mo, W and X = S, Se) layered material for opto-electronic devices", *Advances in Natural Sciences: Nanoscience and Nanotechnology*, vol. 13, no. 023001, pp. 1–18, 2022.
- [7] S. Berciaud, S. Ryu, L. E. Brus, T. F. Heinz, "Probing the Intrinsic properties of exfoliated graphene: Raman spectroscopy of free-standing monolayers", *Nano Letters*, vol. 9, no. 1, pp. 346–352, 2009.
- [8] D. Sercombe, S. Schwarz, O. Del Pozo-Zamudio, F. Liu, B. J. Robinson, E. A. Chekhovich, I. I. Tartakovskii, O. Kolosov, A. I. Tartakovskii, "Optical investigation of the natural electron doping in thin MoS<sub>2</sub> films deposited on dielectric substrates", *Scientific Reports*, vol. 3, no. 3489, pp. 1–6, 2013.
- [9] K. F. Mak, C. Lee, J. Hone, J. Shan, T. F. Heinz, "Atomically thin MoS<sub>2</sub>: A new direct-gap semiconductor", *Physical Review Letters*, vol. 105, no. 13, p. 136805, Sep. 2010.
- [10] N. Scheuschner, O. Ochedowski, A. M. Kaulitz, R. Gillen, M. Schleberger, J. Maultzsch, "Photoluminescence of freestanding single- and few-layer MoS<sub>2</sub>", *Physical Review B - Condensed Matter and Materials Physics*, vol. 89, no. 12, pp. 2–7, 2014.
- [11] H. Fang, H. A. Bechtel, E. Plis, M. C. Martin, S. Krishna, E. Yablonovitch, A. Javey, "Quantum of optical absorption in two-dimensional semiconductors", *Proceedings of the National Academy of Sciences of the United States of America*, vol. 110, no. 29, pp. 11688–11691, 2013.
- [12] S. L. Li, H. Miyazaki, H. Song, H. Kuramochi, S. Nakaharai, K. Tsukagoshi, "Quantitative raman spectrum and reliable thickness identification for atomic layers on insulating substrates", *ACS Nano*, vol. 6, no. 8, pp. 7381–7388, 2012.
- [13] D. Yoon, H. Moon, Y. W. Son, J. S. Choi, B. H. Park, Y. H. Cha, Y. D. Kim, H. Cheong, "Interference effect on Raman spectrum of graphene on SiO<sub>2</sub>/Si", *Physical Review B - Condensed Matter and Materials Physics*, vol. 80, no. 12, pp. 1–6, 2009.
- [14] F. G. Aras, J. Avad, A. Yeltik, "Glass-assisted chemical vapor deposition-grown monolayer MoS<sub>2</sub>: Effective control of size distribution via surface patterning", *Physica Status Solidi*, vol. 219, no. 24, pp. 1–8, 2022.
- [15] F. G. Aras, A. Yeltik, "Role of gas flow direction on monolayer MoS<sub>2</sub> growth on patterned surfaces via CVD", *Semiconductor Science and Technology*, vol. 38, no. 015013, pp. 1–8, 2023.
- [16] H. Zhang, Y. Wan, Y. Ma, W. Wang, Y. Wang, L. Dai, "Interference effect on optical signals of monolayer MoS<sub>2</sub>", *Applied Physics Letters*, vol. 107, no. 10, pp. 1–5, 2015.
- [17] D.-H. Lien, J. S. Kang, M. Amani, K. Chen, M. Tosun, H. -P. Wang, T. Roy, M. S. Eggleston, M. C. Wu, M. Dubey, S. -C. Lee, J. -H. He, A. Javey, "Engineering light outcoupling in 2D materials", *Nano Letters*, vol. 15, no. 2, pp. 1356–1361, 2015.
- [18] F. G. Aras, A. Yilmaz, H. G. Tasdelen, A. Ozden, F. Ay, N. K. Perkgöz, A. Yeltik, "A review on recent advances of chemical vapor deposition technique for monolayer transition metal dichalcogenides (MX<sub>2</sub>: Mo, W; S, Se, Te)", *Materials Science in Semiconductor Processing*, vol. 148, no. 106829, pp. 1–22, 2022.

- [19] G. U. Özküçük, C. Odacı, E. Şahin, F. Ay, N. K. Perkgöz, “Glass-assisted CVD growth of large-area MoS<sub>2</sub>, WS<sub>2</sub> and MoSe<sub>2</sub> monolayers on Si/SiO<sub>2</sub> substrate”, *Materials Science in Semiconductor Processing*, vol. 105, no. 104679, pp. 1–7, 2020.
- [20] I. W. Lisheshar, “Hybrid supercapacitors based on two dimensional materials: MXenes, Graphene and TMDCs”, Eskisehir Technical University, 2019.
- [21] Z. Cheng, M. Xia, S. Liu, R. Hu, G. Liang, S. Zhang, “Role of rough substrate on the growth of large single-crystal MoS<sub>2</sub> by chemical vapor deposition”, *Applied Surface Science*, vol. 476, pp. 1008–1015, May 2019.
- [22] H. Kim, W. Kim, M. O. Brien, N. Mcevoy, “Optimized single-layer MoS<sub>2</sub> field-effect transistors by non-covalent functionalisation”, *Nanoscale*, vol. 10, no. 37, pp. 17557–17566, 2018.
- [23] S. Li, “Salt-assisted chemical vapor deposition of two-dimensional transition metal dichalcogenides”, *iScience*, vol. 24, no. 11, p. 103229, 2021.
- [24] Y. Yoo, Z. P. Degregorio, J. E. Johns, “Seed crystal homogeneity controls lateral and vertical heteroepitaxy of monolayer MoS<sub>2</sub> and WS<sub>2</sub>”, *Journal of The American Chemical Society*, vol. 137, no. 45, pp. 14281–14287, 2015.
- [25] H. Liu, Y. Zhu, Q. Meng, X. Lu, S. Kong, Z. Huang, P. Jiang, X. Bao, “Role of the carrier gas flow rate in monolayer MoS<sub>2</sub> growth by modified chemical vapor deposition”, *Nano Research*, vol. 10, no. 2, pp. 643–651, 2017.
- [26] K. Wang, A. A. Puretzky, Z. Hu, B. R. Srijanto, X. Li, N. Gupta, H. Yu, M. Tian, M. Mahjouri-Samani, X. Gao, A. Oyedele, C. M. Rouleau, G. Eres, B. I. Yakobson, M. Yoon, K. Xiao, D. B. Geohegan, “Strain tolerance of two-dimensional crystal growth on curved surfaces”, *Science Advances*, vol. 5, no. 5, pp. 1–11, 2019.
- [27] T. Yang, X. Huang, H. Zhou, G. Wu, T. Lai, “Excitation mechanism of A<sub>1g</sub> mode and origin of nonlinear temperature dependence of Raman shift of CVD-grown mono- and few-layer MoS<sub>2</sub> films”, *Optics Express*, vol. 24, no. 11, p. 12281, 2016.
- [28] H. Guo, Y. Sun, P. Zhai, J. Zeng, S. Zhang, P. Hu, H. Yao, J. Duan, M. Hou, J. Liu, “Resonant Raman spectroscopy study of swift heavy ion irradiated MoS<sub>2</sub>”, *Nuclear Instruments and Methods in Physics Research B*, vol. 381, pp. 1–5, 2016.



## Ensuring Photocatalyst Properties on Cellulosic Fabric by Using Citric Acid Modified with TiO<sub>2</sub> Degussa P25 Nanoparticles

Sabiha Sezgin Bozok 

Çukurova University, Faculty of Engineering, Department of Textile Engineering, Adana, Türkiye, [sbozok@cu.edu.tr](mailto:sbozok@cu.edu.tr)

### ARTICLE INFO

### ABSTRACT

#### Keywords:

TiO<sub>2</sub>  
Degussa P25  
Citric Acid  
Cotton Dabric  
Photocatalyst

Citric acid, which is a type of polycarboxylic acid, is environmentally friendly, and non-harmful and it can be used as a cross-linker. Titanium dioxide (TiO<sub>2</sub>) nanoparticle is a catalyst that provides many properties for textile products with its large surface area. Present study, a mixture was prepared with different concentrations of citric acid and commercial TiO<sub>2</sub> Degussa P25 nanopowder suspensions. Two different curing temperatures (120°C and 140°C) were applied to the cotton fabrics in the pad-dry-cure method. The adhesion of the chemicals to the fiber surface was confirmed by scanning electron microscopy (SEM) and Fourier transform infrared spectrophotometer (FT/IR) analysis. The yellowing effect caused by citric acid on cotton fabrics was eliminated with white TiO<sub>2</sub> nanoparticles. Methylene blue was used for staining the samples. Color analyses were performed with a spectrophotometer to determine photocatalytic properties of the samples. It was determined that the samples treated with a mixture of 30 g/L citric acid and TiO<sub>2</sub> suspensions were the most discolored samples after exposure to solar light. The photocatalyst properties of the samples were further improved by removing the aggregation of TiO<sub>2</sub> NPs on the fiber surface with the washing procedure.

#### Article History:

Received: 06.09.2023  
Accepted: 03.01.2024  
Online Available: 24.04.2024

## 1. Introduction

Nano-sized titanium dioxide (TiO<sub>2</sub> NP) particles have high chemical stability and they are frequently used in many areas due to their functional properties such as photocatalyst, UV blocker, antibacterial activity, etc. Photocatalysts are the substances that activate the catalyst by light exposure. In photocatalytic reactions, when a photocatalyst is exposed to photon light, it becomes active and generates highly active radicals [1]. The resulting radicals and ions interact with the organic molecule and break it down. As a result of this decomposition, carbon dioxide and water are formed. Titanium dioxide (TiO<sub>2</sub>) is a good photocatalyst as a semiconductor with a band gap ranging from 3.0 to 3.2 eV. TiO<sub>2</sub> can be formed as anatase, rutile, and brookite phases, and these phases have different crystal forms and chemical stabilities.

These structures of titanium dioxide can be found in nature [2]. There is also a commercial titanium dioxide nanoparticle called Degussa P25, which is a mixture of anatase and rutile forms in a 3:1 volumetric ratio [3]. TiO<sub>2</sub> NPs can be produced by different methods such as sol-gel, chemical vapor deposition, and uniform precipitation [4]. The most widely used method for the impregnation of TiO<sub>2</sub> NPs on textile surfaces is the pad-dry-cure method [5]. Citric acid (2-hydroxy-1,2,3-tricarboxylic acid) is one of the low-cost, easily accessible chemicals used to bind the functional substance to the textile surfaces. Citric acid is a polycarboxylic acid that can interact with the hydroxyl groups in the structure of TiO<sub>2</sub> nanoparticles and thus can be modified with applications [6]. In a study, the effect of the surface chemistry of citric acid on TiO<sub>2</sub> nanoparticles in anatase form was examined. It was emphasized that the acidic pH

environment was important for adhesion and making a stable suspension but citric acid could cause an aggregation in an acidic pH environment [7]. In a study, TiO<sub>2</sub> NP anatase phase was impregnated in cotton-polyester blended fabrics by pad-dry-cure method using sodium hydrophosphite and citric acid mixtures in different concentrations [8].

In the results, it was determined that 30 g/L concentration of citric acid and 0.5% TiO<sub>2</sub> suspension were suitable mixture ratios and this mixture gave the material many properties such as self-cleaning and UV blocker. In another study, TiO<sub>2</sub> NPs were obtained by sol-gel method. In order to bind the produced TiO<sub>2</sub> NPs to cotton fabrics, citric acid solutions with different concentrations of 25, 30, 35, and 40 g/L (by also adding sodium hypophosphite) were prepared [9]. The prepared solutions were transferred to the fabrics by the pad-dry-cure method. The samples were then stained and exposed to UV light. Color differences before and after exposure were measured and calculated by a spectrophotometer. It was observed that TiO<sub>2</sub> NPs bonded with 25% citric acid solution provide the best self-cleaning feature on fabrics. In another study; TiO<sub>2</sub> was used as a catalyst and application was made to cotton fabrics at different concentrations, at different curing temperatures, at different times, and also at different citric acid concentrations [10]. The authors stated that the crease recovery of the fabric increased as the curing temperature, curing time, and citric acid concentration.

There is no study examining the effect of Degussa P25, which is stated to be one of the best photocatalysts than other pure TiO<sub>2</sub> phases, on cotton fabrics together with citric acid in the literature [11]. Citric acid was preferred as a crosslinker due to its environmentally friendly and harmless to human health. It was intended to determine the effect of different citric acid concentrations and different temperatures in the applications on photocatalyst activities and optical properties of cotton fabrics and also to investigate washing durability of the treatments. It was determined that the use of TiO<sub>2</sub> nanoparticles increased the whiteness value of the samples despite citric acid, and photocatalytic

properties were achieved with a mixture of 30 g/L citric acid and TiO<sub>2</sub> suspension.

## 2. Materials and Methods

### 2.1. Material

100% cotton, woven, and undyed fabric was used for the study, and the properties of the fabric are presented in Table 1. The chemicals used in the study; Degussa P25 titanium (IV) oxide (21 μm, ≥99.5%, Sigma Aldrich), citric acid (HOC(COOH)(CH<sub>2</sub>COOH)<sub>2</sub> ≥ 99.5%), sodium hydroxide (NaOH, ≥ 97%, Tekkim), Ethanol (96%, Tekkim) methylene blue (AFG Bioscience).

**Table 1.** Properties of the cotton fabric

<b>Fiber Type</b>	100% Cotton
<b>Weight in Grams</b>	240,7 g/m <sup>2</sup>
<b>Warp Yarn - Density</b>	Ne16 - 44 thread/cm
<b>Weft Yarn - Density</b>	Ne12,5 - 20 thread/cm
<b>Pretreatment Processes</b>	Bleached, Washed, Dried and Singed

### 2.2. Methods

#### 2.2.1. Modifying TiO<sub>2</sub> NP suspension and the treatment process

TiO<sub>2</sub> NP was weighed at the rate of 10% according to the fabric weight and mixed with ethanol:water at 1:9 volumetric ratio which is the ideal mixing ratio for the stability of the suspension [12]. Then, citric acid mixtures at different concentrations (10, 20, and 30 g/L) were prepared in distilled water and added to TiO<sub>2</sub> NP suspensions. TiO<sub>2</sub> NP and citric acid suspensions were mixed in a 1:1 volumetric ratio. In order to homogenize these mixtures, the process was applied in an ultrasonic bath (J. P. Selecta) at a frequency of 20 kHz for an hour. The pH level of the different mixtures was measured between 3.3-3.7.

The cotton fabric samples were first treated with 1% NaOH solution and dried at 100 °C. Afterward, the samples were kept in a small vat containing TiO<sub>2</sub> NP and citric acid mixtures for 30 seconds and then they were passed between rollers with 90% pick-up. This process was repeated twice. After the process was completed, all samples were dried at 100 °C degree. For the

curing process; in order to see the effect of the applied temperature on the adhesion of the modified TiO<sub>2</sub> NP to the fibers, some of the samples were cured at 120 °C degrees and some of them were cured at 140 °C degrees for 2 min (Scheme 1).

### 2.2.2. Characterization

In the study, some characterization tests were carried out to verify the processes applied to the samples. In order to examine the fiber surface morphologies of the samples, images were obtained with x5000 magnification using scanning electron microscopy (Scanning Electronic Microscope, FEI Quanta 650 Field Emission). Fourier transform infrared spectroscopy (JASCO FT/IR 6800) analysis was applied for the characterization of the samples by chemical analytical method.

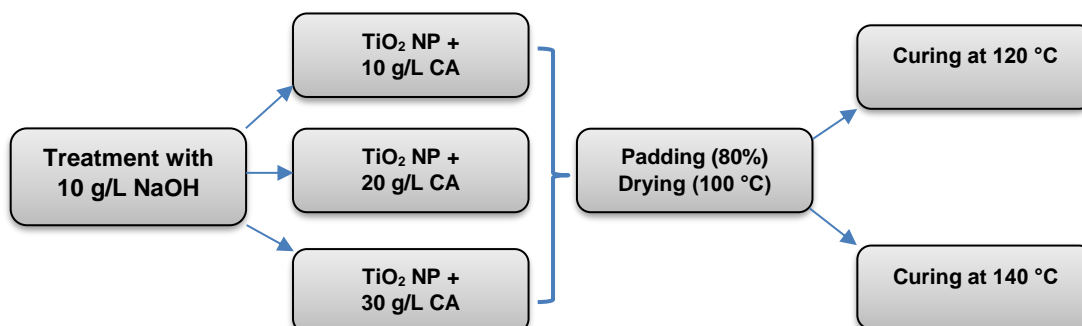
### 2.2.3. Washing durability

The permanence of the applied treatments after washing was determined by applying the ISO 105-C06:2010 standard. In accordance with the standard, the samples were washed in a washing machine at 40°C for 30 minutes by adding 4 g/L ECE detergent and 1 g/L sodium perborate into 150 mL of water in a tube. After washing, the samples were rinsed with distilled water (40 °C) and dried at room temperature. Treated samples were subjected to the performance tests after washing.

### 2.2.4. Photocatalytic and color measurements

Methylene blue (MB) is an aromatic heterocyclic basic dye and its chemical formula is C<sub>16</sub>H<sub>18</sub>ClN<sub>3</sub>S [13]. It can also be used in the treatment of many diseases [14]. In the study, the effect of functional finishing treatments applied to cotton samples on the degradation performance of this dye after light exposure was analyzed by color measurements. 0.02 g/L MB solution was prepared using distilled water to stain the samples with this dye. The cotton fabrics which were cut into small pieces were dipped in this solution for 30 sec.

Color measurements were carried out after the stained samples were dried. Color measurements were done with a spectrophotometer (Minolta CM 3600) at wavelengths between 400-700 nm, with an observer angle of 10°. Measurements were made in specular component included (SCI) mode, where the angle of reflection is equal to the angle of incidence of the light. Color analyses were performed with RealColor1.3® software. The effects of the chemical treatments on the whiteness (CIE W\*) and yellowness (ASTM D1925-70 YI) values of the samples, and the color changes of the samples stained with methylene blue after exposure to solar light were calculated. Treated and untreated samples stained with methylene blue were exposed to solar light directly (between 9:30-11:30 am, May, Adana, Turkey) for periods of 2, 4, 6, and 8 hours.



**Scheme 1.** Chemical treatments applied to the samples

The average UV radiation energy was determined as 23.01 MJ/m<sup>2</sup> (Eppley, Adana) on the days when the samples were exposed to the

sun. At the end of each period, color measurements were made and the total color difference ( $\Delta E$ ) (I) according to the initial color

of the samples and lightness ( $L^*$ ) values were calculated. These analyses were also applied to the washed samples and the washing durability of the process was determined.

$$\Delta E = [(\Delta L^*)^2 + (\Delta a^*)^2 + (\Delta b^*)^2]^{1/2} \quad (1)$$

### 3. Results and Discussion

#### 3.1. SEM and FT/IR analysis

The images of the untreated sample and the treated samples obtained by scanning electron microscope (SEM) with x5000 magnification and FT/IR graphs are presented in Figure 1. When the fiber surface morphology of the untreated sample is compared with the treated ones, it is determined that the applied treatment changed the fiber surface. The applied chemicals were deposited on the fiber's surface. It is seen that citric acid, which is a carboxylic acid, can be chemically bonded to cotton fibers [15]. As the citric acid concentration increased in the TiO<sub>2</sub> NP suspension, the fiber surface became rougher and aggregation occurred in some regions. Citric acid allowed TiO<sub>2</sub> nanoparticles to adhere to the fiber surface. It is observed that the samples treated with 20 and 30 g/L concentrations of citric acid and cured at 140°C degrees and regional tear-like structures were formed on the fiber surface. It can be claimed that the acidic environment and high temperature might have damaged the cellulosic fiber structure.

Fourier transform infrared spectra (FT/IR) are performed to determine characteristic functional groups. When the graphs are examined, it is seen that the absorption peaks of the samples were similar to each other. The peaks around 3328 cm<sup>-1</sup> are thought to originate from the free hydroxyl groups resulting from the O-H stretching vibration and the O-H band of the carboxylic acid attached to the hydroxyl groups of the cellulosic fiber surface [16]. When compared with the untreated sample, citric acid, a type of carboxylic acid, did not significantly contribute to this absorption peak. 2893-2898 cm<sup>-1</sup>, which is one of the major absorption peaks in the graphs, is from the C-H band stretch; 1624-1645 cm<sup>-1</sup> peaks are due to the moisture-induced H<sub>2</sub>O in the structure of the fibers [17]. The most striking difference between the graphs was that some samples

treated with citric acid with a concentration of 20 and 30 g/L showed absorption peaks around 1713-1714 cm<sup>-1</sup>. This is due to the C=O and ester carbonyl stretching of the polycarboxylic acid [10]. In addition, it may also be caused by the attachment of C=O group of citric acid to hydroxyl group (O-H) of TiO<sub>2</sub> nanoparticles [6, 18]. It was concluded that the interactions (modification) occurred on the fiber surfaces by using citric acid at these concentrations (20 and 30 g/L) in the applications. The peaks between 1424-1105 cm<sup>-1</sup> and 659-456 cm<sup>-1</sup> are the fingerprint region, and there is no significant difference between the samples in this region.

#### 3.2. Color measurements

##### 3.2.1. Whiteness and yellowness index

The graphs of the whiteness and yellowness index values of the samples are illustrated in Figure 2. It is accepted that the surface reflected the light more and its whiteness increased as the CIE W value, which expresses the whiteness index, increased. In light of this information, it was observed that the whiteness degrees of all of the treated samples were higher than the untreated control sample. TiO<sub>2</sub> Degussa P25 suspensions containing different concentrations of citric acid increased the whiteness of the samples. This can be explained by the fact that TiO<sub>2</sub>, a white pigment deposited on the cotton samples, caused them to reflect light more thus ensuring the sample to be perceived as whiter. The highest whiteness value belongs to the sample treated with 10 g/L citric acid-TiO<sub>2</sub> mixture and then cured at 120°C. The increase in the citric acid concentration applied to the treated samples also had a decrease in the whiteness values of the samples. In addition, when a comparison is made between the binary groups at the same concentration, it is noteworthy that the increase in the curing temperature caused the whiteness values of the samples to be lower. It is a result that has been also determined in a previous study that citric acid decreases the whiteness of cotton fabric with increasing curing temperature [19].



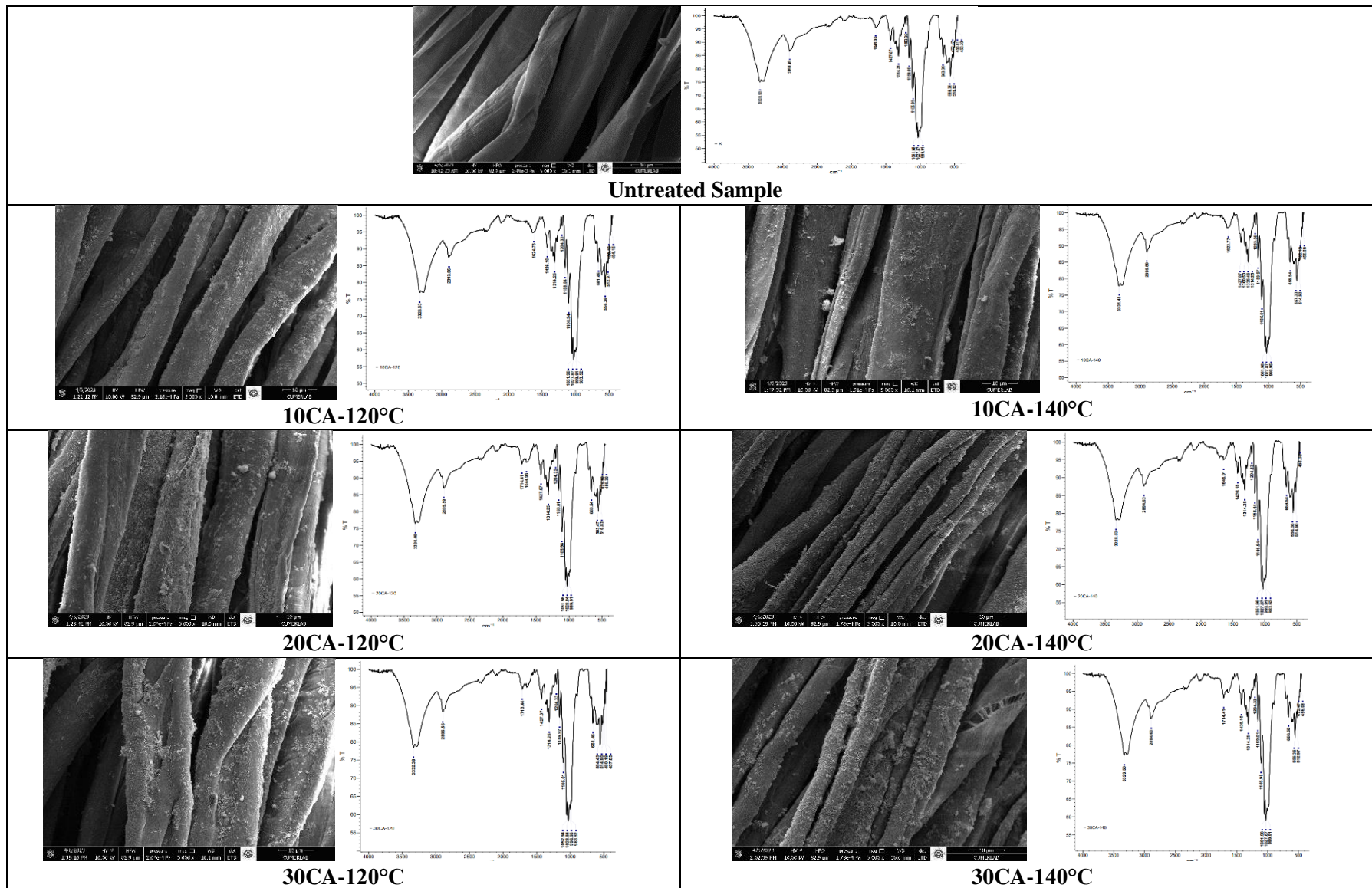


Figure 1. SEM images and FT/IR graphs of the cotton samples



The yellowness index value expresses the degree of shift towards yellow from the desired reference whiteness value. According to the ASTM D1925-70 YI results, the yellowness value of almost all samples decreased after chemical treatments. The yellowness index was lower in samples treated at 120°C, which is the lower curing temperature than in samples treated at 140°C. As the curing temperature increased, the whiteness of the samples decreased and the yellowness value increased. Unsaturated polycarboxylic acid structures of citric acid can cause yellowing [19, 20]. Titanium dioxide nanopowders applied to fabrics were able to eliminate this negative effect of citric acid causing yellowness in cotton fabrics. In another study, treatment with H<sub>2</sub>O<sub>2</sub> solution was applied to reduce the yellowness effect of citric acid and the yellowness index could be reduced by breaking the C=C bond of the carboxylic acid [21]. It was also determined in another study that the increasing concentration of TiO<sub>2</sub> NP was directly proportional to the increase in the whiteness rate and the decrease in the yellowness degree in cotton fabrics [22].

### 3.2.2. Photocatalytic measurements

In Figure 3, the effect of different treatments on the total color difference ( $\Delta E$ ) values of the cotton samples according to changing solar light exposure time is presented. While evaluating; it is assumed that as the  $\Delta E$  value decreased, the structure of MB (methylene blue) deteriorated and the samples came closer to the initial white color before staining. As expected, solar light caused a color change in all samples.

MB underwent oxidation after light exposure and the structure of the complex molecules was disrupted [13, 23]. All of the treated samples have a high tendency to return to their initial color after 2 hours of solar exposure, while this tendency is lower for the untreated control sample. In other words, TiO<sub>2</sub> NPs attached to the fibers with citric acid increased the rate of degradation of the dye. Degradation of MB is expected to be slow in visible light without a catalyst such as TiO<sub>2</sub> [13, 24]. Also, an acidic environment is a suitable condition for the photodegradation of MB by TiO<sub>2</sub> NP [25]. According to the color analysis made in this

period, the applications of TiO<sub>2</sub> NP with 30 g/L citric acid at 140°C were the processes that brought the cotton samples closer to their initial color, the  $\Delta E$  value of this sample is '3.32', while the sample treated at 120°C this value was '3.56'.

The  $\Delta E$  values of the samples treated with 20 g/L citric acid at 120 and 140 °C were '3.88' and '3.47', respectively. These results are very close to each other. This can be explained by the fact that even though the adsorption of TiO<sub>2</sub> Degussa P25 nanoparticles to the fiber is increased with higher citric acid concentrations, the surface area decreases due to the aggregation of nanoparticles and the photocatalyst property is limited [8].

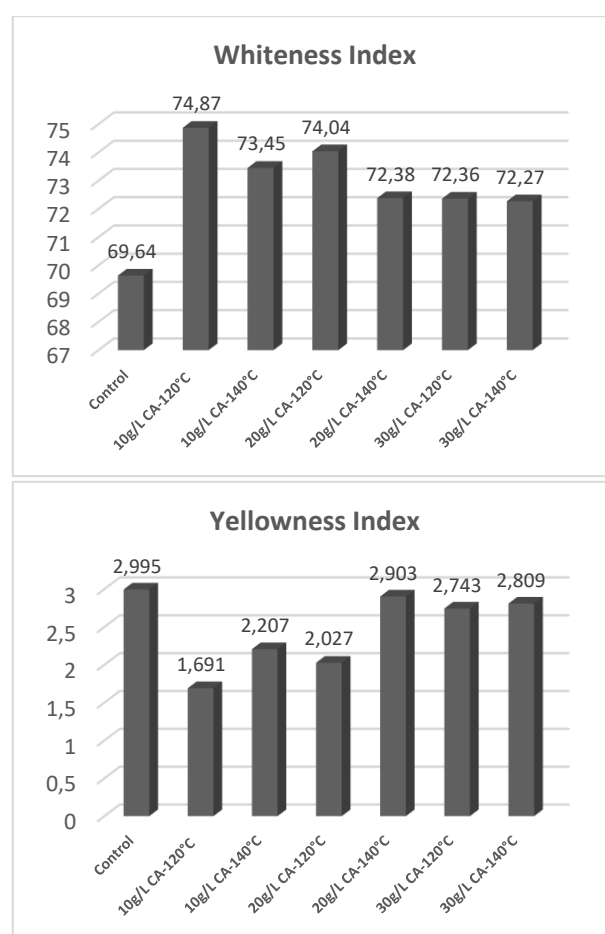


**Figure 2.** Whiteness and Yellowness Index of the untreated and treated samples

Besides, it was determined that the increase of twenty degrees of curing temperature did not have a significant effect on the photocatalyst properties of the samples.

In another study, it was also determined that the curing temperature did not affect the photocatalyst properties of the cotton samples,

using  $\text{TiO}_2$  (in an undetermined phase) together with citric acid [26]. As the curing temperature increases, carboxylic acids are consummated and their esterification with cellulose is accelerated [27]. As the temperature increases, the reaction approaches the equilibrium state. The effect of the higher curing temperature, and the acceleration of the displacement reaction of the -OH groups in the structure of the carboxylic acid with the -OR group did not have a great effect on the photocatalyst activity of  $\text{TiO}_2$  NPs. However, it is possible to observe this more clearly by working with a higher curing temperature. In Figure 4, the lightness ( $L^*$ ) values of the samples are presented after staining with MB and after 2, 4, 6, and 8-hour periods, respectively. As expected, the color of the samples became lighter as the exposure time to light increased. The effect of the applied treatments is remarkable even after the measurements at the end of the 2nd hour. The variation of the lightness values occurring in the colors of the samples according to time shows differences in each of them. The lightness values that change according to the solar exposure show a parallel change with the  $\Delta E$  values in Figure 2.

This shows that the increase in the  $L^*$  value of the samples made it closer to the initial color values of the samples and increased the total color difference ( $\Delta E$ ) according to the formula (I).

In the measurements made at the end of the eighth hour, it is seen that the color lightness of the samples increased as the citric acid concentration increased and the lightness value of the control samples was the lowest. However, the  $L^*$  values of the samples treated with 20 and 30 g/L citric acid are very close to each other. Different curing temperatures applied in the same citric acid concentration groups had almost no significant effect on the  $L^*$  values of the samples.

### 3.2.3. Washing durability

Figure 5 shows the total color difference values ( $\Delta E$ ) between the unstained treated sample and the treated, washed, stained samples that were exposed to solar light for eight hours.

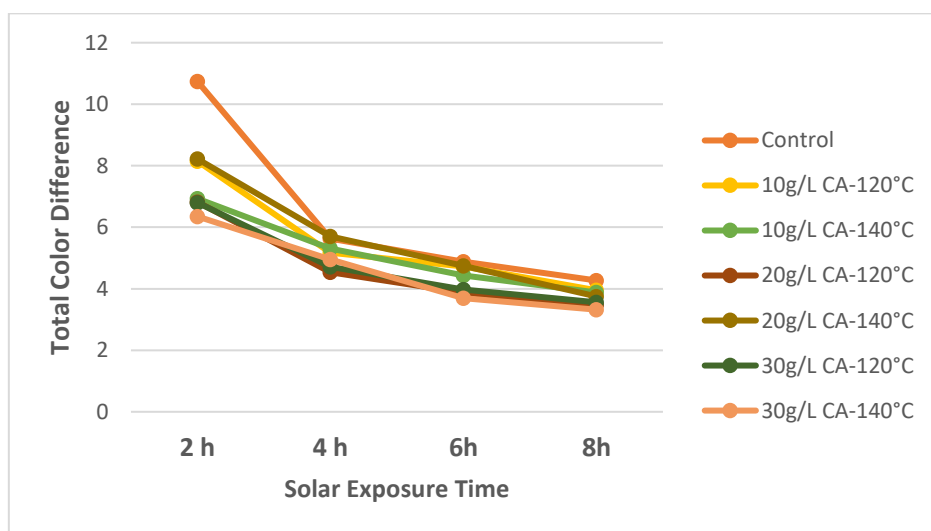


**Figure 3.** Effect of solar exposure time on the total color difference of the untreated and treated samples

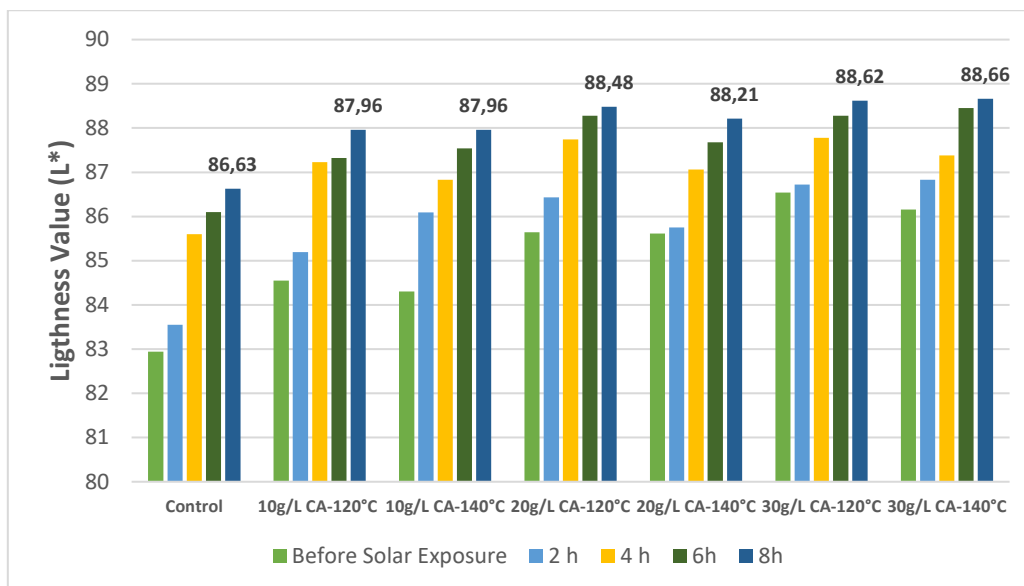


**Figure 4.** The lightness values of the samples before and after solar exposure at different periods

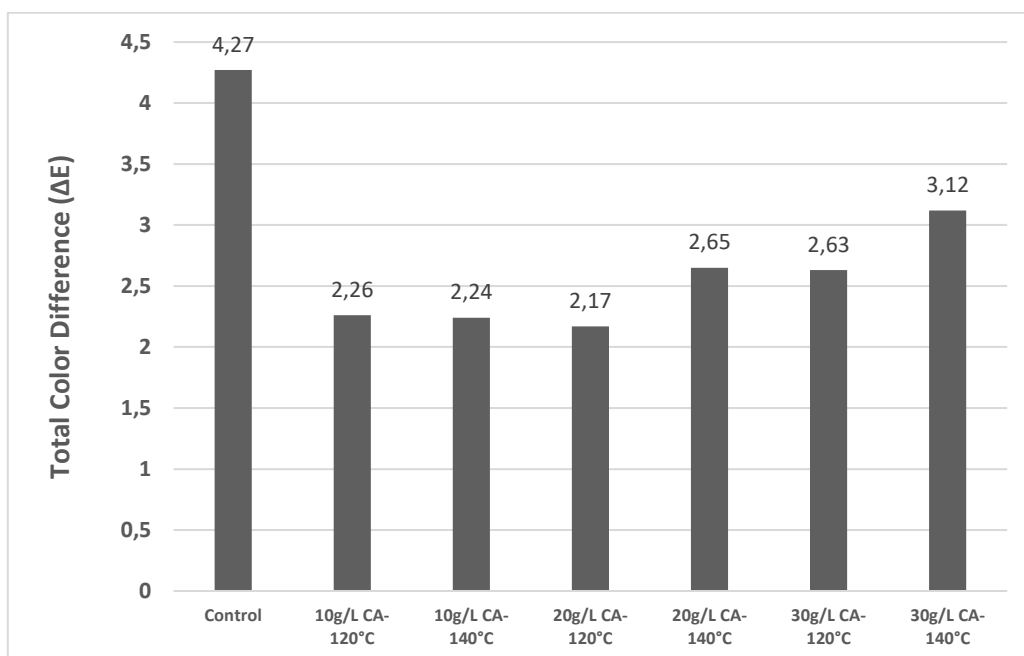


**Figure 5.** Total color difference values of untreated and washed treated samples according to their first color before and after eight hours

For comparison, the  $\Delta E$  values measured at the eighth hour of the untreated sample are also included in the graph. It can be clearly seen that all of the treated samples were closer to their initial color than the untreated sample. It can be stated that TiO<sub>2</sub> Degussa P25 NPs attached to the fiber surface with citric acid showed their permanence against washing conditions. In other previous studies, it has been observed that citric acid adheres tightly to cotton surfaces and maintains its permanence even after repeated washing [28]. In fact, after this washing process, the ability of the samples to return to their

original colors with solar light increased even more (compared to the Figure 3 results). This revealed the necessity of a post-washing process for cotton products after the binding of TiO<sub>2</sub> NPs to the fibers by using carboxylic acid as a cross-linker. In addition, the aggregation formed by TiO<sub>2</sub> nanoparticles formed in the acidic environment may have reduced the amount of radiation absorbed and its functionality by reducing the surface area [8]. It is thought that these agglomerations decreased with the washing process, the TiO<sub>2</sub> surface area increased further, and the photocatalyst performance of the samples

increased. While the tendency of the samples treated with 10 and 20 g/L citric acid concentrations to return to their initial colors is close to each other and the best, the difference is higher than the first color of the samples treated with 30 g/L citric acid.

It is thought that this is due to the result that as the citric acid concentration increases, the nanoparticles adhere more tightly to the fiber and some aggregations that have formed cannot be removed by washing.

#### 4. Conclusion

Citric acid is a polycarboxylic acid that is low-cost and harmless to the environment and human health. TiO<sub>2</sub> nanoparticle is an important semiconductor that plays a role in the degradation of organic pollutants by irradiation. Within the scope of the study, a commercial TiO<sub>2</sub> Degussa P25 nanopowder, which is a mixture of anatase/rutile phases, was mixed with citric acid which was used as a cross-linker to ensure the bonding of nanoparticles to the cellulosic fiber. SEM analysis showed that a higher number of TiO<sub>2</sub> nanoparticles adhered to the fiber surface at high citric acid concentrations. On account of TiO<sub>2</sub> Degussa P25 nanoparticles, yellowing caused by citric acid on cotton products was prevented and the samples became whiter. The samples stained with methylene blue were exposed to sunlight directly at different times and the color measurements of the samples were performed with a spectrophotometer. Accordingly, treatments with citric acid doped with TiO<sub>2</sub> Degussa P25 NP suspension provided accelerated degradation of MB that penetrated the cotton fabric. After 8 hours of irradiation, the color of the samples treated with TiO<sub>2</sub> Degussa P25 NP added 30 g/L citric acid solutions were closest to its initial color. Different curing temperatures did not have a significant effect on the photocatalyst property of the sample. The washing durability of the treatments was high, and even the photocatalyst properties of all samples treated at the end of the washing process increased even more. In future studies, the effect of different catalysts and mixtures of citric acid in varying proportion on self-cleaning

performances of textile products can be evaluated.

#### Article Information Form

##### *Funding*

This work was supported by the Çukurova University/Adana/TURKEY with FBA-2022-14649 project number.

##### *The Declaration of Conflict of Interest/ Common Interest*

No conflict of interest or common interest has been declared by the authors.

##### *The Declaration of Ethics Committee Approval*

This study does not require ethics committee permission or any special permission.

##### *The Declaration of Research and Publication Ethics*

The authors of the paper declare that they comply with the scientific, ethical and quotation rules of SAUJS in all processes of the paper and that they do not make any falsification on the data collected. In addition they declare that Sakarya University Journal of Science and its editorial board have no responsibility for any ethical violations that may be encountered, and that this study has not been evaluated in any academic publication environment other than Sakarya University Journal of Science.

##### *Copyright Statement*

Authors own the copyright of their work published in the journal and their work is published under the CC BY-NC 4.0 license.

#### References

- [1] B. Rani, A. K. Nayak, N. K. Sahu, "Fundamentals principle of photocatalysis", In: Nanostructured Materials for Visible Light Photocatalysis. Amsterdam: Elsevier Inc, 2022, pp. 1-22.
- [2] F. Parrino, F. R. Pomilla, G. Camera-Roda, V. Loddo, L. Palmisano, "Properties of titanium dioxide. In: Titanium Dioxide (TiO<sub>2</sub>) and Its Applications," Netherlands: Elsevier Inc., 2021, pp. 13-62.

- [3] M. A. K. L. Diasanayake, G. K. R. Senadeera, H. N. M. Sarangika, P. M. P. C. Ekanayake, C. A. Thorawattage, H. K. D. W. M. N. R. Divarathne, J. M. K. W. Kumari, "TiO<sub>2</sub> as a low cost, multi functional material," 5th International Conference on Functional Materials & Devices (ICFMD 2015). Materials Today: Proceedings 3S., 2016, pp. 40 - 47.
- [4] Y. Zhaodan, "Application of titanium dioxide nano-particles on textile modification," Advanced Materials Research Vols., vol.821-822, pp. 901-905, 2013.
- [5] M. Radeti c, "Functionalization of textile materials with TiO<sub>2</sub> nanoparticles," Journal of Photochemistry and Photobiology C: Photochemistry Reviews, vol. 16, pp. 62–76, 2013.
- [6] S. Mallakpour, N. Jarang, "Production of bionanocomposites based on poly(vinyl pyrrolidone) using modified TiO<sub>2</sub> nanoparticles with citric acid and ascorbic acid and study of their physicochemical properties" Polymer Bulletin, vol.75, pp. 1441–1456, 2018.
- [7] I. A. Mudunkotuwa, V. H. Grassian, "Citric Acid Adsorption on TiO<sub>2</sub> Nanoparticles in Aqueous Suspensions at Acidic and Circumneutral pH: Surface Coverage, Surface Speciation, and Its Impact on Nanoparticle-Nanoparticle Interactions", Journal of the American Chemical Society, vol. 132, pp. 14986-14994, 2010.
- [8] S. Hashemikia, M. Montazer, "Sodium hypophosphite and nano TiO<sub>2</sub> inorganic catalysts along with citric acid on textile producing multi-functional properties," Carbohydrate Polymers, vol. 147, pp. 139-145, 2016.
- [9] D. K. Maharani, M. M. S. Basukiwardoyo, S. T. Alawiyah, Rusmini, "The Study of self-cleaning properties of TiO<sub>2</sub> coated on cotton fabrics. Mathematics," Informatics, Science, and Education International Conference (MISEIC 2019). Advances in Computer Science Research, vol. 95, pp. 48-50, 2019.
- [10] A. A. Okeil, "Citric acid crosslinking of cellulose using TiO<sub>2</sub> catalyst by pad-dry-cure method," Polymer-Plastics Technology and Engineering, vol. 47, pp.174–179, 2008.
- [11] M. T. Noman, M. A. Ashraf, A. Ali "Synthesis and applications of nano-TiO<sub>2</sub>: a review," Environmental Science and Pollution Research, vol. 26, pp. 3262–3291, 2019.
- [12] S. Lebrette, C. Pagnoux, P. Ab elard, "Stability of aqueous TiO<sub>2</sub> suspensions: influence of ethanol," Journal of Colloid and Interface Science, vol. 280, pp. 400–408, 2004.
- [13] I. Khan, K. Saeed, I. Zekker, , B. Zhang, A. H. Hendi, A. Ahmad, S. Ahmad, N. Zada, H. Ahmad, L. A. Shah, T. Shah, I. Khan, "Review on Methylene Blue: Its Properties, uses, toxicity and photodegradation," Water, vol. 14, no. 242, pp. 1-30, 2022.
- [14] P. R. Ginimuge, S. D. Jyothi, "Methylene Blue: Revisited," Journal of Anaesthesiology Clinical Pharmacology, vol. 26, no.4, pp. 517-520, 2010.
- [15] M. Orhan, D. Kut, C. Gunesoglu, "Improving the antibacterial activity of cotton fabrics finished with triclosan by the use of 1,2,3,4- butanetetracarboxylic acid and citric acid," Journal of Applied Polymer Science, vol. 111, no. 3, pp.1344-1352, 2008.
- [16] W. Zou, H. Bai, S. Gao, X. Zhao, R. Han "Investigations on the batch performance of cationic dyes adsorption by citric acid modified peanut husk," Desalination and Water Treatment, vol. 49, pp. 41-56, 2012.
- [17] A. Haji, S. M. Bidoki, F. Gholami "Isotherm and kinetic studies in dyeing of citric acid-crosslinked cotton with cationic



- natural dye,” *Fibers and Polymers*, vol. 21, no.11, p. 2547-2555, 2020.
- [18] A. León, P. Reuquen, C. Garin, R. Segura, P. Vargas, P. Zapata, P. A. Orihuela, “FTIR and raman characterization of TiO<sub>2</sub> nanoparticles coated with polyethylene glycol as carrier for 2-methoxyestradiol,” *Applied Sciences*, vol. 49, no. 7, pp. 1-9, 2017.
- [19] Y. Lu, Q. Yang, “Fabric yellowing caused by citric acid as a crosslinking agent for cotton,” *Textile Research Journal*, vol. 69, no. 9, pp. 685-690, 1999.
- [20] W. Yao, B. Wang, T. Ye, Y. Yang, “Durable press finishing of cotton fabrics with citric acid: enhancement of whiteness and wrinkle recovery by polyol extenders,” *Industrial & Engineering Chemistry Research*, vol. 52, pp.16118-16127, 2013.
- [21] P. Tang, B. Ji, G. Sun, “Whiteness improvement of citric acid crosslinked cotton fabrics: H<sub>2</sub>O<sub>2</sub> bleaching under alkaline condition,” *Carbohydrate Polymers*, vol. 147, pp.139-145, 2016.
- [22] A. Haji, H. Barani, S. S. Qavamina, “Ag/TiO<sub>2</sub> nanocomposite on cotton fabric,” 5th Texteh International Conference Bucharest, Romania, 18-19 October, 2012.
- [23] K. Saeed, I. Khan, T. Gul, M. Sadiq, “Efficient photodegradation of methyl violet dye using TiO<sub>2</sub>/Pt and TiO<sub>2</sub>/Pd photocatalysts,” *Applied Water Science*, vol. 7, pp. 3841–3848, 2017.
- [24] T. E. Saraswati, I. F. Andhika, Patiha, C. Purnawan, S. Wahyuningsih, M. Anwar, “Photocatalytic degradation of methylene blue using TiO<sub>2</sub>/carbon nanoparticles fabricated by electrical arc discharge in liquid medium,” *Advanced Material Research*, vol. 1123, pp. 285–288, 2015.
- [25] F. Akbal, “Photocatalytic degradation of organic dyes in the presence of titanium dioxide under UV and solar light: effect of operational parameters,” *Environmental Progress.*, vol. 24, no. 3, p. 317-322, 2005.
- [26] A. Abou-Okeil, R. A. A. Eid, A. Amr, “Multi-functional cotton fabrics using nano-technology and environmentally friendly finishing agents,” *Egyptian Journal of Chemistry*, vol.60, pp. 161- 169, 2017.
- [27] H. Wang, C. Zhang, X. Chu, P. Zhu, “Mechanism of antiwrinkle finishing of cotton fabrics using mixed polycarboxylic acids,” *International Journal of Polymer Science*, pp. 1-10, 2020.
- [28] Y. S. Chung, K. K. Lee, J. W. Kim, “Durable press and antimicrobial finishing of cotton fabrics with a citric acid and chitosan treatment,” *Textile Research Journal*, vol. 68, no. 10, pp. 772-775, 1998.

## The Class of Demi-Strongly Order Bounded Operators

Gül Sinem Keleş<sup>1</sup> , Birol Altın<sup>2\*</sup> 

<sup>1</sup> Gazi University, Institute of Science, Department of Mathematics, Ankara, Türkiye, [Sinemkeles@outlook.com](mailto:Sinemkeles@outlook.com)

<sup>2</sup> Gazi University, Faculty of Science, Department of Mathematics, Ankara, Türkiye, [birola@gazi.edu.tr](mailto:birola@gazi.edu.tr)

\*Corresponding Author

### ARTICLE INFO

### ABSTRACT

Keywords:  
Riesz Space  
Strongly Order Bounded Operator  
B-Property  
Pre-Regular Operator

In this paper, we introduce the class of demi-strongly order bounded operators on a Riesz space generalization of strongly order bounded operators. Let  $M$  be a Riesz space, an operator  $H$  from  $M$  into  $M$  is said to be a demi-strongly order bounded operator if for every net  $\{u_\alpha\}$  in  $M^+$  whenever  $0 \leq u_\alpha \uparrow u''$ ,  $u''$  in  $M^{\sim\sim}$  and  $\{u_\alpha - H(u_\alpha)\}$  is order bounded in  $M$ , then  $\{u_\alpha\}$  is order bounded in  $M$ . We obtain a characterization of the b-property by the term of demi-strongly order bounded operators. In addition, we study the relationship between strongly order bounded operators and demi-strongly order bounded operators. Finally, we also investigate some properties of the class of demi-strongly order bounded operators.

### Article History:

Received: 05.10.2023

Accepted: 22.01.2024

Online Available: 24.04.2024

## 1. Introduction

In order to give our results, we need the following definitions and notations: Let  $M$  be a Riesz space. The order dual of  $M$  is denoted by  $M^\sim$ , and the order bidual of  $M$  is denoted by  $M^{\sim\sim}$ . A subset  $A$  of a Riesz space  $M$  is said to be order bounded if there exist  $x$  in  $M^+$  such that  $|y| \leq x$  for all  $y \in A$  [1]. The canonical embedding  $Q_M: M \rightarrow M^{\sim\sim}$  is defined by  $Q_M(x) = \hat{x}$ ,  $\hat{x}(f) = f(x)$ ,  $f \in M^\sim$ ,  $x \in M$  [1]. Let  $A$  be a subset of the Riesz space  $M$ , if  $Q_M(A)$  is order bounded in  $M^{\sim\sim}$ , then  $A$  is called  $b$ -order bounded in  $M$  [2]. A Riesz space  $M$  is said to have  $b$ -property if every  $b$ -order bounded subset of  $M$  is order bounded in  $M$  [3]. An operator  $H: M \rightarrow M$  between two Riesz spaces is said to be regular if it can be written as a difference of two positive operators [1].

Alpay S. and Altın B. introduced the strongly order bounded operators and recall from [4], let  $M, N$  be two Riesz spaces and  $H$  be an operator from  $M$  into  $N$ .  $H$  is said to be a strongly order bounded operator if for each net  $0 \leq u_\alpha \uparrow u''$  for some  $u''$  in  $M^{\sim\sim}$ , then  $H(u_\alpha)$  is order bounded in  $N$ ; in the other words, an operator  $H: M \rightarrow N$  is a strongly order bounded if it maps  $b$ -bounded subsets of  $M$  into order bounded subsets of  $N$ , and the class of all strongly order bounded operators will be denoted by  $L_{sb}(M, N)$ , the operator  $H$  is said to be the pre-regular operator if  $Q_N H$  is order bounded operator from  $M$  into  $N^{\sim\sim}$  [5]. An operator  $H$  from  $M$  into  $N$  is pre-regular if and only if  $H(A)$  is  $b$ -order bounded subset of  $N$  for each  $b$ -order bounded subset  $A$  of  $M$  [3]. The class of all pre-regular operators from  $M$  into  $N$  and on  $M$  are denoted by  $L_{pr}(M, N)$  and  $L_{pr}(M)$  respectively. The class of all linear operator on  $M$  is denoted by  $L(M)$ .

The demi notation was used firstly in [6] by Petryshyn. The class of weakly demicompact operators was studied in [7]. After that, the class of demi Dunford-Pettis operators was introduced in [8], and the class of order weakly demicompact operators was studied in [9]. More recently, another study on the demi class was studied by Benkhaled H. in [10].

In this study, we will introduce the class of demi-strongly order bounded operators which are a generalization of strongly order bounded operators given by [4], and we also investigate some properties of the class of demi-strongly order bounded operators.

In addition, we assume all Riesz spaces in this note have separating order duals. For all other undefined terms and notations, we will adhere to the conventions in [1].

## 2. Main Results

Let's start giving the definition of the demi-strongly order bounded operator.

**Definition 1** Let  $M$  be a Riesz space. An operator  $H$  from  $M$  into  $M$  is said to be a demi-strongly order bounded operator ( $d$  – sobo) if for every net  $\{u_\alpha\}$  in  $M^+$  whenever  $0 \leq u_\alpha \uparrow \leq u''$ ,  $u''$  in  $M^{\sim\sim}$  and  $\{u_\alpha - H(u_\alpha)\}$  is order bounded in  $M$ , then  $\{u_\alpha\}$  is order bounded in  $M$ . The class of all demi-strongly order bounded operators on  $M$  will be denoted by  $DL_{sb}(M)$ .

**Example 1** Let  $M$  be a Riesz space, then for all  $b \neq 1$ ,  $bI$  belongs to  $DL_{sb}(M)$ .

Assume that  $b \neq 1$ ,  $\{u_\alpha\}$  is a net in  $M^+$ ,  $0 \leq u_\alpha \uparrow \leq u''$ ,  $u''$  in  $M^{\sim\sim}$  and  $\{u_\alpha - bI(u_\alpha)\}$  is order bounded in  $M$ . Therefore, there exists  $y$  in  $M$  such that

$$|(u_\alpha - bI(u_\alpha))| \leq y$$

and

$$0 \leq |1 - b|u_\alpha \leq y$$

It follows that

$$0 \leq u_\alpha \leq \frac{y}{|1 - b|}.$$

Thus,  $\{u_\alpha\}$  is order bounded in  $M$ , and  $bI$  is a  $d$ -sobo.

The following theorem states that  $DL_{sb}(M)$  includes  $L_{sb}(M)$  for each Riesz space  $M$ .

**Theorem 1** Every strongly order bounded operator is a  $d$ -sobo.

**Proof.** Let  $M$  be a Riesz space,  $H \in L_{sb}(M)$ ,  $\{u_\alpha\}$  be a net in  $M^+$ ,  $0 \leq u_\alpha \uparrow \leq u''$ ,  $u'' \in M^{\sim\sim}$  and  $\{u_\alpha - H(u_\alpha)\}$  be order bounded in  $M$ . Hence, there exists  $y_1$  in  $M$  such that

$$|(u_\alpha - H(u_\alpha))| \leq y_1$$

for all  $\alpha$ . Since  $H$  is in  $L_{sb}(M)$ , there exists  $y_2$  in  $M$  such that

$$|H(u_\alpha)| \leq y_2$$

for all  $\alpha$ . We can write it as follows:

$$0 \leq u_\alpha = u_\alpha - H(u_\alpha) + H(u_\alpha)$$

$$\leq |(u_\alpha - H(u_\alpha))| + |H(u_\alpha)|$$

$$\leq y_1 + y_2.$$

Hence, we conclude that

$$0 \leq u_\alpha \leq y_1 + y_2.$$

Therefore,  $\{u_\alpha\}$  is order bounded in  $M$ , and  $H$  is a  $d$ -sobo.

The following example shows the converse of the above theorem is not generally true.

**Example 2** Let an operator  $H: c_0 \rightarrow c_0$  and  $H = \frac{1}{2}I$   $H$  is a  $d$ -sobo. Consider the sequence  $\{u_n\}$ , its first  $n$  terms are two, others are zero, and  $u = (2, 2, \dots)$ . It is satisfied  $0 \leq u_n \uparrow \leq u$  in  $c_0^{\sim\sim} = l_\infty$ , but  $H(u_n) = \frac{1}{2}(u_n)$  is not order bounded in  $c_0$ , hence  $H$  is not a strongly order bounded operator.

The next example shows that the inclusion  $DL_{sb}(M) \subseteq L(M)$  can be proper.

**Example 3** Let  $e_n$  be a sequence  $n$ th term is one, the other terms are zero,  $k \in \mathbb{N}$ , and  $H_k: c_0 \rightarrow c_0$  be an operator defined by  $H_k(x) = \sum_{i=1}^k x_i e_i$  for each  $x = (x_i) \in c_0$  where  $c_0$  is the set of all sequences of  $\mathbb{R}$  which converge to zero.  $H_k$  is the strongly order bounded operator, consider the sequence  $\{u_n\}$ , its first  $n$  terms are one, others are zero, and  $u = (1, 1, \dots)$ . Then, we have  $0 \leq u_n \uparrow \leq u$  in  $c_0^{\sim\sim} = l_\infty$ . Define  $S_k = I + H_k$  for each  $k \in \mathbb{N}$ .

$$|I(u_n) - S_k(u_n)| = |I(u_n) - I(u_n) - H_k(u_n)| = |H_k(u_n)|.$$

$H_k(u_n)$  is order bounded in  $c_0$ , but  $\{u_n\}$  is not order bounded in  $c_0$ . Hence,  $S_k$  is not in  $DL_{sb}(c_0)$  for each  $k \in \mathbb{N}$ .

**Theorem 2** Let  $M$  be a Riesz space,  $P: M \rightarrow M$  be a d-sobo, and  $S$  be in  $L_{sb}(M)$ , then  $P + S$  is a d-sobo.

*Proof.* Let  $\{u_\alpha\}$  be a net in  $M^+$ ,  $0 \leq u_\alpha \uparrow \leq u''$ ,  $u''$  in  $M^{\sim\sim}$  and  $\{u_\alpha - (P + S)(u_\alpha)\}$  be order bounded in  $M$ . Hence, there exists  $y_1$  in  $M$  such that

$$|(u_\alpha - (P + S)(u_\alpha))| \leq y_1$$

for all  $\alpha$ . Since  $S$  is in  $L_{sb}(M)$ , there exists  $y_2$  in  $M$  such that

$$|S(u_\alpha)| \leq y_2$$

for all  $\alpha$ . We can write also

$$|u_\alpha - P(u_\alpha)| = |(u_\alpha - P(u_\alpha) - S(u_\alpha) + S(u_\alpha))|$$

$$\leq |(u_\alpha - (P + S)(u_\alpha))| + |S(u_\alpha)|$$

$$\leq y_1 + y_2.$$

We obtain that  $\{u_\alpha - P(u_\alpha)\}$  is order bounded in  $M$ . Since  $P$  belongs to  $DL_{sb}(M)$ , then  $\{u_\alpha\}$  is order bounded in  $M$ . Hence,  $P + S$  is a d-sobo. However, as the next example shows,  $DL_{sb}(M)$  is not a vector space in general.

**Example 4** Let  $H$  be an operator on  $c_0$ , defined as  $H = \frac{1}{2}I$ .  $H$  is a d-sobo, but  $H + H = I$  is not a d-sobo.

The identity operator is not a d-sobo in general. For example, consider the identity operator  $I$  on  $M = c_0$  and the sequence  $\{u_n\}$ , its first  $n$  terms are one, others are zero. It is obvious that  $0 \leq u_n \uparrow \leq u = (1, 1, \dots)$  in  $c_0^{\sim\sim} = l_\infty$ , and  $|I(u_n) - I(u_n)| = |(0)|$  is order bounded in  $M$ , but  $\{u_n\}$  is not order bounded in  $M$ . Hence,  $I$  is not a d-sobo on  $M$ .

Recall that an operator  $T: M \rightarrow N$  between two Riesz spaces is said to be order bounded if it maps order bounded subsets of  $M$  into order bounded subsets of  $N$ , and the class of all order bounded operators from  $M$  into  $N$  will be denoted by  $L_b(M, N)$  [1].

The following theorem gives us a characterization of the b-property.

Let  $M$  and  $N$  be two normed Riesz spaces and  $K = M \oplus N = \{(a, b) : a \in M, b \in N\}$  if  $K$  is equipped with the coordinatewise order that is  $(a_1, b_1) \leq (a_2, b_2) \Leftrightarrow a_1 \leq a_2$  and  $b_1 \leq b_2$  for each  $(a_1, b_1), (a_2, b_2) \in K$  and the norm  $\|(a, b)\|_K = \|a\|_M + \|b\|_N$ , then  $K$  will be the normed Riesz space [1].

**Theorem 3** Let  $M$  and  $N$  be two Riesz spaces. Then the following operators are d-sobo.

(i) All operators  $R$  on  $M$  which  $(I - R)^{-1}$  exists and is order bounded.

(ii)  $(S_\beta)$  is the class of operator on  $K$ , defined by

$$\text{the matrix } \begin{pmatrix} 0 & 0 \\ R & \beta I \end{pmatrix} \text{ on } K \text{ for the every order}$$

bounded operator  $R$  from  $M$  into  $N$  where  $K = M \oplus N$  and  $\beta$  is a real number different to one.

*Proof.* (i) Assume that  $\{u_\alpha\}$  is a net in  $M^+$ ,  $0 \leq u_\alpha \uparrow \leq u''$ ,  $u''$  in  $M^{\sim\sim}$  and  $\{u_\alpha - R(u_\alpha)\}$  be order bounded in  $M$ . Thus, there exists  $y_0$  in  $M$  such that

$$\{u_\alpha - R(u_\alpha) : \alpha \in \Lambda\} \subseteq [-y_0, y_0]$$

for all  $\alpha$ . Since  $[-y_0, y_0]$  is order bounded in  $M$  and  $(I - R)^{-1}$  is order bounded, then there exists  $x_0$  in  $M$  such that  $(I - R)^{-1}([-y_0, y_0]) \subseteq [-x_0, x_0]$ .

Now, we can write

$$\begin{aligned} u_\alpha &= (I - R)^{-1}(I - R)(u_\alpha) \\ &\subseteq (I - R)^{-1}([-y_0, y_0]) \\ &\subseteq [-x_0, x_0]. \end{aligned}$$

Hence,  $\{u_\alpha\}$  is order bounded; consequently,  $R$  belongs to  $DL_{sb}(M)$ .

(ii) Let  $\{z_\alpha\}$  be a net in  $K$ ,  $0 \leq z_\alpha \uparrow \leq z''$ ,  $z''$  in  $K^{\sim\sim}$ ,  $z_\alpha = (x_\alpha, y_\alpha) \in K$ ,  $\{(I - S_\beta)(z_\alpha)\} \subseteq M \oplus N$  be order bounded. It will be shown that  $\{z_\alpha\} = \{(x_\alpha, y_\alpha)\}$  is order bounded in  $K$ .

$$\begin{aligned} (z_\alpha - S_\beta(z_\alpha)) &= ((x_\alpha, y_\alpha) \\ &\quad - (0, R(x_\alpha) + \beta y_\alpha)) \end{aligned}$$

$$= (x_\alpha, y_\alpha - R(x_\alpha) - \beta y_\alpha)$$

$$= (x_\alpha, (1 - \beta)y_\alpha - R(x_\alpha))$$

Since  $\{(I - S_\beta)(z_\alpha)\} \subseteq M \oplus N$  is order bounded and from the above equality, then  $\{x_\alpha\}$  and  $\{(1 - \beta)y_\alpha - R(x_\alpha)\}$  are order bounded in  $M$  and  $N$  respectively. Hence, there exists  $y_1$  in  $N$  such that

$$|(1 - \beta)y_\alpha - R(x_\alpha)| \leq y_1$$

for all  $\alpha$ . Since  $R$  is order bounded, then  $\{R(x_\alpha)\}$  is order bounded in  $N$ . There exists  $y_2$  in  $N$  such that

$$|R(x_\alpha)| \leq y_2$$

for all  $\alpha$ . We can write also

$$|(1 - \beta)y_\alpha| = |(1 - \beta)y_\alpha - R(x_\alpha) + R(x_\alpha)|$$

$$\leq |(1 - \beta)y_\alpha - R(x_\alpha)| + |R(x_\alpha)|.$$

Hence, we obtain that

$$|y_\alpha| \leq \frac{1}{1 - \beta}(y_1 + y_2).$$

Therefore,  $\{y_\alpha\}$  is order bounded in  $N$ , so  $\{z_\alpha\} = \{(x_\alpha, y_\alpha)\}$  is order bounded in  $K$ .

The following example gives that Theorem 3 is not valid in case  $\beta = 1$ .

Now, it is clear that  $K = c_0 \oplus c_0$  is a Banach lattice with the coordinate wise order and the norm  $\|x\| = \|a\| + \|b\|$  for each  $x = (a, b) \in K$  [1].

**Example 5** Let an operator  $H: c_0 \rightarrow c_0$ ,  $K = c_0 \oplus c_0$  equipped with coordinate wise order and operator  $S$  is defined by  $\begin{pmatrix} 0 & 0 \\ H & I \end{pmatrix}$ .  $S$

does not belong to  $DL_{sb}(K)$ . Indeed, consider the sequence  $z_n = (0, u_n)$  and  $u_n$  the first  $n$  term equals one, and others are zero. It is clear that  $0 \leq z_n \uparrow$  and  $\|z_n\| = 1$  for each  $n \in \mathbb{N}$ . Since  $\{z_n\}$  is increasing, norm bounded and  $K$  is a Banach lattice  $\{z_n\}$  is b-order bounded in  $K$  from Corollary 3.4 in [11]. Hence, there exists  $u''$  in  $K''$  such that  $0 \leq z_n \uparrow \leq u''$  where  $K''$  is the second norm dual of  $K$ .

It is clear that

$$(I - S)(z_n) = (z_n - S(z_n))$$

$$= [(0, u_n) - (0, I(u_n))] = (0, 0).$$

Therefore,  $\{(I - S)(z_n)\}$  is order bounded in  $K$ , but  $S$  is not a d-sobo, since  $\{z_n\}$  is not order bounded in  $K$ .

By the term of d-sobo of identity operator it is obtain that a characterization of the b-property.

**Theorem 4** Let  $M$  be a Riesz space, then the following assertions are equivalent.

(i) All pre-regular operators  $H: M \rightarrow M$  are d-sobo.

(ii)  $I: M \rightarrow M$  is d-sobo.

(iii)  $M$  has b-property.

**Proof.** (i)  $\Rightarrow$  (ii) It is clear.

(ii)  $\Rightarrow$  (iii) Assume that  $\{u_\alpha\}$  is a net in  $M^+$ ,  $0 \leq u_\alpha \uparrow \leq u''$ ,  $u''$  in  $M^{\sim\sim}$ . Since  $|(I - I)(u_\alpha)| = 0$  is order bounded in  $M$  and



$I \in DL_{sb}(M)$ , then  $\{u_\alpha\}$  is order bounded in  $M$ . Hence,  $M$  has b-property.

(iii)  $\Rightarrow$  (i) Let  $H$  be a pre-regular operator on  $M$ ,  $\{u_\alpha\}$  be a net  $M^+$ ,  $0 \leq u_\alpha \uparrow \leq u''$ ,  $u''$  in  $M^{\sim\sim}$ .  $H(u_\alpha)$  is b-order bounded in  $M$  from Proposition 1 in [3]. Since  $M$  has b-property, then  $H(u_\alpha)$  is order bounded in  $M$ , and we get  $H$  is in  $L_{sb}(M)$ . Hence,  $H$  is d-sobo from Theorem 1.

Let  $H, S$  be two operators on the Riesz space  $M$  and  $0 \leq S \leq H$ . If  $H$  is a d-sobo, then  $S$  is not a d-sobo in general. Hence, the class of demi-strongly order bounded operators does not satisfy the domination property.

**Example 6** Let  $H, S$  be two operators on  $c_0$ ,  $S = I$  and  $H = 2I$ . It holds  $0 \leq S \leq H$  and  $H$  is a d-sobo, but  $S$  is not a d-sobo.

Domination property for d-sobo is satisfied under certain condition as follows.

**Theorem 5** Let  $S, H$  be two positive operators on the Riesz space  $M$  and  $0 \leq S \leq H \leq I$ . If  $H$  is a d-sobo, then  $S$  is also a d-sobo.

*Proof.* Let  $\{u_\alpha\}$  be a net in  $M^+$ ,  $0 \leq u_\alpha \uparrow \leq u''$ ,  $u''$  in  $M^{\sim\sim}$  and  $\{u_\alpha - S(u_\alpha)\}$  be order bounded in  $M$ . Hence, there exists  $y_1$  in  $M$  such that

$$0 \leq u_\alpha - S(u_\alpha) \leq y_1$$

for all  $\alpha$ . It is clear that

$$0 \leq (I - H)(u_\alpha) \leq (I - S)(u_\alpha) \leq y_1.$$

Hence,  $\{(I - H)(u_\alpha)\}$  is order bounded in  $M$ . Since  $H$  belongs to  $DL_{sb}(M)$ , then  $\{u_\alpha\}$  is order bounded in  $M$ ; consequently,  $S$  belongs to  $DL_{sb}(M)$ .

**Theorem 6** Let  $M$  be a Riesz space,  $S$  and  $H$  be two operators on  $M$  and  $I \leq S \leq H$ . If  $S$  belongs to  $DL_{sb}(M)$ , then  $H$  belongs to  $DL_{sb}(M)$ .

*Proof.* Assume that  $\{u_\alpha\}$  is a net in  $M^+$ ,  $0 \leq u_\alpha \uparrow \leq u''$ ,  $u''$  in  $M^{\sim\sim}$  and  $\{(H - I)(u_\alpha)\}$  is order bounded in  $M$ . Hence, there exists  $y_1$  in  $M$  such that

$$(H - I)(u_\alpha) \leq y_1$$

for all  $\alpha$ . It implies that  $0 \leq (S - I)(u_\alpha) \leq (H - I)(u_\alpha) \leq y_1$ .

Thus,  $\{(S - I)(u_\alpha)\}$  is order bounded in  $M$ . Since  $S$  is a d-sobo, then  $\{u_\alpha\}$  is order bounded in  $M$ , so  $H$  is in  $DL_{sb}(M)$ .

**Theorem 7** Let  $M$  be a Riesz space,  $P, S, N: M \rightarrow M$  be three operators, and  $N \leq S \leq P \leq I + N$ . If  $N$  is in  $L_{sb}(M)$  and  $P$  is in  $DL_{sb}(M)$ , then  $S$  is in  $DL_{sb}(M)$ .

*Proof.* By the hypothesis  $0 \leq S - N \leq P - N \leq I$ . Assume that  $N$  is in  $L_{sb}(M)$ , and  $P$  is in  $DL_{sb}(M)$ . We have  $P - N$  is a d-sobo from Theorem 2 and  $S - N$  is a d-sobo from Theorem 5. Since  $N$  is in  $L_{sb}(M)$ , then by Theorem 2,  $S = S - N + N$  is in  $DL_{sb}(M)$ .

**Remark 1**

(1) An order bounded operator  $H$  may not be a d-sobo whenever its adjoint is a d-sobo in general. For example, choice  $M = c_0$  and  $H$  as an identity operator on  $M$ . Since  $M'$  has b-property [3], then  $I': M' \rightarrow M'$  is a demi-strongly order bounded operator, but  $I: c_0 \rightarrow c_0$  is not a d-sobo.

(2) Since order dual of every Riesz space has b-property and every adjoint of pre-regular operator is order bounded [3], then the adjoint of every pre-regular operator is strongly order bounded. Hence, every adjoint of pre-regular operator is d-sobo.

The following example gives us that the set of all d-sobo on a Riesz space  $M$  is not a lattice in general.

**Example 7** Let  $H$  be an operator on  $M = C[-1,1]$  defined by  $H(f)(k) = f\left(\sin\left(\frac{1}{k}\right)\right) - f\left(\sin\left(k + \frac{1}{k}\right)\right)$  if  $0 < |k| \leq 1$  and  $H(f)(0) = 0$ .  $H$  is an order bounded, but it is not regular operator from Example 1.16 in [1]. Since  $M$  has b-property,  $H$  is in  $L_{sb}(M)$ . Hence,  $H$  is a d-sobo, but  $|H|$  does not exist, since  $H$  is not a regular operator. Consequently,  $DL_{sb}(M)$  is not lattice.

### 3. Conclusion

In this study, the class of demi-strongly order bounded operators on a Riesz space which is a generalization of strongly order bounded operators, is defined. Furthermore, the relationship between strongly order bounded operators and demi-strongly order bounded operators is examined and the conclusion that demi-strongly order bounded operator includes strongly order bounded operator is obtained. It is observed that the demi-strongly order bounded operators are not generally a vector space. A characterization of the b-property is obtained by the term of demi-strongly order bounded operators. It is obtained that the class of demi-strongly order bounded operators does not satisfy the domination property, but the domination property is satisfied when it is bounded from above with the identity operator. It is concluded that the class of demi-strongly order bounded operators does not form generally a lattice.

#### Article Information Form

##### *Funding*

The authors have received no financial support for the research, authorship or publication of this work.

##### *Authors' Contribution*

The authors contributed equally to the study.

##### *The Declaration of Ethics Committee Approval*

This study does not require ethics committee approval or any special permission.

##### *The Declaration of Research and Publication Ethics*

In the writing process of this study, international scientific, ethical and citation rules were followed, and no falsification was made on the collected data. Sakarya University Institute of Science Journal and editorial board bear no responsibility for all ethical violations that may be encountered. All responsibility belongs to the corresponding author and this study has not been evaluated in any academic publications other than Sakarya University Journal of Science.

##### *Copyright Statement*

Authors own the copyright of their work published in the journal and their work is published under the CC BY-NC 4.0 license.



##### References

- [1] C. D. Aliprantis, O. Burkinshaw, Positive Operators, Berlin: Springer, 2006.
- [2] S. Alpay, B. Altın, C. Tonyalı, "On property (b) of vector lattices," Positivity, vol. 7, pp. 135-139, 2003.
- [3] S. Alpay, B. Altın, C. Tonyalı, "A note on Riesz spaces with property-b," Czechoslovak Mathematical Journal, vol. 56, no. 2, pp. 765-772, 2006.
- [4] S. Alpay, B. Altın, "On Riesz spaces with b-property and strongly order bounded operators," Rendiconti del Circolo Matematico di Palermo, vol. 60, pp. 1-12, 2011.
- [5] D. A. Birnbaum, "Preregular maps between Banach lattices," Bulletin of the Australian Mathematical Society, vol. 11, pp. 231-254, 1974.
- [6] W. V. Petryshyn, "Construction of fixed points of demicompact mappings in Hilbert space," Journal of Mathematical Analysis and Applications, vol.14, no.2, pp. 276-284, 1966.
- [7] B. Krichen, D. O'Regan, "Weakly demicompact linear operators and axiomatic measures of weak noncompactness," Mathematica Slovaca, vol. 69, no. 6, pp. 1403-1412, 2019.
- [8] H. Benkhalel, M. Hajji, A. Jeribi, "On the class of Demi Dunford-Pettis Operators," Rendiconti del Circolo Matematico di Palermo Series 2, vol. 72, pp. 901-911, 2023.
- [9] H. Benkhalel, A. Elleuch, A. Jeribi, "The class of order weakly demicompact operators," Revista de la Real Academia

de Ciencias Exactas, Físicas y Naturales.  
Series A. Matemáticas, vol. 114, no. 2,  
2020.

- [10] H. Benkhaled, A. Jeribi, “The class of demi KB-operators on Banach lattices,” Turkish Journal of Mathematics, vol. 47, no. 1, pp. 387-396, 2023.
- [11] N. Machrafi, B. Altın, “A note on topologically  $b$ -order bounded sets and generalized  $b$ -weakly compact operators,” Hacettepe Journal of Mathematics and Statistics, vol. 51, no. 2, pp. 483-493, 2021.

## The Effect of Different Proportions of Waste Rubber Substitution on Alkali-Silica Reaction and Mechanical Properties in Mortars

Ufuk Kandil<sup>1\*</sup> , H. Alperen Bulut<sup>1</sup> 

<sup>1</sup> Erzincan Binali Yıldırım University, Engineering and Architecture Faculty, Department of Civil Engineering, Erzincan, Türkiye, [ukandil@erzincan.edu.tr](mailto:ukandil@erzincan.edu.tr), [habulut@erzincan.edu.tr](mailto:habulut@erzincan.edu.tr)

\*Corresponding Author

### ARTICLE INFO

### ABSTRACT

#### Keywords:

Crumb Rubber

Mortar

Alkali-Silica Reaction (ASR)

Mechanical Properties

SEM



#### Article History:

Received: 16.10.2023

Accepted: 30.12.2023

Online Available: 24.04.2024

This study investigates the alkali-silica reaction (ASR) and mechanical properties of mortars containing crumb and powder rubber instead of river sand. In this regard, mortars were produced using waste rubber whose ratios in the mixture are 0%, 3%, 6%, 9%, 12%, 15%, 18%, and 21%. ASR expansion, compressive and flexural strength tests were conducted on the samples. ASR measurements were performed on days 3, 7, 14, 21, and 28. Besides, at the end of the ASR experiment, the microstructures of the mortars were examined using scanning electron microscope (SEM) images. Examining the results of this study reveals that the use of waste rubber in rising portions in the mortars led to an increase in the ASR expansions of the mortars. The study shows that the ASR expansions of the mortar samples that have 9% and 15% waste rubber replacement are comparatively higher than the other mortar samples. Furthermore, the results of the SEM analysis verified this finding. The study demonstrates that 3% of waste rubber mortar samples have the highest compressive and flexural strengths. On the other side, the ASR expansion of the mortars with 3% substituted waste rubber was considerably low compared to other mortars containing waste rubber. These findings (ASR, compressive and flexural strength tests results) show that using 3% waste rubber is ideal for producing mortars and supports a sustainable production approach in the sector.

## 1. Introduction

Tire production has increased enormously in recent years, along with the rapid development of the automobile industry worldwide [1, 2]. Consequently, waste tires have piled up over the years, and therefore, solid waste management has become one of the most severe environmental problems worldwide [3, 4]. By the end of 2030, it is expected that 5 billion tires will be generated and 1.2 billion rubbers will be discarded [5]. Since rubber is not biodegradable, accumulating waste tires can cause serious environmental problems [6-8].

While landfill is one of the most common waste disposal methods [9], increasingly larger landfill areas are required to store the used tires [10-12].

Moreover, rainwater trapped in waste tires creates a humid environment where insects and pests can reproduce quickly [13, 14]. On the other side, fire is another threat due to the increasing numbers of waste tires because they are flammable, and the accumulation of waste tires piling up may bring about adverse effects on the environment and human health [15-17]. The negative impacts of waste tires on the environment can be minimized by recycling them in other forms, such as crumb or shredded rubber, or using them in construction and different industries [18].

Rubberized concrete (RC) is a type of concrete containing rubber particles recycled from used tires as substitutes for fine and coarse aggregates [19, 20]. Thus, waste tire rubber particles are

recycled by partially substituting the components of cementitious mixtures [21, 22].

Concretes containing reactive aggregates are susceptible to deterioration due to Alkali-Silica Reaction (ASR), which results from sufficient humidity and temperature [23]. ASR is a harmful chemical reaction between specific amorphous silica in various natural aggregates and alkalis in cement paste [24-27]. ASR plays a critical role in the durability of concrete structures. The vital role of ASR is because the gel-form reaction product leads to internal stresses, which in turn cause the concrete structures to expand and crack [28-31]. The processes related to ASR-induced expansion and deterioration of concrete are as follows [32, 33]:

- i) Transport of hydroxide, alkali, and calcium ions towards reactive aggregates,
- ii) Dissolution of the silica and creation of a gel layer,
- iii) Diffusing of the gel into the existing voids, defects, and pores of the aggregates,
- iv) Microcracking due to the swollen gel's expansion results in overall expansion and concrete deterioration.

Replacing natural aggregates with recycled rubber particles in the concrete industry has recently led to growing scientific research [34-38]. In light of these studies, remarkable progress has been achieved regarding knowledge of the structural behavior of these materials [39-43].

### 1.1. Research significance

Even though numerous studies focusing on the mechanical and durability properties of RC have been carried out thus far, the number of research on the expansion and adverse effects of ASR in waste rubber-added composites is low [26]. Therefore, this study used crumb and powder rubber as waste rubber in substitution with aggregates. Different from studies in the literature, this study has a unique aspect: it used wasted rubber in eight different waste rubber

ratios (0%, 3%, 6%, 9%, 12%, 15%, 18% and 21%). Moreover, in the study, ASR, compressive strength and flexural strength tests were carried out to measure mortars' engineering properties. As a result, the study aims to determine which waste rubber ratio is effective on ASR and other mechanical properties.

## 2. Experimental Methodology

### 2.1. Materials

CEM I 42.5 R type Portland cement, which is classified in TS EN 197-1 [44] standard, was used in the study. The specific chemical and physical properties of this cement are shown in Table 1. The river sand potentially resulted in ASR, was extracted from the Artvin region of Turkey, and was utilized as aggregate in this study. The specific gravity of the river sand is 2.64 g/cm<sup>3</sup>. Previously used waste tires were recycled and separated into two different grain grades (crumbs and powder). Additionally, an insignificant amount of steel wire exists inside the waste rubbers. Later, these recycled materials were used as aggregates in mortar production.

**Table 1.** Properties of cement

CEM I 42.5 R	
Chemical Compositions (%)	
SiO <sub>2</sub>	19.47
Al <sub>2</sub> O <sub>3</sub>	4.64
Fe <sub>2</sub> O <sub>3</sub>	3.39
CaO	63.62
MgO	2.55
SO <sub>3</sub>	3.07
Na <sub>2</sub> O	0.43
K <sub>2</sub> O	0.79
Cl <sup>-</sup>	0.006
Insoluble residue	0.61
Loss on ignition	2.96
Physical Characteristics	
Residue on a 32-micron sieve	7.45
Specific surface (cm <sup>2</sup> /g)	3338
Specific gravity	3.11
Beginning of setting	2hrs-30min
End of setting	3hrs-33min
Volume expansion (mm)	1.0
Compressive strength (MPa)	
2nd day	29.8
28th day	55.7

Waste rubbers having different granulometry are given in Figure 1. The specific weight of the



waste rubber used in mortar production is  $1.05 \text{ g/cm}^3$ .

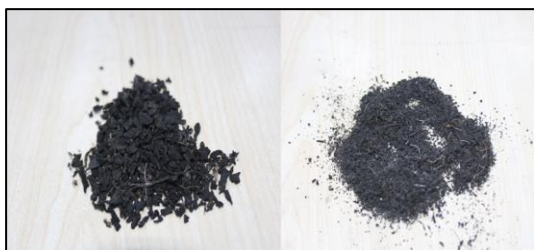


**Figure 1.** Waste rubbers with different granulometry (crumb on the left, powder on the right)

The phase identification of waste rubber was performed by X-ray diffraction (XRD) technique for scan range of  $10\text{--}80^\circ$  with a step size of  $5^\circ$  as shown in Figure 2. The abbreviations and explanations indicated in Figure 2 are C; Carbon, S; Sulfur, O<sub>2</sub>; Oxygen, Mg; Magnesium and Si; Silisium.

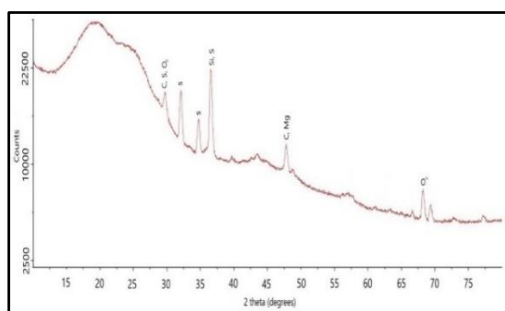


**Figure 2.** X-ray diffraction pattern of waste rubber

## 2.2. Parameters and mortar mix design

This study prepared mortar mixtures using the accelerated mortar-bar method per ASTM C 1260 [45] standard. During the experiments, eight different mortar mixtures were produced by replacing waste rubber aggregate with river sand at 0%, 3%, 6%, 9%, 12%, 15%, 18%, and 21% by volume. In the codes, WR, the abbreviation of waste rubber, is given first, and then the replacement rate is written. For instance, WR6 refers to 6% waste rubber replacement mortar. The control mortar is denoted as C.

## 2.3. Experimental methods

Preparation of the mixtures and execution of the ASR experiments were conducted under ASTM C 1260 [45]. Sand and waste rubbers separated into different grain classes by sifting through the sieves specified in the standard were weighed in

the specified amounts. Subsequently, the mortar mixtures were prepared following the relevant standard. Samples of  $25 \times 25 \times 285 \text{ mm}$  dimensions were taken for ASR from the prepared mortar mixtures. Besides, samples of  $40 \times 40 \times 100 \text{ mm}$  dimensions were taken to determine mortar specimens' compressive and flexural strength. After being retained in the molds for 24 hours, the mortar samples were demolded. The samples produced for the ASR test were kept in  $80^\circ\text{C}$  water for 24 hours and subsequently, their lengths were measured ( $L_0$ ).

Afterward, the specimens were held in 1 mol NaOH solution at  $80^\circ\text{C}$ . Then, their lengths were again measured at the end of the 3<sup>rd</sup>, 7<sup>th</sup>, 14<sup>th</sup>, 21<sup>st</sup>, and 28<sup>th</sup> days. The length changes were calculated in percentage. The samples produced to determine the compressive and flexural strength of the mortar samples were removed from the mold 24 hours later, and they were kept in water in curing pool for 28 days. The mechanical effect of the waste rubber replacement on the mortars was determined by subjecting the samples taken from the curing to compressive and flexural strength tests. Correspondingly, the changes in the internal structure were examined by taking SEM (scanning electron microscope) images on the samples. SEM analysis was performed via the QUANTA FEG 450 brand device. With the help of SEM analysis, the density of the ASR gel in the mortars and the density and structure of the cracks were determined.

## 3. Results and Discussion

### 3.1. Alkali-silica reaction (ASR)

The expansion results depending on the time (3, 7, 14, 21, and 28 days) of the mortar samples containing waste rubber at different rates are in Figure 3. The findings of the measurements show that, regardless of the replacement ratio, the mortars' expansion values increased compared with the control mortar sample when waste rubber was substituted into the mixture. For example, when the results at 14-day regarding the expansion due to ASR are assessed, the mortar sample containing 3% waste rubber (WR3) expanded by 21%, and the sample containing 15% waste rubber (WR15) enlarged

by around 100% compared to the control mortar sample.

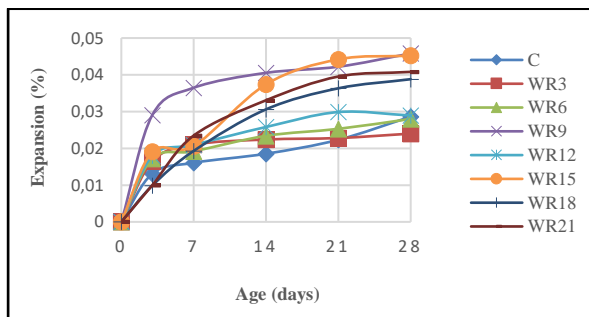


**Figure 3.** The changes in ASR expansion of mortars depending on waste rubber substitution

For instance, investigating the 28-day expansion results indicates the samples having 9% waste rubber (WR9) stretched 60% more than the control sample. Likewise, the samples accommodating 21% waste rubber (WR21) extended approximately 43% of the control sample. Although the expansion value of 3% waste rubber mortar was higher than the control mortar in the 14-day results, these expansion values were equalized in 21 days and much lower expansion values than the control mortar were obtained at the end of 28 days. A few studies investigating the ASR of samples whose aggregates were replaced by waste rubber reveal that the expansions in samples increased compared with the control sample owing to the increase in the substitution ratio [26].

The hydrophobic structure of waste rubbers may have caused a weak adhesion at the interface between the cement paste and waste rubber, thus providing more opportunity for ASR gel formation [46]. Although the rubber particles with high deformability can release some of the internal stress caused by the ASR gel brought about during the process, it is thought that the mixture stiffness declines along with the rising rubber ratio. This way, a more significant deformation occurs by a similar magnitude of internal stress [1, 47].

Therefore, it is concluded that mortars with low hardness and high waste rubber ratio show more expansion. When each sample whose aggregates were substituted is compared to one another, the expansion rates increased linearly with the rising waste rubber proportions, especially on the 14th day and its aftermath. Two special exceptions are

observed in samples that do not fit the trend mentioned above (WR9, WR15). The experiments show that the mortar samples holding 9% and 15% waste rubber reached the highest ASR expansion values compared to the others. As will be discussed further in the following sections, observing this phenomenon in the SEM analysis results indicates the experimental outcomes are consistent. Although the expansion values increased as the substitution rate of waste rubber in the mortar mixes changed, the expansions for all samples dwelled within limits set by ASTM C1260 [45] (for harmful reactive aggregates, the maximum expansion of the samples should be less than 0.2%).

### 3.2. Compressive strength

The compressive strength rates of the prepared samples by ratios of waste rubber aggregate replacement are in Figure 4.

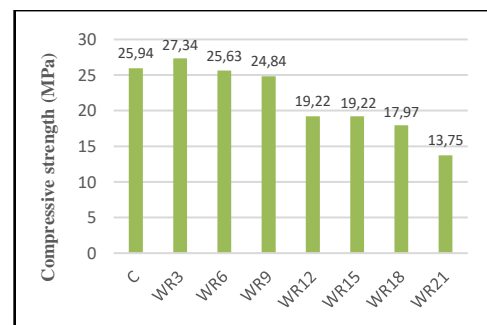


**Figure 4.** The changes in compressive strength of mortars depending on waste rubber substitution

The graph shows that the highest compressive strength value is achieved in the sample containing 3% waste rubber (WR3). On the other hand, the lowest compressive strength value was reached in the sample with 21% waste rubber (WR21). When using 3% of the waste rubber in the mortar, the compressive strength increased by 5% compared to the control sample. Besides, when 6% and 9% of waste rubber were replaced with aggregate in samples, the compressive strength rates did not remarkably decline.

The compressive strength decline has become particularly critical when the waste rubber substitution rate exceeds 9%. The reduction in compressive strength of the sample containing 21% waste rubber is 47% compared to the control sample.

It is thought that the properties of waste rubber, such as deformability, softness and low hardness, are effective on the decreases in compressive strength results observed with the increase in the waste rubber ratio [48, 49]. Previous studies demonstrated that the compressive strengths declined as the waste rubber replacement ratio used in the mortar samples increased. Afshinnia and Poursaee [26] revealed that the compressive strength of samples with 16% and 20% waste rubber substitution declined by 20% and 48%, respectively. This study's experimental outcomes show similar compressive strength reductions when the waste rubber replacement ratio is 15% and 21%. The 3% waste rubber replacement ratio led to the highest compressive strength in samples (27.34 MPa). Therefore, it can be deemed as the ideal ratio for this study.

### 3.3. Flexural strength

The results of the flexural strength test performed on the mortar samples are displayed in Figure 5.

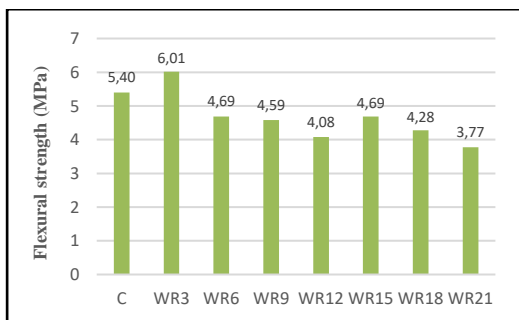


**Figure 5.** The changes in flexural strength of mortars depending on waste rubber substitution

The figure shows that the highest flexural strength is 6.01 MPa, which is achieved when the waste rubber substitute mortar (WR3) is 3%. On the other side, the lowest flexural strength is 3.77 MPa, which occurs with the sample of 21% waste rubber replacement (WR21). The flexural strength of the waste rubber sample with a 3% substitute is 11% higher than the control sample. A decreasing trend was observed in flexural strengths of samples when the replacement ratio was greater than 3%. The reduction in flexural strength of the samples containing 21% waste rubber is approximately 30% compared to the control sample. The 3% waste rubber replacement ratio was ideal, giving rise to the highest flexural strength value (6.01 MPa). The results are in the same trend as the compressive

strength results. Waste rubber aggregate used up to a certain rate (3% for this study) positively affected the strength values by acting as a filling material in the mortar. It has been observed that when waste rubbers are used at higher rates than this ratio, the amount of voids in the internal structure of the mortars increases and mechanical performances decrease [50, 51].

### 3.4. Microstructural analysis

The microstructure of the mortar bars subjected to the ASR test after 28 days was investigated using SEM. SEM images of the mortar samples having the maximum highest ASR expansion, along with the control samples are in Figure 6.

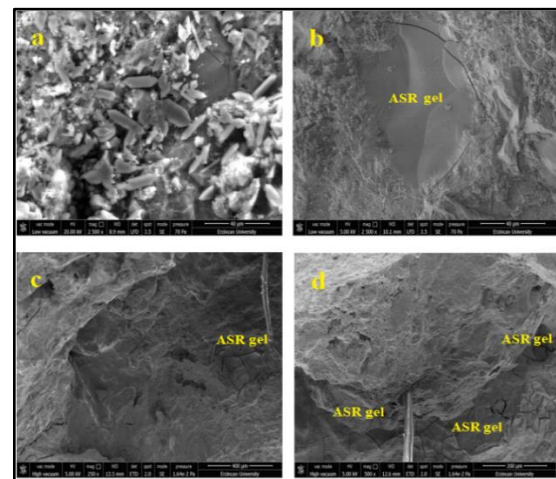


**Figure 6.** SEM images from (a) control sample, (b) sample of 9% waste rubber replacement, (c) and (d) samples of 15% waste rubber replacement sample after 28 days

The SEM image of the control mortar is given in Figure 6 (a), the SEM image of the mortar with 9% waste rubber is given in Figure 6 (b), and the SEM images of the mortar with 15% waste rubber are given in Figure 6 (c, d). Figure 6 (a) displays structures such as CH, CSH, and ettringite, which are hydration products. At this point, it is important to remark that ASR gel formation barely exists in the control sample. In Figure 6 (b), the ASR gel's intensity was slightly higher than the control sample. In Figure 6 (c-d), the intensity of the ASR gel and the map-shaped cracks in the ASR gel were more apparent. Figure 6 (d) mainly presents the ASR gel formation and cracks observed around the crumb rubber containing steel wire. The tensile stress caused by the presence of ASR gel and the soft

material of rubbers developed these microcracks in the mortars [52].

The ASR gel formed around the waste rubber caused expansion in the matrix, creating a cracked structure in the mortar, which negatively affected the mechanical performance [49, 53]. The images are obtained from the SEM image of the mortar sample containing 15% waste rubber replacement. Subsequently, the study has determined that these microstructure formations are parallel with the results of ASR expansion.

#### 4. Conclusion

The main conclusions drawn from the evaluation of the findings obtained from this study are as follows:

1. ASR expansions increased with the rising substitution rate of waste rubbers. The mortar samples containing 9% and 15% waste rubber replacement expanded significantly more than the others, especially on the 14th day and its aftermath.
2. The ASR expansion values of the control sample and the 3% waste rubber replacement mortar were very close, and the expansion rates were the lowest for both mortars. It can be said; when utilized in mortar production, a 3% waste rubber ratio will not pose a problem in ASR terms.
3. The compressive and flexural strength values of the 3% waste rubber substitution sample were significantly higher than the control sample and others with varying waste rubber replacement rates.
4. The microstructure of the ASR gel and cracks in the microstructure of the samples having 9% and 15% waste rubber replacement rates had the highest ASR expansion. The considerably higher expansions in these two groups of samples were seen in the images obtained through SEM. It has been determined that the SEM analysis results are similar to the ASR expansion results.
5. The least adversely affecting rate in terms of ASR and mechanical properties is 3%, but it is

concluded that using waste materials as a positive contribution is important in terms of sustainability and environmental effect.

#### Article Information Form

##### *Funding*

The author (s) has no received any financial support for the research, authorship or publication of this study.

##### *Authors' Contribution*

The authors contributed equally to the study.

##### *The Declaration of Conflict of Interest/ Common Interest*

No conflict of interest or common interest has been declared by the authors.

##### *The Declaration of Ethics Committee Approval*

This study does not require ethics committee permission or any special permission.

##### *The Declaration of Research and Publication Ethics*

The authors of the paper declare that they comply with the scientific, ethical and quotation rules of SAUJS in all processes of the paper and that they do not make any falsification on the data collected. In addition, they declare that Sakarya University Journal of Science and its editorial board have no responsibility for any ethical violations that may be encountered, and that this study has not been evaluated in any academic publication environment other than Sakarya University Journal of Science.

##### *Copyright Statement*

Authors own the copyright of their work published in the journal and their work is published under the CC BY-NC 4.0 license.

#### References

- [1] R. Si, J. Wang, S. Guo, Q. Dai, S. Han, "Evaluation of laboratory performance of self-consolidating concrete with recycled tire rubber", *Journal of Cleaner Production*, vol. 180, pp. 823-831, 2018.
- [2] A. Bala, S. Gupta, "Thermal resistivity, sound absorption and vibration damping of



- concrete composite doped with waste tire Rubber: A review”, *Construction and Building Materials*, vol. 299, pp. 123939, 2021.
- [3] H. Su, J. Yang, G. S. Ghataora, S. Dirar, “Surface modified used rubber tyre aggregates: effect on recycled concrete performance”, *Magazine of Concrete Research*, vol. 67, no.12, pp. 680-691, 2015.
- [4] A. Mohajerani, L. Burnett, J. V. Smith, S. Markovski, G. Rodwell, M. T. Rahman, H. Kurmus, M. Mirzababaei, A. Arulrajah, S. Horpibulsuk, F. Maghool, “Recycling waste rubber tyres in construction materials and associated environmental considerations: A review”, *Resources, Conservation and Recycling*, vol. 155, pp. 104679, 2020.
- [5] A. Gholampour, T. Ozbakkaloglu, R. Hassanli, “Behavior of rubberized concrete under active confinement”, *Construction and Building Materials*, vol. 138, pp. 372-382, 2017.
- [6] S. R. Dahmardeh, M. S. S. Moghaddam, M. H. M. Moghaddam, “Effects of waste glass and rubber on the SCC: rheological, mechanical, and durability properties”, *European Journal of Environmental and Civil Engineering*, vol. 25, no. 2, pp. 302-321, 2019.
- [7] M. Saberian, J. Li, “Long-term permanent deformation behaviour of recycled concrete aggregate with addition of crumb rubber in base and sub-base applications”, *Soil Dynamics and Earthquake Engineering*, vol. 121, pp. 436-441, 2019.
- [8] F. Abbassi, F. Ahmad, “Behavior analysis of concrete with recycled tire rubber as aggregate using 3D-digital image correlation”, *Journal of Cleaner Production*, vol. 274, pp. 123074, 2020.
- [9] W. H. Yung, L. C. Yung, L. H. Hua, “A study of the durability properties of waste tire rubber applied to self-compacting concrete”, *Construction and Building Materials*, vol. 41, pp. 665-672, 2013.
- [10] B. Adhikari, D. De, S. Maiti, “Reclamation and recycling of waste rubber”, *Progress in Polymer Science*, vol. 25, no. 7, pp. 909-948, 2000.
- [11] M. S. Karmacharya, V. K. Gupta, V. K. Jha, “Preparation of activated carbon from waste tire rubber for the active removal of Cr (VI) and Mn (II) ions from aqueous solution”, *Transactions of the Indian Ceramic Society*, vol. 75, no.4, pp. 234-241, 2016.
- [12] F. P. Figueiredo, A. H. Shah, S. Huang, H. Angelakopoulos, K. Pilakoutas, I. Burgess, “Fire protection of concrete tunnel linings with waste tyre fibres”, *Procedia Engineering*, vol. 210, pp. 472-478, 2017.
- [13] Q. Dong, B. Huang, X. Shu, “Rubber modified concrete improved by chemically active coating and silane coupling agent”, *Construction and Building Materials*, vol. 48, pp. 116-123, 2013.
- [14] A. F. Angelin, F. M. Da Silva, L. A. G. Barbosa, R. C. C. Lintz, M. A. G. De Carvalho, R. A. S. Franco, “Voids identification in rubberized mortar digital images using K-Means and Watershed algorithms”, *Journal of Cleaner Production*, vol. 164, pp. 455-464, 2017.
- [15] V. K. Gupta, B. Gupta, A. Rastogi, S. Agarwal, A. Nayak, “Pesticides removal from waste water by activated carbon prepared from waste rubber tire”, *Water Research*, vol. 45, no. 13, pp. 4047-4055, 2011.
- [16] X. Shu, B. Huang, “Recycling of waste tire rubber in asphalt and portland cement concrete: An overview”, *Construction and Building Materials*, vol. 67, no. B, pp. 217-224, 2014.
- [17] A. Bideci, H. Öztürk, Ö. S. Bideci, M. Emiroğlu, “Fracture energy and



- mechanical characteristics of self-compacting concretes including waste bladder tyre”, *Construction and Building Materials*, vol. 149, pp. 669-678, 2017.
- [18] R. Bušić, I. Miličević, T. K. Šipoš, K. Strukar, “Recycled rubber as an aggregate replacement in self-compacting concrete-literature overview”, *Materials*, vol. 11, no. 9, pp. 1729, 2018.
- [19] J. Xu, Z. Yao, G. Yang, Q. Han, “Research on crumb rubber concrete: From a multi-scale review”, *Construction and Building Materials*, vol. 232, pp. 117282, 2020.
- [20] E. Eltayeb, X. Ma, Y. Zhuge, J. Xiao, O. Youssf, “Dynamic performance of rubberised concrete and its structural applications-An overview”, *Engineering Structures*, vol. 234, pp. 111990, 2021.
- [21] F. M. Da Silva, L. A. G. Barbosa, R. C. C. Lintz, A. E. P. G. A. Jacintho, “Investigation on the properties of concrete tactile paving blocks made with recycled tire rubber”, *Construction and Building Materials*, vol. 91, pp. 71-79, 2015.
- [22] T. Gupta, S. Siddique, R. K. Sharma, S. Chaudhary, “Effect of elevated temperature and cooling regimes on mechanical and durability properties of concrete containing waste rubber fiber”, *Construction and Building Materials*, vol. 137, pp. 35-45, 2017.
- [23] T. Iskhakov, C. Giebson, J. J. Timothy, H. M. Ludwig, G. Meschke, “Deterioration of concrete due to ASR: Experiments and multiscale modelling”, *Cement and Concrete Research*, vol. 149, pp. 106575, 2021.
- [24] B. Fournier, M. A. Bérubé, “Alkali-aggregate reaction in concrete: a review of basic concepts and engineering implications”, *Canadian Journal of Civil Engineering*, vol. 27, no. 2, pp. 167-191, 2000.
- [25] L. F. M. Sanchez, S. Multon, A. Sellier, M. Cyr, B. Fournier, M. Jolin, “Comparative study of a chemo–mechanical modeling for alkali silica reaction (ASR) with experimental evidences”, *Construction and Building Materials*, vol. 72, pp. 301-315, 2014.
- [26] K. Afshinnia, A. Poursaee, “The influence of waste crumb rubber in reducing the alkali–silica reaction in mortar bars”, *Journal of Building Engineering*, vol. 4, pp. 231-236, 2015.
- [27] M. Yang, S. R. Paudel, E. Asa, “Comparison of pore structure in alkali activated fly ash geopolymer and ordinary concrete due to alkali-silica reaction using micro-computed tomography”, *Construction and Building Materials*, vol. 236, pp. 117524, 2020.
- [28] L. F. M. Sanchez, B. Fournier, M. Jolin, D. Mitchell, J. Bastien, “Overall assessment of Alkali-Aggregate Reaction (AAR) in concretes presenting different strengths and incorporating a wide range of reactive aggregate types and natures”, *Cement and Concrete Research*, vol. 93, pp. 17-31, 2017.
- [29] R. B. Figueira, R. Sousa, L. Coelho, M. Azenha, J. M. de Almeida, P. A. S. Jorge, C. J. R. Silva, “Alkali-silica reaction in concrete: Mechanisms, mitigation and test methods”, *Construction and Building Materials*, vol. 222, pp. 903-931, 2019.
- [30] R. Hay, C. P. Ostertag, “On utilization and mechanisms of waste aluminium in mitigating alkali-silica reaction (ASR) in concrete”, *Journal of Cleaner Production*, vol. 212, pp. 864-879, 2019.
- [31] W. Dong, W. Li, Z. Tao, “A comprehensive review on performance of cementitious and geopolymeric concretes with recycled waste glass as powder, sand or cullet”, *Resources, Conservation and Recycling*, vol. 172, pp. 105664, 2021.

- [32] F. Rajabipour, E. Giannini, C. Dunant, J. H. Ideker, M. D. A. Thomas, "Alkali-silica reaction: Current understanding of the reaction mechanisms and the knowledge gaps", *Cement and Concrete Research*, vol. 76, pp. 130-146, 2015.
- [33] J. Liaudat, I. Carol, C. M. López, "Model for alkali-silica reaction expansions in concrete using zero-thickness chemo-mechanical interface elements", *International Journal of Solids and Structures*, vol. 207, pp. 145-177, 2020.
- [34] D. Li, J. Mills, T. Benn, X. Ma, R. Gravina, Y. Zhuge, "Review of the performance of high-strength rubberized concrete and its potential structural applications", *Advances in Civil Engineering Materials*, vol. 5, no. 1, pp. 20150026, 2016.
- [35] A. M. Rashad, "A comprehensive overview about recycling rubber as fine aggregate replacement in traditional cementitious materials", *International Journal of Sustainable Built Environment*, vol. 5, no. 1, pp. 46-82, 2016.
- [36] W. Feng, F. Liu, F. Yang, L. Li, L. Jing, "Experimental study on dynamic split tensile properties of rubber concrete", *Construction and Building Materials*, vol. 165, pp.675-687, 2018.
- [37] K. Strukar, T. K. Šipoš, I. Miličević, R. Bušić, "Potential use of rubber as aggregate in structural reinforced concrete element – A review", *Engineering Structures*, vol. 188, pp. 452-468, 2019.
- [38] R. Roychand, R. J. Gravina, Y. Zhuge, X. Ma, O. Youssf, J. E. Mills, "A comprehensive review on the mechanical properties of waste tire rubber concrete", *Construction and Building Materials*, vol. 237, pp. 117651, 2020.
- [39] J. Wang, Q. Dai, R. Si, S. Guo, "Mechanical, durability, and microstructural properties of macro synthetic polypropylene (PP) fiber-reinforced rubber concrete", *Journal of Cleaner Production*, vol. 234, pp. 1351-1364, 2019.
- [40] E. Eltayeb, X. Ma, Y. Zhuge, O. Youssf, J. E. Mills, J. Xiao, A. Singh, "Structural performance of composite panels made of profiled steel skins and foam rubberised concrete under axial compressive loads", *Engineering Structures*, vol. 211, pp. 110448, 2020.
- [41] O. Yi, J. E. Mills, Y. Zhuge, X. Ma, R. J. Gravina, O. Youssf, "Case study of the structural performance of composite slabs with low strength CRC delivered by concrete truck", *Case Studies in Construction Materials*, vol. 13, pp. e00453, 2020.
- [42] O. Youssf, J. E. Mills, T. Benn, Y. Zhuge, X. Ma, R. Roychand, R. Gravina, "Development of crumb rubber concrete for practical application in the residential construction sector – design and processing", *Construction and Building Materials*, vol. 260, pp. 119813, 2020.
- [43] S. Miraldo, S. Lopes, F. Pacheco-Torgal, A. Lopes, "Advantages and shortcomings of the utilization of recycled wastes as aggregates in structural concretes", *Construction and Building Materials*, vol. 298, pp. 123729, 2021.
- [44] TS:EN 197-1, *Cement- Part 1: Composition, specification and conformity criteria for common cements*, 2012.
- [45] ASTM:C1260, *Standard Test Method for Potential Alkali Reactivity of Aggregates (Mortar-Bar Method)*, 2021.
- [46] Q. Ma, Z. Mao, J. Zhang, G. Du, Y. Li, "Behavior evaluation of concrete made with waste rubber and waste glass after elevated temperatures", *Journal of Building Engineering*, vol. 78, pp. 107639, 2023.
- [47] A. Yılmazoğlu, S. T. Yıldırım, "A review on mechanical and durability properties of

- concrete with waste rubber aggregate”, Pamukkale University Journal of Engineering Sciences, vol. 29, no. 5, pp. 513-528, 2023.
- [48] K. Bisht, P. V. Ramana, “Evaluation of mechanical and durability properties of crumb rubber concrete”, vol. 155, pp. 811-817, 2017.
- [49] S. Abbas, A. Ahmed, A. Waheed, W. Abbass, M. Yousaf, S. Shaukat, H. Alabduljabbar, Y. A. Awad, “Recycled untreated rubber waste for controlling the alkali–silica reaction in concrete”, Materials, vol. 15, no. 10, pp. 3584, 2022.
- [50] A. K. H. Kwan, M. McKinley, “Effects of limestone fines on water film thickness, paste film thickness and performance of mortar”, Powder Technology, vol. 261, pp. 33-41, 2014.
- [51] T. Gupta, S. Chaudhary, R. K. Sharma, “Assessment of mechanical and durability properties of concrete containing waste rubber tire as fine aggregate”, Construction and Building Materials, vol. 73, pp. 562-574, 2014.
- [52] M. M. R. Taha, A. S. El-Dieb, M. A. A. El-Wahab, M. E. Abdel-Hameed, “Mechanical, fracture, and microstructural investigations of rubber concrete”, Journal of Materials in Civil Engineering, vol. 20, no. 10, pp. 640–649, 2008.
- [53] Q. Ma, Z. Mao, M. Lei, J. Zhang, Z. Luo, S. Li, G. Du, Y. Li, “Experimental investigation of concrete prepared with waste rubber and waste glass”, Ceramics International, vol. 49, no. 11 (Part A), pp. 16951-16970, 2023.

**Morphological, Molecular Identification and Virulence of Entomopathogenic Fungi Isolated From *Dendroctonus micans* (Kugelann,1794) (Coleoptera: Curculionidae)**Seda Biryol<sup>1\*</sup>, Ali Soyduñç<sup>2</sup>, Sevda İşık<sup>2</sup><sup>1</sup> Trabzon University, Tonya Vocational School, Medical Laboratory Techniques, Trabzon, Türkiye, [sedabiryol@trabzon.edu.tr](mailto:sedabiryol@trabzon.edu.tr)<sup>2</sup> Trabzon Regional Directorate of Forestry, Trabzon, Türkiye, [alisoydinc@ogm.gov.tr](mailto:alisoydinc@ogm.gov.tr), [sevdaisik@ogm.gov.tr](mailto:sevdaisik@ogm.gov.tr)

\*Corresponding Author

## ARTICLE INFO

## ABSTRACT

## Keywords:

*Dendroctonus micans*  
Entomopathogenic fungus  
*Metarhizium*  
Microbiology  
Mycology

In this study, to determine an effective fungal agent against *Dendroctonus micans* (Kugelann, 1794) (Coleoptera: Curculionidae), which causes significant economic losses in forested areas, *Picea orientalis* (L.) Link in Artvin between 2021-2022. *Dendroctonus micans* larvae and adults were collected from the trees, and 18 fungi were isolated from larvae and adult insects. Morphological (infection type, colony morphology, spore form) and molecular (ITS1-5.8S ITS2 gene region) characterization determined that the isolates were *Metarhizium anisopliae* (Metschn.) Sorokin, 1883 (Hypocreales: Clavicipitaceae), *M. robertsii*, *M. pinghaense* and *Clonostachys rosea* Samuels & Rossman, 1999 (Hypocreales: Bionectriaceae). Isolates *M. robertsii* (OZM4) and *M. pinhaense* (OZM9) have been isolated from this pest for the first time. As a result of insecticidal activity tests performed on *D. micans* larvae and adults of  $1 \times 10^7$  spore/ml spore suspension, the larvae, *M. anisopliae* (OZM2), showed a mortality rate of 92% within 7 days and adults mortality was determined 100% at the end of the experiment, and mycosis rates were found to be consistent with mortality rates. These results show that isolates with high virulence are promising in microbial and integrated control applications against important forest pests.



## Article History:

Received: 31.10.2023

Accepted: 26.12.2023

Online Available: 24.04.2024

**1. Introduction**

Bark beetles (Coleoptera: Curculionidae, Scolytinae) are among the most harmful forest beetles in North America and Europe and settle on the host tree via aggregation pheromones establish brood systems in the phloem layer, resulting in tree death [1- 3]. According to Armendáriz-Toledano et al. [4], twenty species of the genus *Dendroctonus* have been recognized as having a significant negative impact on conifer forests [5]. Invasion pest *Dendroctonus micans* (Kugelann,1794) (Coleoptera: Curculionidae), sometimes known as the great spruce bark beetle, has expanded throughout practically all of Türkiye *Picea orientalis* (L.) Link. forests, where it aggressively damages numerous trees [6].

*Dendroctonus* (Coleoptera: Curculionidae) species, which especially like to attack living trees, colonize the tree and can kill all or part of their hosts due to their aggressive behavior during gallery formation [7, 8], and when the population reaches significant levels, they cause widespread tree death [9]. Changes in forest populations (abiotic and biotic) are known to impact species population dynamics. Climate change, degraded forest structure, water stress and drought, and other abiotic factors all contribute to increased bark beetle outbreaks in spruce forests [10- 12].

Chemical, biological, and physical control (or a mix of these approaches) are popular methods for managing various sorts of insects. Initially,

certain management measures were employed to control this pest, such as the using chemical pesticides and mechanical approaches, but effective results were not attained [13]. Several studies have focused on the pathogens and parasitoids of bark beetles searching for effective biocontrol agents in some parts of the world and Türkiye lately [14- 19].

Entomopathogenic fungi are parasitic microorganisms capable of infecting and killing arthropods. They are primarily employed in ecological farming as biopesticides as a safer alternative to hazardous chemical insecticides [20]. Around 750 entomopathogenic fungal species are identified, but the most researched and economically produced are *Beauveria bassiana* (Bals. -Criv.) Vuill. (Ascomycota: Hypocreales) and *Metarhizium anisopliae* (Metschn.) Sorokin, 1883 (Hypocreales: Clavicipitaceae) [21].

The average summer temperature in the Eastern Black Sea Region is 25-30°C, with a RH of 70-80%. At the levels of temperature and humidity explained above, entomopathogenic fungus (EPF) development produces the most the ideal environment for virulence, germination, and continuance. Therefore, entomopathogenic fungi have the potential to be used especially in microbial control against bark pests. The primary objective of this study is to identify the EPF related to *D. micans* and investigate their pathogenicity in adults and larvae in the laboratory.

## 2. General Methods

### 2.1. Insect samples

Between 2021 and 2022, *D. micans* larvae and adults were collected from *Picea orientalis* (L.) Link trees in Artvin were obtained from an ax to open tunnels beneath the bark and transferred to the laboratory. They were subsequently put in 20 x 20 cm plastic cages and fed spruce bark for 2-3 days at room temperature. Pest larvae and adults, which were assumed to be signs of infection other than a natural death, were tested regularly for fungal infestations.

### 2.2. Isolation of fungal strains

Insects collected as cadavers in the forest or died in the laboratory while growing on spruce branches were studied to see whether the fungal infection was the cause of death. To induce mycosis, surface sterilized cadavers were cultured in Petri dishes and kept in an incubator under 25°C for 1-2 weeks to promote fungal growth (Figure 1) [22]. Transfer affected insects to PDAY (Potato dextrose agar + 1% Yeast extract) (Sigma, USA) with 50 g/ml ampicillin (AppliChem, Darmstadt, Germany) to prevent bacterial infection.

A single colony was transplanted to another PDAY medium for a pure culture of the fungal isolate. The isolate's pure culture was plated on PDAY agar and incubated in the dark at 25°C for 1-2 weeks for additional sporulation [19]. After ensuring the purity of the cultures and preparing stock culture. The samples were kept at -80°C in 20% glycerol (BioChemica, A0970).

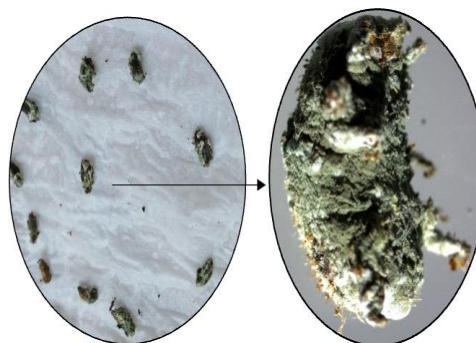


**Figure 1.** Fungus sporulating on *Dendroctonus micans* adults infected by *Metarhizium anisopliae*.

### 2.3. Morphological identification

For the morphological identification of fungal strains, shape, surface, edge, consistency, and height were first observed for each colony trait, such as macroscopic features on the PDA of colonies, and color on the top and bottom of the colonies [23]. The EPF strains were stained with Lactophenol blue solution (Merck, 113741) with slide culture methods [24]. The stained samples showed spore shape, color, mycelium type, and colony height features under light microscopy. All isolates were identified using Humber's identification key [23].



## 2.4. DNA extraction and amplification

Following the manufacturer's recommendations, EPF was resuscitated from stock culture and DNA was obtained using the Quick-DNA Fungal/Bacterial MiniPrep Kit (Zymo Research, Irvine, CA, USA). ITS5 (5'-GGAAGTAAAATCGTAACAAGG-3') and ITS4 (5'-TCCCGCTTGATATGC-3') primers were used in the PCR reaction for the ITS1-5.8S-ITS2 region [25]. Amplified areas were detected on 1.0% agarose gel electrophoresis and purified using a NucleoSpin gel and PCR cleaning kit from MACHery-Nagel in Duren, Germany. Samples were sent for sequence analysis to Macrogen Inc. (Amsterdam, Netherlands), and their phylogenetic relationships were determined using BioEdit and MEGA software version 7.0.26 [26]. *Candida albicans* CBS562 was used as an external group in phylogenetic trees.

## 2.5. Prepared spore suspension and insecticidal activity tests

Bioassay tests were conducted using 4-week-old cultures. These cultures were treated with 10 ml of 0.01% Tween 80 on top of the spores for the spore solution, and the spores were recovered from the Petri surface. The spore suspension was passed through a sterile double-layer cheesecloth to remove mycelial pieces. Conidia viability was determined by spreading spore suspensions on a PDAY medium and evaluating germination after 24 hours of incubation at 25°C in the dark. For bioassay tests, cultures with conidia viability of more than 95% were chosen.

Larvae and adult beetles to be used in the bioassay were obtained from the Trabzon Regional Directorate of Forestry Forest Pests and Biological Control Laboratory. Biotest experiments were also performed on healthy last-instar larvae and same-age adults selected randomly. For evaluation of the virulence of the isolates on *D. micans* larvae and adults, ten larvae and adults (larvae and adults were used in separate experimental setups for each experiment) from all of the groups were sprayed with a hand-operated sprayer and conidial solutions containing  $10^7$  spore/ml. The control groups were given sterilized 0.01% Tween 80. Adults received feed and shells in plastic boxes

(20 cm), while larvae were inserted (square-shaped) between the shells. Spruce bark and meal were used as food for adult insects. All larval and adult test groups were kept in plastic boxes and were conducted in a climate-controlled cabinet at 20°C and %65 RH under L12:D12. For 15 days, dead insects were observed daily. Each treatment was replicated 3× on separate days.

## 2.6. Statistical analysis

The mortality statistics gathered in bioassay experiments were calculated using Abbott's method [27]. For bioassay validation, percent mycosis values were determined using cadaveric mycelial growth. The results were subjected to one-way ANOVA, followed by Duncan's post-hoc tests to compare test isolates with each other and the control group in terms of mortality ( $p < 0.05$ ). SPSS 28.0 (IBM Corp., United States) was used to perform every graphic and statistical analysis for the experiments.

## 3. Results and Discussion

### 3.1. Morphological identification and molecular characterization

Eighteen isolates belonging to two genera from the parasitic fungi family Bionectriaceae and Clavicipitaceae were obtained from *D. micans*. The isolates *Metarhizium* sp. and *Clonostachys* sp. isolates OZM1, OZM2, OZM3, OZM4, OZM6, OZM7, OZM8, OZM9, OZM10, OZM12, OZM18, OZM19, OZM22b, OZM25 and OZM26 were determined as *Metarhizium* sp. and OZM23 was determined as *Clonostachys* sp. All *Metarhizium* sp. isolates generated the characteristic greenish conidial masses on the culture plate with smooth plate reversal, according to the preliminary characterization (Figure 2). Such cultural morphology played a crucial role in separating the desired EPF from its other cousins [28]. Additionally, partial identification of the isolates was supported by microscopic inspection of spore characteristics (spore shape and size). The obtained isolates generated ellipsoid, tiny, and intermediately sized spores (Figure 2). This study noted that the spore characteristics of different *Metarhizium* strains might occasionally differ in terms of color and size [29] (Figure 2).

OZM1, OZM2, OZM3, OZM6, OZM7 OZM8, OZM10, OZM12, OZM18, OZM19, OZM22b OZM25 and OZM26 were determined as *Metarhizium anisopliae*, OZM4 was determined as *Metarhizium robertsii*, OZM9 as *Metarhizium pinghaense* (Figure 3), OZM23 was determined as *Clonostachys rosea* (Figure 3). In particular, OZM4 isolate *M. robertsii* ARSEF 2575 was determined to be closely related and OZM9 isolates to be closely related to *M. pinghaense*.

### 3.2. Insecticidal activity tests *D. micans* larvae and adults

In bioassay, all isolates were tested *D. micans* larvae and adults at concentrations of  $1 \times 10^7$  spore/ml. The larvae mortality rates ranged from 30-100% testing within 15 days ( $F = 256.377$ ,  $df = 18$ ,  $p < 0.05$ ) (Figure 4). The adult mortality rates varied from 28-100% after 15 days of testing ( $F = 273.041$ ,  $df = 18$ ,  $p < 0.05$ ) (Figure 5). It was established that mortality happened, particularly within three days, and the mortality rate rapidly increased.

It was determined that OZM2, OZM4, OZM6, and OZM22b isolates were extremely effective on larvae ( $p < 0.05$ ). These isolates 7-day larvae mortality rates were 92.2%, 82.2%, 80% and 88.9%, while their 15-day mortality rates were 100%, respectively ( $p < 0.05$ ) (Figure 4). Mycosis rates after death were calculated to be 96.4%, 97.3%, 93.3 and 94.0, respectively ( $p < 0.05$ ).

As a result of the adult experiments, it was determined that the mortality rates increased after seven days and at the end of the experiment, most of the isolates exhibited 100% mortality ( $p < 0.05$ ) (Figure 5). OZM2, in particular, was shown to be the most effective strain on both larvae and adults, with an 80% mycosis value ( $p < 0.05$ ). The mortality rate of *D. micans* larvae and adults in control treatment ranged between 5 and 15% and mycosis was not observed.

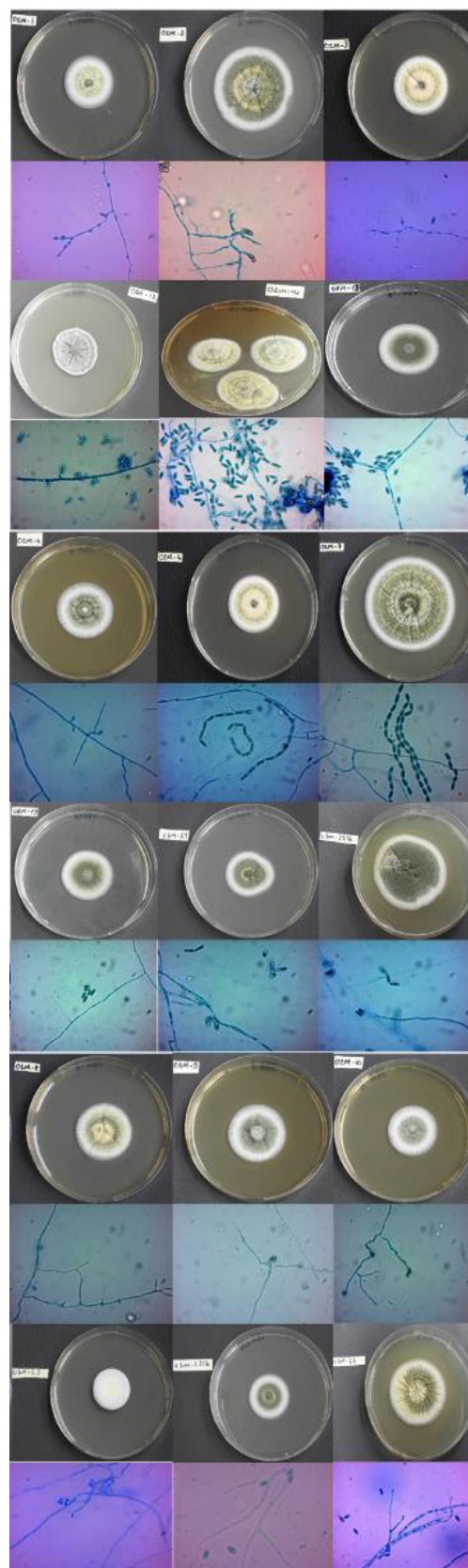


**Figure 2.** PDA colony growth, morphological structures of entomopathogenic fungus isolates and microphotographs of samples stained with lactophenol blue cotton.

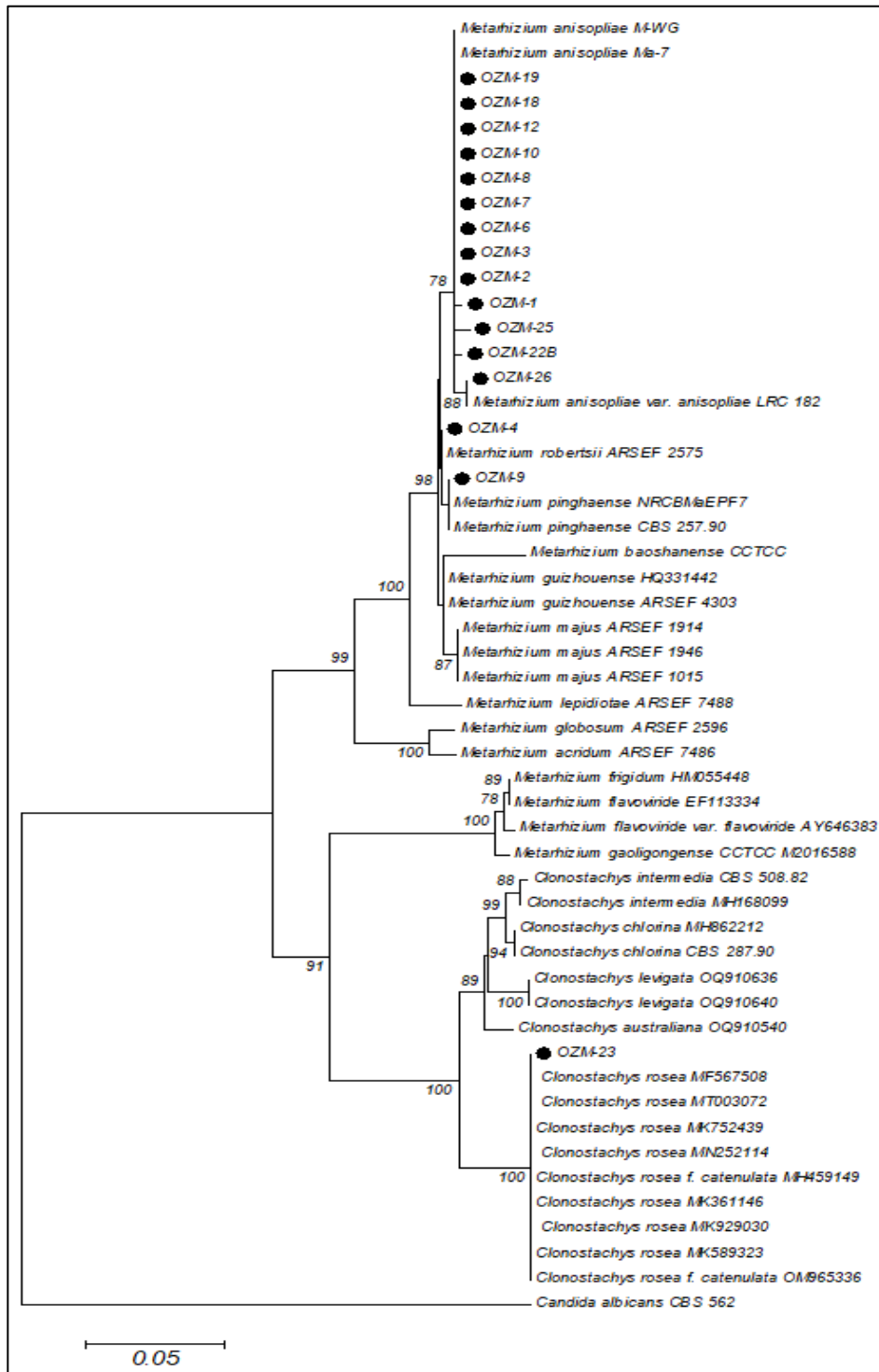


**Figure 3** Phylogenetic tree of strains isolated from *Dendroctonus micans*. The approximately 580-bp sequence of the ITS1-5.8S-ITS2 gene region was used to construct the dendrogram. Bootstrap values based on 1000 replicates were indicated above the nodes. Bootstrap values  $C \geq 70$  are labeled. All isolates were indicated with a black circle. The scale on the bottom of the dendrogram indicates the degree of dissimilarity [26].

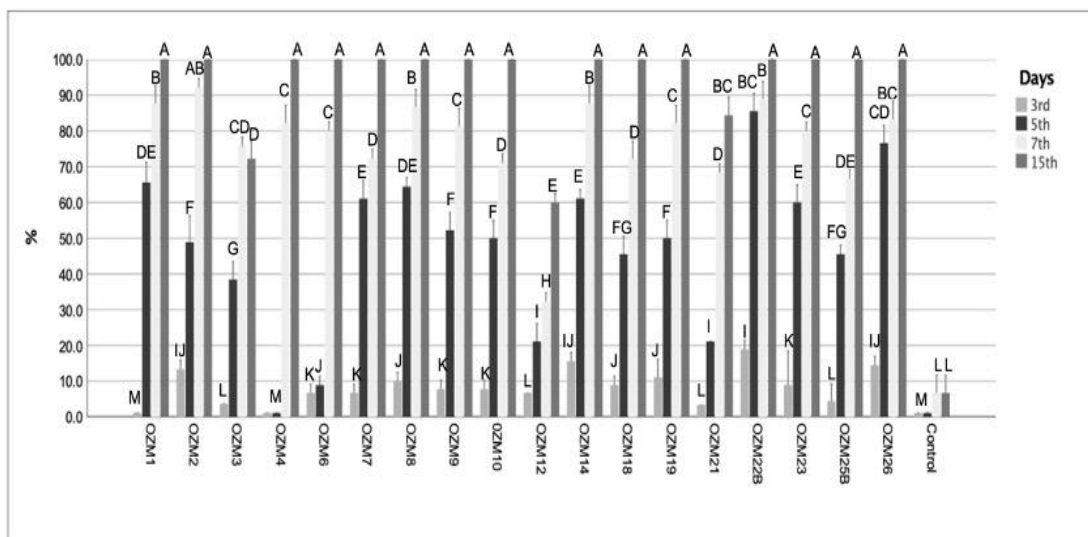


**Figure 4** Mortality of *Dendroctonus micans* larvae after application of 18 entomopathogenic fungal isolates within 15 days after application of  $1 \times 10^7$  spore/ml. Mortality data were corrected according to Abbott’s formula [26]. Different uppercase letters represent statistically significant differences among treatments concerning mortality according to Duncan’s post-hoc tests ( $p < 0.05$ ). Bars show standard deviation.

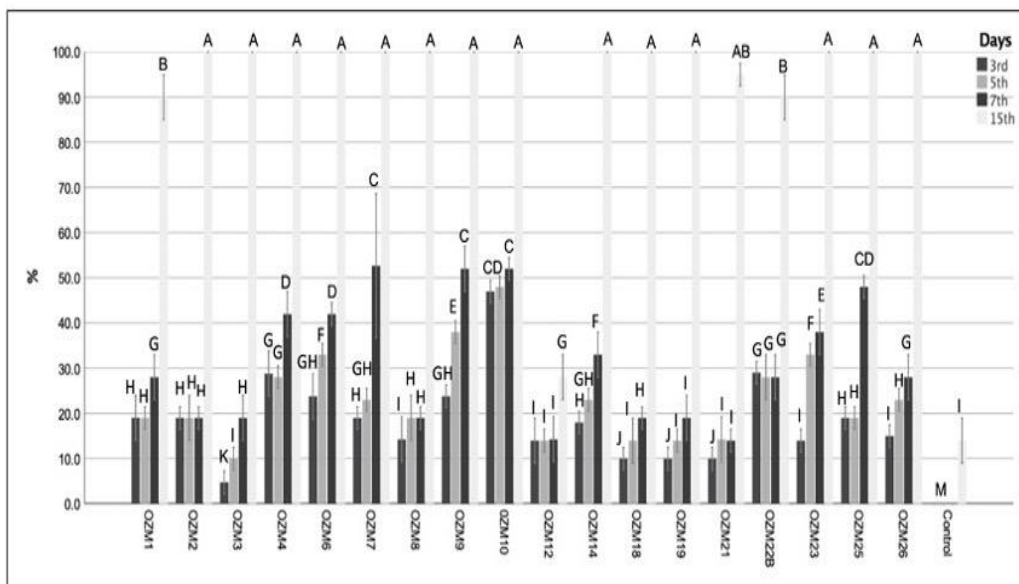


**Figure 5** Mortality of *Dendroctonus micans* adults after application of 18 entomopathogenic fungal isolates within 15 days after application of  $1 \times 10^7$  spore/ml. Mortality data were corrected according to Abbott’s formula [27]. Different uppercase letters represent statistically significant differences among treatments concerning mortality according to Duncan’s post-hoc tests ( $p < 0.05$ ). Bars show standard deviation.

Bark beetles cause significant infestations, especially in needle forests, and often cause the death of older trees [30, 31]. Especially, *D. micans* is one of the important bark beetle species that cause significant economic damage in spruce forests in Europe and Asia [32, 33]. By this time, the most effective method of control among the methods of control is the production and release of the predator beetle of the pest. Biological methods of controlling the pests have also been

tried. In particular, the potential of EPF to be used in the control against pests is higher than other microorganisms.

According to Sevim et al. [17], *Metarhizium anisopliae* (2), *Beauveria cf. bassiana* (2), *Beauveria bassiana* (2), *Isaria fumosorosea* (1), *Metarhizium* sp. (1), and *Evlachovaea* sp. (1) fungi were identified from this pest. In particular, it has been emphasized that there may be efficacy



potential of *Metarhizium* sp. strains in which *B. bassiana* KTU-53 isolate has high lethal activity on the pest. In our study, seventeen species of *Metarhizium* were identified especially in *D. micans* and it was determined that *Metarhizium* isolates were effective on the pest.

*Beauveria bassiana*, an EPF species, has been found in studies to be effective against various bark beetles, particularly spruce bark beetles [34-36]. There are few studies on the use of *M. anisopliae*, particularly against spruce bark beetles. Some research has been carried out with *Ips typographus* Linnaeus [37] and *D. micans* [17]. Due to its powerful spore-producing ability and virulence, *M. anisopliae* is recognized to be an effective biocontrol agent against several pests [38, 39]. This investigation demonstrated that *M. anisopliae* OZM-2 is also effective against *D. micans*. Especially among bark beetles, in his study, Moore [40], found two species of *M. anisopliae* and 37 *Penicillium* sp., especially from the *D. frontalis* pest. Pabst and Sikorowski [41], also described *Paecilomyces viridis* and also *B. bassiana*, and *M. anisopliae* species. In another study, on the *Ips typographus* adults, Takov et al. [42], for the first time evaluated the virulence of *M. pempighi* (isolated from unidentified carabid beetle) and found the cumulative mortality caused by *M. pempighi* at four different conidial concentrations ( $2 \times 10^4$ - $2 \times 10^7$  spore/ml) should range from 75% to 100% ten days after treatment, with an  $LC_{50}$  value of  $2.9 \times 10^3$  conidia/ml and an  $LC_{90}$  value of  $6.4 \times 10^4$  conidia/ml. In our study, *M. robertsii* and *M. pinhaense* were isolated for the first time, especially from *D. micans*, for the first time, and in the bioassay studies, it was determined that they showed 100% mortality at the end of the application (15 days) on both larvae and adults.

In another study conducted by Draganova et al. [35], different fungi species showed high efficacy in both laboratory and natural environments, especially in a laboratory environment (4. day 100% mortality) log experiments performed in the natural environment of *M. anisopliae* 619 strain determined that it was especially *I. typographus* and *Hylastes cunicularius*.

#### 4. Conclusion

Worldwide, *Metarhizium* spp. has been used in the biological control of Coleoptera species. However, in our study and other studies, it was also revealed that spruce bark beetles can cause high mortality. Although the isolation and identification of *Metarhizium* species from the soil is remarkable, it has been shown to have a high potential for use, especially on bark beetles. Of course, the high virulence of the tested strains is optimistic, as our study was carried out under laboratory conditions, but field trials are necessary to determine the performance of bark beetles under their true ecological conditions.

#### Article Information Form

##### Acknowledgments

We thank the Trabzon Regional Directorate of Forestry for their support in the making of this study.

##### Funding

The authors have no received any financial support for the research, authorship or publication of this study.

##### Authors' Contribution

Conceptualization, S. B.; methodology, S. B., A. S. and S. İ.; software, S. B.; validation, S. B., A. S. and S. İ.; formal analysis, S. B.; investigation, S.B., A. S. and S. İ.; resources, S. B., A. S. and S. İ.; data curation, S. B.; writing—original draft preparation, S. B.; writing—review and editing, S.B., A. S. and S. İ.; visualization, S.B., A. S. and S. İ.; supervision, S.B.; All authors have read and agreed to the published version of the manuscript.

##### The Declaration of Conflict of Interest/ Common Interest

No conflict of interest or common interest has been declared by the authors.

##### The Declaration of Ethics Committee Approval

This study does not require ethics committee permission or any special permission.



### ***The Declaration of Research and Publication Ethics***

The authors of the paper declare that they comply with the scientific, ethical and quotation rules of SAUJS in all processes of the paper and that they do not make any falsification on the data collected. In addition, they declare that Sakarya University Journal of Science and its editorial board have no responsibility for any ethical violations that may be encountered and that this study has not been evaluated in any academic publication environment other than Sakarya University Journal of Science.

### ***Copyright Statement***

Authors own the copyright of their work published in the journal and their work is published under the CC BY-NC 4.0 license.

### **References**

- [1] D. L. Wood, "The role of pheromones, kairomones, and allomones in the host selection and colonization behavior of bark beetles," *Annual Review of Entomology*, vol. 27, pp. 411-446, 1982.
- [2] S. Seybold, D. Huber, J. Lee, A. Graves, J. Bohlmann, "Pine monoterpenes and pine bark beetles: a marriage of convenience for defense and chemical communication," *Phytochemistry Reviews*, vol. 5, pp. 143-178, 2006.
- [3] A. Martín, I. Etxebeste, G. Pérez, G. Álvarez, E. Sánchez, J. Pajares, "Modified pheromone traps help reduce bycatch of bark-beetle natural enemies," *Agricultural and Forest Entomology*, vol. 15, no. 1, pp. 86-97, 2013.
- [4] F. Armendáriz-Toledano, A. Niño, B. T. Sullivan, L. R. Kirkendall, G. Zúñiga, "A new species of bark beetle, *Dendroctonus mesoamericanus* sp. nov. (Curculionidae: Scolytinae), in southern Mexico and Central America," *Annals of the Entomological Society of America*, vol. 108, no. 3, pp. 403-414, 2015.
- [5] D. L. Six, R. Bracewell, "*Dendroctonus*," in *Bark beetles: Biology and ecology of native and invasive species*, Academic Press, ed., London: Vega FE, Hofstetter RW, 2017 pp. 305-350.
- [6] A. Büyükterzi, G. E. Özcan, O. E. Sakici, "Variations in the attack pattern of *Dendroctonus micans* and the colonization rate of *Rhizophagus grandis* in *Picea orientalis* stands," *Biologia*, vol. 77, no. 9, pp. 2475-2485, 2022.
- [7] J. D. Reeve, F. E. Anderson, S. T. Kelley, "Ancestral state reconstruction for *Dendroctonus* bark beetles: evolution of a tree killer," *Environmental Entomology*, vol. 41, no. 3, pp. 723-730, 2012.
- [8] H. Alkan Akıncı, F. E. Bak, B. A. Çalışkan, "Some tree features affecting host selection by *Dendroctonus micans* (Kugelann) (Coleoptera: Curculionidae, Scolytinae): experimental results from Artvin spruce forests," *Artvin Çoruh University Journal of Forestry Faculty*, vol. 19, no. 2, pp. 186-193, 2018.
- [9] CABI, "*Dendroctonus micans* (great spruce bark beetle)," Feb. 16, 2021. [Online]. Available: <https://www.cabi.org/isc/datasheet/18352>.
- [10] G. Rouault, J. N. Candau, F. Lieutier, L. M. Nageleisen, J. C. Martin, N. Warzée, "Effects of drought and heat on forest insect populations in relation to the 2003 drought in Western Europe," *Annals of Forest Science*, vol. 63, no. 6, pp. 613-624, 2006.
- [11] J. Hushaw, "Forest pests and climate change," Apr. 1, 2021. [Online]. Available: [https://www.manomet.org/wpcontent/uploads/old-files/Forest Pests-and-Climat e\\_Change\\_FullBulletin.pdf](https://www.manomet.org/wpcontent/uploads/old-files/Forest_Pests-and-Climat e_Change_FullBulletin.pdf).
- [12] D. Kulakowski, "Managing bark beetle outbreaks (*Ips typographus*, *Dendroctonus* spp.) in conservation areas in the 21st century," *Forest Research Papers*, vol. 77, no. 4, pp. 352-357, 2016.

- [13] B. Yuksel. "The Damaging Insect Species at Oriental Spruce Forests and Their Predators and Parasite Species. II. Eastern Black Sea Forestry Research Institute Technical Notes, Trabzon, Turkey, vol. 6, pp. 46, 1997.
- [14] D. W. Langor, "Arthropods and nematodes co-occur with the eastern larch beetle, *Dendroctonus simplex* (Col.: Scolytidae), in Newfoundland," Entomophaga, vol. 36, pp. 303-313, 1991.
- [15] H. Yılmaz, K. Sezen, H. Kati, Z. Demirbag, "The first study on the bacterial flora of the European spruce bark beetle, *Dendroctonus micans* (Coleoptera: Scolytidae)," Biologia Bratislava, vol. 61, pp. 679-686, 2006.
- [16] M. Yaman, R. Radek, "Pathogens and parasites of adults of the great spruce bark beetle, *Dendroctonus micans* (Kugelann) (Coleoptera: Curculionidae, Scolytinae) from Turkey," Journal of Pest Science, vol. 81, pp. 91-97, 2008.
- [17] A. Sevim, İ. Demir, E. Tanyeli, Z. Demirbag, "Screening of entomopathogenic fungi against the European spruce bark beetle, *Dendroctonus micans* (Coleoptera: Scolytidae)," Biocontrol Science and Technology, vol. 20, pp. 3-11, 2010.
- [18] M. Yaman, Ö. Ertürk, İ. Aslan, "Isolation of some pathogenic bacteria from the great spruce bark beetle, *Dendroctonus micans* and its specific predator, *Rhizophagus grandis*," Folia Microbiologica, vol. 55, pp. 35-38, 2010.
- [19] S. Kocacevik, A. Sevim, M. Eroglu, Z. Demirbag, I. Demir, "Molecular characterization, virulence and horizontal transmission of *Beauveria pseudobassiana* from *Dendroctonus micans* (Kug.) (Coleoptera: Curculionidae)," Journal of Applied Entomology, vol. 139, no. 5, pp. 381-389, 2015.
- [20] B. Lovett, R. J. St Leger, "The insect pathogens," Microbiology Spectrum, vol. 5, no. 2, pp.10-1128, 2017.
- [21] L. A. Lacey, D. Grzywacz, D. I. Shapiro-Ilan, R. Frutos, M. Brownbridge, M. S. Goettel, "Insect pathogens as biological control agents: back to the future," Journal of Invertebrate Pathology, vol. 132, pp. 1-41, 2015.
- [22] M. S. Ali-Shtayeh, A. B. B. Marai, R. M. Jamous, "Distribution, occurrence and characterization of entomopathogenic fungi in agricultural soil in the Palestinian area," Mycopathologia, vol. 156, no.3, pp. 235-244, 2003.
- [23] R. A. Humber, "Fungi: identification," INManual of techniques in insect pathology, Academic Press, 1997, pp. 153-185.
- [24] J. L. Harris, "Modified method for fungal slide cultures," Journal of Clinical Microbiology, vol. 24, no. 3, pp. 460-461, 1986.
- [25] T. J. T. White, S. Bruns, J. Taylor, "Amplification and Direct Sequencing of Fungal Ribosomal RNA Genes for Phylogenetics," in PCR Protocols: A Guide to Methods and Applications, M. A. Innis, D. H. Gelfand, J. J. Sninsky, T. J. White. Academic Press, San Diego,1990, pp. 482.
- [26] K. Tamura, G. Stecher, D. Peterson, A. Filipski, S. Kumar, "MEGA6: molecular evolutionary genetics analysis version 6.0.," Molecular Biology and Evolution, vol. 30, no. 12, pp. 2725-2729, 2013.
- [27] W. S. Abbott, "A method of computing the effectiveness of an insecticide," Journal of Economic Entomology, vol. 18, pp. 265-267, 1925.
- [28] C. L. Du, B. Yang, J. H. Wu, S. Ali, "Identification and virulence characterization of two *Akanthomyces*

- attenuatus* isolates against *Megalurothrips usitatus* (Thysanoptera: Thripidae),” *Insects*, vol.10, no. 6, pp. 168, 2019.
- [29] N. Tangthirasunun, S. Poeaim, K. Soyong, P. Sommartya, S. Popoonsak, “Variation in morphology and ribosomal DNA among isolates of *Metarhizium anisopliae* from Thailand,” *Journal of Agricultural Technology*, vol. 6, no. 2, pp. 317-329, 2010.
- [30] B. J. Bentz, A. M. Jönsson, “Modeling Bark Beetle Responses to Climate Change, 533-53,” in *Reviews the Modeling Approach to The Bark Beetle Dynamics Under A Climate Change Scenario*. ed., F. E. Vega, R. W. Hofstetter. San Diego, Academic Press, 2015, pp. 533-53 pp.
- [31] K.F. Raffa, B. H. Aukema, B. J. Bent, A. L. Carroll, J. A. Hicke, M. G. Turner, W. H. Romme, “Cross-scale drivers of natural disturbances prone to anthropogenic amplification: the dynamics of bark beetle eruptions,” *Bioscience*, vol. 58, no. 6, pp. 501-517, 2008.
- [32] C. I. Fraser, O. Brahy, P. Mardulyn, L. Dohet, F. Mayer F, J. C. Grégoire, “Flying the nest: male dispersal and multiple paternity enables extrafamilial matings for the invasive bark beetle *Dendroctonus micans*,” *Heredity*, vol. 113, no. 4, pp. 327-333, 2014.
- [33] F. Mayer, F. B. Piel, A. Cassel-Lundhagen, N. Kirichenko, L. Grumiau, B. Økland, P. Mardulyn, “Comparative multilocus phylogeography of two Palaearctic spruce bark beetles: influence of contrasting ecological strategies on genetic variation,” *Molecular Ecology*, vol. 24, no. 6, pp. 1292-1310, 2015.
- [34] J. Kreutz, O. Vaupel, G. Zimmermann, “Efficacy of *Beauveria bassiana* (Bals.) Vuill. against the spruce bark beetle, *Ips typographus* L, in the laboratory under various conditions,” *Journal of Applied Entomology*, vol. 128, pp. 384–389, 2004.
- [35] S. A. Draganova, D. D. Doychev, D. K. Pilarska, D. I. Takov, “Bioassays of entomopathogenic fungi against xylophagous insects in Bulgaria: laboratory and field experiments,” *Acta Zoologica Bulgarica*, vol. 69, no. 3, pp. 411-419, 2017.
- [36] Y. A. Batta, “Biocontrol of almond bark beetle (*Scolytus amygdali* Geurin-Meneville, Coleoptera: Scolytidae) using *Beauveria bassiana* (Bals.) Vuill. (Deuteromycotina: Hyphomycetes),” *Journal of Apply Microbiology*, vol. 103, pp. 1406–1414, 2007.
- [37] S. Keller, C. Epper, B. Wermelinger, “*Metarhizium anisopliae* as a New Pathogen of the Spruce Bark Beetle *Ips typographus*,” *Mitteilungen der Schweizerischen Entomologischen Gesellschaft*, vol. 77, pp. 121 – 123, 2004.
- [38] F. Ihara, M. Toyama, T. Sato, “Pathogenicity of *Metarhizium anisopliae* to the chestnut weevil larvae under laboratory and field conditions,” *Applied Entomology and Zoology*, vol. 38, no. 4, pp. 461-465, 2003.
- [39] P. Marannino, C. Santiago-Álvarez, E. de Lillo, E. Quesada-Moraga, “A new bioassay method reveals pathogenicity of *Metarhizium anisopliae* and *Beauveria bassiana* against early stages of *Capnodis tenebrionis* (Coleoptera; Buprestidae),” *Journal of Invertebrate Pathology*, vol. 93, no. 3, pp. 210-213, 2006.
- [40] G. E. Moore, “Mortality factors caused by path- bacteria and fungi of the southern pine beetle in North Carolina,” *Journal of Invertebrate Pathology*, vol. 17, pp. 28-37, 1971.
- [41] G. S. Pabst, P. P. Sikorowski, “Susceptibility of southern pine beetle (*Dendroctonus frontalis*) on oligidic medium to *Paecilomyces viridis* and also *Beauveria bassiana*, and *Metarhizium anisopliae*,” *Journal of Georgia*

Entomology Society, vol. 15, pp.235-241, 1980.

- [42] D. Takov, M. Barta, T. Toshova, D. Doychev, D. Pilarska, “On the Pathogenicity of *Metarhizium pempigi* against *Ips typographus* L,” Proceedings of the Bulgarian Academy of Sciences, vol. 75, no. 4, pp. 554-560, 2022.

## Myrmecofauna (Hymenoptera, Formicidae) of Gökçeada Island, Türkiye

Esra Sert<sup>1</sup> , Celal Karaman<sup>2\*</sup> 

<sup>1</sup>Trakya University, Institute of Natural and Applied Sciences, Edirne, Türkiye, [esrasert@windowslive.com](mailto:esrasert@windowslive.com)

<sup>2</sup>Trakya University, Faculty of Science, Department of Biology, Edirne, Türkiye, [celalkaraman@trakya.edu.tr](mailto:celalkaraman@trakya.edu.tr)

\*Corresponding Author

### ARTICLE INFO

### ABSTRACT

Keywords:  
Biodiversity  
Ant Fauna  
New Records  
Ergatoid Queen  
*Hypoponera eduardi*

#### Article History:

Received: 13.11.2023

Accepted: 09.01.2024

Online Available: 24.04.2024

Türkiye is a very important country for faunal and floral studies due to its geographical location, the zoogeographic importance of its location and the biological richness it brings. This important area has been the subject of research on ants since second half of 19th century. However, studies on the ant fauna of the islands of Türkiye are very old and insufficient. For this reason, the ant fauna of Gökçeada, the largest island of Türkiye, was investigated by direct collecting and litter sifting methods in 2017-2018. 72 species belonging to 4 subfamilies and 23 genera were identified from 1105 ant samples obtained from 73 different localities and 16 different habitats. Among these species, *Messor maculifrons* Santschi, 1927 and *Tetramorium sahlbergi* Finzi, 1936 are new records for the ant fauna of Türkiye. In addition, the ergatoid queen of *Hypoponera eduardi* (Forel, 1894) was recorded for the first time outside the Afrotropical region.

## 1. Introduction

Studies on ants in Türkiye started with the work of Rigler in 1852 [1]. Since then, many studies have been carried out, and as a result of these studies, 380 ant taxa have been recorded from Türkiye (Karaman & Kiran, unpublished data). The majority of these studies are related to the Turkish mainland, and very few studies have been carried out on the ant fauna of the Turkish islands. In 5 studies carried out by foreign researchers between the end of the 1800s and 1950, 7 ant species [*Camponotus sylvaticus* (Olivier, 1792), *C. samius* Forel, 1889, *C. thoracicus* (Fabricius, 1804), *C. vagus* (Scopoli, 1763) *Creumatogaster ionia* Forel, 1911, *Lasius brunneus* (Latreille, 1798) and *Lepisiota frauenfeldi* (Mayr, 1855)] were recorded from the Prince Islands of İstanbul [2-6]. However, as can be seen, these studies are far from reflecting the ant fauna of the Prince Islands.

Later, [7] investigated the ant fauna of Gökçeada (Çanakkale) and Bozcaada (Çanakkale) Islands in 1992 and 1994, respectively [7, 8]. [7]

recorded 35 ant taxa belonging to 3 subfamilies and 16 genera from Gökçeada as a result of their research in 9 different localities in 5 days in 1992.

Afterwards, in 1994, [8] conducted research on the ant fauna of Bozcaada and recorded 26 taxa belonging to 3 subfamilies and 13 genera.

Gökçeada, district of Çanakkale Province, is the largest island of Türkiye with an area of 289 km<sup>2</sup>. Although Gökçeada, located in the Aegean Sea, is in the Mediterranean climate type and specifically included in the "Marmara Transition Climate" type. 77% of the island area is mountainous (highest point is Doruktepe with 673m), 12% is hilly and 11% is plain [9]. Such different geographical structures contain many different vegetation types. It is inevitable that all this diversity in Gökçeada will affect ant biodiversity positively.

This information made us think that Gökçeada's ant fauna contains more than what is known. Therefore, the ant fauna of Gökçeada was investigated in this study.



## 2. Material and Methods

The ant samples were collected from the region in 2017 and 2018. Specimens were collected by hand collecting (direct sampling). This method has sometimes been supplemented by litter sifting in suitable habitats. Study details (locality numbers, geographic coordinates, altitudes, habitat types and study dates) are shown in Table 1 and Figure 1. In the Results section the ant records are given as “(G1), 18/0001, 1♀, 3♂♂, 1♂, 39♀♀”. (G1) indicates the locality number in Table 1 and Figure 1. 18/0001 and/or 17/0001 indicates the protocol number of the material in the author database. “1♀, 3♂♂, 1♂, 39♀♀”: this expression shows how many individuals represent each caste of the species obtained from the research area. Description of symbols used in the results section: ♀: queen, ♂: male, ♂: soldier, ♀: worker. ♀♀ symbol means more than 50 individuals. “\*” symbol after the species names in the Results section indicates recorded species by [7] from the Gökçeada Island.



Figure 1. Studied localities in Gökçeada

The ant photographs were taken using Nikon D800e camera attached to 3.2× and 8× microscope objectives. The Helicon Focus software (Helicon Soft Ltd., Kharkiv Ukraine) were used to stack the photos. The map of the studied localities was prepared with Google Earth.

The study material is deposited in Entomological Museum of Trakya University (EMTU), Edirne, Türkiye.

## 3. Results

Family: FORMICIDAE

Subfamily: DOLICHODERINAE Forel

1. *Bothriomyrmex communista* Santschi, 1919  
Material: (G4), 18/0051, 9♀♀; (G7), 18/0088, 11♀♀; (G14), 18/0161, 21♀♀; (G16), 18/0182, 10♀♀; (G20), 18/0211b, 1♀; (G21), 18/0222, 27♀♀; (G22), 18/0233, 2♀♀; (G23), 18/0252, 15♀♀; (G54), 18/7092a, ♀♀.

2. *Dolichoderus quadripunctatus* (Linnaeus, 1771)\*

Material: (G9), 18/0111, 17♀♀; (G33), 18/0362a, 8♀♀; (G52), 18/7076b, 4♀♀; (G68), 17/0008e, 2♀♀; (G72), 17/0020b, 14♀♀.

3. *Tapinoma cf. festae* Emery, 1925

Material: (G12), 18/0147, 5♀♀; (G51), 18/7064a, 18♀♀; (G66), 17/0003d, 5♀♀.

Remarks: According to [10], we left our material as *Tapinoma cf. festae*. Aras and Aktaç recorded *T. erraticum* (Latreille, 1798) and *T. nigerrimum* (Nylander, 1856) from Gökçeada island. However, [11] stated that *T. nigerrimum* distributed in the West and Central Mediterranean parts of Europe and Africa, but not distributed in Balkans and Asia Minor. Thus, [10] excluded this species from Turkish ant fauna and clarified the status of the *T. erraticum* species complex, giving *T. erraticum* as a common species only in the northern Balkan Peninsula, and reported that based on personal contact with Lech Boroweic another species, *Tapinoma cf. erraticum* BALC., present in Türkiye. Our *Tapinoma* Foerster, 1850 material did not congruent with *T. erraticum* species complex.

4. *Tapinoma subboreale* Seifert, 2012

Material: (G66), 17/0003d, 5♀♀.

Subfamily: FORMICINAE Latreille

5. *Camponotus aethiops* (Latreille, 1798)\*

Material: (G1), 18/0008b, 1♀; (G2), 18/0014b, 1♀; (G4), 18/0049, 12♀♀; (G7), 18/0090c, 18/0091, 3♂♂, 18♀♀; (G8), 18/0100a, 24♂♂, 6♀♀; (G10), 18/0128d, 1♀; (G13), 18/0153b, 1♀; (G16), 18/0184a, 4♀♀; (G17), 18/0196, 14♀♀; (G20), 18/0216b, 1♂, 12♀♀; (G21), 18/0229e, 1♀; (G22), 18/0237, 1♀; (G24), 18/0257b, 8♀♀; (G35), 18/0384, 7♀♀; (G36), 18/0400b, 1♀;

(G37), 18/0417, 20♀♀; (G38), 18/0421, 19♀♀; (G40), 18/0450, 11♀♀; (G42), 18/0467, 9♀♀; (G43), 18/0484, 14♀♀; (G44), 18/0498, 14♀♀; (G49), 18/7046c, 1♀; (G50), 18/7054, 18/7055b, 18/7060, 1♀, 5♀♀; (G51), 18/7064e, 1♀; (G52), 18/7077, ♀♀; (G54), 18/7090b, 18/7095d, 11♀♀; (G58), 18/7131, 12♀♀; (G59), 18/7150a, 14♀♀; (G72), 17/0020i, 3♀♀.

#### 6. *Camponotus baldaccii* Emery, 1908

Material: (G6), 18/0074b, 10♀♀; (G14), 18/0166, 1♀; (G15), 18/0176b, 1♀; (G19), 18/0204, 5♀♀; (G26), 18/0274b, 3♀♀; (G33), 18/0368, 12♀♀; (G36), 18/0387c, 2♀♀; (G47), 18/7027a, 5♀♀; (G48), 18/7037b, 10♀♀; (G49), 18/7052, 17♀♀; (G56), 18/7113, 2♀♀; (G58), 18/7140, 3♂♂, 12♀♀; (G60), 18/7180, 5♀♀; (G61), 18/7184, 3♀♀; (G63), 18/7205, 4♀♀; (G64), 18/7211, 18/7216, 21♀♀; (G66), 17/0005, 23♀♀; (G71), 17/0013b, 1♀.

#### 7. *Camponotus dalmaticus* (Nylander, 1849)\*

Material: (G8), 18/0105, 1♀; (G30), 18/0329d, 1♀; (G31), 18/0335a, 16♀♀; (G58), 18/7133a, 2♀♀.

#### 8. *Camponotus fallax* (Nylander, 1856)

Material: (G31), 18/0344a, 2♀♀; (G53), 18/7084, 18/7085b, 1♀, 25♀♀; (G72), 17/0019, 17/0020k, 5♀♀.

**Table 1.** Details of the researched localities

Loc.	Coordinates	Alt.	Habitat	Date
G1	40° 14.156' N, 25° 56.636' E	84 m	<i>Pinus silvestris</i> L. forest	04.VI.2018
G2	40° 12.912' N, 25° 56.136' E	73 m	Mixed forest	04.VI.2018
G3	40° 11.865' N, 25° 53.917' E	74 m	<i>P. silvestris</i> forest	04.VI.2018
G4	40° 10.783' N, 25° 55.499' E	407 m	Bushes + Meadow	04.VI.2018
G5	40° 13.272' N, 25° 54.621' E	192 m	Bushes	04.VI.2018
G6	40° 14.061' N, 25° 53.955' E	97 m	Bushes	05.VI.2018
G7	40° 13.940' N, 25° 54.984' E	224 m	Milk vetch	05.VI.2018
G8	40° 13.307' N, 25° 53.135' E	52 m	Maquis	05.VI.2018
G9	40° 12.488' N, 25° 52.689' E	18 m	Olive orchard	05.VI.2018
G10	40° 13.194' N, 25° 57.947' E	133 m	Milk vetch	05.VI.2018
G11	40° 12.254' N, 25° 57.821' E	64 m	Oak forest	05.VI.2018
G12	40° 11.633' N, 25° 58.026' E	61 m	Bushes + Milk vetch	05.VI.2018
G13	40° 09.631' N, 25° 54.538' E	232 m	Bushes + Milk vetch	06.VI.2018
G14	40° 08.997' N, 25° 54.785' E	98 m	Bushes	06.VI.2018
G15	40° 09.245' N, 25° 54.098' E	146 m	Oak forest	06.VI.2018
G16	40° 09.152' N, 25° 57.394' E	28 m	Maquis	06.VI.2018
G17	40° 10.537' N, 25° 57.942' E	13 m	Barren land	06.VI.2018
G18	40° 08.047' N, 25° 58.372' E	0 m	Coastal dune	06.VI.2018
G19	40° 08.544' N, 25° 59.518' E	7 m	Bushes	06.VI.2018
G20	40° 08.618' N, 25° 56.831' E	30 m	Maquis	07.VI.2018
G21	40° 07.808' N, 25° 56.113' E	28 m	River bank	07.VI.2018
G22	40° 07.084' N, 25° 53.479' E	12 m	Maquis	07.VI.2018
G23	40° 06.555' N, 25° 50.900' E	67 m	Barren land	07.VI.2018
G24	40° 06.151' N, 25° 49.369' E	65 m	Barren land	07.VI.2018
G25	40° 06.897' N, 25° 48.300' E	51 m	Milk vetch	07.VI.2018
G26	40° 06.217' N, 25° 47.555' E	35 m	Milk vetch	07.VI.2018
G27	40° 19.350' N, 25° 53.111' E	99 m	Mixed forest	08.VI.2018
G28	40° 11.582' N, 25° 52.601' E	41 m	Olive orchard	08.VI.2018
G29	40° 10.501' N, 25° 52.260' E	99 m	Maquis	08.VI.2018

**Table 1.** Details of the researched localities (Continue)

Loc.	Coordinates	Alt.	Habitat	Date
G30	40° 09.899' N, 25° 51.996' E	143 m	Maquis	08.VI.2018
G31	40° 09.248' N, 25° 51.198' E	193 m	<i>Pinus brutia</i> Ten. forest	08.VI.2018
G32	40° 08.338' N, 25° 50.622' E	238 m	Bushes	23.VII.2018
G33	40° 07.563' N, 25° 49.911' E	79 m	River bank	23.VII.2018
G34	40° 07.917' N, 25° 52.051' E	122 m	Mixed forest	23.VII.2018
G35	40° 11.575' N, 25° 50.749' E	148 m	Mixed forest	23.VII.2018
G36	40° 09.989' N, 25° 49.983' E	98 m	Olive orchard	24.VII.2018
G37	40° 09.576' N, 25° 49.495' E	119 m	<i>P. brutia</i> forest	24.VII.2018
G38	40° 08.512' N, 25° 48.480' E	272 m	Maquis	24.VII.2018
G39	40° 08.636' N, 25° 46.929' E	153 m	<i>P. brutia</i> forest	24.VII.2018
G40	40° 09.570' N, 25° 46.629' E	278 m	Barren land	24.VII.2018
G41	40° 09.197' N, 25° 45.405' E	169 m	<i>P. brutia</i> forest	24.VII.2018
G42	40° 09.352' N, 25° 44.156' E	155 m	Mixed forest	24.VII.2018
G43	40° 10.235' N, 25° 45.203' E	175 m	<i>P. brutia</i> forest	25.VII.2018
G44	40° 11.349' N, 25° 45.052' E	13 m	Mixed forest	25.VII.2018
G45	39° 53.872' N, 25° 34.977' E	56 m	<i>P. brutia</i> forest	25.VII.2018
G46	40° 08.395' N, 25° 43.866' E	76 m	<i>P. brutia</i> forest	25.VII.2018
G47	40° 07.527' N, 25° 43.898' E	30 m	Milk vetch	25.VII.2018
G48	40° 07.732' N, 25° 44.825' E	98 m	Olive orchard	25.VII.2018
G49	40° 06.205' N, 25° 43.695' E	40 m	Barren land	25.VII.2018
G50	40° 12.620' N, 25° 50.270' E	46 m	Maquis	26.VII.2018
G51	40° 12.423' N, 25° 49.861' E	146 m	Marsh area	26.VII.2018
G52	40° 12.422' N, 25° 49.408' E	188 m	Oak forest	26.VII.2018
G53	40° 11.460' N, 25° 49.094' E	339 m	Barren land	26.VII.2018
G54	40° 11.486' N, 25° 47.811' E	553 m	Barren land	26.VII.2018
G55	40° 09.463' N, 25° 41.076' E	0 m	Maquis	27.VII.2018
G56	40° 10.057' N, 25° 41.985' E	3 m	Maquis	27.VII.2018
G57	40° 09.235' N, 25° 41.898' E	141 m	<i>P. brutia</i> forest	27.VII.2018
G58	40° 08.719' N, 25° 41.629' E	408 m	Maquis	27.VII.2018

**Table 1.** Details of the researched localities (Continue)

Loc.	Coordinates	Alt.	Habitat	Date
G59	40° 10.217' N, 25° 48.372' E	525 m	Barren land	17.IX.2018
G60	40° 07.316' N, 25° 46.323' E	76 m	Dry river bank	17.IX.2018
G61	40° 06.288' N, 25° 45.235' E	12 m	Barren land	17.IX.2018
G62	40° 08.414' N, 25° 42.534' E	92 m	<i>P. brutia</i> forest	18.IX.2018
G63	40° 07.222' N, 25° 42.248' E	23 m	<i>P. brutia</i> forest	18.IX.2018
G64	40° 07.546' N, 25° 44.123' E	38 m	<i>P. brutia</i> forest	18.IX.2018
G65	40° 08.528' N, 25° 40.723' E	163 m	<i>P. brutia</i> forest	18.IX.2018
G66	40° 13' 53" N 25° 53' 41" E	79 m	Bushes	14.V.2017
G67	40° 14' 02" N 25° 54' 13" E	0 m	Bushes	14.V.2017
G68	40° 13' 16" N 25° 54' 22" E	139 m	Urban area	14.V.2017
G69	40° 11' 38" N 25° 54' 16" E	50 m	Urban area	14- 15.V.2017
G70	40° 11' 23" N 25° 52' 17" E	105 m	Urban area	14.V.2017
G71	40° 11' 24" N 25° 50' 03" E	288 m	Urban area	14.V.2017
G72	40° 12' 07" N 25° 49' 58" E	253 m	Maquis	14.V.2017
G73	40° 09' 03" N 25° 46' 17" E	258 m	Urban area	15.V.2017

**9. *Camponotus gestroi* Emery, 1878**

Material: (G1), 18/0001b, 18/0004b, 18/0009, 8♀♀; (G2), 18/0028b, 13♀♀; (G5), 18/0061c, 1♀; (G7), 18/0086c, 1♀; (G8), 18/0099a, 18/0106d, 2♀♀; (G10), 18/0124, 1♀; (G13), 18/0153c, 1♀; (G15), 18/0177b, 1♀; (G17), 18/0192b, 18/0199b, 2♀♀; (G23), 18/0242b, 18/0251b, 2♀♀; (G25), 18/0262b, 18/0263b 12♀♀; (G38), 18/0424a, 1♀; (G68), 17/0008i, 17/0009e, 2♀♀; (G70), 17/0011f, 1♀.

**10. *Camponotus ionius* Emery, 1920**

Material: (G5), 18/0061a, 13♀♀; (G29), 18/0309a, 18/0314b, 16♀♀; (G30), 18/0329b, 1♀; (G36), 18/0398, 20♀♀; (G45), 18/7011a, 19♀♀; (G48), 18/7041, 1♀; (G53), 18/7081a, 2♀♀; (G64), 18/7218, 19♀♀.

**11. *Camponotus kiesenwetteri* (Roger, 1859)**

Material: (G1), 18/0004a, 18/0008a, 15♀♀; (G2), 18/0021a, 18/0028a, 9♀♀; (G8), 18/0101a, 17♀♀;

(G14), 18/0159d, 1♀; (G15), 18/0174, 28♂♂; (G20), 18/0213, 1♀; (G25), 18/0263c, 3♂♂; (G26), 18/0278, 1♀; (G27), 18/0280b, 23♂♂; (G29), 18/0309b, 18/0313, 17♂♂; (G30), 18/0322, 25♂♂; (G31), 18/0333, 7♂♂; (G37), 18/0406, 18/0414, 24♂♂; (G38), 18/0427, 2♂♂; (G39), 18/0443, 23♂♂; (G42), 18/0466a, 18/0474d, 27♂♂; (G43), 18/0479, 18♂♂; (G44), 18/0495b, 1♂, 6♂♂; (G45), 18/7003, 12♂♂; (G46), 18/7015, 7♂♂; (G47), 18/7027c, 2♂♂; (G48), 18/7038, 3♂♂; (G49), 18/7046b, 5♂♂; (G50), 18/7053a, 5♂♂; (G53), 18/7088a, 1♀; (G55), 18/7102c, 18/7107, 1♀, 1♂, 19♂♂; (G57), 18/7126, 1♀; (G58), 18/7138a, 1♀; (G60), 18/7178b, 1♀; (G63), 18/7201, 12♂♂; (G64), 18/7212, 18/7213, 9♀♀, 19♂♂, ♀♀.

#### 12. *Camponotus lateralis* (Olivier, 1792)\*

Material: (G3), 18/0032b, 18/0041, 20♂♂; (G7), 18/0089, 4♂♂; (G9), 18/0110a, 4♂♂; (G11), 18/0130, 18/0134, 23♂♂; (G12), 18/0148a, 3♂♂; (G15), 18/0171, 18/0179e, 31♂♂; (G17), 18/0198b, 1♀; (G19), 18/0207c, 2♂♂; (G20), 18/0218, 1♀; (G21), 18/0227a, 1♀; (G23), 18/0248, 1♀, 21♂♂; (G25), 18/0262c, 1♀; (G31), 18/0336a, 18/0337a, 22♂♂; (G32), 18/0348, 18/0353b, 18/0356b, 28♂♂; (G33), 18/0366, 1♀, 4♂♂; (G34), 18/0369a, 5♂♂; (G35), 18/0379d, 1♀; (G39), 18/0430b, 18/0434d, 13♂♂; (G41), 18/0454, 18/0456a, 1♀, 3♂♂, 39♂♂; (G43), 18/0476, 7♀♀, 11♂♂; (G44), 18/0490, 18/0493f, 42♂♂; (G46), 18/7012a, 18/7016, 18/7024, 1♀, 5♂♂, 21♂♂; (G48), 18/7037a, 2♂♂; (G52), 18/7069a, 18/7079b, 1♀, 4♂♂, 36♂♂; (G54), 18/7096b, 18/7101a, 4♀♀, 1♂, 49♂♂; (G58), 18/7133c, 1♀; (G60), 18/7177a, 20♂♂; (G63), 18/7203, 18/7204, 1♀, 4♂♂, ♀♀; (G65), 18/7233, 14♂♂; (G70), 17/0012c, 3♂♂.

#### 13. *Camponotus lateralis* morph 2 sensu Seifert

Material: (G2), 18/0027, 12♂♂; (G12), 18/0148b, 1♀; (G13), 18/0150c, 18/0154, 26♂♂; (G14), 18/0159c, 2♂♂; (G16), 18/0186, 7♂♂; (G19), 18/0207a, 3♂♂; (G20), 18/0212b, 1♀; (G25), 18/0263a, 5♂♂; (G26), 18/0273, 5♂♂; (G27), 18/0282b, 18/0283a, 18/0291, 1♀, 11♂♂; (G28),

18/0303, 32♂♂; (G29), 18/0316, 17♂♂; (G30), 18/0324, 18/0327, 1♀, 7♂♂; (G31), 18/0342b, 2♂♂; (G32), 18/0350a, 1♀, 3♂♂; (G35), 18/0380, 3♂♂, 9♂♂; (G37), 18/0404, 18/0409, 1♀, 14♂♂; (G39), 18/0432, 1♀, 2♂♂; (G42), 18/0468, 21♂♂; (G45), 18/7005a, 13♂♂; (G52), 18/7076a, 3♂♂; (G53), 18/7082a, 1♀; (G55), 18/7105a, 1♀, 13♂♂; (G57), 18/7125, 18♂♂; (G58), 18/7142, ♀♀; (G60), 18/7179, 6♂♂; (G64), 18/7214, 25♂♂.

Remarks: The all records of *Camponotus candiotes* Emery, 1894 in [12-15], from Türkiye are belong to *Camponotus lateralis* morph 2 sensu Seifert. [13] described the queen and male of *C. candiotes* but these descriptions are also belonging to *C. lateralis* morph 2. Moreover, [16] mentioned this taxon as a setose form of *C. lateralis* in monograph of "Greek Ants" book.

#### 14. *Camponotus piceus* (Leach, 1825)\*

Material: (G3), 18/0031a, 1♀; (G8), 18/0099b, 1♀; (G9), 18/0118a, 5♂♂; (G22), 18/0236e, 4♂♂; (G26), 18/0270a, 1♀; (G40), 18/0449, 6♂♂; (G42), 18/0472, 1♀; (G51), 18/7064c, 3♂♂; (G52), 18/7074a, 1♀; (G55), 18/7108a, 5♂♂; (G65), 18/7222b, 18/7224, 19♂♂; (G74), 1♀.

#### 15. *Camponotus samius* Forel, 1889\*

Material: (G1), 18/0001a, 2♂♂; (G2), 18/0028c, 1♀; (G3), 18/0039, 11♂♂; (G5), 18/0061b, 3♂♂; (G8), 18/0101b, 9♂♂; (G11), 18/0133b, 1♀; (G13), 18/0152, 7♂♂; (G15), 18/0175a, 18/0176c, 2♀♀, 7♂♂, 10♂♂; (G20), 18/0215, 2♂♂; (G22), 18/0240, 16♂♂; (G25), 18/0267a, 8♂♂; (G27), 18/0286, 7♂♂; (G28), 18/0301, 3♂♂; (G34), 18/0374b, 8♂♂; (G35), 18/0386, 8♂♂; (G37), 18/0403, 18/0416, 9♂♂; (G41), 18/0460, 1♀; (G42), 18/0474b, 1♀; (G43), 18/0483, 11♂♂; (G44), 18/0492, 1♀; (G45), 18/7009, 14♂♂; (G46), 18/7022, 18/7025b, 5♂♂; (G52), 18/7078c, 16♂♂; (G53), 18/7082c, 18/7087c, 2♂♂; (G57), 18/7116, 9♂♂; (G58), 18/7134, 8♂♂; (G62), 18/7198, 13♂♂; (G65), 18/7226, 20♂♂; (G72), 17/0015b, 14♂♂.



16. *Camponotus sanctus* Forel, 1904\*

Material: (G2), 18/0014a, 1♀; (G25), 18/0268, 2♀♀; (G36), 18/0392b, 1♀.

17. *Cataglyphis nodus* (Brullé, 1833)\*

Material: (G1), 18/0005, 5♂♂, 2♀♀; (G2), 18/0018, 1♀; (G3), 18/0043, 1♀; (G5), 18/0064, 11♀♀; (G8), 18/0108a, 1♀; (G9), 18/0115, 2♀♀; (G10), 18/0121, 1♀, 1♀; (G14), 18/0170b, 1♀; (G15), 18/0173d, 1♀; (G16), 18/0187, 1♀; (G17), 18/0202, 1♀; (G18), 18/0203, 2♀♀; (G19), 18/0207b, 1♀; (G24), 18/0253a, 1♂, 2♀♀; (G25), 18/0260a, 7♀♀; (G28), 18/0306, 1♀; (G29), 18/0309c, 2♀♀; (G32), 18/0350b, 1♀; (G33), 18/0359, ♀♀; (G34), 18/0374d, 1♀; (G38), 18/0423, 3♀♀; (G45), 18/7000, 2♀♀; (G46), 18/7025a, 1♀; (G47), 18/7031, 1♀; (G48), 18/7033c, 1♀; (G49), 18/7045, 1♀; (G51), 18/7064d, 1♀; (G52), 18/7067, 2♀♀; (G53), 18/7081b, 1♀; (G58), 18/7144d, 2♀♀; (G63), 18/7207, 1♀; (G65), 18/7232, 1♀; (G68), 17/0008d, 3♀♀; (G73), 17/0021, 4♀♀.

18. *Colobopsis truncata* (Spinola, 1808)

Material: (G5), 18/0061d, 18/0065b, 18/0066a, 14♀♀; (G12), 18/0141b, 18/0142a, 6♀♀; (G15), 18/0172b, 29♀♀; (G19), 18/0206, 2♀♀, 1♂, 3♀♀; (G22), 18/0236d, 1♀, 8♀♀; (G25), 18/0264a, 3♀♀, 3♂♂, 8♀♀; (G27), 18/0281, 6♀♀, 8♀♀; (G28), 18/0296, 1♀, 5♂♂, 28♀♀; (G31), 18/0345a, 15♀♀; (G32), 18/0354b, 1♀; (G36), 18/0393, 1♀; (G46), 18/7013a, 16♀♀; (G47), 18/7029b, 1♀; (G50), 18/7057a, 1♀; (G53), 18/7083c, 2♀♀; (G61), 18/7185b, 18/7186, 5♀♀; (G68), 17/0008j, 1♀; (G71), 17/0013a, 2♀♀; (G72), 17/0014b, 17/0020g, 10♀♀.

19. *Lasius alienus* (Foerster, 1850)\*

Material: (G3), 18/0030b, 1♀; (G5), 18/0067, 1♂, 23♀♀; (G21), 18/0229a, 9♀♀; (G27), 18/0288, 1♀, 20♂♂, 12♀♀; (G31), 18/0335b, 2♀♀; (G52), 18/7075, 26♀♀; (G54), 18/7098b, 2♀♀; (G59), 18/7153, 18/7172, 35♀♀; (G68), 17/0008c, 17♀♀; (G72), 17/0016, 25♀♀.

Remarks: [7] recorded *L. brunneus* (Latreille, 1798) from Gökçeada in 1992. *Lasius brunneus* is an arbicol species and characteristic with almost bicolored body, and smooth body with appressed and short pubescence on its whole surface without erect seta. Although many arbicolous *Lasius* Fabricius, 1804 specimens were obtained in this study, no specimens consistent with *L. brunneus* characteristics were obtained. This shows us that the record of *L. brunneus* given by [7] should be rechecked.

20. *Lasius turcicus* Santschi, 1921

Material: (G2), 18/0023b, 1♂, 11♀♀; (G3), 1♀, 30♀♀; (G6), 18/0084a, 11♀♀; (G9), 18/0113, 9♀♀; (G14), 18/0164, 7♀♀; (G23), 18/0246, 12♀♀; (G25), 18/0266, 3♀♀; (G27), 18/0283c, 1♀; (G28), 18/0298, 18/0299b, 5♀♀; (G29), 18/0319a, 2♀♀; (G30), 18/0326, 9♀♀; (G36), 18/0392a, 12♀♀; (G51), 18/7064b, 12♀♀; (G52), 18/7076d, 1♀; (G54), 18/7100a, 15♀♀; (G60), 18/7177b, 6♀♀.

21. *Lepisiota frauenfeldi* (Mayr, 1855)\*

Material: (G1), 18/0001c, 18/00013, 1♀, 11♀♀; (G2), 18/0016b, 3♀♀; (G4), 18/0044, 18♀♀; (G5), 18/0061h, 18/0062b, 8♀♀; (G6), 18/0075c, 18/0082, 34♀♀; (G7), 18/0086b, 6♀♀; (G8), 18/0107, 4♀♀; (G9), 18/0119, 4♀♀; (G10), 18/0120a, 3♀♀; (G12), 18/0138a, 1♀, 22♀♀; (G13), 18/0149, 44♂♂, 30♀♀; (G14), 18/0160, 1♂, 18♀♀; (G15), 18/0175f, 1♀; (G16), 18/0188b, 1♀; (G17), 18/0195b, 10♀♀; (G19), 18/0205a, 5♀♀; (G20), 18/0216a, 2♀♀; (G21), 18/0220, 10♀♀; (G22), 18/0234, 22♀♀; (G23), 18/0241c, 4♀♀; (G24), 18/0259b, 7♀♀; (G25), 18/0260d, 9♀♀; (G26), 18/0271a, 3♀♀; (G27), 18/0285, 4♀♀; (G28), 18/0304, 2♀♀, 45♀♀; (G30), 18/0330c, 5♀♀; (G31), 18/0338, 11♀♀; (G33), 18/0357, 9♀♀; (G34), 18/0369e, 18/0370e, 18/0374e, 3♀♀; (G35), 18/0382, 24♀♀; (G36), 18/0395a, ♀♀; (G37), 18/0402b, 5♀♀; (G38), 18/0419a, ♀♀; (G40), 18/0447, 6♀♀; (G43), 18/0482b, 7♀♀; (G46), 18/7026, 1♀; (G47), 18/7030, 11♀♀; (G48), 18/7033b, 2♀♀; (G49), 18/7043a, 6♀♀; (G50), 18/7059, 10♀♀; (G52), 18/7068, 15♀♀; (G53), 18/7080b, 7♀♀;



(G54), 18/7090a, 18/7095a, 1♀, ♀♀; (G55), 18/7106, ♀♀; (G56), 18/7115, ♀♀; (G58), 18/7132, 18/7136b, 5♀♀; (G59), 18/7149, 8♀♀, 3♀♀; (G60), 18/7176a, 1♀; (G61), 18/7194, 16♀♀; (G62), 18/7200, 28♀♀; (G65), 18/7222a, 15♀♀; (G66), 17/0003f, 17/0006a, 104♀♀; (G67), 17/0007b, 20♀♀; (G70), 17/0011b, 36♀♀; (G72), 17/0020e, 9♀♀.

22. *Plagiolepis pallescens* Forel, 1889\*

Material: (G23), 18/0241d, 1♀; (G25), 18/0263d, 1♀; (G37), 18/0408, 15♀♀; (G46), 18/7013b, 18/7017, 5♀♀; (G72), 17/0020d, 7♀♀.

23. *Plagiolepis perperamus* Salata, Borowiec & Radchenko, 2018

Material: (G9), 18/0117, 8♀♀; (G12), 18/0139, 6♀♀; (G17), 18/0197b, 8♀♀; (G19), 18/0208c, 2♀♀; (G20), 18/0209, 50♀♀; (G21), 18/0226a, 2♀♀; (G22), 18/0236a, 1♀, 13♀♀; (G24), 18/0257a, 3♀♀; (G40), 18/0446b, 18/0453b, 15♀♀; (G44), 18/0489, ♀♀; (G47), 18/7027b, 1♀; (G50), 18/7062b, 1♀; (G52), 18/7074c, 1♀; (G62), 18/7196, ♀♀; (G64), 18/7220, 31♀♀; (G67), 17/0007c, 40♀♀; (G69), 17/0010b, 2♀♀.

24. *Plagiolepis pygmaea* (Latreille, 1798)\*

Material: (G1), 18/0002, ♀♀; (G2), 18/0016a, 18/0021b, 18/0029, 2♀♀, 31♀♀; (G3), 18/0031b, 18/0037, 26♂♂, 16♀♀; (G4), 18/0045, 10♀♀; (G5), 18/0062c, 18/0065c, 1♀, 2♀♀; (G6), 18/0072a, 1♂, 20♀♀; (G7), 18/0086e, 18/0090b, 1♀, 8♂♂, 19♀♀; (G8), 18/0100b, 2♂♂, 4♀♀; (G10), 18/0125, 6♀♀; (G11), 18/0132, 18/0137c, 35♀♀; (G13), 18/0151, 6♀♀, 14♂♂, 27♀♀; (G15), 18/0172a, 18/0175e, 8♀♀; (G16), 18/0185, 5♂♂, 7♀♀; (G26), 18/0276, 3♀♀; (G27), 18/0282a, 2♀♀, 10♂♂, 25♀♀; (G28), 18/0294, 18/0299d, 2♀♀, 1♂♂, ♀♀; (G29), 18/0312, 2♀♀; (G30), 18/0320, ♀♀; (G31), 18/0331b, 14♀♀; (G32), 18/0355b, 2♀♀; (G33), 18/0367b, 3♀♀; (G39), 18/0431, 18/0439, 1♂, ♀♀; (G41), 18/0455a, 18/0457c, 36♀♀; (G42), 18/0470, 23♀♀; (G43), 18/0477d, 1♀; (G45), 18/0499, 1♀, ♀♀; (G46), 18/7014c, 1♀; (G50), 18/7058, 27♀♀; (G52), 18/7071, ♀♀; (G53),

18/7089a, ♀♀; (G54), 18/7098a, 18/7101b, 1♀, 53♀♀; (G58), 18/7135a, 5♀♀; (G66), 17/0003g, 2♀♀; (G68), 17/0008f, 17/0009b, 7♀♀, ♀♀.

25. *Plagiolepis xene* Starcke, 1936

Material: (G54), 18/7101c, 29♀♀, 4♂♂.

Subfamily: MYRMICINAE Lepeletier de Saint-Fargeau

26. *Aphaenogaster balcanica* (Emery, 1898)

Material: (G3), 18/0032a, 3♀♀; (G5), 18/0061g, 1♀; (G6), 18/0074a, 2♀♀; (G9), 18/0114, 1♂, 7♀♀; (G27), 18/0290b, 3♀♀; (G28), 18/0307, 7♀♀; (G29), 18/0309d, 5♀♀; (G36), 18/0387b, 3♀♀; (G37), 18/0401b, 2♀♀; (G66), 17/0003a, 27♀♀; (G68), 17/0008h, 2♀♀; (G70), 17/0011e, 2♀♀.

Remarks: [7] recorded *A. simonellii* Emery, 1894 from Gokceada. However, according to [17], the distribution of *A. simonellii* is known only from Greece. The known records of the species from other countries belong to the *A. balcanica* species. For this reason, the specimens previously recorded from Turkiye as *A. simonelli* are actually records of the *A. balcanica* species.

27. *Aphaenogaster festae* Emery, 1915

Material: (G6), 18/0078, 5♀♀; (G8), 18/0106b, 2♀♀; (G11), 18/0133a, 33♀♀; (G30), 18/0330a, ♀♀; (G31), 18/0334, 25♀♀; (G39), 18/0444, 2♀♀, ♀♀; (G40), 18/0451, 6♀♀; (G44), 18/0493b, 1♀; (G45), 18/7007, 34♀♀; (G46), 18/7019b, 44♀♀; (G52), 18/7074b, 18/7078b, 2♀♀, 6♂♂, ♀♀; (G57), 18/7121, 2♀♀; (G65), 18/7227, ♀♀; (G68), 17/0009a, 14♀♀.

Remarks: [7] recorded *A. subterranea* (Latreille, 1798) from the Gokceada island. *Aphaenogaster subterranea* is a widespread species known from Western Europe to Iran and Caucasus. *A. subterranea* species is grouped in the *subterranea* group by [18] with other five *Aphaenogaster* Mayr, 1853 species (*A. graeca* Schulz 1994, *A. ichnusa* Santschi, 1925, *A. illyrica* Brako, Lapeva-Gjonova, Salata, Borowiec & Polak, 2019, *A. kurdica* (Ruzsky, 1905), *A. maculifrons* Kiran and Akta, 2008)

and characteristics of the species group was described in detail. This characteristic species could not found in our study from Gökçeada, thus the identification of the Aras and Aktaç [7] should be checked.

28. *Cardiocondyla bulgarica* Forel, 1892

Material: (G49), 18/7048a, 8♀♀.

29. *Chalepoxenus muellerianus* (Finzi, 1922)

Material: (G4), 18/0048c, 2♂♂, 1♀; (G12), 18/0144b, 1♂, 2♀♀; (G13), 18/0157b, 7♀♀, 15♂♂; (G28), 18/0299e, 1♀; (G44), 18/0496a, 1♀, 7♀♀.

30. *Crematogaster schmidtii* (Mayr, 1853)

Material: (G1), 18/0003b, 18/0010, 10♀♀; (G2), 18/0015, 20♀♀; (G3), 18/0030a, 26♀♀; (G4), 18/0059, 19♀♀; (G5), 18/0071, 34♀♀; (G6), 18/0084b, 23♀♀; (G7), 18/0097, 2♀♀; (G8), 18/0102, 13♀♀; (G9), 18/0112, 19♀♀; (G10), 18/0128b, 4♀♀; (G11), 18/0129, 18/0137a, 13♀♀; (G12), 18/0141a, 18/0142c, 9♀♀; (G13), 18/0150a, 7♀♀; (G14), 18/0159a, 10♀♀; (G15), 18/0179b, 13♀♀; (G16), 18/0183, 2♀♀; (G17), 18/0192a, 12♀♀; (G19), 18/0205b, 4♀♀; (G20), 18/0212a, 8♀♀; (G21), 18/0225, 13♀♀; (G22), 18/0236b, 8♀♀; (G23), 18/0241b, 21♀♀; (G24), 18/0258, 24♀♀; (G25), 18/0262a, 18♀♀; (G26), 18/0272a, 1♀; (G27), 18/0283b, 6♀♀; (G28), 18/0293, 18/0299c, 25♀♀; (G29), 18/0309e, 18/0319b, 11♀♀; (G30), 18/0321a, 18/0321b, 18/0329a, ♀♀; (G31), 18/0332, 18/0346e, 18♀♀; (G32), 18/0349a, 7♀♀; (G33), 18/0360b, 18/0361b, 19♀♀; (G34), 18/0370b, 18/0373, 17♀♀; (G35), 18/0376a, 18/0379c, 11♀♀; (G36), 18/0388, 18/0389, 10♀♀; (G37), 18/0402a, 18/0407a, 15♀♀; (G38), 18/0420, 40♀♀; (G39), 18/0433, 18/0434c, 31♀♀; (G40), 18/0448a, 16♀♀; (G41), 18/0455b, 18/0457a, 8♀♀; (G42), 18/0466b, 13♀♀; (G43), 18/0475b, 18/0477a, 26♀♀; (G44), 18/0486, 18/0493c, 18/0496c, 38♀♀; (G45), 18/7005b, 18/7010, 18/7011b, 23♂♂, ♀♀; (G46), 18/7012c, 18/7014a, 3♀♀; (G47), 18/7029a, 20♀♀; (G48), 18/7032a, 8♀♀; (G49), 18/7049, 20♀♀; (G50), 18/7056, 8♀♀;

(G52), 18/7069b, 12♀♀; (G53), 18/7082b, 9♀♀; (G54), 18/7092b, 23♀♀; (G55), 18/7104, 13♀♀; (G57), 18/7120a, 18/7129c, 4♀♀; (G58), 18/7133b, 18/7137, 18/7144b, 1♀, 10♂♂, 34♀♀; (G60), 18/7177c, 15♀♀; (G61), 18/7190, 1♂, 38♀♀; (G62), 18/7195, ♀♀; (G63), 18/7202, 23♀♀; (G64), 18/7209, ♂♂, ♀♀; (G65), 18/7230, 44♀♀; (G68), 17/0008b, 18♀♀; (G70), 17/0012b, 6♀♀; (G72), 17/0018d, 17/0020f, 12♀♀.

Remarks: [7] recorded *Crematogaster ionia* Forel, 1911 from Gökçeada island. At that time, the distribution of *C. schmidtii* from our region was not known yet. Only *C. ionia* and *C. scutellaris* (Olivier, 1798) species were known from our region. Thus, any specimen that was not *C. scutellaris* was diagnosed as *C. ionia*. Therefore, the specimens identified as *C. ionia* in Aras and Aktaç were refer to *C. schmidtii*. *Crematogaster scutellaris* is excluded from the Turkish ant fauna by [15] according to its Western Palearctic distribution. Therefore, the specimens previously recorded from Türkiye as *C. scutellaris* are actually records of the *C. schmidtii* species.

31. *Crematogaster sordidula* (Nylander, 1849)\*

Material: (G1), 18/0007, ♀♀; (G2), 18/0024, 12♀♀; (G4), 18/0052a, 42♀♀; (G5), 18/0063b, 18/0070, 6♀♀, ♂♂, 20♀♀; (G6), 18/0076, 3♀♀, 1♂, 30♀♀; (G7), 18/0086a, 8♂♂; (G8), 18/0108b, 2♂♂, 27♀♀; (G12), 18/0140a, 7♂♂, 18♀♀; (G13), 18/0156a, 3♀♀, 14♂♂, 34♀♀; (G16), 18/0184b, 10♂♂, 8♀♀; (G21), 18/0231, 10♂♂, 48♀♀; (G23), 18/0245, 31♀♀; (G27), 18/0287, 24♂♂, ♀♀; (G28), 18/0297a, 29♂♂, 6♀♀; (G32), 18/0349b, 8♀♀; (G35), 18/0381, 10♀♀; (G36), 18/0397, ♀♀; (G37), 18/0412, ♀♀; (G39), 18/0442, 1♀; (G40), 18/0445, ♀♀; (G41), 18/0464, 2♀♀, 25♀♀; (G47), 18/7028a, 43♀♀; (G48), 18/7035b, 35♀♀; (G50), 18/7055a, 26♀♀; (G53), 18/7086, ♀♀; (G55), 18/7102a, 35♀♀; (G61), 18/7191, 46♀♀; (G63), 18/7208, 3♀♀; (G64), 18/7219, ♀♀; (G65), 18/7225, 39♀♀; (G66), 17/0006b, 1♀; (G72), 17/0018c, 17/0020a, 41♀♀.

32. *Messor caducus* (Victor, 1839)

Material: (G5), 18/0068, 8♀♀; (G6), 18/0072b, 10♀♀; (G14), 18/0162, 10♀♀; (G21), 18/0221, 19♀♀; (G23), 18/0250a, 13♀♀; (G24), 18/0254, 1♀; (G26), 18/0270b, 4♀♀; (G36), 18/0387a, 29♀♀; (G40), 18/0448b, 1♀; (G43), 18/0485, 10♀♀; (G56), 18/7114, 7♀♀; (G58), 18/7130b, 3♀♀; (G59), 18/7147b, 18/7171, 25♀♀.

33. *Messor maculifrons* Santschi, 1927 (Figure 2)

Material: (G20), 18/0211a, 27♀♀.



Figure 2. *Messor maculifrons* Santschi, worker: A - Whole body (lateral), B - Head (profile)

Remarks: *Messor maculifrons* is characterized by presence of psammophore (J-shaped long bristle) on the ventral surface of the head (Figure 2A), reddish head and mesosoma, superficially dot sculptured head, more or less bicolored body (at least part of the mesosoma is lighter colored than the rest of the body), without spines or tubercles on the posterior corners of the propodeum, and without erect setae on first tergite of the gaster. The record of the species from Türkiye should be considered a normal result, considering the geographic distribution of the species.

34. *Messor mcarthuri* Steiner et al., 2018

Material: (G2), 18/0025, 48♀♀; (G5), 18/0063a, 3♀♀; (G7), 18/0090a, 39♀♀; (G10), 18/0128a, 5♀♀; (G23), 18/0242a, 4♀♀; (G25), 18/0260b, 18/0269b, 17♀♀; (G28), 18/0297b, ♀♀; (G34), 18/0374a, 1♀; (G42), 18/0466c, 2♀♀; (G48), 18/7039, 2♀♀; (G49), 18/7046a, 18/7050, 28♀♀; (G51), 18/7065c, 1♀; (G61), 18/7187, 8♀♀.

35. *Messor oertzeni* Forel, 1910\*

Material: (G25), 18/0267b, 6♀♀; (G36), 18/0400a, 24♀♀; (G42), 18/0474c, 1♀; (G48), 18/7033a, 18/7040, 12♀♀; (G49), 18/7047, 5♀♀; (G50), 18/7053b, 9♀♀; (G53), 18/7085c, 1♀; (G60), 18/7183a, 9♀♀; (G61), 18/7192, 6♀♀; (G65), 18/7221, 13♀♀.

36. *Messor cf. rufotestaceus*

Material: (G36), 18/0399, 27♀♀.

Remarks: [7] identified *Messor meridionalis* (André, 1883) and *M. sultanus* Santschi, 1917 species from Gökçeada. *Messor meridionalis* was removed from the ant list of Turkey by [8] and thus the absence of species in this study is an expected result. The fact that *M. sultanus*, which is known to be distributed in Egypt, Jordan, Israel, Palestine, Iran and Turkey, was not detected in this study can be explained by the fact that *Messor cf. rufotestaceus*, which is morphologically similar to *M. sultanus*, was detected in this study.

37. *Messor structor* (Latreille, 1798)\*

Material: (G54), 18/7095c, 28♀♀; (G72), 17/0014a, 50♀♀.

38. *Messor wasmanni* Krausse, 1910

Material: (G4), 18/0054, 18/0056, 68♀♀; (G6), 18/0081, 12♀♀; (G8), 18/0103, 26♀♀; (G13), 18/0158, 4♀♀; (G14), 18/0167, 22♀♀; (G16), 18/0190, 20♀♀; (G17), 18/0194, 34♀♀; (G20), 18/0219c, 1♀; (G21), 18/0223a, 24♀♀; (G22), 18/0235, 30♀♀; (G24), 18/0256, 4♀♀; (G27), 18/0292, 19♀♀; (G36), 18/0396, 21♀♀; (G38), 18/0418, 18/0422, 55♀♀; (G49), 18/7044, 15♀♀; (G50), 18/7062a, 10♀♀; (G52), 18/7076h, 18/7079c, 40♀♀; (G53), 18/7089b, 4♀♀; (G54),



18/7100b, 25♀♀; (G55), 18/7108b, 5♀♀; (G56), 18/7112, 4♀♀; (G57), 18/7127, 9♀♀; (G58), 18/7139, 18/7143, 38♀♀; (G59), 18/7148, 18/7155, ♀♀; (G60), 18/7175, 18/7182, 18/7183b, 16♀♀; (G61), 18/7189, 18/7193a, 22♀♀; (G64), 18/7215, 17♀♀; (G66), 17/0003e, 8♀♀; (G67), 17/0007a, 25♀♀; (G70), 17/0011a, 20♀♀.

39. *Monomorium monomorium* Bolton, 1987\*

Material: (G2), 18/0022b, 4♀♀; (G3), 18/0038b, 3♀♀; (G4), 18/0048b, 14♀♀; (G5), 18/0061e, 6♀♀; (G6), 18/0073b, 1♀; (G8), 18/0106a, 2♀♀; (G10), 18/0128c, 1♀; (G14), 18/0159e, 1♀; (G15), 18/0179d, 5♀♀; (G16), 18/0191, 7♀♀; (G19), 18/0208b, 1♀; (G21), 18/0230, 2♀♀; (G22), 18/0238b, 1♀; (G23), 18/0250b, 6♀♀; (G25), 18/0260e, 18/0264b, 11♀♀; (G26), 18/0271b, 1♀; (G27), 18/0290d, 2♀♀; (G28), 18/0295, 3♀♀; (G32), 18/0351d, 1♀; (G33), 18/0367a, 4♀♀; (G34), 18/0369c, 18/0370a, 13♀♀; (G35), 18/0379e, 1♀; (G36), 18/0395b, 1♀; (G37), 18/0413, 5♀♀; (G38), 18/0426, 3♀♀; (G40), 18/0446a, 7♀♀; (G42), 18/0473, 14♀♀; (G45), 18/7011d, 1♀; (G48), 18/7032b, 4♀♀; (G49), 18/7043c, 18/7051d, 3♀♀; (G51), 18/7065b, 4♀♀; (G52), 18/7076g, 11♀♀; (G53), 18/7089c, 1♀; (G54), 18/7093b, 3♀♀; (G57), 18/7119c, 18/7129b 7♀♀; (G58), 18/7144c, 6♀♀; (G59), 18/7150b, 18/7158, 3♀♀; (G66), 17/0003h, 1♀♀; (G68), 17/0008g, 2♀♀; (G72), 17/0015a, 87♀♀.

40. *Myrmoxenus cf. krausseii*

Material: (G14), 18/0169b, 1♀.

41. *Pheidole cf. pallidula*\*

Material: (G1), 18/0006, 1♂, 6♀♀; (G2), 18/0017, 36♀♀; (G3), 18/0034, 7♀♀; (G5), 18/0065a, 2♂♂, 1♂, 11♀♀; (G6), 18/0073a, 2♂♂, 17♀♀; (G7), 18/0096, 18/0098, 1♀, 5♀♀; (G8), 18/0104, 1♂, 24♀♀; (G9), 18/0110b, 5♀♀; (G10), 18/0122, 18/0126, 1♀, 8♂♂, 6♀♀; (G11), 18/0131b, 18/0136a, 4♂♂, 15♀♀; (G12), 18/0145, 8♂♂, 26♀♀; (G13), 18/0155, 26♀♀; (G14), 18/0159b, 10♀♀; (G15), 18/0175b,

18/0179c, 1♀, 1♂, 17♀♀; (G17), 18/0195a, 1♂, 29♀♀; (G20), 18/0210, 18/0219b, 9♀♀; (G21), 18/0223b, 18/0224, 18♀♀; (G22), 18/0232, 2♂♂, 8♀♀; (G23), 18/0243, 8♀♀; (G25), 18/0260c, 18/0263e, 6♀♀; (G26), 18/0272c, 2♀♀; (G27), 18/0280a, 18/0290a, 3♂♂, 22♀♀; (G28), 18/0302, 1♂, 17♀♀; (G29), 18/0318, 10♂♂, 37♀♀; (G31), 18/0346d, 2♀♀; (G32), 18/0347a, 18/0355c, 18/0356a, 1♂, 21♀♀; (G33), 18/0358a, 18/0364, 4♂♂, 35♀♀; (G34), 18/0369d, 18/0370c, 18/0374c, 8♀♀; (G35), 18/0376b, 18/0379a, 28♀♀; (G36), 18/0390, 32♀♀; (G37), 18/0401a, 18/0410b, 1♂, 19♀♀; (G39), 18/0429, 3♂♂, 5♀♀; (G41), 18/0458, 18/0463, 4♂♂, 39♀♀; (G42), 18/0474a, 1♀; (G43), 18/0481, 1♂, 1♀; (G44), 18/0493a, 18/0494, 18/0495a, 1♀, 6♂♂, 7♂♂, 43♀♀; (G45), 18/7002, 18/7011c, 10♂♂, 43♀♀; (G46), 18/7021, 8♀♀; (G47), 18/7027d, 1♂, 8♀♀; (G48), 18/7034, 1♂, 9♀♀; (G49), 18/7051b, 5♀♀; (G52), 18/7066, 2♂♂, 8♀♀; (G53), 18/7083a, 2♂♂, 1♀; (G54), 18/7093c, 1♀; (G55), 18/7102b, 10♂♂, 38♀♀; (G56), 18/7111, 2♂♂, 10♀♀; (G57), 18/7119b, 18/7128, 18/7129d, 2♂♂, 5♀♀; (G58), 18/7130a, 18/7138b, 3♀♀; (G59), 18/7156, 18/7170, 18♂♂, 8♀♀; (G60), 18/7174, 3♂♂, 38♀♀; (G61), 18/7193b, 3♂♂, 4♀♀; (G62), 18/7199, 1♂, 18♀♀; (G63), 18/7206a, 10♀♀; (G64), 18/7217, 1♀; (G65), 18/7223, 7♂♂, 8♀♀; (G68), 17/0008a, 17/0009c, 2♂♂, 25♀♀; (G69), 17/0010c, 1♀; (G70), 17/0011c, 17/0012d, 1♂, 5♀♀; (G72), 17/0015e, 17/0018b, 17/0020c, 69♀♀.

42. *Solenopsis lusitanica/fugax* (Latreille, 1798)\*

Material: (G4), 18/0046a, 33♀♀; (G6), 18/0075a, 18/0080, 54♀♀; (G11), 18/0135b, 18/0137b, 2♀♀; (G23), 18/0247b, 1♀; (G29), 18/0315, 40♀♀; (G30), 18/0320b, 8♀♀; (G31), 18/0339a, 18/0340a, 18/0346c, 1♀, 8♀♀; (G34), 18/0375b, 10♀♀; (G35), 18/0378, 22♀♀; (G37), 18/0411b, 1♀; (G39), 18/0437, 25♀♀; (G41), 18/0456b, 18/0465, 65♀♀; (G42), 18/0471, 8♀♀; (G43), 18/0477c, 18/0478, 29♀♀; (G44), 18/0491, 8♀♀; (G45), 18/7001, 18/7011e, 46♀♀; (G46),

18/7012b, 18/7018, ♀♀; (G52), 18/7078a, 16♀♀; (G55), 18/7103a, 1♀; (G57), 18/7117a, 18/7118b, ♀♀; (G59), 18/7147a, 15♀♀; (G63), 18/7206, 3♀♀; (G65), 18/7228, ♀♀; (G66), 17/0004b, 4♀♀; (G72), 17/0017b, 10♀♀.

43. *Temnothorax aeolius* (Forel, 1911)

Material: (G6), 18/0077b, 18/0085, 16♂♂, 12♀♀; (G12), 18/0143b, 1♂, 5♀♀; (G15), 18/0173b, 3♀♀, 11♀♀; (G21), 18/0229b, 5♀♀; (G22), 18/0236c, 1♂, 1♀; (G24), 18/0255, 2♀♀; (G61), 18/7185a, ♀♀.

44. *Temnothorax affinis* (Mayr, 1855)

Material: (G17), 18/0201, 2♀♀.

45. *Temnothorax antigoni* (Forel, 1911)

Material: (G1), 18/0011, 18/0012, 2♀♀, 26♀♀; (G2), 18/0020, 18/0021c, 1♀, 1♂, 13♀♀; (G3), 18/0033, 18/0040, 18/0042, 3♀♀, 22♀♀; (G5),

18/0062a, 1♀; (G12), 18/0142b, 18/0143a, 18/0144a, 4♀♀, 1♂, 40♀♀; (G14), 18/0169a, 10♀♀; (G15), 18/0178, 10♀♀; (G28), 18/0299f, 18/0305, 5♀♀; (G30), 18/0325, 18/0328, 18/0329c, 17♀♀; (G31), 18/0336c, 18/0346b, 7♀♀; (G32), 18/0347b, 18/0351c, 18/0356c, 2♀♀, 3♀♀; (G33), 18/0360a, 18/0361a, 18/0363, 28♀♀; (G34), 18/0370f, 1♀; (G39), 18/0434b, 18/0435, 1♀, 44♀♀; (G41), 18/0462, 25♀♀; (G42), 18/0469, 1♀, 37♀♀; (G44), 18/0496b, 13♀♀; (G46), 18/7020, 26♀♀; (G53), 18/7087a, 29♀♀; (G55), 18/7105b, 1♀, 18♀♀; (G57), 18/7122, ♀♀; (G63), 18/7206c, 1♀; (G72), 17/0015d, 1♀.

46. *Temnothorax bulgaricus* (Forel, 1892)

Material: (G2), 18/0023c, 1♀, 2♀♀; (G11), 18/0131a, 1♀, 8♀♀; (G15), 18/0177a, 18/0179a, 5♀♀, 47♀♀; (G23), 18/0247a, 5♀♀, 3♂♂, 35♀♀; (G29), 18/0309f, 1♀; (G31), 18/0331a, 18/0336b, 18/0344b, 18/0346a, 3♀♀, ♀♀; (G35), 18/0377, 18/0379b, 1♀, 39♀♀; (G37), 18/0405, 18/0407c, ♀♀; (G39), 18/0440, 1♀, 11♀♀; (G43), 18/0477b, 2♀♀; (G44), 18/0497, 18♀♀; (G45), 18/7008, 49♀♀; (G49), 18/7048a, 8♀♀; (G52),

18/7079a, 32♀♀; (G53), 18/7087b, 1♀; (G72), 17/0020, 1♀.

47. *Temnothorax dessyi* (Menozzi, 1936)

Material: (G15), 18/0175d, 1♀; (G31), 18/0345b, 1♀.

48. *Temnothorax flavicornis* (Emery, 1870)

Material: (G31), 18/0343, 1♀; (G37), 18/0415a, 1♀; (G46), 18/7014b, 1♀.

49. *Temnothorax graecus* (Forel, 1911)\*

Material: (G37), 18/0410a, 29♀♀.

50. *Temnothorax helenae* Csösz, Heinze & Miko, 2015

Material: (G39), 18/0434a, 1♀, 6♀♀.

Remarks: This species was recorded from Gökçeada island only by litter sifting method. This record shows us that the species nests among leaf litter.

51. *Temnothorax kemali* (Santschi, 1934)

Material: (G17), 18/0199a, 18/0201, 22♀♀.

52. *Temnothorax lucidus* Csösz, Heinze & Miko, 2015

Material: (G52), 18/7073, 2♀♀, ♀♀.

53. *Temnothorax nadigi* (Kutter, 1925)

Material: (G72), 17/0015c, 2♀♀.

54. *Temnothorax semiruber* (André, 1881)

Material: (G7), 18/0086d, 18/0094, 18/0095, 1♀, 3♂♂, 37♀♀; (G10), 18/0123, 18/0128e, 1♀, 22♀♀; (G12), 18/0146, 25♀♀; (G13), 18/0153a, 1♀; (G16), 18/0180, 31♀♀; (G17), 18/0200, 1♀, 8♀♀; (G23), 18/0244b, 11♀♀; (G35), 18/0385, 2♀♀; (G45), 18/7004, 30♀♀; (G54), 18/7091, 1♀, 12♀♀; (G57), 18/7124, 23♀♀; (G59), 18/7146, 1♀, ♀♀.

55. *Temnothorax strymonensis* Csösz, Salata & Borowiec, 2018

Material: (G27), 18/0290c, 8♀♀; (G28), 18/0299a, 1♀, 18♀♀; (G37), 18/0411a 1♀, 21♀♀.

56. *Temnothorax subtilis* Csösz, Heinze & Miko, 2015



Material: (G37), 18/0407b, 2♀♀.

57. *Temnothorax turcicus* (Santschi, 1934)

Material: (G3), 18/7083b, 1♀.

58. *Temnothorax unifasciatus* (Latreille, 1798)

Material: (G7), 18/0093, 2♂♂, 18♀♀.

59. *Tetramorium chefketi* Forel, 1911\*

Material: (G68), 17/0008k, 1♀.

60. *Tetramorium diomedea* Emery, 1908

Material: (G15), 18/0176a, 8♀♀; (G36), 18/0391, 3♀♀; (G54), 18/7094, 2♀♀, 1♀; (G57), 18/7120b, 4♀♀; (G58), 18/7141, 18/7144a, 1♀; (G59), 18/7159, 1♀.

61. *Tetramorium ferox* Ruzsky, 1903\*

Material: (G1), 18/0003a, 43♀♀; (G47), 18/7028b, 1♀; (G69), 17/0010a, 10♀♀.

62. *Tetramorium feroxoides* Dlussky & Zabelin, 1985

Material: (G9), 18/0116, 40♀♀.

63. *Tetramorium galaticum* Menozzi, 1936

Material: (G7), 18/0092, 13♀♀; (G13), 18/0156b, 1♀; (G14), 18/0165, 18/0170a, 1♀; (G20), 18/0217, 5♀♀; (G22), 18/0238a, 6♀♀; (G23), 18/0244a, 19♀♀; (G29), 18/0311, 6♀♀; (G38), 18/0425, 18/0428, 1♀; (G53), 18/7085a, 1♀; (G57), 18/7119a, 18/7129a, 17♀♀; (G59), 18/7145, 18/7157, 47♀♀; (G60), 18/7176b, 1♀.

64. *Tetramorium hippocrate* Agosti & Collingwood, 1987\*

Material: (G2), 18/0019, 18/0023a, 17♀♀; (G4), 18/0050, 18/0052b, 29♀♀; (G6), 18/0079, 3♀♀; (G7), 18/0087, 2♀♀, 7♂♂, 9♀♀; (G10), 18/0120b, 18/0127, 2♀♀, 31♀♀; (G11), 18/0135a, 18/0136b, 6♀♀; (G12), 18/0138b, 18/0140b, 2♀♀; (G15), 18/0173c, 18/0175c, 1♀, 2♀♀; (G16), 18/0189, 8♀♀; (G17), 18/0193, 18/0197a, 2♀♀, 51♀♀; (G19), 18/0208a, 5♀♀; (G20), 18/0214, 37♀♀; (G21), 18/0229c, 5♀♀; (G25), 18/0260f, 18/0261, 12♀♀; (G27), 18/0284, 18/0289, 4♀♀, 31♂♂, 55♀♀; (G29), 18/0308, 18/0317, 52♀♀; (G32), 18/0351b,

18/0352, 18/0354a, 33♀♀; (G33), 18/0362b, 18/0365, 15♀♀; (G34), 18/0371, 18/0375a, 23♀♀; (G35), 18/0383, 13♀♀; (G36), 18/0394, 1♀; (G37), 18/0415b, 6♀♀; (G38), 18/0424b, 11♀♀; (G40), 18/0452a, 20♀♀; (G43), 18/0482a, 6♀♀; (G44), 18/0487, 18/0493d, 9♀♀; (G48), 18/7035a, 18/7036, 1♀; (G52), 18/7079d, 1♀; (G53), 18/7080a, 1♀; (G54), 18/7093a, 17♀♀; (G55), 18/7103b, 15♀♀; (G58), 18/7135b, 18/7136a, 1♀; (G59), 18/7151, 18/7152, 66♀♀; (G62), 18/7197, 12♀♀; (G66), 17/0004a, 82♀♀; (G67), 17/0007d, 20♀♀; (G70), 17/0011d, 3♀♀; (G72), 17/0017a, 17/0018a, 17/0020h, 85♀♀.

65. *Tetramorium immigrans* Santschi, 1927

Material: (G2), 18/0022a, 22♀♀; (G3), 18/0035, 29♀♀; (G13), 18/0150b, 1♀; (G15), 18/0173a, 2♀♀; (G24), 18/0259c, 6♀♀; (G32), 18/0355d, 2♀♀; (G34), 18/0369b, 2♀♀; (G49), 18/7043b, 1♀; (G57), 18/7123, 9♀♀; (G61), 18/7188, 8♀♀; (G64), 18/7210, 1♀.

Remarks: [7] recorded *Tetramorium caespitum* (Linnaeus, 1758), *T. forte* Forel, 1904 and *Tetramorium* sp. from Gökçeada. They did not give any information about *Tetramorium* sp. It could be any recorded *Tetramorium* Mayr, 1855 species in this study and that's why it is normal not to record this taxon in this study. *Tetramorium forte* was excluded from Turkish ant list by [14] according to its Western Palearctic distribution and its material attributed to *T. chefketi* which was recorded in this study. One other species, *T. caespitum*, could not be recorded from Gökçeada in this study.

According to the study of [19], *T. caespitum* is not very common in Türkiye, while *T. immigrans* is known to be more common. Therefore, the detection of *T. immigrans* and the absence of *T. caespitum* should be considered normal in our study. Furthermore, [7] detected the social parasite species *Strongylognathus testaceus* (Schenck, 1852) in *Tetramorium* nest.

Although 114 different *Tetramorium* nest samples were detected in the study, the fact that any *Strongylognathus* Mayr, 1853 sample was not detected and this can be explained by chance

factor. It is thought that parasite species belonging to this genus can be recorded as a result of detailed studies to be carried out in order to identify possible parasites in *Tetramorium* nests.

66. *Tetramorium lucidulum* Menozzi, 1933

Material: (G4), 18/0058, 18♀♀; (G6), 18/0072c, 18/0073c, 1♀, 1♂; (G7), 18/0086f, 1♀; (G23), 18/0241a, 1♂.

67. *Tetramorium moravicum* Novák & Sadil, 1941

Material: (G26), 18/0279, 12♀♀; (G49), 18/7051a, 6♀♀.

68. *Tetramorium rhodium* Emery, 1924

Material: (G4), 18/0053a, ♀♀; (G15), 18/0173e, 1♂; (G21), 18/0226b, 18/0228, 1♀, 47♀♀; (G24), 18/0259a, 1♀, 7♀♀; (G38), 18/0419b, 13♀♀.

69. *Tetramorium sahlbergi* Finzi, 1936 (Figures 3-5)

Material: (G2), 18/0026, 3♀♀; (G4), 18/0055, 18/0057, 2♀♀, 2♂♂, ♀♀; (G5), 18/0069, 4♀♀, 10♂♂, ♀♀.

New record for Turkish ant fauna.

Remarks: *Tetramorium sahlbergi* is distinguished from other similar species by the fact that superficially sculptured head and mesosoma, wide petiole and postpetiole, small propodeal spines and brown to darkbrown-black body color. Due to the taxonomically chaotic situation in the species group in which *T. sahlbergi* is located, the taxonomic position of the species may change as a result of the revision in this species group.

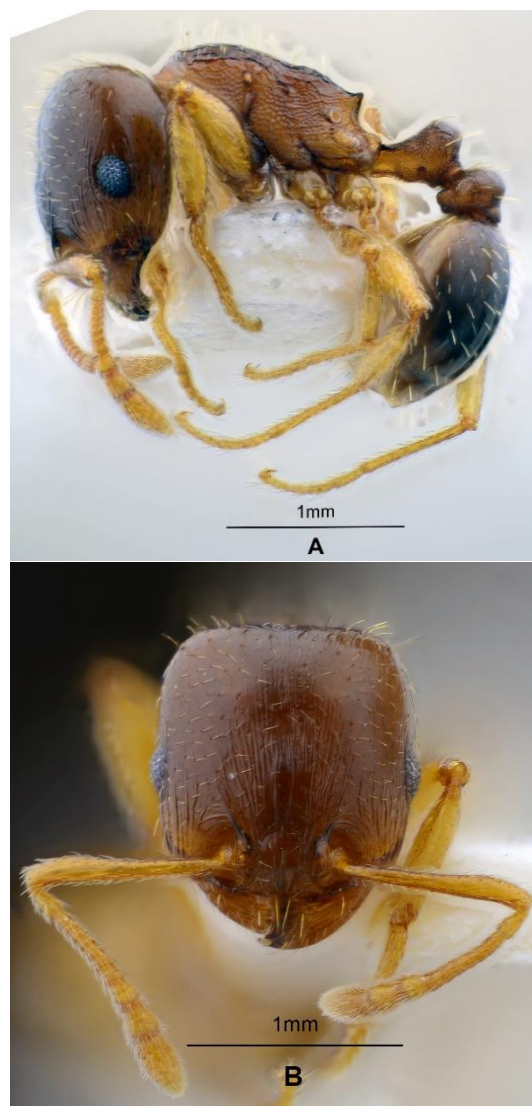


Figure 3. *Tetramorium sahlbergi* Finzi, worker: A - Whole body (lateral), B - Head (profile)

70. *Trichomyrmex perplexus* (Radchenko, 1997)

Material: (G6), 18/0083, 5♀♀; (G14), 18/0163, 25♀♀; (G23), 18/0251a, 10♀♀; (G24), 18/0253b, 1♂; (G25), 18/0269a, 15♀♀; (G26), 18/0277, 20♀♀; (G34), 18/0370d, 18/0372, 2♂♂, 1♂; (G49), 18/7048b, 4♀♀; (G60), 18/7173, 1♀, 16♂♂, 23♀♀; (G66), 17/0003b, 36♀♀.



**Figure 4.** *Tetramorium sahlbergi* Finzi, queen: A - Whole body (lateral), B - Head (profile)



**Figure 5.** *Tetramorium sahlbergi* Finzi, male: A - Whole body (lateral), B - Head (profile)

Subfamily: PONERINAE Lepeletier de Saint-Fargeau

71. *Hypoponera eduardi* (Forel, 1894) (Figures 6, 7)

Material: (G32), 18/0355a, 2♀♀; (G51), 18/7065a, 2♀♀, 3♂♂, 35♀♀.

Remarks: During the research, one of the workers from the samples collected from the G51 locality had multi-faceted compound eyes as in the queens, while the remaining had compound eyes with a few ommatidiums (Fig. 6A and Fig. 7A). When the reason for this situation was investigated, we found that [20] stated in their study that some workers belonging to the same colony in the Afrotropical region had compound eyes with zero-seven ommatidiums, while some workers had 7-30 ommatidiums as in queens.

They also reported that individuals with these different characters also usually have a shorter petiole in profile and a slightly enlarged gaster, and sometimes a queen-like horizontal sulcus in the mesopleuron, and defined such individuals as an ergatoid queen (worker-queen intermediate caste). In the individuals with multi-faceted compound eyes we found during the study, the mesosoma is more developed, the junction of the mesopleuron with the mesonotum is in a narrower structure compared to the workers with few facets.

Moreover, it is also seen that there is a small sulcus in the mesopleuron. These data indicate that the worker-like individuals with multiple facets are ergatoid queens. This situation has been recorded for the first time in our country and Palearctic region, and added the data *Hypoponera eduardi* forms ergatoid queens outside the Afrotropical region to its biology.

72. *Ponera testacea* Emery, 1895

Material: (G30), 18/0330b, 1♀; (G31), 18/0339b, 18/0341, 10♀♀; (G39), 18/0438, 6♀♀; (G52), 18/7076c, 1♀.



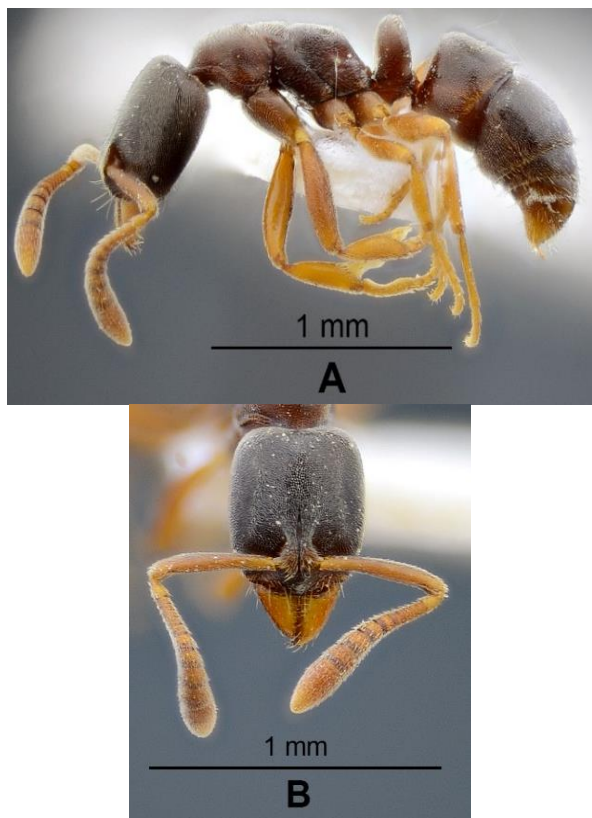


**Figure 6.** *Hypoponera eduardi* (Forel), worker: A - Whole body (lateral), B - Head (profile)

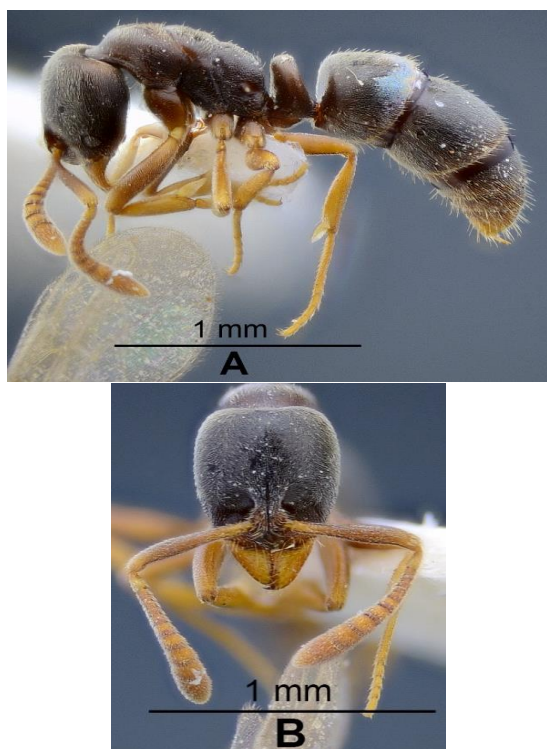


**Figure 7.** *Hypoponera eduardi* (Forel), ergatoid queen: A - Whole body (lateral), B - Head (profile)

#### 4. Discussion

In this study, 1185 ant materials obtained as a result of field studies carried out in 73 different

localities in 2017 and 2018 were evaluated and 72 taxa belonging to 4 subfamilies (Dolichoderinae, Formicinae, Myrmicinae, Ponerinae) and 23 genera were identified. Ponerinae subfamily and seven of (*Cardiocondyla* Emery, 1969, *Chalepoxenus* Menozzi, 1923, *Colobopsis* Mayr, 1861, *Hypoponera* Santschi, 1938, *Myrmoxenus* Ruzsky, 1902, *Ponera* Latreille, 1804 and *Trichomyrmex* Mayr, 1865) 23 genera are new records for the ant fauna of Gökçeada. Moreover, two of the identified species (*Messor maculifrons* and *Tetramorium sahlbergi*) are new records for the ant fauna of Türkiye.

22 of the 72 taxa identified (which mentioned by \* in the results section) (*Camponotus aethiops*, *C. dalmaticus*, *C. lateralis*, *C. piceus*, *C. samius*, *C. sanctus*, *Cataglyphis nodus*, *Crematogaster sordidula*, *Dolichoderus quadripunctatus*, *Lasius alienus*, *Lepisiota frauenfeldi*, *Messor oertzeni*, *M. structor*, *Monomorium monomorium*, *Pheidole cf. pallidula*, *Plagiolepis pallelescens*, *P. pygmaea*, *Solenopsis fugax*, *Temnothorax graecus*, *Tetramorium chefketi*, *T. ferox*, *T. hippocratis*) are common with the species recorded by [7]. We could not record 13 taxa (*Aphaenogaster simonelli*, *A. subterranea*, *Crematogaster ionia*, *C. scutellaris*, *Lasius brunneus*, *Messor meridionalis*, *M. sultanus*, *Strongylognathus testaceus*, *Tapinoma erraticum*, *T. nigerrimum*, *Tetramorium caespitum*, *T. forte* and *Tetramorium sp.*) recorded by [7]. The reasons for why not detecting the species recorded in [7] but not detected in our study are discussed under the relevant species in the results section.

During the study, besides the classical hand collecting method, the litter sifting method was also used. This method was used when a leaf litter present on the ground in the studied habitats. With this method, 21 ant taxa (*Aphaenogaster festae*, *Camponotus dalmaticus*, *C. ionius*, *C. lateralis*, *Chalepoxenus muellerianus*, *Crematogaster schmidtii*, *Lasius alienus*, *Lepisiota frauenfeldi*, *Monomorium monomorium*, *Pheidole cf. pallidula*, *Plagiolepis pygmaea*, *Solenopsis fugax*, *Temnothorax antigoni*, *T. bulgaricus*, *T. flavicornis*, *T. helenae*, *T. subtilis*, *T. strymonensis*, *Tetramorium galaticum*, *Te. hippocratis* and

*Trichomyrmex perplexus*) were recorded in the study. Among these taxa, *Temnothorax helenae* and *T. subtilis* species were determined only by litter sifting method. These findings once again demonstrated the necessity of using different methods together for the detection of rare ant species in the field.

When the distribution of the detected species according to the genera was examined, it was determined that the genus represented by the highest number of species was *Temnothorax* with 16 taxa. The genus *Temnothorax* is followed by the genus *Camponotus* represented by 12 species. It was determined that 13 genera (*Bothriomyrmex*, *Cardiocondyla*, *Cataglyphis*, *Chalepoxenus*, *Colobopsis*, *Dolichoderus*, *Hypoconer*, *Monomorium*, *Myrmoxenus*, *Pheidole*, *Ponera*, *Solenopsis* and *Trichomyrmex*) are represented by a single species in Gökçeada. The genus *Temnothorax*, which is represented by 42 species all over Türkiye, is the genus represented with the most species after the genus *Camponotus*, which is represented by 50 taxa [15], at recently. The fact that the genus *Temnothorax* is represented by 38% of total number of species in Türkiye in a very small region like Gökçeada is clearly an unexpected situation in this study. However, the real richness of the genus *Temnothorax* in Türkiye is unknown and it is expected and known that the true species richness of *Temnothorax* will emerge with many new species for the science still waiting to be defined, and it is expected to surpass *Camponotus* in terms of species number (Karaman and Kiran, unpublished data).

In addition, when the distribution of the species according to the habitats was examined, *Lepisiota frauenfeldi* was found to be the species with the highest ecological value, which was determined from 14 of the 16 habitats examined. After *Lepisiota frauenfeldi*, *Camponotus lateralis*, *Cataglyphis nodus*, *Crematogaster schmidtii*, *Monomorium monomorium*, *Pheidole* cf. *pallidula* and *Plagiolepis pygmaea* species recorded from 13 of 16 different habitats were identified as the second species with the highest ecological valance. Among the 16 habitats studied, the habitat with the highest number of species was barren soil with 53 taxa. The barren soil habitat was followed by maquis with 48 taxa

and then *Pinus brutia* forest with 43 taxa. It is an expected result that barren soil and maquis habitats are the habitats represented by the highest number of taxa. Because these habitats are the dominant habitats in the region and most of the field studies were carried out in these habitats.

*Pinus brutia* forest is also the dominant forest type in Gökçeada and although these forests do not cover much area, this result can be explained by the high species diversity and microhabitats suitable for ants despite the other habitats. The habitat represented by the fewest ant species was the coastal dune habitat (one species = *Cataglyphis nodus*). In this habitat, no ant species other than *C. nodus* was found, despite surveying for about two hours. This can be explained by the fact that coastal dune habitat is not suitable for ants to build nests due to the very loose soil structure.

*Crematogaster schmidtii*, which was recorded from 64 of the 73 localities surveyed, was found to be the most dominant species in the study area. In addition, this species nests in all kinds of microhabitats and exhibits a different behavior model in Gökçeada, which is different from the previous behavior of the species. This situation is also unprecedented when compared to the mainland. *Crematogaster schmidtii*, normally known as arboricolous, has been recorded to exhibit unusual behavior in Gökçeada, such as "forming paths of successive individuals" and dominating a large part of the area, which is known as the typical behavior of *Messor* colonies. *Crematogaster schmidtii* was followed by *Pheidole pallidula* and *Lepisiota frauenfeldi* species recorded from 59 and 55 localities each, respectively.

It is obvious that many new and valuable information will be obtained as a result of detailed studies on the ant fauna of the Turkish islands. For this reason, it is necessary to continue the ant fauna studies of the Turkish islands in the future.



## Article Information Form

### **Acknowledgments**

We would like to thank Kadri KIRAN (Trakya University) for his help of preparation of the ant photographs. This paper was produced from part of MSc thesis of Esra SERT.

### **Funding**

This study is supported by Trakya University Scientific Research Projects Coordination Unit. Project Number: 2018-135.

### **Authors' Contribution**

Conceptualization, E.S. and C.K.; Design: E.S. and C.K.; Execution: E.S. and C.K.; Material supplying: C.K.; Data acquisition: E.S. and C.K.; Data analysis/interpretation: E.S. and C.K.; Writing: E.S. and C.K.; Critical review: C.K. All authors have read and agreed to the published version of the manuscript.

### **The Declaration of Conflict of Interest/ Common Interest**

No conflict of interest or common interest has been declared by the authors.

### **The Declaration of Ethics Committee Approval**

This study does not require ethics committee permission or any special permission.

### **The Declaration of Research and Publication Ethics**

The authors of the paper declare that they comply with the scientific, ethical and quotation rules of SAUJS in all processes of the paper and that they do not make any falsification on the data collected. In addition, they declare that Sakarya University Journal of Science and its editorial board have no responsibility for any ethical violations that may be encountered, and that this study has not been evaluated in any academic publication environment other than Sakarya University Journal of Science.

### **Copyright Statement**

Authors own the copyright of their work published in the journal and their work is published under the CC BY-NC 4.0 license.

## References

- [1] L. Rigler, “Die Turkei und deren Bewohner in ihren naturhistorischen, physiologischen und pathologischen Verhältnissen vom Standpunkte Constantinopel's,” Wien, Verlag von Carl Gerold, 1852, p. 137.
- [2] C. Emery, “Studi mirmecologici,” *Bullettino della Società Entomologica Italiana*, vol. 2, pp. 193-201, 1870.
- [3] C. Emery, “Le forme paleartiche del *Camponotus maculatus* F.,” *Rendiconto delle Sessioni della R. Accademia delle Scienze dell'Istituto di Bologna*, vol. (n.s.) 9, pp. 27-44, 1905.
- [4] A. Forel, “Fourmis d'Asie mineure et de la Dobrudscha récoltées par M. le Dr. Oscar Vogt et Mme Cécile Vogt, Dr. méd.,” *Annales de la Société Entomologique de Belgique*, vol. 50, pp. 187-190, 1906.
- [5] B. Schkaff, “Formiche di Constantinopoli,” *Bollettino della Società Entomologica Italiana*, vol. 56, pp. 90-96, 1924.
- [6] H. Donisthorpe, “A first instalment of the ants of Turkey,” *Annals and Magazine of Natural History*, vol. 12, no. 3, pp. 1057-1067, 1950.
- [7] A. Aras, N. Aktaç, “Gökçeada karınca faunası hakkında ön araştırma,” in *Proceeding of 11<sup>th</sup> National Congress of Biology, Journal of Zoology*, Elazığ, Turkey, 24-27 June 1992, pp. 45-53.
- [8] A. Aras, N. Aktaç, “Bozcaada Karınca Faunası,” in *Proceeding of 12<sup>th</sup> National Congress of Biology*, Edirne, Turkey, 1994, pp. 234-241.
- [9] O. Yaşar, “Turizm coğrafyası açısından bir araştırma: Gökçeada (İmroz),” *Fırat University Journal of Social Science*, vol. 16, no. 1, pp. 1-32, 2006.

- [10] K. Kiran, C. Karaman, "Ant fauna (Hymenoptera: Formicidae) of Central Anatolian Region of Turkey," *Turkish Journal of Zoology*, vol. 45, pp. 161-196, 2021.
- [11] B. Seifert, D. d'Eustacchio, B. Kaufmann, M. Centorame, P. Lorite, M. Modica, "Four species within the supercolonial ants of the *Tapinoma nigerrimum* complex revealed by integrative taxonomy (Hymenoptera: Formicidae)," *Myrmecological News*, vol. 24, pp. 123-144, 2017.
- [12] K. Kiran, N. Aktaç, "The Vertical Distribution of the Ant Fauna (Hymenoptera: Formicidae) of the Samanlı Mountains, Turkey," *Linzer Biologische Beiträge*, vol. 38, no. 2, pp. 1105-1122, 2006.
- [13] C. Karaman, N. Aktaç, K. Kiran, "Ants of the genus *Camponotus* Mayr, 1861 (Hymenoptera: Formicidae) in the Kaz Mountains, Turkey, with descriptions of sexuals of *Camponotus candiotes* Emery, 1894 and *Camponotus ionius* Emery, 1920," *Turkish Journal of Zoology*, vol. 35, no. 2, pp. 183-197, 2011.
- [14] K. Kiran, C. Karaman, "First annotated checklist of the ant fauna of Turkey (Hymenoptera: Formicidae)," *Zootaxa*, vol. 3548, pp. 1-38, 2012.
- [15] K. Kiran, C. Karaman, "Additions to the Ant Fauna of Turkey (Hymenoptera, Formicidae)," *Zoosystema*, vol. 42, no. 18, pp. 285-329, 2020.
- [16] L. Borowiec, S. Salata, "A *monographic review of ants of Greece (Hymenoptera: Formicidae)*," *Bytom: Natural History Monographs of the Upper Silesian Museum*, 2022, p. 297.
- [17] L. Borowiec, "Catalogue of ants of Europe, the Mediterranean Basin and adjacent regions (Hymenoptera: Formicidae)," *Genus*, vol. 25, no. 1-2, pp. 1-340, 2014.
- [18] E. Schifani, A. Alicata, M. Menchetti, L. Borowiec, B. L. Fisher, C. Karaman, K. Kiran, W. Oueslati, S. Salata, R. Blatrix, "Revisiting the morphological species groups of West-Palaearctic *Aphaenogaster* ants (Hymenoptera: Formicidae) under a phylogenetic perspective: toward an evolutionary classification," *Arthropod Systematics & Phylogeny*, vol. 80, pp. 627-648, 2022.
- [19] C. H. Wagner, W. Arthofer, B. Seifert, C. Muster, F. M. Steiner, B. Schlick-Steiner, "Light at the end of the tunnel: Integrative taxonomy delimits cryptic species in the *Tetramorium caespitum* complex (Hymenoptera: Formicidae)," *Myrmecological News*, vol. 25, pp. 95-129, 2017.
- [20] B. Bolton, B. L. Fisher, "Taxonomy of Afrotropical and West Palaearctic ants of the ponerine genus *Hypoponera* Santschi (Hymenoptera: Formicidae)," *Zootaxa*, vol. 2843, pp. 1-118, 2011.

## Schwarz Problem for Model Partial Differential Equations with One Complex Variable

Bahriye Karaca 

Izmir Bakircay University, Faculty of Engineering and Architecture, Department of Fundamental Sciences, Izmir, Türkiye, [bahriye.karaca@bakircay.edu.tr](mailto:bahriye.karaca@bakircay.edu.tr)

### ARTICLE INFO

### ABSTRACT

#### Keywords:

Schwarz Problem  
Complex model homogeneous partial differential equation  
Complex model inhomogeneous partial differential equations

#### Article History:

Received: 14.11.2023

Accepted: 19.01.2024

Online Available: 24.04.2024

This paper investigates the Schwarz problem. Initially, the focus lies on analyzing the problem for the first, second orders. Subsequently, attention shifts towards studying the same problem for equations of higher order. In the realm of second-order equations, the Schwarz problem is specifically examined for some operators; Laplace, Bitsadze and its complex conjugate. The findings demonstrate that the Schwarz problem for an n-order equation, when equipped with solely one boundary condition, exhibits an infinite number of solutions. However, by incorporating additional boundary conditions, it becomes feasible to obtain a unique solution for problem concerning n-order equations, effectively rendering it a well-posed problem.

## 1. Introduction

Explicit solutions to different boundary value problems are investigated in [1-8] for different domains. The Schwarz problem has an important place in both real and complex analysis as one of the fundamental problems. This boundary value problem is widely recognized and extensively studied.

This paper aims to investigate the Schwarz problem for one complex variable with arbitrary order.

We will define  $\mathbb{D}$  as the unit disc with a smooth boundary  $\partial\mathbb{D}$ ,  $\zeta \in \mathbb{C}$ ,  $\zeta = \xi + i\eta$ .

The following problem was solved with  $w \equiv 0$  in [1].

$$w_z = 0 \text{ in } \mathbb{D}, \Re w = 0 \text{ on } \partial\mathbb{D}, \Im w(0) = 0 \quad (1)$$

The same problem with nonhomogeneous boundary conditions has a unique solution in the same domain and proved in Theorem 9 in [1].

The following problem is the complex conjugate of the problem (1). It has a trivial solution in  $\mathbb{D}$ .

$$w_z = 0 \text{ in } \mathbb{D}, \Re w = 0 \text{ on } \partial\mathbb{D}, \Im w(0) = 0 \quad (2)$$

## 2. Schwarz Problem for Second Order Equations

In the realm of complex analysis, Laplace and Bitsadze operators hold fundamental importance. In this section, our focus is on addressing the Schwarz problem pertaining to these operators as well as the conjugate operator of the Bitsadze.

**Lemma 1:** [1] Within the context of the Laplace equation, the following Schwarz problem has infinitely many solutions

$$w_{z\bar{z}} = 0 \text{ in } \mathbb{D}, \Re w = 0 \text{ on } \partial\mathbb{D}, \Im w(0) = 0$$

**Proof.** Since  $w_{z\bar{z}} = 0$  in  $\mathbb{D}$ ,  $w_z$  is analytic in  $\mathbb{D}$ . Integrating the quantity, we get

$$w(z) = \varphi_1(z) + \overline{\varphi_2(z)},$$

where  $\varphi_1, \varphi_2$  are both analytic functions in  $\mathbb{D}$ . Since  $\Re w = 0$  on  $\partial\mathbb{D}$  and  $\Im w(0) = 0$ , we

obtain  $\Re\varphi_1(z) = -\Re\varphi_2(z)$  on  $\partial\mathbb{D}$  and  $\Im\varphi_1(0) = \Im\varphi_2(0)$ .

From Theorem 9 in [1], we write

$$\varphi_1(z) = \frac{1}{2\pi i} \int_{\partial\mathbb{D}} -\Re\varphi_2(\zeta) \frac{\zeta + z d\zeta}{\zeta - z \zeta} + i \Im\varphi_2(0) \tag{3}$$

It follows that

$$\varphi_1(z) = -\varphi_2(z) + \varphi_2(0) - \overline{\varphi_2(0)}.$$

Substituting  $\varphi_1(z)$  into the  $w(z)$ , we have  $w(z) = -2\Im\varphi_2(z) + 2\Im\varphi_2(0)$  for arbitrary analytic function  $\varphi_2(z)$ .  $\square$

The problem above has a unique solution over  $\mathbb{C}$  with additional boundary conditions as shown in Theorem 1 in [1].

By swapping the roles of  $z$  and  $\bar{z}$  in the result of Theorem 1 in [1], we obtain the dual result presented in [1].

**Lemma 2:** [1] The Schwarz problem for the Bitsadze equation

$$w_{\bar{z}\bar{z}} = 0 \text{ in } \mathbb{D}, \Re w = 0 \text{ on } \partial\mathbb{D}, \Im w(0) = 0,$$

has infinitely many solutions.

**Proof.**  $w_{\bar{z}}$  is analytic in  $\mathbb{D}$ . Integrating  $w_{\bar{z}\bar{z}} = 0$ , we have  $w(z) = h_1(z) + \bar{z}h_2(z)$ , where  $h_1, h_2$  are both analytic in  $\mathbb{D}$ . From the boundary conditions  $\Re h_1(z) = -\Re \bar{z}h_2(z)$  on  $\partial\mathbb{D}$  and  $\Im h_1(0) = 0$  follows. This Schwarz problem has a unique solution as

$$h_1(z) = \frac{1}{2\pi i} \int_{\partial\mathbb{D}} -\Re \bar{\zeta} h_2(\zeta) \frac{\zeta + z d\zeta}{\zeta - z \zeta} + i \Im h_1(0)$$

and it follows

$$h_1(z) = \frac{-1}{z} h_2(z) + \frac{1}{z} h_2(0) - \overline{zh_2(0)} + \frac{1}{2} h_2'(0) - \frac{1}{2} \overline{h_2'(0)}$$

Then, we have the following

$$w(z) = h_2(z) \left( \frac{|z|^2 - 1}{z} \right) + \frac{1}{z} h_2(0) - \overline{zh_2(0)} + \frac{1}{2} h_2'(0) - \frac{1}{2} \overline{h_2'(0)}$$

with arbitrary analytic function  $h_2(z)$  in  $\mathbb{D}$ .  $\square$

In Theorem 2 in [1], it is proved that by taking additional boundary conditions, the Schwarz problem in Lemma 2 has a unique solution.

Presently, we have the opportunity to examine the Schwarz problem concerning the subsequent equation

$$w_{zz} = 0 \text{ in } \mathbb{D}, \Re w = 0 \text{ on } \partial\mathbb{D}, \Im w(0) = 0. \tag{4}$$

Lemma 3 follows from this result.

**Lemma 3:** The Schwarz problem (4) exhibits an infinite number of solutions over the complex plane,  $\mathbb{C}$ .

**Proof.** First the following transformation is applied.

$$\overline{w}_{\bar{z}\bar{z}} = 0 \text{ in } \mathbb{D}, \Re \overline{w} = 0 \text{ on } \partial\mathbb{D}, \Im \overline{w}(0) = 0.$$

Then from Lemma 2 applied to  $\overline{w}$ , we get

$$w(z) = \overline{\varphi_2(z)} \left( \frac{|z|^2 - 1}{\bar{z}} \right) + \frac{1}{\bar{z}} \overline{\varphi_2(0)} - \bar{z}\varphi_2(0) + \frac{1}{2} \overline{\varphi_2'(0)} - \frac{1}{2} \varphi_2'(0)$$

with arbitrary analytic function  $\varphi_2(z)$  in  $\mathbb{D}$ .  $\square$

Using boundary conditions again, the following result is obtained.

**Corollary 4:** The following Schwarz problem in  $\mathbb{D}$

$$w_{zz} = f(z) \text{ in } \mathbb{D}, \Re w = \gamma_0(z), \Re w_z = \gamma_1(z) \text{ on } \partial\mathbb{D}, \Im w(0) = c_0, \Im w_z(0) = c_1$$

has a unique solution for

$f \in L_1(\mathbb{D}; \mathbb{C})$  and  $\gamma_0, \gamma_1 \in C(\partial\mathbb{D}; \mathbb{R}), c_0, c_1 \in \mathbb{R}$  with solution

$$\begin{aligned} w(z) &= i c_0 + i c_1(z + \bar{z}) \\ &\quad + \frac{1}{2\pi i} \int_{\partial\mathbb{D}} \gamma_0(\zeta) \frac{\overline{\zeta + z}}{\zeta - z} \frac{d\zeta}{\zeta} \\ &\quad - \frac{1}{2\pi i} \int_{\partial\mathbb{D}} \gamma_1(\zeta) \frac{\overline{\zeta + z}}{\zeta - z} (\zeta - z + \overline{\zeta - z}) \frac{d\zeta}{\zeta} \\ &\quad + \frac{1}{2\pi} \iint_{\mathbb{D}} \left( \frac{f(\zeta)}{\zeta} \frac{\overline{\zeta + z}}{\zeta - z} + \frac{\overline{f(\zeta)}}{\zeta} \frac{1 + \bar{z}\zeta}{1 - \bar{z}\zeta} \right) (\zeta - z \\ &\quad \quad + \overline{\zeta - z}) d\xi d\eta \end{aligned}$$

**Proof.** The issue can be rephrased in the following manner by taking the complex conjugation:

$$\overline{w_{\bar{z}\bar{z}}} = \overline{f(z)} \text{ in } \mathbb{D}, \Re e \overline{w} = \gamma_0(z),$$

$$\begin{aligned} \Re e \overline{w_{\bar{z}}} &= \gamma_1(z) \text{ on } \partial\mathbb{D}, \\ \Im m w(0) &= c_0, \Im m w_z(0) = c_1 \end{aligned}$$

The desired result is obtained by applying the result in Theorem 2 in [1] to  $\overline{w}$ .  $\square$

### 3. Schwarz Problem for Higher Order Differential Equations

In this section, we explored the Schwarz problem concerning n-order model differential equations in the complex domain,  $\mathbb{C}$ .

#### 3.1. Auxiliary lemmas

**Lemma 5:** [2] Suppose that  $f(z)$  is analytic function in  $\mathbb{D}$ . We obtain the equation (5).

$$\begin{aligned} \frac{1}{2\pi i} \int_{\partial\mathbb{D}} \bar{\zeta}^l f(\zeta) \frac{d\zeta}{\zeta - z} &= \frac{f(z)}{z^l} \\ - \sum_{r=1}^l \frac{1}{z^{l-r+1}} \frac{f^{(r-1)}(0)}{(r-1)!}, \quad l \geq 0. \end{aligned} \tag{5}$$

**Lemma 6:** [2] Suppose that  $f(z)$  is analytic function in  $\mathbb{D}$ . We get the equation (6) for  $k \geq 0$ .

$$\frac{1}{2\pi i} \int_{\partial\mathbb{D}} \zeta^k \overline{f(\zeta)} \frac{d\zeta}{\zeta - z} = \sum_{m=0}^k \frac{z^{k-m} \overline{f^{(m)}(0)}}{m!} \tag{6}$$

#### 3.2. The Schwarz problem for polyanalytic equations

The solution of  $w_{\bar{z}^n} = 0$  is called polyanalytic function. Theorem 2 in [1] is generalized as follows:

**Lemma 7:** The Schwarz problem below exhibits an infinite number of solutions in the unit disc of the complex plane. For  $l > 2$  we get,

$$w_{\bar{z}^l} = 0 \text{ in } \mathbb{D}, \Re e w = 0 \text{ on } \partial\mathbb{D}, \Im m w(0) = 0,$$

**Proof.** By integrating the given quantity, it follows that:

$$w(z) = \sum_{n=1}^l \bar{z}^{n-1} \varphi_n(z),$$

for  $\varphi_i, i = 1, \dots, l$ . They are analytic in  $\mathbb{D}$ . We have

$$\Re e \varphi_1(z) = -\Re e \sum_{n=2}^l \bar{z}^{n-1} \varphi_n(z) \text{ on } \partial\mathbb{D}$$

and

$$\Im m \varphi_1(0) = 0.$$

We get the equation below after applying the Theorem 9 in [1].

$$\begin{aligned} \varphi_1(z) &= \frac{1}{2\pi i} \int_{\partial\mathbb{D}} -\Re e \sum_{n=2}^l \bar{\zeta}^{n-1} \varphi_n(\zeta) \left( \frac{\zeta + z}{\zeta - z} \right) \frac{d\zeta}{\zeta} + i0, \\ \varphi_1(z) &= \frac{-1}{2\pi i} \int_{\partial\mathbb{D}} \sum_{n=2}^l \left( \bar{\zeta}^{n-1} \varphi_n(\zeta) + \zeta^{n-1} \overline{\varphi_n(\zeta)} \right) \frac{d\zeta}{\zeta - z} \\ &\quad + \frac{1}{2} \frac{1}{2\pi i} \int_{\partial\mathbb{D}} \sum_{n=2}^l \left( \bar{\zeta}^{n-1} \varphi_n(\zeta) + \zeta^{n-1} \overline{\varphi_n(\zeta)} \right) \frac{d\zeta}{\zeta}. \end{aligned}$$

From Lemma 5 and Lemma 6, we have

$$\begin{aligned} \varphi_1(z) &= - \sum_{n=2}^l \frac{\varphi_n(z)}{z^{n-1}} + \sum_{n=2}^l \sum_{m=0}^{n-2} \frac{1}{z^{n-m-1}} \frac{\varphi_n^{(m)}(0)}{m!} \\ &\quad - \sum_{n=2}^l \sum_{m=0}^{n-2} z^{n-m-1} \frac{\overline{\varphi_n^{(m)}(0)}}{m!} \\ &\quad + \frac{1}{2} \sum_{n=2}^l \left( \frac{\varphi_n^{(n-1)}(0)}{(n-1)!} - \frac{\overline{\varphi_n^{(n-1)}(0)}}{(n-1)!} \right). \end{aligned}$$

Therefore,  $w(z)$  is equal to

$$\begin{aligned} \sum_{n=2}^l \varphi_n(z) \left( \frac{|z|^{2(n-1)} - 1}{z^{n-1}} \right) \\ + \sum_{n=2}^l \sum_{m=0}^{n-2} \left( \frac{1}{z^{n-m-1}} \frac{\varphi_n^{(m)}(0)}{m!} - z^{n-m-1} \frac{\overline{\varphi_n^{(m)}(0)}}{m!} \right) \end{aligned}$$



$$+ \frac{1}{2} \sum_{n=2}^l \left( \frac{\varphi_n^{(n-1)}(0)}{(n-1)!} - \overline{\frac{\varphi_n^{(n-1)}(0)}{(n-1)!}} \right) \quad \square$$

Unless additional boundary conditions are imposed, the Schwarz problem for higher order model equations is known to be undetermined.

**Theorem 8:** [1] The Schwarz problem for inhomogeneous polyanalytic equation

$$w_{\bar{z}^k} = f(z) \text{ in } \mathbb{D}, \quad \Re \partial_{\bar{z}}^{\nu} w = \gamma_{\nu} \text{ on } \partial \mathbb{D},$$

$$\Im \partial_{\bar{z}}^{\nu} w(0) = c_{\nu} \quad 0 \leq \nu \leq k-1,$$

has a unique solution for  $\gamma_{\nu} \in C(\partial \mathbb{D}; \mathbb{C}), c_{\nu} \in \mathbb{R}, 0 \leq \nu \leq k-1$  as

$$\begin{aligned} w(z) &= i \sum_{\nu=0}^{k-1} \frac{c_{\nu}}{\nu!} (z + \bar{z})^{\nu} \\ &+ \sum_{\nu=0}^{k-1} \frac{(-1)^{\nu}}{\nu!} \frac{1}{2\pi i} \int_{\partial \mathbb{D}} \gamma_{\nu}(\zeta) \frac{\zeta + z}{\zeta - z} \left( \zeta - z + \overline{\zeta - z} \right)^{\nu} \frac{d\zeta}{\zeta} \\ &+ \frac{(-1)^k}{(k-1)!} \frac{1}{2\pi} \iint_{\mathbb{D}} \left( \frac{f(\zeta) \zeta + z}{\zeta \zeta - z} + \frac{\overline{f(\zeta)} \overline{1 + z\zeta}}{\overline{\zeta} \overline{1 - z\zeta}} \right) \\ &\quad \times (\zeta - z + \overline{\zeta - z})^{k-1} d\xi d\eta \end{aligned}$$

**Lemma 9:** The Schwarz problem

$$\begin{aligned} w_{z^k} &= 0 \text{ in } \mathbb{D}, \quad \Re w = 0 \text{ on } \partial \mathbb{D}, \\ \Im w(0) &= 0, \quad k \in \mathbb{Z}^+, \quad k > 2 \end{aligned}$$

has infinitely many solutions in the complex space.

**Proof.** Taking the complex conjugation of the problem in Lemma 7 and then replacing  $\bar{w}$  by  $w$  leads to

$$w_{z^k} = 0 \text{ in } \mathbb{D}, \quad \Re w = 0 \text{ on } \partial \mathbb{D}, \quad \Im w(0) = 0.$$

Therefore, we get  $w(z)$  as

$$\begin{aligned} w(z) &= \sum_{n=2}^k \overline{\varphi_n(z)} \left( \frac{|z|^{2(n-1)} - 1}{\bar{z}^{n-1}} \right) \\ &+ \sum_{n=2}^k \sum_{m=0}^{n-2} \left( \frac{1}{\bar{z}^{n-m-1}} \frac{\overline{\varphi_n^{(m)}(0)}}{m!} - \bar{z}^{n-m-1} \frac{\varphi_n^{(m)}(0)}{m!} \right) \end{aligned}$$

$$+ \frac{1}{2} \sum_{n=2}^k \left( \frac{\overline{\varphi_n^{(n-1)}(0)}}{(n-1)!} - \frac{\varphi_n^{(n-1)}(0)}{(n-1)!} \right)$$

for analytic functions  $\varphi_i(z), i = 2, \dots, k$  in  $\mathbb{D}$ .  $\square$

Similarly, the unique solution for the problem

$$\begin{aligned} w_{z^k} &= 0 \text{ in } \mathbb{D}, \quad \Re \partial_z^{\nu} w = \\ \gamma_{\nu} &\text{ on } \partial \mathbb{D}, \quad \Im \partial_z^{\nu} w(0) = c_{\nu}, \\ k &\in \mathbb{Z}^+, \quad 0 \leq \nu \leq k-1 \end{aligned}$$

can be obtained, as stated in Theorem 10.

**Theorem 10:** The Schwarz problem for inhomogeneous equation

$$\begin{aligned} w_{z^k} &= f(z) \text{ in } \mathbb{D}, \quad \Re \partial_z^{\nu} w = \gamma_{\nu} \text{ on } \partial \mathbb{D}, \\ \Im \partial_z^{\nu} w(0) &= c_{\nu} \quad 0 \leq \nu \leq k-1, \end{aligned} \quad (7)$$

has a unique solution for  $\gamma_{\nu} \in C(\partial \mathbb{D}; \mathbb{C}), c_{\nu} \in \mathbb{R}, 0 \leq \nu \leq k-1$  as

$$\begin{aligned} w(z) &= i \sum_{\nu=0}^{k-1} \frac{c_{\nu}}{\nu!} (z + \bar{z})^{\nu} \\ &+ \sum_{\nu=0}^{k-1} \frac{(-1)^{\nu}}{\nu!} \frac{1}{2\pi i} \int_{\partial \mathbb{D}} \gamma_{\nu}(\zeta) \frac{\overline{\zeta + z}}{\overline{\zeta - z}} (\zeta - z + \overline{\zeta - z})^{\nu} \frac{d\zeta}{\zeta} \\ &+ \frac{(-1)^k}{(k-1)!} \frac{1}{2\pi} \iint_{\mathbb{D}} \left( \frac{f(\zeta) \overline{\zeta + z}}{\overline{\zeta} \overline{\zeta - z}} + \frac{f(\zeta) \overline{1 + z\zeta}}{\overline{\zeta} \overline{1 - z\zeta}} \right) \\ &\quad \times (\zeta - z + \overline{\zeta - z})^{k-1} d\xi d\eta \end{aligned}$$

**Proof.** The anticipated outcome is a consequence of applying Theorem 8 to the complex conjugate of equation (7) with respect to the variable  $\bar{w}$ .  $\square$

### 3.3. The Schwarz problem for mixed higher order partial differential equations

**Lemma 11:** The Schwarz problem

$$\begin{aligned} w_{z^m \bar{z}^n} &= 0 \text{ in } \mathbb{D}, \\ \Re w &= 0 \text{ on } \partial \mathbb{D}, \quad \Im w(0) = 0, \\ n + m &> 2, \quad n \geq 1, m \geq 1 \end{aligned}$$

has infinitely many solutions.

**Proof.** Upon integrating  $w_{z^m \bar{z}^n} = 0$  with respect to both  $z$  and  $\bar{z}$  we obtain

$$\omega(z) = \sum_{k=1}^n \bar{z}^{n-k} \varphi_{k-1}(z) + \sum_{k=n+1}^{n+m} z^{n+m-k} \overline{\varphi_{k-1}(z)}, \quad z \in \mathbb{D},$$

where  $\varphi_k(z)$ ,  $0 \leq k \leq n+m-1$  are analytic functions. Since  $\Re e \omega = 0$  on  $\partial \mathbb{D}$ , and  $\Im m \omega(0) = 0$ , we obtain

$$\Re e \varphi_{n-1}(z) = -\Re e \sum_{k=1}^{n-1} \bar{z}^{n-k} \varphi_{k-1}(z) - \Re e \sum_{k=0}^{m-1} z^{m-k-1} \overline{\varphi_{n+k}(z)} \text{ on } \partial \mathbb{D}$$

and

$$\Im m \varphi_{n-1}(0) = \Im m \varphi_{n+m-1}(0).$$

$\varphi_{n-1}(z)$  is analytic in  $\mathbb{D}$ . Therefore, from Theorem 9 in [1], we obtain

$$\varphi_{n-1}(z) = \frac{-1}{2\pi i} \int_{\partial \mathbb{D}} R e \left( \sum_{k=1}^{n-1} \bar{\zeta}^{n-k} \varphi_{k-1}(\zeta) + \sum_{k=0}^{m-1} \zeta^{m-k-1} \overline{\varphi_{n+k}(\zeta)} \right) \frac{\zeta+z}{\zeta-z} + i \Im m \varphi_{n+m-1}(0).$$

From Lemma 5 and Lemma 6, we have

$$\begin{aligned} \varphi_{n-1}(z) = & - \sum_{k=1}^{n-1} \left( \frac{\varphi_{k-1}(z)}{z^{n-k}} - \sum_{m=1}^{n-k} \frac{1}{z^{n-k-m+1}} \frac{\varphi_{k-1}^{(m-1)}(0)}{(m-1)!} \right) \\ & - \sum_{k=1}^{n-1} \left( \sum_{m=0}^{n-k} z^{n-k-m} \frac{\overline{\varphi_{k-1}^{(m-1)}(0)}}{m!} \right) \\ & - \sum_{k=0}^{m-1} \left( \sum_{l=0}^{m-k-1} z^{m-k-1-l} \frac{\overline{\varphi_{n+k}^{(l)}(0)}}{l!} \right) \\ & - \sum_{k=0}^{m-1} \left( \frac{\varphi_{n+k}(z)}{z^{m-k-1}} - \sum_{l=1}^{m-k-1} \frac{1}{z^{m-k-l}} \frac{\varphi_{n+k}^{(l-1)}(0)}{(l-1)!} \right) \end{aligned}$$

$$\begin{aligned} & + \sum_{k=1}^{n-1} \left( \frac{\varphi_{k-1}^{(n-k)}(0)}{(n-k)!} + \frac{\overline{\varphi_{k-1}^{(n-k)}(0)}}{(n-k)!} \right) \\ & + \sum_{k=0}^{m-1} \left( \frac{\overline{\varphi_{n+k}^{(m-k-1)}(0)}}{(m-k-1)!} + \frac{\varphi_{n+k}^{(m-k-1)}(0)}{(m-k-1)!} \right) \\ & + \frac{\varphi_{n+m-1}(0)}{2} - \frac{\overline{\varphi_{n+m-1}(0)}}{2}. \end{aligned}$$

Substituting  $\varphi_{n-1}(z)$  into  $\omega(z)$ , we get

$$\begin{aligned} \omega(z) = & \sum_{k=1}^{n-1} \left( \frac{|z|^{2(n-k)} - 1}{z^{n-k}} \right) \varphi_{k-1}(z) \\ & + \sum_{k=1}^{n-1} \sum_{m=0}^{n-k-1} \left( \frac{1}{z^{n-k-m}} \frac{\varphi_{k-1}^{(m)}(0)}{m!} - z^{n-k-m} \frac{\overline{\varphi_{k-1}^{(m)}(0)}}{m!} \right) \\ & + \sum_{k=0}^{m-1} \sum_{l=0}^{m-k-2} \left( \frac{1}{z^{m-k-l-1}} \frac{\varphi_{n+k}^{(l)}(0)}{l!} - z^{m-k-l-1} \frac{\overline{\varphi_{n+k}^{(l)}(0)}}{l!} \right) \\ & + \sum_{k=0}^{m-1} \left( z^{m-k-1} \overline{\varphi_{n+k}(z)} - \frac{1}{z^{m-k-1}} \varphi_{n+k}(z) \right) \\ & + \frac{\varphi_{n+m-1}(0)}{2} - \frac{\overline{\varphi_{n+m-1}(0)}}{2} \end{aligned}$$

for arbitrary analytic functions  $\varphi_k(z)$ ,  $0 \leq k \leq n-2$ ,  $n \leq k \leq n+m-1$ .  $\square$

**Theorem 12:** The Schwarz problem for the inhomogeneous higher order equation in  $\mathbb{D}$

$$\omega_{z^m \bar{z}^n} = f(z) \text{ in } \mathbb{D}, \quad \Re \partial_z^v \omega = \gamma_v,$$

$$\Re \partial_z^\mu (\partial_z^m \omega) = Y_\mu \text{ on } \partial \mathbb{D},$$

$$\Im \partial_z^v \omega(0) = c_v, \quad \Im \partial_z^\mu (\partial_z^m \omega)(0) = c_\mu,$$

$$0 \leq v \leq m-1, \quad 0 \leq \mu \leq n-1, \\ m, n \in \mathbb{Z}^+, \quad m+n > 2, \quad n, m \geq 1$$

is uniquely solvable for  $\gamma_v, Y_\mu \in C(\partial \mathbb{D}; \mathbb{C})$  as

$$\begin{aligned} \omega(z) = & i \sum_{v=0}^{m-1} \frac{c_v}{v!} (z + \bar{z})^v \\ & + \sum_{v=0}^{m-1} \frac{(-1)^v}{v!} \frac{1}{2\pi i} \int_{\partial \mathbb{D}} \gamma_v(\zeta) \frac{\overline{\zeta+z}}{\zeta-z} \left( \zeta-z + \overline{\zeta-z} \right)^v \frac{d\zeta}{\zeta} \\ & + i \sum_{v=0}^{n-1} \frac{(-1)^m}{(m-1)!} \frac{c_v}{v!} A(\zeta, z) \\ & + \frac{(-1)^m}{(m-1)!} \sum_{v=0}^{n-1} \frac{(-1)^v}{v!} \frac{1}{2\pi i} \int_{\partial \mathbb{D}} \gamma_v(\zeta) B(\zeta, z) \frac{d\zeta}{\zeta} \\ & + \frac{(-1)^m}{(m-1)!} \frac{(-1)^n}{(n-1)!} \frac{1}{2\pi} \iint_{\mathbb{D}} \frac{f(\zeta)}{\zeta} (C(\zeta, z) + F(\zeta, z)) d\xi d\eta \\ & + \frac{(-1)^m}{(m-1)!} \frac{(-1)^n}{(n-1)!} \frac{1}{2\pi} \iint_{\mathbb{D}} \frac{\overline{f(\zeta)}}{\bar{\zeta}} (D(\zeta, z) + E(\zeta, z)) d\xi d\eta \end{aligned}$$

where

$$A(\zeta, z) = \frac{1}{2\pi} \iint_{\mathbb{D}} (\zeta + \bar{\zeta})^v \left( \frac{1 + \overline{\zeta+z}}{\bar{\zeta}\zeta-z} - \frac{1 + \bar{z}\zeta}{\zeta 1 - \bar{z}\zeta} \right) x \left( \zeta - z + \overline{\zeta - z} \right)^{m-1} d\xi d\eta,$$

$$B(\zeta, z) = \frac{1}{2\pi} \iint_{\mathbb{D}} (\tilde{\zeta} - \zeta + \overline{\tilde{\zeta} - \zeta})^v \left( \frac{\tilde{\zeta} + \zeta 1 + \overline{\zeta+z}}{\tilde{\zeta} - \zeta \bar{\zeta} \zeta - z} + \frac{\overline{\tilde{\zeta} + \zeta 1 + \bar{z}\zeta}}{\tilde{\zeta} - \zeta \bar{\zeta} 1 - \bar{z}\zeta} \right) x \left( \zeta - z + \overline{\zeta - z} \right)^{m-1} d\xi d\eta,$$

$$C(\zeta, z) = \frac{1}{2\pi} \iint_{\mathbb{D}} \frac{\tilde{\zeta} + \zeta 1 + \overline{\zeta+z}}{\tilde{\zeta} - \zeta \bar{\zeta} \zeta - z} (\tilde{\zeta} - \zeta + \overline{\tilde{\zeta} - \zeta})^{n-1} d\xi d\eta,$$

$$x \left( \zeta - z + \overline{\zeta - z} \right)^{m-1} d\xi d\eta,$$

$$D(\zeta, z) = \frac{1}{2\pi} \iint_{\mathbb{D}} \frac{1 + \zeta \bar{\zeta}}{1 - \zeta \bar{\zeta}} (\tilde{\zeta} - \zeta + \overline{\tilde{\zeta} - \zeta})^{n-1} x \frac{1 + \overline{\zeta+z}}{\zeta \zeta - z} \left( \zeta - z + \overline{\zeta - z} \right)^{m-1} d\xi d\eta,$$

$$E(\zeta, z) = \frac{1}{2\pi} \iint_{\mathbb{D}} \frac{\overline{\tilde{\zeta} + \zeta 1}}{\tilde{\zeta} - \zeta \bar{\zeta}} \frac{1}{\zeta} (\tilde{\zeta} - \zeta + \overline{\tilde{\zeta} - \zeta})^{n-1} x \frac{1 + \bar{z}\zeta}{1 - \bar{z}\zeta} \left( \zeta - z + \overline{\zeta - z} \right)^{m-1} d\xi d\eta,$$

$$F(\zeta, z) = \frac{1}{2\pi} \iint_{\mathbb{D}} \frac{1 + \zeta \bar{\zeta}}{1 - \zeta \bar{\zeta}} (\tilde{\zeta} - \zeta + \overline{\tilde{\zeta} - \zeta})^{n-1} x \frac{1 + \bar{z}\zeta}{\zeta 1 - \bar{z}\zeta} \left( \zeta - z + \overline{\zeta - z} \right)^{m-1} d\xi d\eta.$$

**Proof.** The problem can be stated in another way as follows:

$$\partial_z^m \omega = \omega \text{ in } \mathbb{D}, \quad \Re \partial_z^v \omega = \gamma_v \text{ on } \partial \mathbb{D},$$

$$\Im \partial_z^v \omega = c_v, \quad 0 \leq v \leq m-1,$$

$$\partial_z^n \omega = f(z) \text{ in } \mathbb{D}, \quad \Re \partial_z^\mu (\partial_z^m \omega) = Y_\mu \text{ on } \partial \mathbb{D},$$

$$\Im \partial_z^\mu (\partial_z^m \omega) = c_\mu, \quad 0 \leq \mu \leq n-1.$$

Using theorems 10 and 8 respectively, the unique solutions are given as follows

$$\begin{aligned} \omega(z) = & i \sum_{v=0}^{m-1} \frac{c_v}{v!} (z + \bar{z})^v \\ & + \sum_{v=0}^{m-1} \frac{(-1)^v}{v!} \frac{1}{2\pi i} \int_{\partial \mathbb{D}} \gamma_v(\zeta) \frac{\overline{\zeta+z}}{\zeta-z} \left( \zeta-z + \overline{\zeta-z} \right)^v \frac{d\zeta}{\zeta} \\ & + \frac{(-1)^m}{(m-1)!} \frac{1}{2\pi} \iint_{\mathbb{D}} \left( \frac{\omega(\zeta) \overline{\zeta+z}}{\bar{\zeta} \zeta - z} + \frac{\overline{\omega(\zeta)} 1 + \bar{z}\zeta}{\zeta 1 - \bar{z}\zeta} \right) x \left( \zeta - z + \overline{\zeta - z} \right)^{m-1} d\xi d\eta, \end{aligned} \tag{8}$$

$$\omega(z) = i \sum_{v=0}^{n-1} \frac{c_v}{v!} (z + \bar{z})^v$$

$$\begin{aligned}
& + \sum_{v=0}^{n-1} \frac{(-1)^v}{v!} \frac{1}{2\pi i} \int_{\partial \mathbb{D}} \gamma_v(\zeta) \frac{\zeta+z}{\zeta-z} \left( \zeta-z \right. \\
& \quad \left. + \overline{\zeta-z} \right)^v \frac{d\zeta}{\zeta} \\
& + \frac{(-1)^n}{(n-1)!} \frac{1}{2\pi} \iint_{\mathbb{D}} \left( \frac{f(\zeta) \zeta+z}{\zeta \zeta-z} + \frac{\overline{f(\zeta)} \overline{1+z\bar{\zeta}}}{\bar{\zeta} \overline{1-z\bar{\zeta}}} \right) \\
& \quad x \left( \zeta-z + \overline{\zeta-z} \right)^{n-1} d\xi d\eta
\end{aligned}$$

Inserting  $\omega$  into (8), we achieve the desired outcome.  $\square$

#### 4. Conclusion

This paper explores the analysis of higher order complex partial differential equations in  $\mathbb{C}$ . The focus lies on investigating the uniqueness of the Schwarz problem. The findings reveal that there exist an infinite number of solutions for the Schwarz problem in the context of higher order complex partial differential equations in  $\mathbb{C}$  with only two boundary conditions. The ideas here can be extended to the multidimensional case.

#### Article Information Form

##### Funding

The author has no received any financial support for the research, authorship or publication of this study.

##### The Declaration of Conflict of Interest/ Common Interest

No conflict of interest or common interest has been declared by the authors.

##### The Declaration of Ethics Committee Approval

This study does not require ethics committee permission or any special permission.

##### The Declaration of Research and Publication Ethics

The author of the paper declares that she complies with the scientific, ethical and quotation rules of SAUJS in all processes of the paper and that they do not make any falsification on the data collected. In addition, they declare that Sakarya University Journal of Science and its editorial board have no responsibility for any ethical violations that may be encountered, and that this study has not been evaluated in any

academic publication environment other than Sakarya University Journal of Science.

#### Copyright Statement

Author owns the copyright of their work published in the journal and their work is published under the CC BY-NC 4.0 license.

#### References

- [1] H. Begehr, "Boundary Value Problems in Complex Analysis I, II," *Boletin de la Asosiacion*, vol. XII, no. 2, pp. 65-85, 217-250, 2005.
- [2] B. Karaca, "Dirichlet Problem for Complex Model Partial Differential Equations," *Complex Variables and Elliptic Equations*, vol. 65, no. 10, pp. 1748-1762, 2020.
- [3] H. Begehr, S. Burgumbayeva, B. Shupeyeva, "Harmonic Green Functions for a Plane Domain With Two Touching Circles As Boundary," *Advanced Mathematical Models & Applications*, vol. 3, no. 1, pp. 18-29, 2018.
- [4] Ü. Aksoy, AO. Çelebi, "Schwarz Problem for Higher Order Linear Equations in a Polydisc," *Complex Variables and Elliptic Equations*, vol. 62, no. 10, pp. 1558-1569, 2017.
- [5] M. Akel, M. Hidan, M. Abdalla, "Complex Boundary Value Problems for the Cauchy–Riemann Operator on a Triangle," *Fractals*, vol. 30, no. 10, pp. 1-15, 2022.
- [6] M. Akel, H. Begehr, A. Mohammed, "A Neumann Problem for the Polyanalytic Operator in Planar Domains with Harmonic Green Function," *Applicable Analysis*, vol. 101, no. 11, pp. 3816-3824, 2022.
- [7] H. Begehr, S. Burgumbayeva, A. Dauletkulova, H. Lin, "Harmonic Green Functions for the Almaty Apple," *Complex Variables and Elliptic Equations*, vol. 65, no. 11, pp. 1814-1825, 2020.

- [8] Ü. Aksoy, H. Begehr, AO. Çelebi, “Schwarz Problem for Higher-Order Complex Partial Differential Equations in the Upper Half Plane,” *Mathematische Nachrichten*, vol. 292, no. 6, pp. 1183-1193, 2019.



## Computer Vision-Based Lane Detection and Detection of Vehicle, Traffic Sign, Pedestrian Using YOLOv5

Gülyeter Öztürk<sup>1\*</sup>, Osman Eldoğan<sup>1</sup>, Raşit Köker<sup>2</sup>

<sup>1</sup> Sakarya University of Applied Sciences, Faculty of Technology, Mechatronics Engineering, Sakarya, Türkiye, [gulyeterozturk@subu.edu.tr](mailto:gulyeterozturk@subu.edu.tr), [eldogan@subu.edu.tr](mailto:eldogan@subu.edu.tr)

<sup>2</sup> Sakarya University of Applied Sciences, Faculty of Technology, Electrical and Electronics Engineering, Sakarya, Türkiye, [rkoker@subu.edu.tr](mailto:rkoker@subu.edu.tr)

\*Corresponding Author

### ARTICLE INFO

### ABSTRACT

#### Keywords:

YOLOv5

Object Detection

Lane Detection

Computer Vision

Deep Learning



#### Article History:

Received: 20.11.2023

Accepted: 08.01.2024

Online Available: 24.04.2024

There has been a global increase in the number of vehicles in use, resulting in a higher occurrence of traffic accidents. Advancements in computer vision and deep learning enable vehicles to independently perceive and navigate their environment, making decisions that enhance road safety and reduce traffic accidents. Worldwide accidents can be prevented in both driver-operated and autonomous vehicles by detecting living and inanimate objects such as vehicles, pedestrians, animals, and traffic signs in the environment, as well as identifying lanes and obstacles. In our proposed system, road images are captured using a camera positioned behind the front windshield of the vehicle. Computer vision techniques are employed to detect straight or curved lanes in the captured images. The right and left lanes within the driving area of the vehicle are identified, and the drivable area of the vehicle is highlighted with a different color. To detect traffic signs, pedestrians, cars, and bicycles around the vehicle, we utilize the YOLOv5 model, which is based on Convolutional Neural Networks. We use a combination of study-specific images and the GRAZ dataset in our research. In the object detection study, which involves 10 different objects, we evaluate the performance of five different versions of the YOLOv5 model. Our evaluation metrics include precision, recall, precision-recall curves, F1 score, and mean average precision. The experimental results clearly demonstrate the effectiveness of our proposed lane detection and object detection method.

## 1. Introduction

In recent years, although it varies from country to country, there has been a rapid increase in the number of vehicles worldwide, leading to a rise in accidents each year. Many people have been injured or killed in these accidents, where human mistakes play a major role [1]. According to a survey conducted by the World Health Organization in 2018, road traffic accidents affect approximately 1.25 million people each year [2]. To reduce the number of traffic accidents, it is crucial for drivers to prioritize their attention on the road, maintain focus while

driving, and adhere to traffic rules. Human distraction while driving can occur for various reasons. In such cases, Advanced Driver Assistance Systems (ADAS) and smart transportation systems can play a vital role in ensuring the safety and comfort of drivers, passengers, and pedestrians. These systems can proactively develop strategies to prevent accidents before they occur. The rapid growth of China's automotive industry, combined with advancements in deep learning technology, has led to an increasing number of vehicles equipped with assisted driving and autonomous driving functions. By the year 2020, more than 50% of

vehicles in the market were equipped with these capabilities [3]. This trend underscores the growing attention and significance of ADAS in recent years. ADAS assists vehicles by helping them maintain their designated lanes, detecting objects in their surroundings, and continuously analyzing and interpreting the environment to ensure traffic safety. These systems encompass modules for detecting traffic signs, traffic lights, and other objects on the road, as well as lane detection, lane tracking, collision avoidance, and more. Companies such as Google, Tesla, Audi, Mercedes, General Motors, and Ford are utilizing deep learning infrastructure to develop self-driving vehicles without drivers. These companies rely on these multifunctional modules for various aspects of autonomous driving.

Computer vision and deep learning technologies enable vehicles to comprehend their surroundings by detecting lanes and objects. Detecting road lanes helps keep the vehicles within drivable areas, and accidents during lane-changing processes can be prevented with the assistance of lane departure warning systems. Studies on lane detection have been conducted using various methods throughout the years, from the past to the present. Lane detection studies can generally be classified into four categories: (i) lane detection based on extracting road features through machine learning or computer vision, (ii) lane detection through the creation of road models that capture features on roads with specific templates, (iii) lane detection achieved by employing a multi-sensor fusion detection method using GPS, radar, high-resolution cameras, and other fusion techniques, and (iv) lane detection enhanced by leveraging deep learning technologies [4].

Object detection is a task that involves predicting the locations of desired living or inanimate objects in an image or video and classifying them into different categories. In object detection studies, the features of the objects you want to detect are obtained through machine learning algorithms, which are then given to a neural network for classification. In deep learning methods, objects' features are acquired using convolutional kernels of various sizes in convolutional layers, and the classification process takes place in the final layer of the same

model. Object detection models based on deep learning can be divided into two main categories: two-stage and one-stage object detection models. Region-based object detection models, such as Region-Based Convolutional Neural Network (R-CNN), Fast R-CNN, and Faster R-CNN, initially identify regions that have the potential to contain the object and then perform the classification process within these regions. Due to their two-stage detection process, this results in an increase in computation for the model and a decrease in frames per second (FPS). The You Only Look Once (YOLO), Single Shot MultiBox Detector (SSD), and Retina-Net models process the input image through CNN all at once to obtain the classes and coordinates of all objects in the image. In this paper, we present a study aimed at assisting drivers and self-driving vehicles in avoiding traffic mistakes. Our research focuses on lane detection and the identification of pedestrians, vehicles, and traffic signs on the road using five different versions of the YOLOv5 model, each trained with varying batch and input sizes. Our goal is to prevent accidents on the road and enhance overall road safety.

The remaining sections of the paper are organized as follows: Section 2 provides an overview of the literature related to lane detection and object detection. Section 3 explains the methodology used for detecting both straight and curved lanes, as well as objects on the road. Section 4 presents the experimental results of our proposed method. Finally, Section 5 concludes our study and offers suggestions for future research.

## 2. Related Work

Numerous studies have been conducted to enhance driving within a lane and ensure road safety by detecting objects on the road. These studies encompass lane detection, traffic sign detection, vehicle detection, and pedestrian detection. They hold significant importance in both computer vision and deep learning technologies. These studies have been conducted independently for traffic sign detection, pedestrian detection, vehicle detection, and lane detection. Additionally, research has been undertaken to combine multiple detection

techniques, such as detecting both vehicles and pedestrians or detecting lanes and vehicles. In this section, we present a review of the existing literature on lane detection and detection of object on the road.

Lane markings, usually yellow or white in color, can take the form of straight or curved lines. In lane detection studies, common techniques include Gaussian filtering, Kalman filtering [5], Canny edge detection [6], and the Hough transform [7]. Recent years have witnessed a growing trend in lane detection studies utilizing deep learning approaches [8]. Furthermore, various camera-based lane detection studies have been conducted by researchers [9-11].

Kumar and his colleagues employed Hough transform optimization to enhance the accuracy of detecting both straight and curved lanes on the highway. They also utilized a Kalman filter to track the detected lanes. They compared the detection performance of straight and curved lanes based on specific metrics [12]. Dubey and Bhurchandi utilized the Hough transform and Gaussian filter for lane detection in their work [13]. Huang et al. employed inverse perspective transformation and the Kalman filter for lane detection and lane line tracking [14].

Muthalagu and his team developed a lane detection algorithm for autonomous cars, creating a Convolutional Neural Network (CNN)-based model that learns to drive from the driver's driving data [1]. This model acquires its learning by capturing data from the car's onboard cameras. The developed system underwent performance evaluation for an autonomous vehicle application capable of detecting stop signs and other vehicles. Ji and Zheng utilized the improved YOLOv3 algorithm for lane line detection, achieving better results in terms of detection accuracy and FPS compared to the original YOLOv3 algorithm [4].

Traffic signs can vary from country to country, consisting of various colors such as red, blue, white, yellow, black, and green, as well as simple shapes like triangles, rectangles, circles, polygons, and more. Shustanov and Yakimov conducted an analysis on a dataset of German traffic signs using several CNN architectures,

comparing their performance in detecting and identifying traffic signs [15]. Kilic and Aydin carried out detection and recognition experiments on Turkey's 41 traffic signs using an Nvidia GTX 1080 Ti graphics card in their studies [16].

Wang et al. conducted research on object detection in the field of autonomous driving technology. In their object detection studies, they modified the structure of the YOLOv4 model to achieve high speed and accuracy in detecting both large and small objects. It was found that these modifications led to improvements in both models' performance [17]. While lane detection, pedestrian detection, traffic sign detection, and vehicle detection studies are often conducted separately, there are also studies that combine multiple detection tasks. Yang et al., using the KITTI dataset, performed pedestrian and vehicle detection with Faster R-CNN, YOLO v2, and their proposed YOLOv2-based model, providing a comparison of the accuracy and FPS of these detection models [18].

Ćorović et al. employed the YOLOv3 model for real-time detection of cars, trucks, pedestrians, traffic signs, and traffic lights. Their training, conducted up to 120 epochs, considered precision, recall, mean average precision (mAP), and average IoU (Intersection over Union) metrics [19]. Ozturk et al. conducted vehicle, pedestrian, and traffic sign detection using four different CNN models, comparing the mAP metrics of these models in detecting objects of various sizes [20]. Kemsaram and colleagues proposed a pipeline on the Nvidia Drive PX 2 platform, enabling real-time object detection, lane detection, and free space detection simultaneously [21].

### 3. Method and Experiment

In this study, with the aim of ensuring proper lane keeping, we conducted a computer vision-based detection process to identify straight or curved lanes within the vehicle's surroundings. We utilized the YOLOv5 model, renowned for its performance and speed in object detection studies, to analyze the surroundings by detecting traffic signs, pedestrians, and vehicles on the road.

### 3.1. Computer vision-based lane detection

The flow diagram of the lane detection algorithm, which displays the drivable areas in front of vehicles and helps prevent lane violations, ultimately aiming to reduce potential accidents, is depicted in Figure 1.

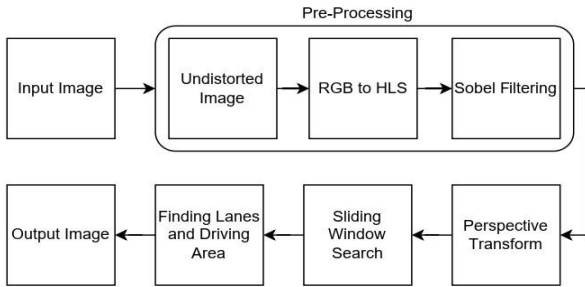


Figure 1. Flow diagram of the lane detection

Due to the camera lenses, objects in the raw image captured by the camera may appear closer or farther than they actually are. These distortions can lead to incorrect measurements in computer vision applications, affecting the size and shape of objects. To address this issue, camera calibration was performed using a chessboard pattern image.

When attempting color filtering on the raw image in the RGB color space to extract both yellow and white lanes, finding a suitable threshold value proved challenging. To reduce noise in both colors and enhance their visibility, thereby improving the detection of lane markings, we transformed the undistorted image from the RGB color space to the HLS color space. In the H (hue), L (lightness), and S (saturation) channels of the HLS color space, we determined lower and upper threshold values for both yellow and white colors.

After color filtering, the 3-channel, 24-bit color image was converted to a single-channel, 8-bit grayscale image. In the grayscale image, pixels take on values ranging from 0 to 255, representing different shades of gray from black (0) to white (255).

To detect edges in the grayscale image, we perform gradient detection to identify areas with high contrast. Figure 2 illustrates the changes in the x and y directions and shows low and high

gradients. To detect high gradients, the Sobel filter was applied.

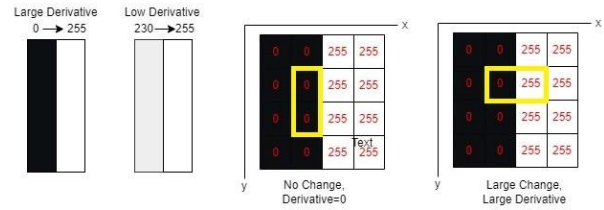


Figure 2. Gradient change in pixels

Using the Sobel filter, the gradient ( $G_x$ ) on the horizontal axis and the gradient ( $G_y$ ) on the vertical axis are obtained. Thus, for each pixel in the image, the edge gradient magnitude ( $G$ ) and its direction ( $\theta$ ) are calculated as shown in Equations 1 and 2.

$$G = \sqrt{G_x^2 + G_y^2} \tag{1}$$

$$\theta = \tan^{-1} \left( \frac{G_y}{G_x} \right) \tag{2}$$

The 3x3 filters used in Sobel edge detection for detecting edges in the horizontal and vertical directions are shown in Figure 3.

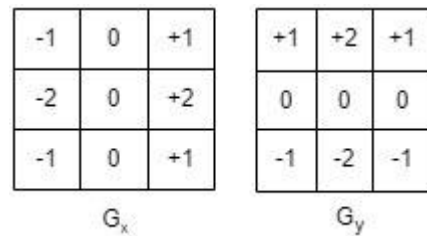
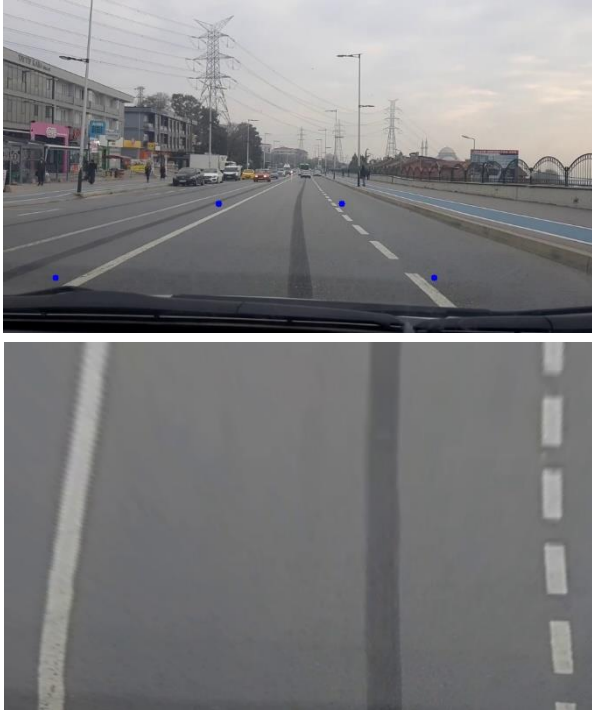


Figure 3. Filter used in detecting horizontal and vertical edges

Detecting curved lanes in the camera field of view can be challenging. To resolve this difficulty, a bird's-eye view of the road obtained with the use of perspective transformation. For this purpose, coordinates are determined to obtain a bird's eye view of the lanes as shown in Figure 4.





**Figure 4.** Obtaining bird's eye view from the image

To identify the starting points of the left and right lane markings in the bird's-eye view, we begin by calculating a histogram along the x-axis at the bottom of the image to find the two highest pixel values. We then create a window of defined width and height centered on these points. Subsequently, we employ a sliding window search method, using windows of the same size, to iteratively center on the highest pixel value from the bottom to the top of the image. The x and y coordinates of the highest value pixels detected using this method are used to generate a second-degree polynomial curve, as described in Equation 3. Figure 5 shows the sliding window search method and the polynomial curve.

$$f(y) = ay^2 + by + c = 0 \tag{3}$$

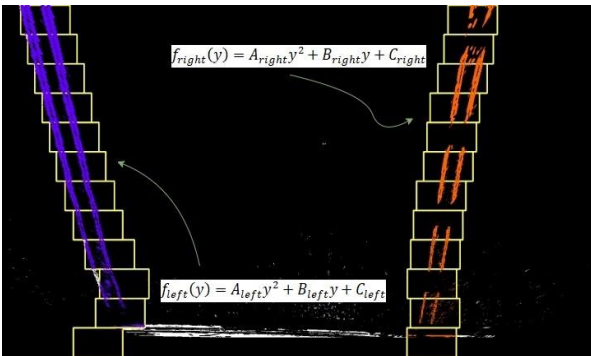


**Figure 5.** The sliding window search method and polynomial curve

### 3.2. YOLOv5 object detection model

YOLO treats object detection as a regression problem, reducing computational complexity while maintaining real-time detection with high accuracy. YOLO models with CNN structures process the input image just once to detect objects, determine bounding boxes, classifications, and confidence scores all in a single step. The first version of the YOLO family, YOLOv1, consisting of 24 convolution layers, was released by Joseph Redmon and his research team in May 2016. YOLOv1 takes raw input images sized at 448x448 pixels with three color channels.

The model divides the input image into SxS grids, and the grid containing the center point of detected objects is responsible for estimating the object's class probability, bounding box values, and confidence score. In December 2016, Redmon and Farhadi introduced YOLOv2, which employs the Darknet-19 network with 19 convolution layers for feature extraction. Subsequently, they released YOLOv3 in 2018, featuring the Darknet-53 base network with 53 convolution layers. YOLOv4 introduced in 2020 by Alexey Bochkovskiy and his team. Each new model modifies the structure of the previous versions to improve the performance of the model in object detection. Approximately two months after YOLOv4's release, Glenn Jocher introduced YOLOv5 [22]. Notably, YOLOv5 utilized PyTorch instead of Darknet, which had been used in previous YOLO versions.

YOLOv5 offers five different versions, each with varying network layer depths and processing density. These versions are denoted as YOLO v5n, YOLO v5s, YOLO v5m, YOLO v5l, and YOLO v5x. Figure 6 presents a comparison of the speed and AP values for these models. YOLOv5 versions have different depths, the computational load increases as the depth goes up. YOLO v5n stands out as the fastest version, thanks to its lower depth, although it exhibits the lowest AP value. Conversely, YOLO v5x boasts the highest depth and, as a result, performs more computationally intensive calculations.



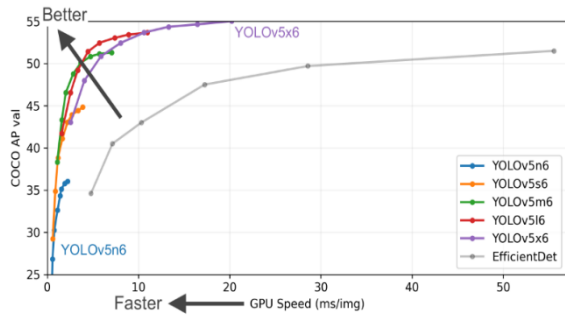


**Figure 6.** Speed and AP comparison of YOLOv5 versions [22]

The YOLOv5 architecture is divided into three sections: the backbone, the neck, and the head. The backbone primarily extracts key features from the input image. Feature pyramids obtained in the neck allow for the definition of objects at different sizes and scales. In the head part of the model, class probabilities, objectness scores, and bounding boxes of objects are obtained. As shown in Figure 7, YOLOv5 mainly consists of CBL, SPP (Spatial Pyramid Pooling), Upsample, and Concat modules used in YOLOv3 and YOLOv4 models, along with Focus and CSP (Cross Stage Partial) modules. Leaky rectified linear unit (Leaky ReLU) and Sigmoid are used as activation functions, while Stochastic Gradient Descent (SGD) or Adam is used as optimization functions.

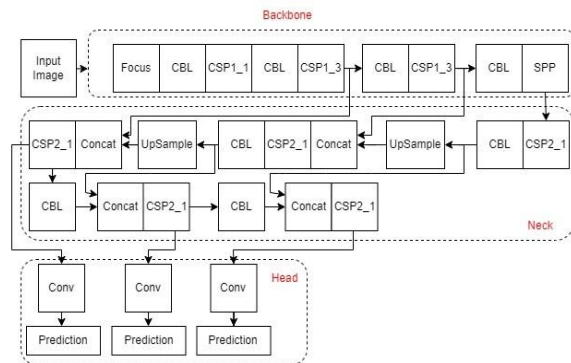


**Figure 7.** Network architecture of the YOLOv5

### 3.3. Dataset

Object detection models are significantly affected by the the dataset. It is important that the data to be given to the model is obtained from different aspects of daily life and under different conditions. Proper labeling also affects the training and validation.

The training and validation data were obtained from the GRAZ dataset and via a smartphone

camera in different lighting and weather conditions and consist of a total of 497 images. Each image in the dataset may contain multiple objects. And after labelling, the dataset is obtained in txt format and it includes pedestrian, car, bicycle objects as well as stop, pedestrian crossing, give way, roundabout, uneven road, 20-speed limit, and 30-speed limit traffic sign objects.

The bounding box width and height values, and the coordinate values of the center points of the bounding boxes that cover each image's objects, are all contained in the txt file. The dataset is split into two parts: 80% for training and 20% for validation. Daily life videos were used for the testing process. Figure 8 displays some images from the dataset and Figure 9 illustrates the number of objects it contains. In this study, car class represents bus, automobile and minibus objects; and bicycle class represents motorcycle and bicycle objects.



**Figure 8.** Images from the dataset

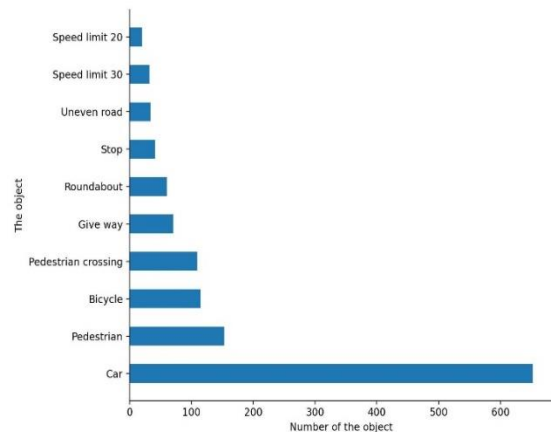


**Figure 9.** Number of the object in the dataset

#### 4. Result and Discussion

On Google Collaboratory, the YOLOv5 model was trained for 1000 epochs using a Tesla T4 GPU. Increasing the number of epochs can lead to a higher risk of overfitting. This issue can be mitigated by increasing the number of images and diversifying them. The testing phase for object and lane detection was conducted on an Intel Core i5-9400 CPU. The variations in the loss values and performance metrics for different versions of YOLOv5 during the training process are shown in Figure 10 and Figure 11, respectively.

Each color in Figure 10 and Figure 11 denote the trained model. The names of the models in Table 1 represents the YOLOv5 version that has been used, the batch size value used in that version, and the size of the input image, respectively.

**Table 1.** The trained models

Model Name	Batch Size	Image Size	Epoch	Best Epoch
YOLO v5n_32_416	32	416	1000	792
YOLO v5n_32_640	32	640	1000	882
YOLO v5s_32_416	32	416	1000	847
YOLO v5s_32_640	32	640	1000	842
YOLO v5l_16_416	16	416	1000	804
YOLO v5l_32_416	32	416	1000	812
YOLO v5l_64_416	64	416	1000	614
YOLO v5x_16_416	16	416	1000	875
YOLO v5x_32_416	32	416	1000	738

Performance metric values for the trained models are presented in Table 2. From the table, it is evident that increasing the size of input images in the YOLO v5n and YOLO v5s models while keeping the batch size constant leads to improvements in performance metrics. However, there is no clear correlation between the results obtained when the input image size is held constant and the batch size is increased in the YOLO v5l and YOLO v5x models. In the input image size of 146x416, YOLO v5l exhibited better performance with a batch size of 64, while

YOLO v5x performed better with a batch size of 16. Notably, in the YOLO v5l and YOLO v5x models, attempting to train with a larger input image size, such as 640, posed challenges due to insufficient memory resources. Consequently, training studies could not be conducted at these input image sizes or larger.

Table 2 shows that the YOLO v5x model, using a batch size of 16 and an input image size of 416, achieves the best results. The YOLO v5x model's deeper architecture and incorporation of a greater number of parameters enable it to capture more extensive and detailed features from various objects. As demonstrated in Figure 6, the unique attribute of YOLO v5x has enabled us to attain better outcomes when compared to alternative models. In this study, we will refer to this model as YOLO v5x in the subsequent process. Figure 12 depicts the variation in the loss values and performance metrics of the YOLO v5x model.

Figure 13 displays the confusion matrix obtained from the YOLO v5x model. The matrix indicates that the YOLO v5x model achieved a 100% detection rate for the stop traffic sign in the dataset. Generally, incorrect classifications were observed in relation to the background. Figure 14 presents the precision, recall, and mAP\_0.5 performance values for each class in the YOLO v5x model. Precision measures how much of the objects that the model detects as positive are actually positive. It quantifies the rate at which the model detects the object as if it were present in the image, even when the object is not actually in the image. Recall measures the proportion of objects that should have been detected in the image but were not identified by the model. High precision and recall values indicate that the detection processes are performed very effectively. The F1 score, which aims to balance the performance of the model in both precision and recall in object detection, is calculated as the harmonic mean of these two metrics. The area under the PR curve, denoted as AP, represents how well the object detection model balances precision and recall. It visualizes how the model achieves a balance between precision and recall. The mean mAP is obtained by calculating the average of the AP values computed for each individual class. Considering Figure 14, it is generally observed that the precision value is

close to 1. This situation indicates that the model's tendency to falsely detect an object as if it were present in the image, when there is actually no object, is very low. A low recall value negatively affected the F1 and mAP values. The low recall value is a result of the model's inability to detect an object in the image, even when the object is present. The lowest recall value was

obtained in the speed limit 20 object. The limited number of images associated with the speed limit 20 object may be attributed to the model's inability to acquire sufficient features for detecting this object, hence resulting in a low recall value in detection. However, overall, the model achieved good results in detecting other classes.

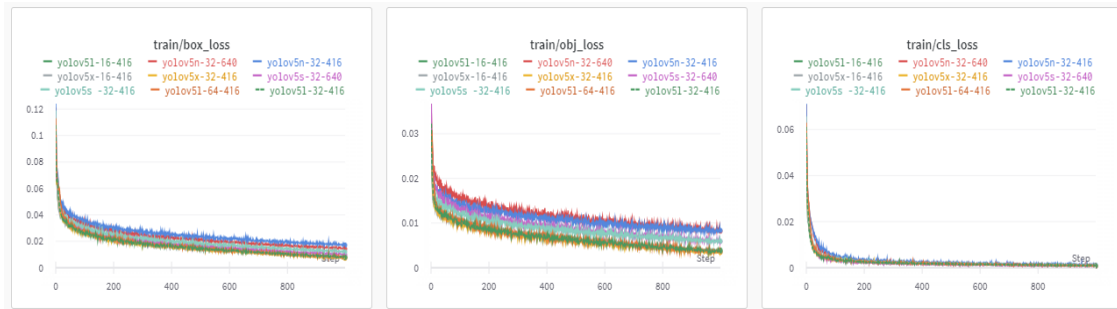


Figure 10. Graphs of losses of the models during the training processes

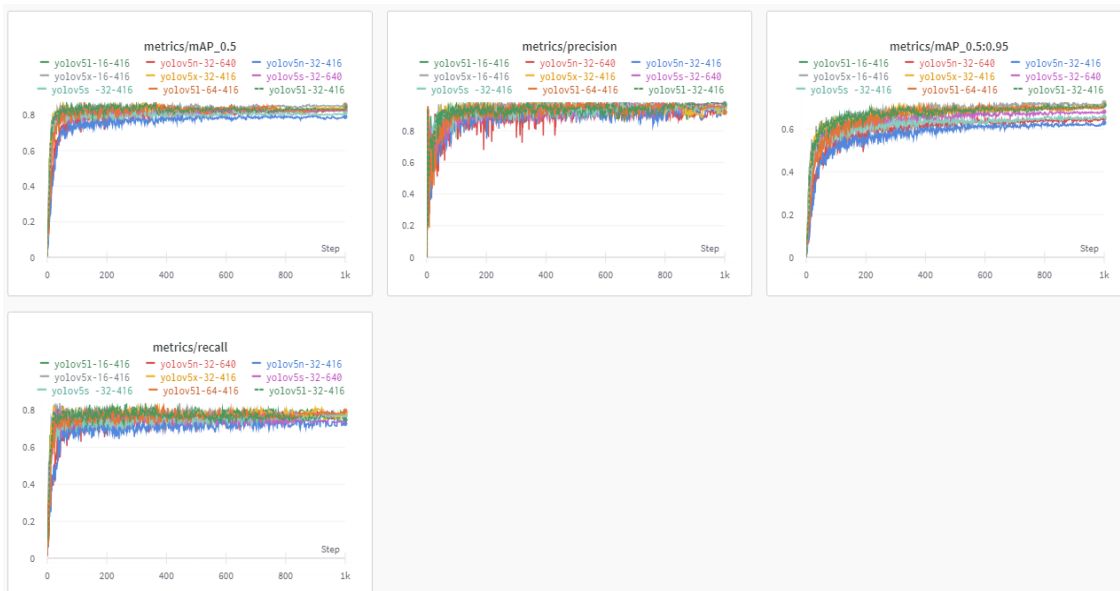


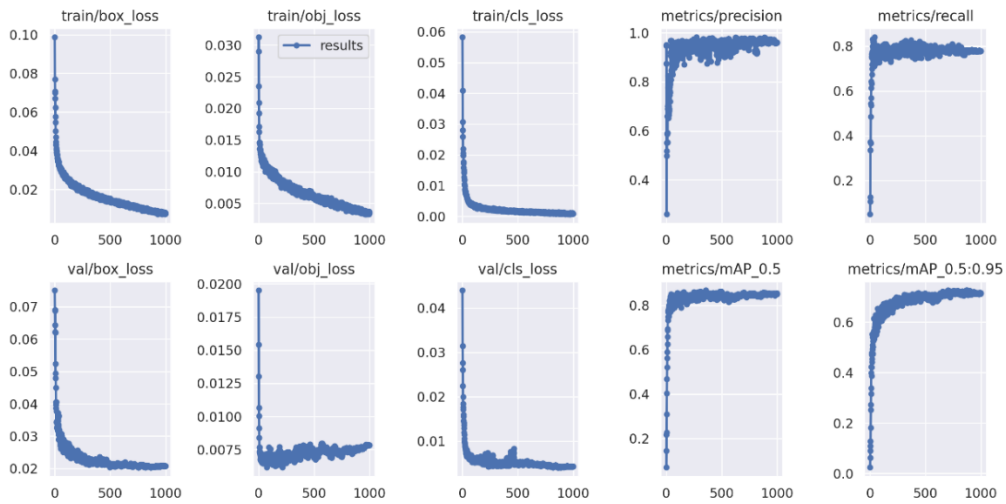
Figure 11. The variation of performance metrics of YOLOv5 versions during the training processes

Table 2. Comparison of the performance measures of the trained models

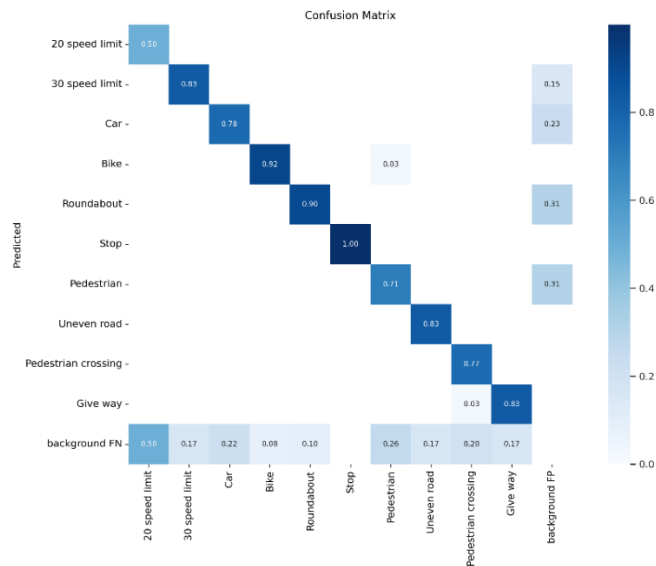
Model Name	P Curve	R Curve	PR Curve or mAP_0.5	F1 Curve	mAP_0.5:0.9
YOLO v5n_32_416	1.00	0.81	0.791	0.81	0.630
YOLO v5n_32_640	1.00	0.84	0.823	0.84	0.650
YOLO v5s_32_416	1.00	0.82	0.811	0.84	0.656
YOLO v5s_32_640	1.00	0.84	0.830	0.84	0.681
YOLO v5l_16_416	1.00	0.86	0.845	0.84	0.712
YOLO v5l_32_416	1.00	0.85	0.845	0.84	0.711
YOLO v5l_64_416	1.00	0.87	0.852	0.85	0.713
<b>YOLO v5x_16_416</b>	<b>1.00</b>	<b>0.88</b>	<b>0.869</b>	<b>0.86</b>	<b>0.726</b>
YOLO v5x_32_416	1.00	0.84	0.832	0.85	0.712

Figure 15 depicts the results of object detection tests performed on videos shot in various driving environments. Lane detection is shown in Figure 16. The image showing the object and lane detection together is given in Figure 17.

Figure 16. The image showing the object and lane detection together is given in Figure 17.



**Figure 12.** Observed changes in performance metrics during the training and the validation process



**Figure 13.** The confusion matrix obtained in the validation process

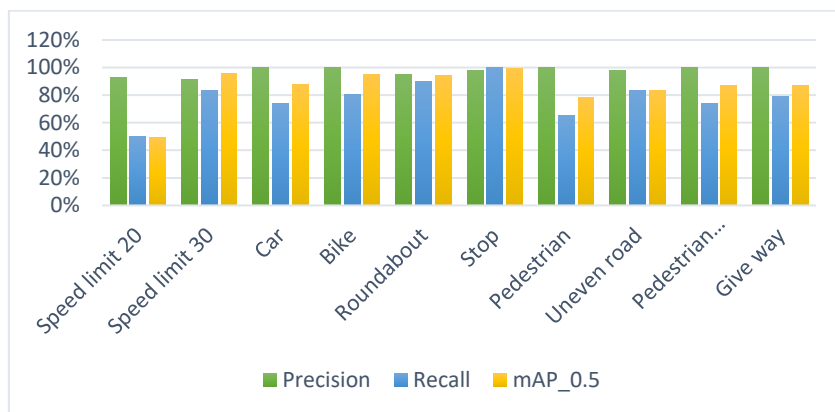


**Figure 14.** Comparison of classes based on precision, recall, and mAP





**Figure 15.** Detection of objects in various environments

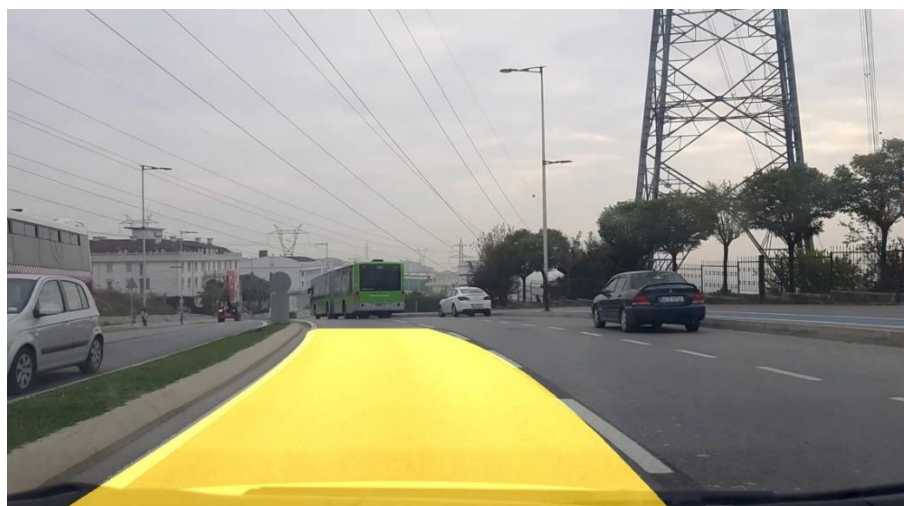


**Figure 16.** Detection of the lane





**Figure 17.** Detection of the lane and the objects

## 5. Conclusion

This research aimed to study lane and surrounding object detection for cars, with the goal of preventing accidents in advanced driver support systems and autonomous driving vehicles. The proposed lane detection approach effectively identified both straight and curved lanes. However, lane detection may occasionally fail due to various road conditions, weather changes, and traffic congestion caused by other vehicles and objects.

Future studies could explore deep learning-based lane detection methods or other approaches to improve detection accuracy and address the challenges faced in lane detection. Additionally, a control system can be established for detected lanes. Furthermore, in situations where the vehicle approaches the boundary of any lane or deviates by a certain proportion from the center of the driving area, the control system can intervene.

The success of object detection models is determined by their accuracy in detecting objects

and their detection time. In some cases, it may be necessary to use a memory-efficient model. The YOLOv5 model offers an advantage in this regard as it has a smaller file size compared to its previous versions, making it applicable in a wider range of scenarios. In this study, we trained 9 object detection models using five different versions of YOLOv5 on a Tesla T4 GPU. We compared the performance metrics of these models and identified the one that yielded the best results.

We utilized a set of 10 objects, encompassing traffic signs, pedestrians, and vehicles, commonly encountered in traffic. Thus, the study has been expanded by incorporating a greater variety of objects compared to literature studies that simultaneously perform lane and object detection. The images of these objects were obtained in rainy, sunny, and snowy weather conditions during both daytime and late afternoon hours. In future studies, the goal is to conduct detection using a broader range of objects encountered in traffic and to achieve detection in dark weather. Additionally, in future

research, the aim is to develop systems that offer superior performance in terms of detection time, accuracy, and especially in the detection of small objects.

### Article Information Form

#### *Funding*

The author (s) has no received any financial support for the research, authorship or publication of this study.

#### *Authors' Contribution*

Conceptualization, G.Ö., O.E. and R.K.; methodology, G.Ö.; software, G.Ö.; performing analysis, G.Ö.; data collection, G.Ö.; writing—original draft preparation, G.Ö.; writing—review and editing, G.Ö., O.E. and R.K. All authors have read and agreed to the published version of the manuscript.

#### *The Declaration of Conflict of Interest/ Common Interest*

No conflict of interest or common interest has been declared by the authors.

#### *The Declaration of Ethics Committee Approval*

This study does not require ethics committee permission or any special permission.

#### *The Declaration of Research and Publication Ethics*

The authors of the paper declare that they comply with the scientific, ethical and quotation rules of SAUJS in all processes of the paper and that they do not make any falsification on the data collected. In addition, they declare that Sakarya University Journal of Science and its editorial board have no responsibility for any ethical violations that may be encountered, and that this study has not been evaluated in any academic publication environment other than Sakarya University Journal of Science.

#### *Copyright Statement*

Authors own the copyright of their work published in the journal and their work is published under the CC BY-NC 4.0 license.

### References

- [1] R. Muthalagu, A. S. Bolimera, D. Duseja, S. Fernandes, "Object and Lane Detection Technique for Autonomous Car Using Machine Learning Approach," *Transport and Telecommunication*, vol. 22, no. 4, pp. 383–391, 2021.
- [2] V. Nguyen, H. Kim, S. Jun, K. Boo, "A Study on Real-Time Detection Method of Lane and Vehicle for Lane Change Assistant System Using Vision System on Highway," *Engineering Science and Technology, an International Journal*, vol. 21, no. 5, pp. 822–833, 2018.
- [3] H. G. Zhu, "An Efficient Lane Line Detection Method Based on Computer Vision," *Journal of Physics: Conference Series*, vol. 1802, no. 3, 2021, p. 032006.
- [4] G. Ji, Y. Zheng, "Lane Line Detection System Based on Improved Yolo V3 Algorithm," *In Review*, preprint, 2021.
- [5] B. Dorj, S. Hossain, D.-J. Lee, "Highly Curved Lane Detection Algorithms Based on Kalman Filter," *Applied Sciences*, vol. 10, no. 7:2372, 2020.
- [6] X. Yan, Y. Li, "A method of lane edge detection based on Canny algorithm," in *Chinese Automation Congress (CAC)*, Jinan, China, 2017, pp. 2120–2124.
- [7] M. L. Talib, X. Rui, K. H. Ghazali, N. Mohd. Zainudin, S. Ramli, "Comparison of Edge Detection Technique for Lane Analysis by Improved Hough Transform," in *Advances in Visual Informatics*, H. B. Zaman, P. Robinson, P. Olivier, T. K. Shih, and S. Velastin, Eds., in *Lecture Notes in Computer Science*. Cham: Springer International Publishing, 2013, pp. 176–183.
- [8] Q. Zou, H. Jiang, Q. Dai, Y. Yue, L. Chen, Q. Wang, "Robust Lane Detection from Continuous Driving Scenes Using Deep Neural Networks," *IEEE Transactions on*

- Vehicular Technology, vol. 69, no. 1, pp. 41–54, 2020.
- [9] T. M. Hoang, H. G. Hong, H. Vokhidov, K. R. Park, “Road Lane Detection by Discriminating Dashed and Solid Road Lanes Using a Visible Light Camera Sensor,” *Sensors*, vol. 16, no. 8, 2016.
- [10] Y. Li, W. Zhang, X. Ji, C. Ren, J. Wu, “Research on Lane a Compensation Method Based on Multi-Sensor Fusion,” *Sensors*, vol. 19, no. 7, 2019.
- [11] J. Wang, H. Ma, X. Zhang, X. Liu, “Detection of Lane Lines on Both Sides of Road Based on Monocular Camera,” in *2018 IEEE International Conference on Mechatronics and Automation (ICMA)*, 2018, pp. 1134–1139.
- [12] S. Kumar, M. Jailia, S. Varshney, “An efficient approach for highway lane detection based on the Hough transform and Kalman filter,” *Innovative Infrastructure Solutions*, vol. 7, no. 5, p. 290, 2022.
- [13] A. Dubey, K. M. Bhurchandi, “Robust and Real Time Detection of Curvy Lanes (Curves) with Desired Slopes for Driving Assistance and Autonomous Vehicles,” in *International Conference on Signal and Image Processing (AIRCC)*, 2015.
- [14] Y. Huang, Y. Li, X. Hu, W. Ci, “Lane Detection Based on Inverse Perspective Transformation and Kalman Filter,” *KSII Transactions on Internet and Information Systems, TIIS*, vol. 12, no. 2, pp. 643–661, 2018.
- [15] A. Shustanov, P. Yakimov, “CNN Design for Real-Time Traffic Sign Recognition,” *Procedia Engineering.*, vol. 201, pp. 718–725, 2017.
- [16] I. Kilic, G. Aydin, “Traffic Sign Detection and Recognition Using TensorFlow’ s Object Detection API With A New Benchmark Dataset,” in *2020 International Conference on Electrical Engineering (ICEE)*, Istanbul, Turkey, 2020, pp. 1–5.
- [17] R. Wang, Z. Wang, Z. Xu, C. Wang, Q. Li, Y. Zhang, H. Li, “A Real-Time Object Detector for Autonomous Vehicles Based on YOLOv4,” *Computational Intelligence and Neuroscience*, vol. 2021, p. e9218137, 2021.
- [18] Z. Yang, J. Li, H. Li, “Real-time Pedestrian and Vehicle Detection for Autonomous Driving,” in *2018 IEEE Intelligent Vehicles Symposium (IV)*, Suzhou, China, 2018, pp. 179–184.
- [19] A. Ćorović, V. Ilić, S. Đurić, M. Marijan, B. Pavković, “The Real-Time Detection of Traffic Participants Using YOLO Algorithm,” in *2018 26th Telecommunications Forum (TELFOR)*, Belgrade, Serbia, 2018, pp. 1–4.
- [20] G. Ozturk, R. Koker, O. Eldogan, D. Karayel, “Recognition of Vehicles, Pedestrians and Traffic Signs Using Convolutional Neural Networks,” in *2020 4th International Symposium on Multidisciplinary Studies and Innovative Technologies (ISMSIT)*, Istanbul, Turkey, 2020, pp. 1–8.
- [21] N. Kemsaram, A. Das, G. Dubbelman, “An Integrated Framework for Autonomous Driving: Object Detection, Lane Detection, and Free Space Detection,” in *2019 Third World Conference on Smart Trends in Systems Security and Sustainability (WorldS4)*, London, UK, 2019, pp. 260–265.
- [22] G. Jocher, K. Nishimura, T. Mineeva, R. Vilariño. YOLOv5 Code Repository. June, 2020. [Online]. Available: <https://github.com/ultralytics/yolov5>

## A Note on the Laplacian Energy of the Power Graph of a Finite Cyclic Group

Nurşah Mutlu Varlıoğlu<sup>1\*</sup> , Şerife Büyükköse<sup>2</sup> 

<sup>1</sup> Istanbul Kültür University, Faculty of Science and Letters, Department of Mathematics and Computer Science, Istanbul, Türkiye, [n.varlioglu@iku.edu.tr](mailto:n.varlioglu@iku.edu.tr)

<sup>2</sup> Gazi University, Faculty of Science, Department of Mathematics, Ankara, Türkiye, [sbuyukkose@gazi.edu.tr](mailto:sbuyukkose@gazi.edu.tr)

\*Corresponding Author

### ARTICLE INFO

### ABSTRACT

#### Keywords:

Cyclic Group  
Laplacian Matrix  
Laplacian Energy  
Bound

#### Article History:

Received: 02.10.2023

Accepted: 31.01.2024

Online Available: 24.04.2024

In this study, the Laplacian matrix concept for the power graph of a finite cyclic group is redefined by considering the block matrix structure. Then, with the help of the eigenvalues of the Laplacian matrix in question, the concept of Laplacian energy for the power graphs of finite cyclic groups was defined and introduced into the literature. In addition, boundary studies were carried out for the Laplacian energy in question using the concepts the trace of a matrix, the Cauchy-Schwarz inequality, the relationship between the arithmetic mean and geometric mean, and determinant. Later, various results were obtained for the Laplacian energy in question for cases where the order of a cyclic group is the positive integer power of a prime.

## 1. Introduction

The power graph  $P(G)$  of a finite group  $G$ , is the graph whose vertices are represented by the elements of  $G$ , and with adjacency relation between different two vertices  $v_x$  and  $v_y$  is defined as

$$v_x \sim v_y \Leftrightarrow v_x = v_y^m \text{ and } v_y = v_x^m, m \in \mathbb{Z}^+.$$

Kelarev and Quinn introduced the concept of power graph to the mathematical literature in 2000 with their work on directed power graphs of finite semigroups [1]. Later, the concept of directed power graph for groups was defined, and various studies were carried out for directed power graphs on semigroups and groups [2-3]. Chakrabarty et al., inspired by these studies, introduced the concept of undirected power graph to the mathematical literature with their study in 2009 [4]. In addition, this study also revealed the relationship between the power graph being a complete graph and the structure and order of the group. Later, Cameron et al.

abbreviated the concept of undirected power graph and named it as power graph [5-6] and this name passed into the mathematics literature and after that, studies for undirected power graphs were published under the name of power graph.

Another name that directs the study of power graph on the basis of spectral graph theory is Chattopadhyay. The study of Chattopadhyay et al. in 2018, the adjacency matrix concept was redefined on a power graph. Additionally, in this study, they obtained bounds for the largest eigenvalues of power graphs [7].

The energy of a graph was originated from the  $\pi$ -electron energy in the Hückel molecular orbital theory and motivated by this study, Gutman in 1978 defined the energy of a graph [8]. At the first time, the concept of graph energy did not receive much attention. However, in the past decade, the concept of graph energy has become popular with its widespread use in both theoretical and application areas and many different versions have been conceived. One of



the most important of these versions is the Laplacian energy. The concept of Laplacian energy for graphs was defined as the sum of the absolute deviations of the eigenvalues of its Laplacian matrix by Gutman and Zhou in 2006 [9]. It is very important to do boundary studies in graph theory because it is not always easy to find the spectral structures of graphs with a large number of points. In this sense, boundary studies for the Laplacian energy of a graph has received much interest and has appeared frequently in many papers.

In this study, for the power graph on a finite cyclic group, the concept of Laplacian matrix is redefined by considering the block matrix structure, and then the concept of Laplacian energy is given with the help of Laplacian eigenvalues. Briefly mention the structures that we will use throughout the study.

Let  $C_n$  be a cyclic group with  $n$  elements,  $V_1$  be the set of its the identity and generators and  $V_2$  the set of its remaining elements. Thus  $|V_1| = 1 + \varphi(n) = t$  (say), where  $\varphi(n)$  is Euler's  $\varphi$  function. In this case, the Laplacian matrix can be redefined as the block matrix structure below, considering the  $V_1$  and  $V_2$  structures.

$$L = \begin{pmatrix} (nI - J)_{t \times t} & -J_{t \times (n-t)} \\ -J_{(n-t) \times t} & L(P(V_2))_{(n-t) \times (n-t)} \end{pmatrix}$$

where  $J$  is the matrix with all entries being 1 and  $I$  is the identity matrix. Also let  $L(P(V_2)) = (l_{ij})$  is the Laplacian matrix formed by the elements of  $V_2$ , i.e.,

$$l_{ij} = \begin{cases} -1 & ; & i \sim j \\ d(i) & ; & i = j \\ 0 & ; & \text{otherwise} \end{cases},$$

where  $d(i)$ , is the degree of a vertex  $i$ . The Laplacian matrix of the power graph is a symmetric and real matrix. Therefore, all eigenvalues are real and are given in the following order.

$$\mu_n \geq \mu_{n-1} \geq \dots \geq \mu_2 \geq \mu_1 = 0.$$

In the next section, in order to bring a different perspective to boundary studies, the Laplacian

energy is defined by using the fact that the Laplacian matrix for a power graph is a block matrix and the structures of the Laplacian eigenvalues, and then the bounds on this concept are obtained.

## 2. Main Results

Let  $L$  be the Laplacian matrix of  $P(C_n)$  and its eigenvalues are  $\mu_n \geq \mu_{n-1} \geq \dots \geq \mu_2 \geq \mu_1 = 0$ . Using the concept of the Laplacian energy of a simple graph and the Laplacian matrix of a power graph being a block matrix, the Laplacian energy  $LE$  of the power graph  $P(C_n)$  is defined as

$$LE = \sum_{i=1}^n |\gamma_i|,$$

where

$$\gamma_i = \mu_i - \frac{s}{n},$$

$$s = t(2n - t - 1) - 2 \sum_{t+1 \leq i < j \leq n} l_{ij}.$$

**Lemma 1.** Let  $LE$  be the Laplacian energy of the power graph  $P(C_n)$  and  $n \geq 3$ . Then

$$\begin{aligned} \sum_{i=1}^n \mu_i &= t(2n - t - 1) - 2 \sum_{t+1 \leq i < j \leq n} l_{ij} \\ &= s, \end{aligned}$$

$$\sum_{i=1}^n \mu_i^2 = s + t(n - 1)^2 + \sum_{i=t+1}^n d^2(i),$$

where  $d(i)$ , is the degree of a vertex  $i$ .

**Proof.** Since the trace of a matrix is the sum of its eigenvalues, we have

$$\begin{aligned} \sum_{i=1}^n \mu_i &= \text{tr}(L) \\ &= t(n - 1) + \sum_{i=t+1}^n d(i) \\ &= t(n - 1) + \sum_{i=t+1}^n (-\sum_{j=1, i \neq j}^n l_{ij}) \\ &= t(n - 1) - \sum_{i=t+1}^n (-t + \sum_{j=t+1, i \neq j}^n l_{ij}) \\ &= t(2n - t - 1) - 2 \sum_{t+1 \leq i < j \leq n} l_{ij}. \end{aligned}$$

We now consider the matrix  $L^2$ .

$$\sum_{i=1}^n \mu_i^2 = \text{tr}(L^2)$$



$$= t((n - 1)^2 + t - 1) + 2t(n - t) + tr \left[ L(P(V_2))^2 \right].$$

The  $ii$ -th entry of  $L^2(P(V_2))$  is

$$\sum_{i=t+1}^n d^2(i) - 2 \sum_{t+1 \leq i < j \leq n} l_{ij}.$$

Thus

$$\begin{aligned} \sum_{i=1}^n \mu_i^2 &= t(2n - t - 1) - 2 \sum_{t+1 \leq i < j \leq n} l_{ij} + t(n - 1)^2 + \sum_{i=t+1}^n d^2(i) \\ &= s + t(n - 1)^2 + \sum_{i=t+1}^n d^2(i) \end{aligned}$$

This completes the proof.

**Lemma 2.** Let  $LE$  be the Laplacian energy of the power graph  $P(C_n)$  and  $n \geq 3$ . Then

$$\sum_{i=1}^n \gamma_i = 0$$

and

$$\sum_{i=1}^n \gamma_i^2 = s + \sum_{i=1}^n \left( d(i) - \frac{s}{n} \right)^2.$$

**Proof.** Using the definition of  $\gamma_i$  and Lemma 1, we have

$$\sum_{i=1}^n \gamma_i = -s + \sum_{i=1}^n \mu_i = 0.$$

For the proof of the second equality, we have

$$\begin{aligned} \sum_{i=1}^n \gamma_i^2 &= \sum_{i=1}^n \mu_i^2 - 2 \frac{t(2n-t-1)-2 \sum_{t+1 \leq i < j \leq n} l_{ij}}{n} \sum_{i=1}^n \mu_i \\ &\quad + \frac{(t(2n-t-1)-2 \sum_{t+1 \leq i < j \leq n} l_{ij})^2}{n}. \end{aligned}$$

From Lemma 1, we have

$$\begin{aligned} &= t(2n - t - 1) - 2 \sum_{t+1 \leq i < j \leq n} l_{ij} \\ &\quad + t(n - 1)^2 + \sum_{i=t+1}^n d^2(i) \\ &\quad - \frac{(t(2n-t-1)-2 \sum_{t+1 \leq i < j \leq n} l_{ij})^2}{n} \end{aligned}$$

$$\begin{aligned} &= \sum_{i=t+1}^n d^2(i) + n^2t - nt \\ &\quad + \sum_{i=t+1}^n d^2(i) - \frac{(t(2n-t-1)-2 \sum_{t+1 \leq i < j \leq n} l_{ij})^2}{n} \\ &= t(2n - t - 1) - 2 \sum_{t+1 \leq i < j \leq n} l_{ij} \\ &\quad + \sum_{i=1}^n \left( d(i) - \frac{t(2n-t-1)-2 \sum_{t+1 \leq i < j \leq n} l_{ij}}{n} \right)^2 \\ &= s + \sum_{i=1}^n \left( d(i) - \frac{s}{n} \right)^2 \end{aligned}$$

so the proof is complete.

**Lemma 3.** Let  $LE$  be the Laplacian energy of the power graph  $P(C_n)$  and  $n = q^k \geq 3$ . Then

$$\sum_{i=1}^n \gamma_i^2 = n(n - 1),$$

where  $q$  is a prime number and  $k \in \mathbb{Z}^+$ .

**Proof.** Since  $n$  is the positive integer power of a prime number then  $P(C_n)$  is a complete graph. Using Lemma 1, we have

$$\sum_{i=1}^n \mu_i = tr(L) = n(n - 1), \tag{1}$$

$$\sum_{i=1}^n \mu_i^2 = tr(L^2) = n^2(n - 1) \tag{2}$$

and

$$\begin{aligned} \gamma_i &= \mu_i - \frac{t(2n-t-1)-2 \sum_{t+1 \leq i < j \leq n} l_{ij}}{n}, \\ &= \mu_i - \frac{n(2n-n-1)}{n} \\ &= \mu_i - (n - 1). \end{aligned} \tag{3}$$

From (1), (2), (3), we have

$$\begin{aligned} \sum_{i=1}^n \gamma_i^2 &= \sum_{i=1}^n (\mu_i - (n - 1))^2 \\ &= \sum_{i=1}^n \mu_i^2 + n(n - 1)^2 \\ &\quad - 2(n - 1) \sum_{i=1}^n \mu_i(P(C_n)) \\ &= n(n - 1). \end{aligned}$$

This completes the proof.

**Theorem 4.** Let  $LE$  be the Laplacian energy of the power graph  $P(C_n)$  and  $n \geq 3$ . Then

$$\sqrt{ns + n \sum_{i=1}^n \left(d(i) - \frac{s}{n}\right)^2} \geq LE$$

and

$$LE \geq \sqrt{s + \sum_{i=1}^n \left(d(i) - \frac{s}{n}\right)^2}.$$

**Proof.** Using the Cauchy-Schwarz inequality and Lemma 2, we have

$$\begin{aligned} LE^2 &= \left(\sum_{i=1}^n |\gamma_i|\right)^2 \\ &\leq n \sum_{i=1}^n \gamma_i^2 \\ &= ns + n \sum_{i=1}^n \left(d(i) - \frac{s}{n}\right)^2 \end{aligned}$$

and thus

$$LE \leq \sqrt{ns + n \sum_{i=1}^n \left(d(i) - \frac{s}{n}\right)^2}.$$

For the second inequality of the theorem, we obtain

$$\begin{aligned} LE^2 &= \left(\sum_{i=1}^n |\gamma_i|\right)^2 \\ &\geq s + \sum_{i=1}^n \left(d(i) - \frac{s}{n}\right)^2. \end{aligned}$$

Therefore,

$$LE \geq \sqrt{s + \sum_{i=1}^n \left(d(i) - \frac{s}{n}\right)^2}.$$

**Corollary 5.** Let  $LE$  be the Laplacian energy of the power graph  $P(C_n)$  and  $n = q^k \geq 3$ . Then

$$\sqrt{n^2 - n} \leq LE \leq \sqrt{n^3 - n^2},$$

where  $q$  is a prime number and  $k \in \mathbb{Z}^+$ .

**Proof.** Since  $n$  is the positive integer power of a prime number then  $P(C_n)$  is a complete graph. Using definition of Laplacian energy and Lemma 3, we have

$$LE^2 \geq \sum_{i=1}^n \gamma_i^2 = n(n - 1)$$

and then

$$LE \geq \sqrt{n^2 - n}.$$

For the proof of the second inequality, we have

$$LE^2 \leq n \sum_{i=1}^n \gamma_i^2 = n^2(n - 1),$$

i.e.,

$$LE \leq \sqrt{n^3 - n^2}.$$

so the proof is completed.

**Theorem 6.** Let  $LE$  be the Laplacian energy of the power graph  $P(C_n)$  and  $n \geq 3$ . Then

$$\begin{aligned} LE &\leq \frac{s}{n} \\ &+ \sqrt{(n - 1) \left[ s + \sum_{i=1}^n \left(d(i) - \frac{s}{n}\right)^2 - \frac{s^2}{n^2} \right]}. \end{aligned}$$

**Proof.** Since the definition of the Laplacian energy, Cauchy-Schwarz inequality and Lemma 2, we have

$$\begin{aligned} \left(LE - \frac{s}{n}\right)^2 &= \left(\sum_{i=2}^n |\gamma_i|\right)^2 \\ &\leq (n - 1) \left[ \sum_{i=1}^n \gamma_i^2 - \frac{s^2}{n^2} \right] \\ &= (n - 1) \left[ s + \sum_{i=1}^n \left(d(i) - \frac{s}{n}\right)^2 - \frac{s^2}{n^2} \right], \end{aligned}$$

and thus

$$\begin{aligned} LE &\leq \frac{s}{n} \\ &+ \sqrt{(n - 1) \left[ s + \sum_{i=1}^n \left(d(i) - \frac{s}{n}\right)^2 - \frac{s^2}{n^2} \right]}. \end{aligned}$$

The proof is complete.

**Corollary 7.** Let  $LE$  be the Laplacian energy of the power graph  $P(C_n)$  and  $n = q^k \geq 3$ . Then

$$LE = 2(n - 1),$$

where  $q$  is a prime number and  $k \in \mathbb{Z}^+$ .

**Proof.** Since  $n$  is the positive integer power of a prime number then  $P(C_n)$  is a complete graph. Thus

$$\begin{aligned} s &= t(2n - t - 1) - 2 \sum_{t+1 \leq i < j \leq n} l_{ij} \\ &= n(2n - n - 1) \\ &= n(n - 1). \end{aligned}$$

From Lemma 3, the definition of the Laplacian energy, Cauchy-Schwarz inequality and the spectrum of a complete graph, we obtain

$$\begin{aligned} \left(LE - \frac{s}{n}\right)^2 &= (n - 1) \left[ \sum_{i=1}^n \gamma_i^2 - \frac{s^2}{n^2} \right] \\ &= (LE - (n - 1))^2 = (n - 1)^2 \end{aligned}$$

and then

$$LE = 2(n - 1)$$

so the proof is completed.

**Theorem 8.** Let  $LE$  be the Laplacian energy of the power graph  $P(C_n)$  and  $n \geq 3$ . Then

$$LE \geq \sqrt{s + \sum_{i=1}^n \left(d(i) - \frac{s}{n}\right)^2 + n(n - 1) \det \left(L - \frac{s}{n}I\right)^{\frac{2}{n}}}.$$

**Proof.** By Lemma 2, we have

$$\begin{aligned} LE^2 &= \sum_{i=1}^n \gamma_i^2 + 2 \sum_{1 \leq i, j \leq n} |\gamma_i| |\gamma_j| \\ &= s + \sum_{i=1}^n \left(d(i) - \frac{s}{n}\right)^2 + \sum_{i \neq j} |\gamma_i| |\gamma_j|. \end{aligned} \quad (4)$$

Because the arithmetic mean of nonnegative numbers is greater than the geometric mean. So we have

$$\begin{aligned} \frac{1}{n(n-1)} \sum_{i \neq j} |\gamma_i| |\gamma_j| &\geq \left( \prod_{i \neq j} |\gamma_i| |\gamma_j| \right)^{\frac{1}{n(n-1)}} \\ &= \left( \prod_{i=1}^n |\gamma_i|^{2(n-1)} \right)^{\frac{1}{n(n-1)}} \end{aligned}$$

$$= \det \left( L - \frac{s}{n}I \right)^{\frac{2}{n}}, \quad (5)$$

where  $I$  is the identity matrix. By (4) and (5), we obtain

$$LE \geq \sqrt{s + \sum_{i=1}^n \left(d(i) - \frac{s}{n}\right)^2 + n(n - 1) \det \left( L - \frac{s}{n}I \right)^{\frac{2}{n}}}.$$

Hence the proof is completed.

**Corollary 9.** Let  $LE$  be the Laplacian energy of the power graph  $P(C_n)$  and  $n = q^k \geq 3$ . Then

$$LE \geq \sqrt{n(n - 1) \left[ 1 + (n - 1)^{\frac{2}{n}} \right]},$$

where  $q$  is a prime number and  $k \in \mathbb{Z}^+$ .

**Proof.** Since  $n$  is the positive integer power of a prime number then  $P(C_n)$  is a complete graph. Using Theorem 8 and Lemma 3, we have

$$\begin{aligned} LE^2 &\geq \sum_{i=1}^n \gamma_i^2 + n(n - 1) \det \left( L - \frac{s}{n}I \right)^{\frac{2}{n}} \\ &= n(n - 1) + n(n - 1) \det \left( L - \frac{s}{n}I \right)^{\frac{2}{n}} \\ &= n(n - 1) \left[ 1 + \det \left( L - \frac{s}{n}I \right)^{\frac{2}{n}} \right]. \end{aligned}$$

Since  $\mathcal{P}(C_n)$  is a complete graph,

$$s = n(n - 1)$$

and then

$$\begin{aligned} \det \left( L - \frac{s}{n}I \right) &= \det(L - (n - 1)I) \\ &= \det \left( -A(\mathcal{P}(C_n)) \right) \\ &= (-1)^n \det \left( A(\mathcal{P}(C_n)) \right) = 1 - n. \end{aligned}$$

Thus,

$$LE^2 \geq n(n-1) \left[ 1 + (1-n)^{\frac{2}{n}} \right]$$

and then

$$LE \geq \sqrt{n(n-1) \left[ 1 + (1-n)^{\frac{2}{n}} \right]}.$$

The proof is complete.

**Theorem 10.** Let  $LE$  be the Laplacian energy of the power graph  $P(C_n)$ ,  $n \geq 3$  and  $|\gamma_1| \geq |\gamma_2| \geq \dots \geq |\gamma_n| \geq 0$ . Then

$$LE \geq \frac{s + \sum_{i=1}^n \left( d(i) - \frac{s}{n} \right)^2 + n|\gamma_1||\gamma_n|}{|\gamma_1| + |\gamma_n|}.$$

**Proof.** We note that, since  $C_n$  is a cyclic group with  $n \geq 3$ ,  $\mathcal{P}(C_n)$  has at least two edges. Thus,  $L$  has at least one non-zero eigenvalue. Now for every  $i = 1, 2, \dots, n$ ,  $|\gamma_1| \geq |\gamma_i| \geq |\gamma_n|$ . Thus

$$(|\gamma_1| - |\gamma_i|)(|\gamma_i| - |\gamma_n|) \geq 0. \tag{6}$$

On the other hand

$$\begin{aligned} (|\gamma_1| - |\gamma_i|)(|\gamma_i| - |\gamma_n|) &= |\gamma_i|(|\gamma_1| + |\gamma_n|) \\ &- (\gamma_i^2 + |\gamma_1||\gamma_n|). \end{aligned} \tag{7}$$

From (6) and (7), we obtain

$$|\gamma_i|(|\gamma_1| + |\gamma_n|) \geq \gamma_i^2 + |\gamma_1||\gamma_n|. \tag{8}$$

By summing the sides of the (8) for every  $1 \leq i \leq n$ , we have

$$\begin{aligned} (|\gamma_1| + \dots + |\gamma_n|)(|\gamma_1| + |\gamma_n|) &\geq \\ (\gamma_1^2 + \dots + \gamma_n^2) + n|\gamma_1||\gamma_n| \end{aligned}$$

and thus

$$LE \geq \frac{\sum_{i=1}^n \gamma_i^2 + n|\gamma_1||\gamma_n|}{|\gamma_1| + |\gamma_n|}.$$

From Lemma 2, we obtain

$$LE \geq \frac{s + \sum_{i=1}^n \left( d(i) - \frac{s}{n} \right)^2 + n|\gamma_1||\gamma_n|}{|\gamma_1| + |\gamma_n|}.$$

Hence the proof is completed.

**Corollary 11.** Let  $LE$  be the Laplacian energy of the power graph  $P(C_n)$  and  $n = q^k \geq 3$ . Assume that  $|\gamma_1| \geq |\gamma_i| \geq |\gamma_n|$ . Then

$$LE = 2(n-1),$$

where  $q$  is a prime number and  $k \in \mathbb{Z}^+$ .

**Proof.** Since  $n$  is the positive integer power of a prime number then  $P(C_n)$  is a complete graph and its Laplacian spectrum is  $\left\{ 0, \underbrace{n, n, \dots, n}_{n-1} \right\}$ .

Also

$$s = n(n-1)$$

and for every  $i = 2, 3, \dots, n$ ,  $\gamma_i = \mu_i - \frac{s}{n}$ , we obtain

$$\gamma_1 = n-1, \gamma_2 = \dots = \gamma_n = 1.$$

Thus, using by Teorem 10 and Lemma 3, we have

$$\begin{aligned} LE &= \frac{\sum_{i=1}^n \gamma_i^2 + n|\gamma_1||\gamma_n|}{|\gamma_1| + |\gamma_n|} \\ &= \frac{n(n-1) + n(n-1)}{n-1+1} \\ &= 2(n-1). \end{aligned}$$

The proof is complete.

### 3. Conclusion

In this study, Laplacian matrix concept is defined for power graphs of finite cyclic groups, inspired by the concepts of Laplacian matrix defined on simple connected graphs and adjacency matrix defined on power graphs. Then, using Laplacian eigenvalues, the concept of Laplacian energy for the power graph of a cyclic group is given and boundary studies are done on it. Although some bounds give results very close to the Laplacian energy, it is not always possible to make comparison between the bounds as the boundary results will change as the graph structure changes.

## Article Information Form

### Acknowledgments

The authors wish to thank the referee for a careful reading and valuable comments and suggestions for the original draft.

### Funding

The author (s) has no received any financial support for the research, authorship or publication of this study.

### Authors' Contribution

The authors contributed equally to the study.

### The Declaration of Conflict of Interest/ Common Interest

No conflict of interest or common interest has been declared by the authors.

### The Declaration of Ethics Committee Approval

This study does not require ethics committee permission or any special permission.

### The Declaration of Research and Publication Ethics

The authors of the paper declare that they comply with the scientific, ethical and quotation rules of SAUJS in all processes of the paper and that they do not make any falsification on the data collected. In addition, they declare that Sakarya University Journal of Science and its editorial board have no responsibility for any ethical violations that may be encountered, and that this study has not been evaluated in any academic publication environment other than Sakarya University Journal of Science.

### Copyright Statement

Authors own the copyright of their work published in the journal and their work is published under the CC BY-NC 4.0 license.

## References

- [1] A. V. Kelarev, S. J. Quinn, "A Combinatorial Property and Power Graphs of Groups," *Contributions to General Algebra*, vol. 12, pp. 229-235, 2000.
- [2] A. V. Kelarev, S. J. Quinn, "Directed Graphs and Combinatorial Properties of Semigroups," *Journal of Algebra*, vol. 251, no. 1, pp. 16-26, 2002.
- [3] A. V. Kelarev, S. J. Quinn, "A Combinatorial Property and Power Graphs of Semigroups," *Commentationes Mathematicae Universitatis Carolinae*, vol. 45, no. 1, pp. 1-7, 2004.
- [4] I. Chakrabarty, S. Ghosh, M. K. Sen, "Undirected Power Graphs of Semigroups," *Semigroup Forum*, vol. 78, pp. 410-426, 2009.
- [5] P. J. Cameron, "The Power Graph of A Finite Group II.," *Journal of Group Theory*, vol. 13, no. 6, pp. 779-783, 2010.
- [6] P. J. Cameron, S. Ghosh, "The Power Graph of A Finite Group," *Discrete Mathematics*, vol. 311, no. 13, pp. 1220-1222, 2011.
- [7] S. Chattopadhyay, P. Panigrahi, F. Atik, "Spectral Radius of Power Graphs on Certain Finite Groups," *Indagationes Mathematicae*, vol.29, no. 2, pp. 730-737, 2018.
- [8] I. Gutman, "The Energy of Graph," *Berichteder Mathematisch Statistischen Sektion im Forschungszentrum Graz*, vol. 103, pp. 1-22, 1978.
- [9] I. Gutman, B. Zhou, "Laplacian Energy of A Graph," *Linear Algebra and its Applications*, vol. 414, no. 1, pp. 29-37, 2006.



## Comparison of Deep Learning Models and Optimization Algorithms in the Detection of Scoliosis and Spondylolisthesis from X-Ray Images

Harun Güneş<sup>1\*</sup>, Cengiz Hark<sup>2</sup>, Abdullah Erhan Akkaya<sup>2</sup>

<sup>1</sup> Hakkari University, Vocational School of Health Services, Medical Services and Techniques, Hakkari, Türkiye, harungunes@hakkari.edu.tr

<sup>2</sup> Inonu University, Faculty of Engineering, Department of Computer Engineering, Malatya, Türkiye, cengiz.hark@inonu.edu.tr, erhan.akkaya@inonu.edu.tr

\*Corresponding Author

### ARTICLE INFO

### ABSTRACT

Keywords:  
Deep-learning  
Classification  
Spine X-ray Images  
Scoliosis  
Spondylolisthesis



The spine is composed of pieces of bone called vertebrae that lie between the skull and the tailbone. Various medical conditions can affect the spine. In this study, two types of degenerative diseases, scoliosis, and spondylolisthesis, were studied. Deep AI architectures have recently enabled further disease diagnosis innovation using medical images. Various traditional and deep learning studies use medical images for disease diagnosis in the literature. This study aims to classify spine X-ray images according to three possible conditions (Normal, Scoliosis, and Spondylolisthesis) and to exploit the potential of these X-ray images to detect possible diseases occurring in the spine. The performance of deep learning models and optimization algorithms used in this process was evaluated. The study uses a data set created and/or analyzed during an existing study. This data set consists of images that belong to three different classes: scoliosis, spondylolisthesis, or x-ray images of normal (i.e. healthy) individuals. A total of 338 spine X-ray images, 188 scoliosis images, 79 spondylolisthesis images, and 71 normal images. Six different deep-learning architectures have been used in the study. These architectures are Alexnet, GoogLeNet, ResNet-18, ResNet-50, ResNet-101, and EfficientNet-bo. While working on these deep architectures, each model has been evaluated using different optimization algorithms. These optimization algorithms are RmsProp, SGDM, and Adam. According to the classification processes, the deep learning model with the highest accuracy value was Alexnet, and the optimization algorithm used with it, Sgdm (99.01%), and the training time lasted 38 seconds. According to the classification processes, the deep learning model with the fastest completion time (30 seconds) was Alexnet and the optimization algorithm used with it was RmsProp. An accuracy rate of 98.02% has been obtained in the training of this model.

### Article History:

Received: 01.02.2023

Accepted: 01.02.2024

Online Available: 24.04.2024

## 1. Introduction

The spine is composed of pieces of bone called vertebrae that lie between the skull and the tailbone. Intervertebral discs and facet joints are arranged symmetrically between the vertebrae. While these joints increase the spine's mobility, they also increase the strength and flexibility of the spine. The tissue in front of each vertebra is called the intervertebral disc, and the tissue behind it is called the facet joint [1]. Among these structures, soft tissue extending from the skull to

the tailbone surrounds and protects the spinal cord, which is an important part of the central nervous system. Like the brain, the spinal wire is wrapped through membranes known as the meninges. The cerebrospinal fluid is between this membranous structure representing the cerebral cortex's and spinal cord's continuity. The spine of the human skeleton consists of 7 cervical vertebrae, 12 thoracic or dorsal vertebrae, 5 lumbar vertebrae, pseudolumbar vertebrae, and 5 sacral vertebrae. The spine is also supported by

connective and muscle tissue, known medically as ligaments [2].

Various medical conditions can affect the spine. In this study, two different spinal diseases, scoliosis, and spondylolisthesis, were examined. Scoliosis is the most common three-dimensional spinal deformity among spinal deformities and causes severe postural dysfunction in advanced stages. The diagnosis of scoliosis, a degenerative disease, can be made by an expert using magnetic resonance imaging (MRI) or an X-ray of the spine. The rate of scoliosis varies from country to country in the world and it is considered to be one of the most important spinal diseases with a prevalence of 0.47-5.2% [3].

A Cobb angle value greater than  $10^\circ$  on spine images indicates scoliosis [4]. According to estimates and studies, it is stated that 6-9 million people in the United States have some degree of scoliosis [5]. Spondylolisthesis is caused by a damaged vertebral carrier or anterior displacement of the underlying vertebra. It is generally classified in various degrees (low-grade, high-grade, etc.) according to the degree of slip [6]. Spondylosis disease can be seen in 6% of adults. It can lead to weakness and numbness in the legs of individuals with this disease [6]. Spondylolisthesis is the change of the upper segment of the spine relative to the lower segment. It is a deformation in which it moves forward [7]. Spondylolisthesis can be seen as a focal abnormality in the sagittal plane, in which the spine slides from the adjacent anterior or posterior plane [8].

Vertebral deformities are often accompanied by cosmetic concerns or concerns about the progression of the deformity. The most common are; adults experiencing symptoms, pain, and limitation in daily life. Therefore, it is very important to document the type, severity, location, and change of patient pain over time [9]. In addition, it is necessary to clarify which factors lead to increases and decreases in axial low back pain as well as leg pain and their effects [10].

In recent years, they have contributed to the literature in the field of deep learning in disease diagnosis using medical images. Fraiwan et al.

(2022) examined the utilization of deep transfer learning techniques for diagnosing scoliosis and spondylolisthesis from X-ray images. Their research focuses on the application of 14 deep transfer learning algorithms to automate the diagnosis of scoliosis and spondylolisthesis. Deep learning networks are employed to perform classification and diagnostic operations on the X-ray image data.

The authors' study investigates the effectiveness of deep transfer learning techniques in identifying scoliosis and spondylolisthesis from X-ray images. The most favorable outcome was achieved by DensNet-201, which exhibited a success rate of 99.01%. The article's findings provide information regarding the diagnostic efficacy and accuracy of these procedures [11]. Rao Farhat Masood et al. (2022), in their study, focus on deep learning-based spinal body segmentation, extraction of spine measurements, and disease classification. In this article, the segmentation of spinal objects in spine images using deep learning methods is discussed. In addition, the usability of deep learning-based approaches for spine measurements and disease classification is also examined. This study investigates how automated segmentation and classification methods can be potentially helpful tool in the diagnosis of spinal diseases. Using the angular deviation metric for spondylolisthesis classification, they achieved 89% accuracy, while calculating the area within the closed lumbar curve region, they achieved 93% accuracy in determining adequacy/inadequacy in the LL assessment [12].

Mahsa Tajdari et al. (2021) focus on image-based modeling for Idiopathic Scoliosis in adolescents. The article focuses on understanding and predicting Idiopathic Scoliosis using image-based modeling methods, focusing on mechanistic machine learning analysis and prediction. This study explores the usability of deep learning and machine learning techniques to understand the mechanistic features and progression of Idiopathic Scoliosis [13].

The aim of this study is to classify spine X-ray images according to three possible conditions (Normal, Scoliosis, and Spondylolisthesis) and to exploit the potential of these X-ray images to

detect possible diseases occurring in the spine. Performance evaluation and comparison of 6 different deep learning architectures, which can be classified into three categories, on the same dataset were made using different optimization algorithms. The neural networks used in this study were used to investigate the optimal estimation method. Other parts of the study continue as follows. Chapter 2 discusses materials and methods. This section explains data sets, deep learning architectures, and optimization algorithms used in experimental studies. Chapter 3 presents the experimental studies and results.

## 2. Material and Methods

In this study; data set created and/or analyzed during an existing study was used [14]. This dataset was created from three different classes of images: chest X-ray images of scoliosis, spondylolisthesis, or normal (i.e. healthy) people. There are 338 x-ray images in total, with 188 scoliosis images, 79 spondylolisthesis images, and 71 normal images. In this study, 6 different deep-learning architectures were studied. These architectures; Alexnet, GoogLeNet, ResNet-18, ResNet-50, ResNet-101 and EfficientNet-bo. While working on these deep learning architectures, each model was evaluated using different optimization algorithms. These optimization algorithms are RmsProp, SGDM, and Adam.

### 2.1.Dataset

In this study, a data set created and/or analyzed during an existing study was used [13]. The dataset included 338 subjects (240 females, 98 males) aged 9 months to 79 years with a mean  $\pm$  SD of  $24.9 \pm 18.58$  years. There were 71 radiographically normal subjects (40 females, 31 males) aged 9 months to 56 years, with a mean  $\pm$  SD of  $19.41 \pm 11.19$ . 79 people (49 females, 30 males) aged between 15 and 79 were diagnosed with spondylolisthesis, with a mean  $\pm$  SD of  $53.59 \pm 14.02$ . The number of people aged 5-35 years diagnosed with scoliosis was 188 (151 females, 37 males), and the mean  $\pm$  SD was  $14.73 \pm 3.36$ .

This dataset is composed of images belonging to three different classes: scoliosis, spondylolisthesis, or vertebral X-ray images of normal (i.e. healthy) people. There are 338 X-ray images in total, with 188 scoliosis images, 79 spondylolisthesis images, and 71 normal images. Figure 1 shows image examples of scoliosis, spondylolisthesis, and normal (i.e. healthy) individuals from this dataset [14].



**Figure 1.** Sample normal, scoliosis, and spondylolisthesis x-ray images in the dataset

### 2.1. Convolutional Neural Network (CNN)

Deep learning, a hot topic of late, is a machine learning approach that has emerged with the deepening of multilayer feedforward neural networks. Due to the limited number of hardware products, the number of layers in traditional neural networks is limited by learned parameters, and the relationships between layers are computationally intensive. High-end computer generation makes it possible to train deep architectures using multilevel neural networks [15].

It is a high-performing convolutional neural network method in many areas such as deep learning, image processing, machine learning, speech recognition, and object tracking. A CNN (Convolutional Neural Network) is a type of multilayer neural network. One of the main advantages of CNN algorithms is feature extraction, which minimizes preprocessing steps. Therefore, no preliminary search is required to find features in the image [16].

Currently, many deep learning architectures have been developed and used in various research. Some of these architectures are LeNet, AlexNet, ZFNet, GoogLeNet, VGGNet, LSTM, RNN, SqueezeNet, ResNet, and EfficientNet. The mentioned architectures are just a few of the deep learning architectures. In this study, AlexNet, GoogLeNet, ResNet-18, ResNet-50, ResNet-

101, and EfficientNet-b0 architectures were used.

### 2.2.1. Alexnet

It is a deep neural network architecture developed by Krizhevsky, Sutskever, and Hinton. It won the 2012 ImageNet competition, making deep learning a global voice. There are sequential convolution and link layers. This architecture increased the performance of computer-aided object identification from 10.8% to 83.6% [17].

Alexnet; is a neural network with 60 million parameters and 650 000 neurons. Most consist of 5 layers of convolution followed by a max pooling layer and 3 fully connected layers.

The ImageNet dataset contains 1000 different image classes. Therefore, the output layer consists of 1000 units. The resulting model will be a deeper and larger model, but the architecture is very similar to LeNet. In the AlexNet diagram in Figure 2, we can see that he splits the problem into two parts. Half are running on GPU1 and half on GPU2 [18]. This way, it keeps the communication load low, resulting in good overall performance. The data processing of the two channels intersects only at the third feature extraction layer. ReLU as the activation function, a dilution method is applied to prevent overfitting [18].

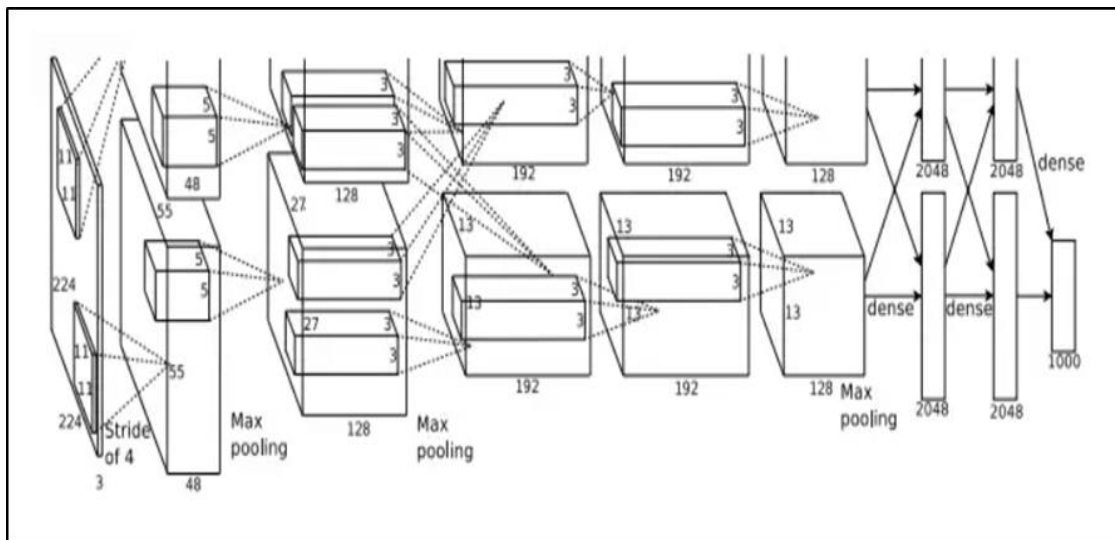


Figure 2. Alexnet

### 2.2.2. Googlenet

GoogLeNet (Szegedy, Liu et al. 2015) is a complex architecture due to its output modules. In 2014, GoogLeNet beat ImageNet's competition with 22 layers and 5.7% error rate [19]. This architecture is usually one of the first CNN architectures to move away from stacking convolutional and pooling layers in a sequential structure. Storage and power consumption also play an important role in this new model. Stacking all the layers and adding many filters increases computation and storage costs and increases the potential for memorization. GoogLeNet overcomes this by using modules connected in parallel. The GoogLeNet network architecture is shown in figure 3 [19].

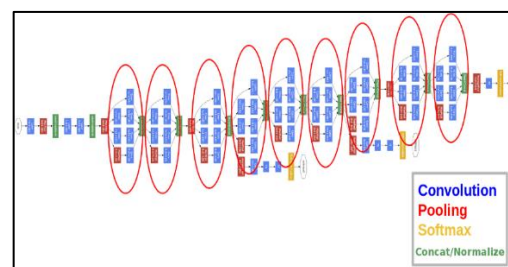


Figure 3. GoogLeNet

### 2.2.3. ResNet

In 2015, ResNet ranked first and the error rate detected by GoogLeNet decreased from 6.67% the previous year to 3.57%. In this deep network model, a different approach is applied by adding a new structure called a residual block.



The structure of the residual layer is shown in Figure 4 [19]. As you can see, the block output is equal to  $(F(x) + x)$ , where  $x$  is the block input. Here  $F(x)$  represents the weight layer output for  $x$  input data.

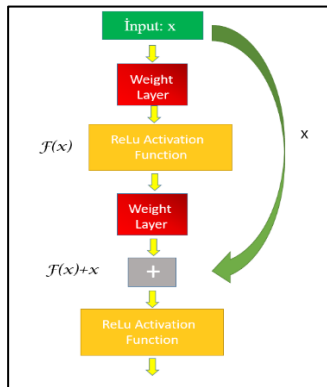


**Figure 4.** Residual block structure in ResNet architecture

**a. ResNet-18**

A residual block structure is introduced to solve the vanishing gradient problem. The disappearing gradient problem causes the error derivative to shrink and disappear during training. For this reason, the updating of the weights is interrupted and the training is terminated. Theoretically, the training error should decrease as the number of layers in the network increases. However, in practice, gradient flux decreases and training error increases as layers are added to the network. With the deepening network, thanks to residual blocks in ResNet, a way to reduce the training error has been found [19].

The ResNet model has three different versions, ResNet-18, ResNet-50, and ResNet101, depending on the number of deep layers involved.

**b. ResNet-50**

Resnet 50 is obtained by replacing each 2-layer block in a 34-layer network with a 3-layer bottleneck block. For each remainder function  $F$ , a three-layer stack is used instead of two. The dimensions of these three layers are  $1 \times 1$ ,  $3 \times 3$ , and  $1 \times 1$ . Here the  $1 \times 1$  layer causes the size to decrease and then increase (return). On the other

hand,  $3 \times 3$  layers still have the bottleneck of small input/output sizes. This structure is shown in figure 5 [19].

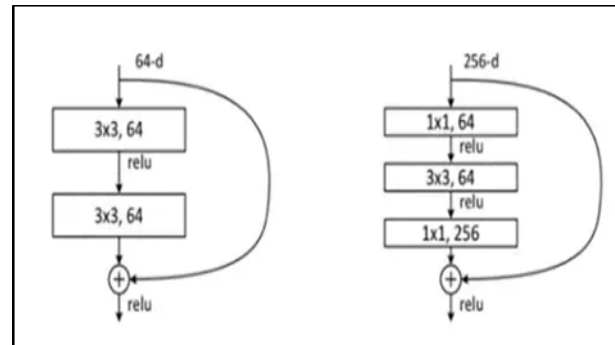


**Figure 5.** Left: A building block for ResNet-34 Right: A “bottleneck” building block for ResNet-50/101/152

**c. ResNet-101-152**

Other 3-layer blocks are used to create 101 and 152-layer ResNets. A 50/101/152 layer ResNet is much more accurate than a 34-layer ResNet. The problem of distortion is avoided thanks to the residual mesh, and the increased depth greatly improves the accuracy. Figure 6 shows the classification errors of some imagenet models [19].

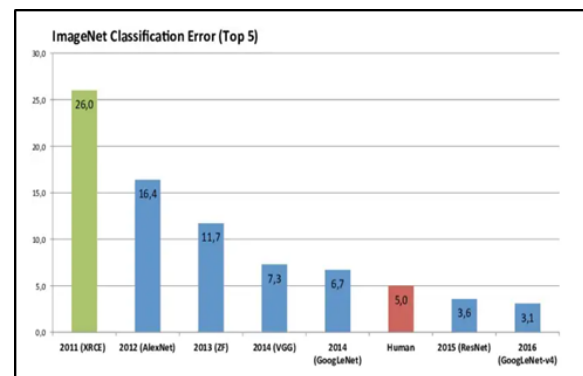


**Figure 6.** Imagenet classification error (Top 5)

As a result, ResNet uses shortcut links to skip some layers, thus improving model performance in deeper networks and overcoming optimization/degradation issues in deeper networks.

The building blocks in the Resnet model are shown in brackets in Figure 7 with their stacked block numbers [19].



layer name	output size	18-layer	34-layer	50-layer	101-layer	152-layer
conv1	112×112	7×7, 64, stride 2				
conv2_x	56×56	3×3 max pool, stride 2				
		$\begin{bmatrix} 3 \times 3, 64 \\ 3 \times 3, 64 \end{bmatrix} \times 2$	$\begin{bmatrix} 3 \times 3, 64 \\ 3 \times 3, 64 \end{bmatrix} \times 3$	$\begin{bmatrix} 1 \times 1, 64 \\ 3 \times 3, 64 \\ 1 \times 1, 256 \end{bmatrix} \times 3$	$\begin{bmatrix} 1 \times 1, 64 \\ 3 \times 3, 64 \\ 1 \times 1, 256 \end{bmatrix} \times 3$	$\begin{bmatrix} 1 \times 1, 64 \\ 3 \times 3, 64 \\ 1 \times 1, 256 \end{bmatrix} \times 3$
conv3_x	28×28	$\begin{bmatrix} 3 \times 3, 128 \\ 3 \times 3, 128 \end{bmatrix} \times 2$	$\begin{bmatrix} 3 \times 3, 128 \\ 3 \times 3, 128 \end{bmatrix} \times 4$	$\begin{bmatrix} 1 \times 1, 128 \\ 3 \times 3, 128 \\ 1 \times 1, 512 \end{bmatrix} \times 4$	$\begin{bmatrix} 1 \times 1, 128 \\ 3 \times 3, 128 \\ 1 \times 1, 512 \end{bmatrix} \times 4$	$\begin{bmatrix} 1 \times 1, 128 \\ 3 \times 3, 128 \\ 1 \times 1, 512 \end{bmatrix} \times 8$
conv4_x	14×14	$\begin{bmatrix} 3 \times 3, 256 \\ 3 \times 3, 256 \end{bmatrix} \times 2$	$\begin{bmatrix} 3 \times 3, 256 \\ 3 \times 3, 256 \end{bmatrix} \times 6$	$\begin{bmatrix} 1 \times 1, 256 \\ 3 \times 3, 256 \\ 1 \times 1, 1024 \end{bmatrix} \times 6$	$\begin{bmatrix} 1 \times 1, 256 \\ 3 \times 3, 256 \\ 1 \times 1, 1024 \end{bmatrix} \times 23$	$\begin{bmatrix} 1 \times 1, 256 \\ 3 \times 3, 256 \\ 1 \times 1, 1024 \end{bmatrix} \times 36$
conv5_x	7×7	$\begin{bmatrix} 3 \times 3, 512 \\ 3 \times 3, 512 \end{bmatrix} \times 2$	$\begin{bmatrix} 3 \times 3, 512 \\ 3 \times 3, 512 \end{bmatrix} \times 3$	$\begin{bmatrix} 1 \times 1, 512 \\ 3 \times 3, 512 \\ 1 \times 1, 2048 \end{bmatrix} \times 3$	$\begin{bmatrix} 1 \times 1, 512 \\ 3 \times 3, 512 \\ 1 \times 1, 2048 \end{bmatrix} \times 3$	$\begin{bmatrix} 1 \times 1, 512 \\ 3 \times 3, 512 \\ 1 \times 1, 2048 \end{bmatrix} \times 3$
	1×1	average pool, 1000-d fc, softmax				
FLOPs		1.8×10 <sup>9</sup>	3.6×10 <sup>9</sup>	3.8×10 <sup>9</sup>	7.6×10 <sup>9</sup>	11.3×10 <sup>9</sup>

Figure 7. Building blocks are shown in brackets with their stacked block numbers. Down-sampling is performed by conv3, conv4 1, and conv5 in steps of 2

### 2.2.4. EfficientNet-b0

EfficientNet is a CNN architecture that achieves high accuracy with fewer data compared to other convolutional neural networks. The EfficientNet architecture is based on the principle of scaling several dimensions of the network simultaneously, such as depth, width, and image resolution, using fixed complex factors [20].

In fact, this composite scaling idea also works with existing MobileNet and ResNet architectures. It should be optimized for accuracy and efficiency measured in floating point operations per second (FLOPs). This advanced architecture uses MBConv (Mobile Inverted Bottleneck Convolution). Unlike other cutting-edge models, EfficientNet achieves more efficient results by scaling depth, width, and resolution equally while downsizing the model.

The EfficientNet family consists of eight models, from EfficientNet-B0 to EfficientNet-B7. As the model number increases, the number of parameters and mesh depth increases. Therefore, higher performance is achieved. A block diagram of the basic network structure of the EfficientNet B0 model is shown in figure 8 [21].

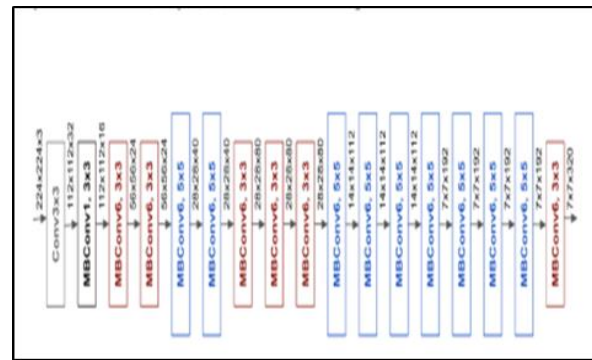


Figure 8. EfficientNet B0 basic network structure block representation

### 2.2. Optimization algorithms

There are six commonly used optimization methods to minimize machine learning error rates. These methods are; SGD, Momentum, Adagrad, RMSProp, Adadelta and Adam methods. In Table 1 [22], the characteristics of the gradient descent methods are compared. The evolution map of gradient descent is shown in Figure 9 [22].

Table 1. Comparison of Gradient Descent Methods

Algorithm	Year	Learning Coefficient	Gradient
SGD	1951	√	√
Momentum	1964		√
Adam	2014	√	√
AdaGrad	2011	√	
RMSProp	2012	√	
Adadelta	2012	√	

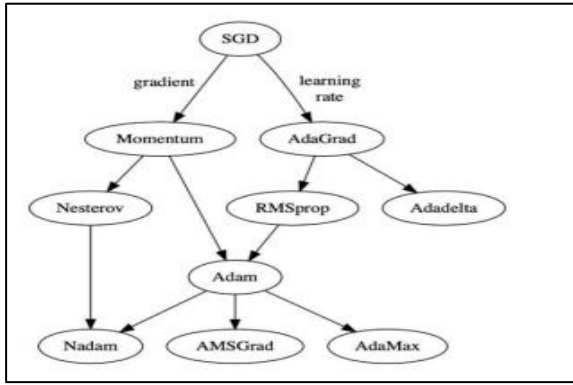


**Figure 9.** Evolutionary map of gradient descent methods

### 2.3.1.SGDM

Many studies in the literature use SGD as stochastic gradient descent. SGD randomly updates weights using some but not all gradients. It is necessary to update the current weights ( $w_t$ ) by multiplying the current gradient ( $\partial L / \partial w_t$ ) by the learning factor ( $a$ ) [22].

$$w_{t+1} = w_t - a \frac{\partial L}{\partial w_t} \quad (1)$$

There are many variations when looking for the best spot in SGD. The Momentum method is recommended to reduce these vibrations and increase the speed of reaching your goals [22]. This method uses pulsed gradients instead of existing gradients. In fact, the name Monemntum is somewhat disappointing and the method can be described as 'controlled beats' [23].

$$w_{t+1} = w_t - a v_t \quad (2)$$

$$v_t = \beta v_{t-1} + (1 - \beta) \frac{\partial L}{\partial w_t} \quad (3)$$

Here the initial value of  $V_t$  is 0.  $\beta$  ranges from 0 to 1, and the commonly used value of 0.9 is used to set how much of the historical gradient is included in the process. In figure 10 we see that the momentumless SGD oscillates strongly on the way to the solution. On the other hand, in

$$v_t = \beta_1 v_{t-1} + (1 - \beta_1) \frac{\partial L}{\partial w_t} \quad (9)$$

$$S_t = \beta_2 S_{t-1} + (1 - \beta_2) \left[ \frac{\partial L}{\partial w_t} \right]^2 \quad (10)$$

figure 10 b the SGD with momentum reaches a solution with fewer oscillations [23].

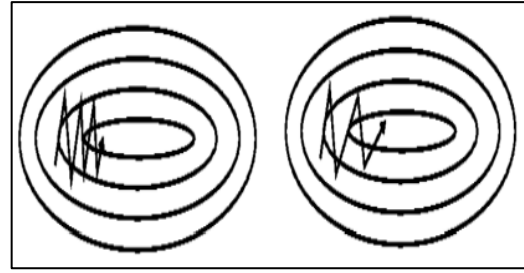


**Figure 10.** a.) SGD without momentum b.) SGD with momentum

### 2.3.2.RMSprop

It is proposed to solve the continuous learning coefficient problem like Adagrad. The difference is that the Adagrad method does not square the slope, it squares the slope by momentum [24].

$$w_{t+1} = w_t - \frac{a}{\sqrt{S_t + \epsilon}} \cdot \frac{\partial L}{\partial w_t} \quad (4)$$

$$S_t = \beta S_{t-1} + (1 - \beta) \left[ \frac{\partial L}{\partial w_t} \right]^2 \quad (5)$$

Here,  $S$  is initially prioritized as 0,  $a=0.001$ ,  $\beta=0.9$ ,  $\epsilon=10^{-6}$  [23].

### 2.3.3.Adam

Gradient descent is proposed by combining the advantages of RMSprop and impulse methods.  $V$  is used for the pulse method and  $S$  is used for rmsprop [24].

$$w_{t+1} = w_t - \frac{a}{\sqrt{\hat{S}_t + \epsilon}} \cdot \hat{v}_t \quad (6)$$

$$\hat{v}_t = \frac{v_t}{1 - \beta_1^t} \quad (7)$$

$$\hat{S}_t = \frac{S_t}{1 - \beta_2^t} \quad (8)$$

Here, firstly  $S$  and  $V$  are initially 0;  $a=0.001$ ;  $\beta_1=0.9$ ;  $\beta_2=0.999$ ;  $\epsilon$  is preferred as  $10^{-8}$  [24].

### 2.3. Method used

The aim of this study is to take X-Ray images of the spine; scoliosis, spondylolisthesis, and normal (i.e. healthy) to classify according to three possible conditions and to detect the disease. While doing this process, 6 different deep-learning architectures were used. These architectures are: AlexNet, GoogleNet, ResNet-18, ResNet50, ResNet100, and EfficientNet-b0. During the training process, 3 different optimization algorithms were used in each model. These optimization algorithms are Sgdm,

Adam, and RmsProp. After performing the classification process, the success rate and training time of the models and algorithms were compared. Performance evaluation and comparison of 6 different deep learning techniques, which can be classified into three categories, on the same dataset were made using different optimization algorithms.

The best estimation method was investigated with the neural networks used in this study (Figure 11).

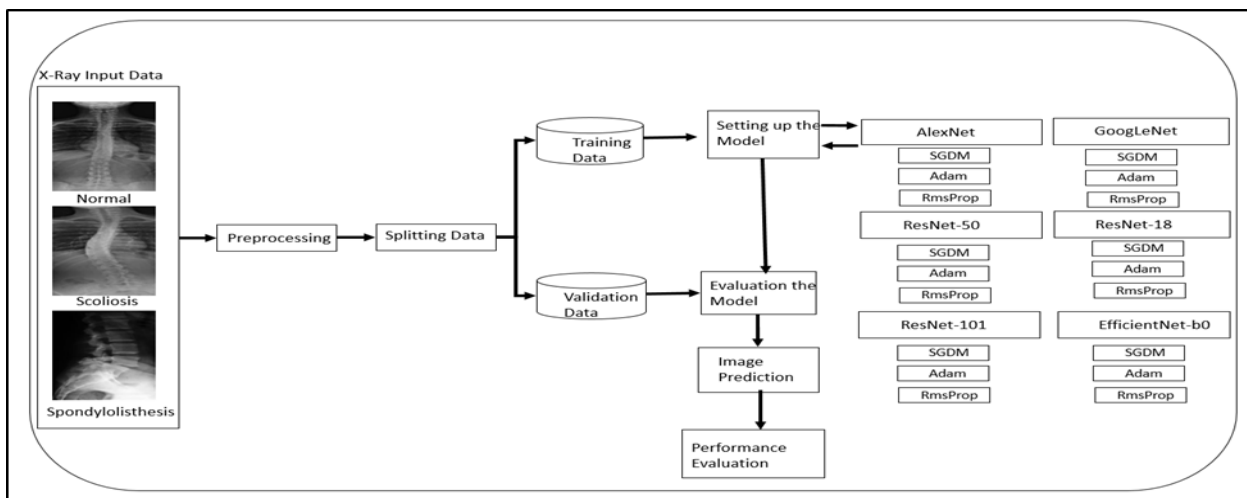


**Figure 11.** Architecture used to compare different models in x-ray image classification with deep learning technique

### 3. Results and Discussion

In this study, the classification process and disease detection were tried to be done by using deep-learning neural networks from X-Ray vertebra images. It is trained with previously trained deep neural networks and 80% of the X-Ray dataset is taken randomly. The system was then validated with 20% of the data taken randomly. While this process is being done, the classification process in neural network models is done separately with optimization algorithms (Sgdm, Adam, RmsProp). The application was prepared in a Matlab environment [25]. The work done; It is built on Intel Core-i7 6800K 3.4GHz

processor, GPU Nvidia GeForce RTX 3060 Ti graphics card, 16 GB RAM, and 64-bit Windows 10 hardware. After the classification process was performed, the best accuracy rate was obtained with the Alexnet model and Sgdm optimization algorithm with a rate of 99.01%. When comparing the training times, the model that completed the training time the fastest was the Alexnet and RmsProp optimization algorithm with 30 seconds. In Table 2, the sample numbers and rates in the classification process for all models are presented.

**Table 2.** X-Ray dataset sample numbers, training and validation rate

Dataset	% Rate	Number of samples
<b>Total</b>	% 100	338
<b>Train</b>	% 80	270
<b>Validation</b>	% 20	68

In table 3, the results obtained as a result of the classification process and the training periods are presented. According to the classification processes, the deep learning model that gave the highest accuracy value was Alexnet and the optimization algorithm used with it, Sgdm (99.01%), and the training time lasted 38 seconds. Performance graphics of this process are presented in figure 12 and figure 13.

**Table 3.** Deep-learning models used, Optimization algorithms, accuracy values , and training time

Deep Learning Model	Optimization Algorithm	Accuracy (%)	Model Training Time (Second)
Alexnet	Sgdm	99.01	38
Alexnet	Adam	96.04	40
Alexnet	RmsProp	98.02	30
GoogLeNet	Sgdm	94.06	67
GoogLeNet	Adam	98.02	94
GoogLeNet	RmsProp	97.03	76
ResNet-18	Sgdm	97.06	67
ResNet-18	Adam	92.65	42
ResNet-18	RmsProp	97.06	40
ResNet-50	Sgdm	97.03	97
ResNet-50	Adam	97.06	96
ResNet-50	RmsProp	98.53	131
ResNet-101	Sgdm	98.02	221
ResNet-101	Adam	98.02	286
ResNet-101	RmsProp	98.02	210
EfficientNet-b0	Sgdm	98.02	607
EfficientNet-b0	Adam	99.00	647
EfficientNet-b0	RmsProp	94.06	625



**Figure 12.** Alexnet and sgd performance graph (Accuracy)

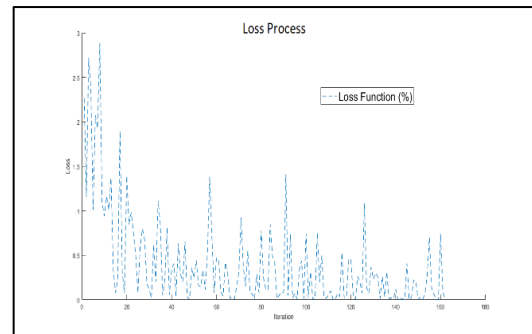


**Figure 13.** Alexnet and sgd performance graph (Loss)

The complexity matrices of the training and validation data obtained after the completion of the training of the model are given in figure 14 and figure 15.

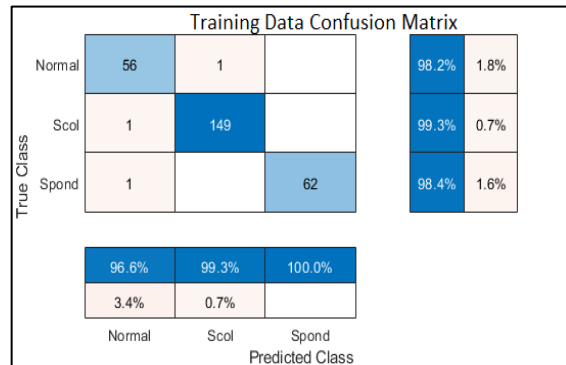


**Figure 14.** Alexnet and Sgdm; Training Data Confusion Matrix

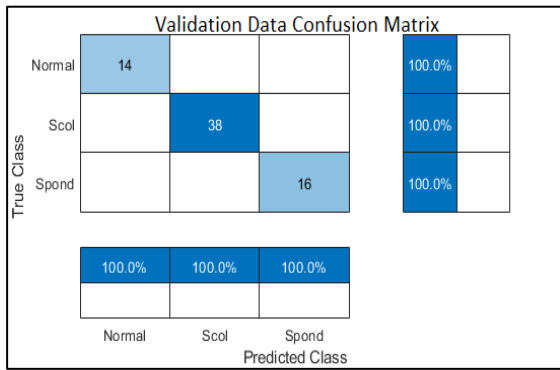


Figure 15. Alexnet and Sgdm; Validation Data Confusion Matrix

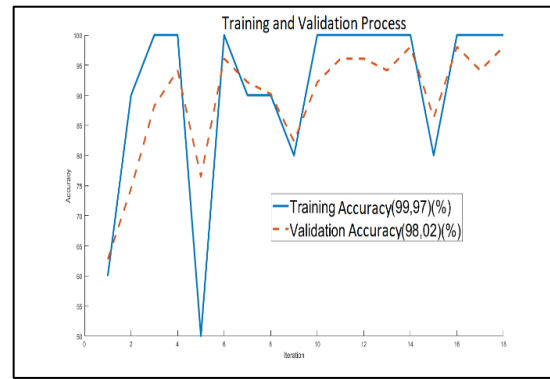


Figure 17. Alexnet and RmsProp performance graph (Accuracy)

After the training of the model is completed, the ratios of determining the classes to which the X-Ray images randomly sent to the classifier belong are given in Figure 16.

As shown in Figure 16a, an X-ray image sent randomly to the classifier is evaluated and it is determined that the image belongs to the normal class at the rate of 95% by the classifier. By following the same path, it was determined that the randomly selected image in figure 16b belongs to the scoliosis class at the rate of 100%, and the image in figure 16c is 100% of the spondylolisthesis class.

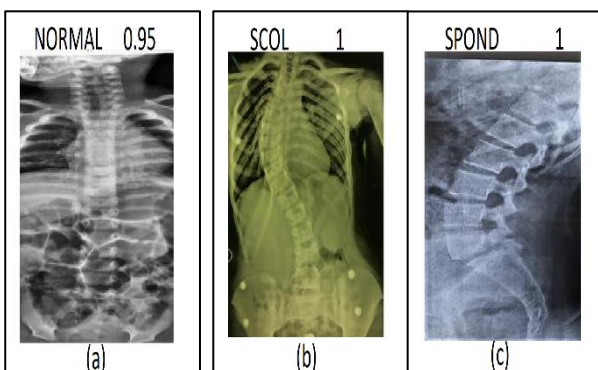


Figure 16. Alexnet and sgdm; x-ray image detection

According to the classification processes, the deep learning model with the fastest completion of the training period was Alexnet, and the optimization algorithm used with it, RmsProp. An accuracy rate of 98.02% was obtained in the training of this model. Performance graphics of this process are presented in figure 17 and figure 18.

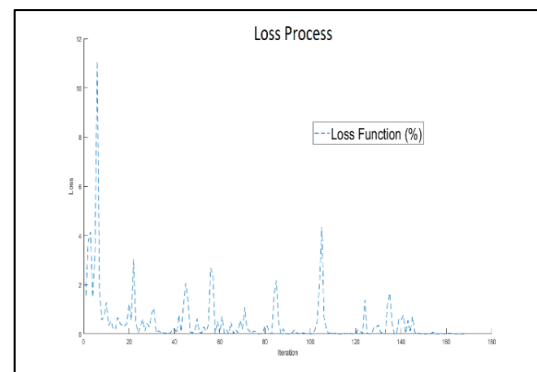


Figure 18. Alexnet and rmsprop performance graph (Loss)

The complexity matrices of the training and validation data obtained after the completion of the training of the model are given in figure 19 and figure 20.

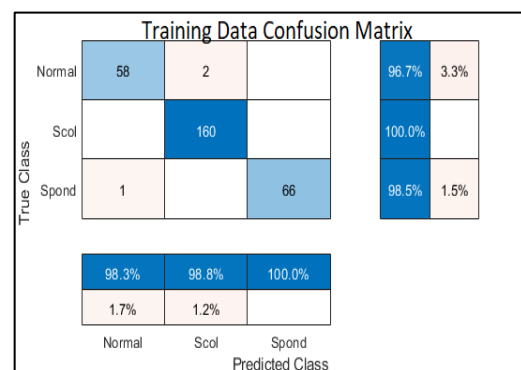
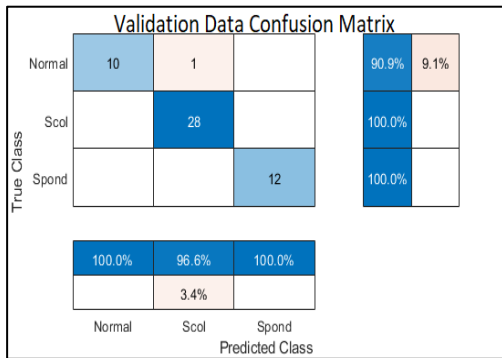
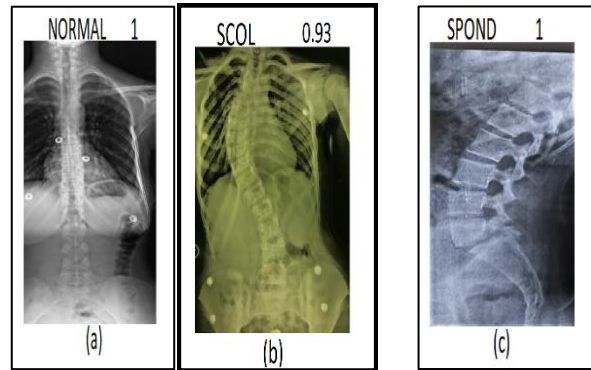


Figure 19. Alexnet and rmsprop; training data confusion matrix





**Figure 20.** Alexnet and rmsprop; validation data confusion matrix



**Figure 21.** Alexnet and rmsprop; x-ray image detection

After the training of the model is completed, the ratios of determining the classes to which the X-Ray images randomly sent to the classifier belong are given in Figure 21.

As shown in Figure 21a, an X-ray image sent randomly to the classifier is evaluated and it is determined that the image belongs to the normal class at 100% by the classifier. Following the same path, it was determined that the randomly selected image in figure 21b belongs to the scoliosis class at a rate of 93% and the image in figure 21c belongs to the spondylolisthesis class at a rate of 100%.

Table 4 illustrates a performance comparison between relevant studies. Although previous studies [1, 26, 29] achieved notable levels of accuracy, their methodologies necessitate extensive and error-prone measurements of biomechanical parameters, which may not be essential for the specific detection of disease cases. To the best of our knowledge, no other investigation has employed deep learning techniques for the classification of scoliosis and spondylolisthesis using normal X-ray images. Kolombo et al. [27] focused on discriminating scoliosis from a healthy condition and attained a maximum accuracy of approximately 85%. Likewise, Wang et al. [28] did not achieve satisfactory accuracy in detecting scoliosis progression, while Yang et al. obtained an average accuracy of around 80% in differentiating scoliosis severity based on Cobb angles ( $< 10^\circ$ ,  $10^\circ$ - $19^\circ$ ,  $20^\circ$ - $44^\circ$ , or  $\geq 45^\circ$ ).

**Table 4.** Comparison with related studies in the literature.

Study	Classification Problem	Dataset	Accuracy (%)
Alafeef et al. [1]	3-class classification	422 subjects	99.5
Fraiwan et al. [3]	3-class pair-wise classification	331 subjects	96.34-99.33
Yang et al. [4]	4-class for scoliosis severity	3640 back images	80
Reshi et al. [26]	3-class classification	310 records	99.5
Colombo et al. [27]	Healthy vs scoliosis	272 scoliosis and 20 healthy	85
Wang et al. [28]	Progressing vs non-progressive scoliosis	490 subjects	76
Unal et al. [29]	Pairwise	310 records	96
<b>This Work</b>	3-class pair-wise classification	331 subjects	92.65-99.01

However, despite the absence of directly comparable literature, our current study demonstrates superior accuracy with a reduced number of input processing and measurements. Unal et al. [29] investigated a pairwise Fuzzy C-Means based feature weighting method to improve the classification of spinal diseases. This study, which stands out to overcome the limitations of traditional methods, was able to achieve more accurate classification results while demonstrating the effective use of artificial intelligence and data mining in disease diagnosis. This article focuses on the comparison of deep learning models and optimization algorithms in detecting spinal diseases such as scoliosis and spondylolisthesis from X-ray images, and it contributes to the literature in various ways. Here are the potential contributions of this article to the literature:

1. **Effectiveness of deep learning models:** The article investigates the use of six different deep learning architectures in detecting spinal diseases such as scoliosis and spondylolisthesis. This is an important contribution that evaluates the effectiveness of deep learning models in accurately diagnosing these diseases.
2. **Comparison of optimization algorithms:** The article examines the impact of different optimization algorithms on the performance of deep learning models. This can provide guidance to researchers on which optimization algorithms yield better results in this type of disease detection.
3. **Dataset creation:** The article discusses the creation and utilization of a dataset containing spinal images of scoliosis, spondylolisthesis, and normal individuals. This provides a foundation for similar studies and enables researchers to use this dataset in their own work.
4. **Performance evaluation:** The article presents a comprehensive analysis evaluating the performance of different deep learning models and optimization algorithms. This can assist researchers in comparing their performance when conducting similar studies.

These contributions of the article emphasize the importance of using deep learning and

optimization techniques in the diagnosis of spinal diseases such as scoliosis and spondylolisthesis. This study inspires progress in the relevant field of literature and encourages further research.

## **Article Information Form**

### ***Funding***

The author(s) received no financial support for the research, authorship, or publication of this study.

### ***Authors' Contribution***

All authors contributed equally to the writing of this article. All authors have read and approved the final manuscript.

### ***The Declaration of Conflict of Interest/ Common Interest***

No conflicts of interest or common interest have been stated by the authors.

### ***The Declaration of Ethics Committee Approval***

This study did not require permission from the ethics committee or any special permission.

### ***The Declaration of Research and Publication Ethics***

The authors of the article declare to respect SAUJS scientific, ethical, and citation rules in all processes of the paper and that they did not falsify the collected data. Furthermore, they state that the Sakarya University Journal of Science and its editorial board are not responsible for any ethical violations that may be encountered and that this study has not been evaluated in any environment. Scholarly publications other than the Sakarya University Journal of Science.

### ***Copyright Statement***

Authors own the copyright of their work published in the journal and their work is published under the CC BY-NC 4.0 license.

## **References**

- [1] M. Alafeef, M. Fraiwan, H. Alkhalaf, Z. Audat, "Shannon entropy and fuzzy C-means weighting for AI-based diagnosis of vertebral column diseases" *Journal of Ambient Intelligence and Humanized*

- Computing, Springer, 2020, vol. 11, pp. 2557-2566.
- [2] M. R. Konieczny, H. Senyurt, R. Krauspe, "Epidemiology of adolescent idiopathic scoliosis," *Journal of children's orthopaedics*, London, England, vol 7, no. 1, pp. 3-9, 2013.
- [3] M. Alafeef, Z. Audat, L. Fraiwan, T. Manasreh, "Using deep transfer learning to detect scoliosis and spondylolisthesis from X-ray images," *Plos one*, vol. 17, no. 5, pp. e0267851, 2022.
- [4] J. Yang, K. Zhang, H. Fan, Z. Huang, Y. Xiang, J. Yang, H. Lin, "Development and validation of deep learning algorithms for scoliosis screening using back images," *Communications biology*, vol. 2, no. 1, pp. 390, 2019.
- [5] American Association of Neurological Surgeons, "Scoliosis", Jan. 22, 2023. [Online]. Available:<https://www.aans.org/Patients/Neurosurgical-Conditions-andTreatments/Scoliosis>
- [6] S. The American Academy of Orthopaedic Surgeons, "Spondylolysis and Spondylolisthesis", Jan. 22, 2023. [Online]. Available:<https://orthoinfo.aaos.org/en/diseases--conditions/spondylolysis-and-spondylolisthesis>
- [7] M. A. Deveci, A. Şenköylü, "Gelişimsel spondilolisteziste bel ağrısı: tanı ve tedavi yaklaşımı," *TOTBİD Dergisi*:14, pp. 282-289.
- [8] J. S. Smith, C. I. Shaffrey, K. M. Fu, J. K. Scheer, S. Bess, V. Lafage, C.P. Ames, "Clinical and radiographic evaluation of the adult spinal deformity patient," in *Neurosurgery Clinics*, Elsevier, vol. 24, no. 2, pp. 143-156, 2013.
- [9] S. Bess, O. Boachie-Adjei, D. Burton, M. Cunningham, C. Shaffrey, A. Shelokov, International Spine Study Group, "Pain and disability determine treatment modality for older patients with adult scoliosis, while deformity guides treatment for younger patients," *Spine*, vol. 34, no. 20, pp. 2186-2190, 2009.
- [10] J. S. Smith, C. I. Shaffrey, S. D. Glassman, S. H. Berven, F. J. Schwab, C. L. Hamill, Spinal Deformity Study Group, "Risk-benefit assessment of surgery for adult scoliosis: an analysis based on patient age," *Spine*, vol. 36, no.10, pp. 817-824, 2019.
- [11] M. Fraiwan, Z. Audat, L. Fraiwan, T. Manasreh, "Using deep transfer learning to detect scoliosis and spondylolisthesis from X-ray images," *Plos one*, vol.17, no. 5, pp. e0267851, 2022.
- [12] R. F. Masood, I. A Taj, M. B. Khan, M. A. Qureshi, T. Hassan, "Deep learning based vertebral body segmentation with extraction of spinal measurements and disorder disease classification," in *Biomedical Signal Processing and Control*, Elsevier, vol. 71, pp. 103230, 2022.
- [13] M. Tajdari, A. Pawar, H. Li, F. Tajdari, A. Maqsood, E. Cleary, W. K. Liu, "Image-based modeling for adolescent idiopathic scoliosis: mechanistic machine learning analysis and prediction," *Computer methods in applied mechanics and engineering*, Elsevier, vol. 374, pp. 113590, 2021.
- [14] M. Fraiwan, Z. Audat, L. Fraiwan, T. Manasreh, "Using deep transfer learning to detect scoliosis and spondylolisthesis from X-ray images," *Plos one*, vol. 17, no. 5, pp. e0267851, 2022.
- [15] I. Özkan, E. Ülker, "Derin öğrenme ve görüntü analizinde kullanılan derin öğrenme modelleri," *Gaziosmanpaşa Bilimsel Araştırma Dergisi*, vol. 6, no. 3, pp. 85-104, 2017.
- [16] M. Turkoglu, D. Hanbay, A. Sengur, "Multi-model LSTM-based convolutional

- neural networks for detection of apple diseases and pests,” in *Journal of Ambient Intelligence and Humanized Computing*, Springer, pp. 1-11, 2019.
- [17] A. Krizhevsky, I. Sutskever, G. E. Hinton, “Imagenet classification with deep convolutional neural networks,” *Communications of the ACM*, vol. 60, no. 6, pp. 84-90, 2017.
- [18] S. Gökalp, İ. Aydın, “Farklı Derin Sinir Ağı Modellerinin Duygu Tanımadaki Performansların Karşılaştırılması,” *Muş Alparslan Üniversitesi Mühendislik Mimarlık Fakültesi Dergisi*, vol. 2, no.1, pp. 35-43, 2021.
- [19] K. He, X. Zhang, S. Ren, j. Sun, “Deep residual learning for image recognition” In *Proceedings of the IEEE conference on computer vision and pattern recognition*, pp. 770-778, 2016.
- [20] B. Anadolu, “Dijital hikâye anlatıcılığı bağlamında yapay zekânın sinemaya etkisi: Sunspring ve It’s No Game filmlerinin analizi,” *Erciyes İletişim Dergisi*, vol.1, pp. 39-56, 2019.
- [21] M. Tan, Q. Le, “Efficientnet: Rethinking model scaling for convolutional neural networks,” In *International conference on machine learning*, PMLR, pp. 6105-6114, 2019.
- [22] E. Seyyarer, F. Ayata, T. Uçkan, A. Krci, “Derin öğrenmede kullanılan optimizasyon algoritmalarının uygulanması ve kıyaslanması,” *Computer Science*, vol. 5, no. 2, pp. 90-98, 2020.
- [23] M. F. Akca “Gradient Descent Nedir?” Jan.22,2023[Online]. Available:<https://medium.com/deep-learning-turkiye/gradient-descent-nedir-3ec6afcb9900>.
- [24] S. Ruder “An overview of gradient descent optimization algorithms” Jan. 22,2023 [Online]. Available:<https://ruder.io/optimizing-gradient-descent/>
- [25] Matlab [Online] Available:<https://www.mathworks.com/products/matlab.html>
- [26] A. A. Reshi, I. Ashraf, F. Rustam, H. F. Shahzad, A. Mehmood, G. S. Choi, “Diagnosis of vertebral column pathologies using concatenated resampling with machine learning algorithms,” *Peer Journal Computer Science*, vol 7, pp. e547, 2021.
- [27] T. Colombo, M. Mangone, F. Agostini, A. Bernetti, M. Paoloni, V. Santilli, L. Palagi, “Supervised and unsupervised learning to classify scoliosis and healthy subjects based on non-invasive rasterstereography analysis,” *Plos one*, vol.16, no. 12, pp. e0261511, 2021.
- [28] H. Wang, T. Zhang, K. M. C. Cheung, G. K. H. Shea, “Application of deep learning upon spinal radiographs to predict progression in adolescent idiopathic scoliosis at first clinic visit,” *EClinicalMedicine*, vol 42, pp. 101220, 2021.
- [29] Y. Unal, K. Polat, H. E. Kocer, “Pairwise FCM based feature weighting for improved classification of vertebral column disorders,” *Computers in biology and medicine*, vol. 46, pp. 61-70, 2014.